

U. S. A R M Y
TRANSPORTATION RESEARCH COMMAND
FORT EUSTIS, VIRGINIA

TRECOM TECHNICAL REPORT 64-27

RECIRCULATION PRINCIPLE FOR GROUND EFFECT MACHINE:
PRELIMINARY DESIGN OF A RESEARCH VEHICLE

Task 1D021701A04804
Contract DA 44-177-AMC-96(T)

August 1964

6.02
1.50
300p
MICROFILM

AD 608523
AD 608523

prepared by:

MARTIN COMPANY
Orlando, Florida



ARCHIVE COPY

DISCLAIMER NOTICE

When Government drawings, specifications, or other data are used for any purpose other than in connection with a definitely related Government procurement operation, the United States Government thereby incurs no responsibility nor any obligation whatsoever; and the fact that the Government may have formulated, furnished, or in any way supplied the said drawings, specifications, or other data is not to be regarded by implication or otherwise as in any manner licensing the holder or any other person or corporation, or conveying any rights or permission, to manufacture, use, or sell any patented invention that may in any way be related thereto.

DDC AVAILABILITY NOTICE

Qualified requesters may obtain copies of this report from

**Defense Documentation Center
Cameron Station
Alexandria, Virginia 22314**

This report has been released to the Office of Technical Services, U.S. Department of Commerce, Washington 25, D. C., for sale to the general public.

The findings and recommendations contained in this report are those of the contractor and do not necessarily reflect the views of the U.S. Army Mobility Command, the U.S. Army Materiel Command, or the Department of the Army.

BLANK PAGE

HEADQUARTERS
U S ARMY TRANSPORTATION RESEARCH COMMAND
FORT EUSTIS, VIRGINIA 23604

The ejector recirculation lift system was investigated as a means of improving the internal-flow and performance characteristics of air cushion vehicles. The concept permits larger unobstructed stowage areas and lower structural weight. In addition, the system minimizes the performance degradation of air cushion vehicles associated with higher speed and increased base pressure.

The study involved two phases: ejector optimization and fabrication of an air source having the mass flow and pressure characteristics necessary for a vehicle of moderate size.

The results indicate that an energy recovery system of this type is feasible and that performance may be predicted with the same degree of accuracy as for conventional axial flow fan/duct/nozzle systems.

W. E. Sickles

WILLIAM E. SICKLES

Leader

Ground Effect Research Group

APPROVED.

FOR THE COMMANDER:

Larry M. Hewin
LARRY M. HEWIN
Technical Director

**Task 1D021701A04804
Contract DA 44-177-AMC-96(T)
TRECOM Technical Report 64-27**

August 1964

**Recirculation Principle for
Ground Effect Machine:
Preliminary Design of a
Research Vehicle**

Martin Report OR 3725-1

**Prepared by
Martin Company
Orlando, Florida**

**For
U.S. Army Transportation Research Command
Fort Eustis, Virginia**

FOREWORD

The Martin Company, a Division of the Martin-Marietta Corporation, Orlando, Florida, has prepared this report of work accomplished under the sponsorship of the U.S. Army Transportation Research Command during the period from August through December 1963.

It is submitted in accordance with the requirements of Contract No. DA 44-177-AMC-96(T) and contains an account of the execution of the tasks specified in that contract, pursuant to the modification of the Man Carrying Test Vehicle, which was constructed under a preceding contract, No. DA 44-177-TC-710, and was discussed in TRECOM Technical Report 63-27.

The program was conducted under the direction of Mr. K. Cossairt and reflects the contributions of Messers J. Burns and M. Rosenberg.

The consultation services of Dr. G. D. Boehler of Aerophysics Co., N. K. Walker of Walker Associates, P. Payne of Frost Engineering Corporation, and Dr. K. Millsaps of the University of Florida, have been employed in this effort, and their assistance is gratefully acknowledged. Also, extremely valuable assistance for the " Propulsion Investigation" was given by both the General Electric Company and the Continental Aviation and Engineering Corporation.

CONTENTS

Foreword	iii
Illustrations	vi
Tables	x
List of Symbols	xi
Summary	1
Conclusions.	1
Recommendations.	1
Vehicle Characteristics.	3
Component Testing	24
Analytical Studies.	95
Propulsion Investigation	236
Bibliography	246
Appendix I: The Case for the Simple Autopilot	247
Appendix II: Water Analogy of the Recirculation GEM	261
Appendix III: Vehicle Performance Estimates (IBM Machine Program)	272
Distribution.	280

ILLUSTRATIONS

1	Research Test Vehicle, General View	5
2	Research Test Vehicle, Inboard Profile	5
3	Ejector Geometry and Nomenclature	6
4	Driver Controls, Schematic	12
5	Primary Air Control Valve	14
6	Exit Flap Actuator	16
7	Performance, Lift Versus Height	22
8	Two-Dimensional Stability and Control Model	25
9	Stability and Control Model Geometry, Sketch	25
10	Ejector Configuration.	26
11	Primary Nozzle Installation	26
12	Location of Static Pressure Taps	28
13	Base Pressure Versus Height (Half-Scale Model)	32
14	Base Pressure Versus Height, $\delta_i = 20^\circ$, $\delta_o = 30 \pm 10^\circ$	32
15	Base Pressure Versus Height, $\delta_i = 30^\circ$, $\delta_o = 30 \pm 10^\circ$	33
16	Base Pressure Versus Height, $\delta_i = 40^\circ$, $\delta_o = 30 \pm 10^\circ$	33
17	Cavity Pressure Versus Height, $\delta_i = 20^\circ$, $\delta_o = 30 \pm 10^\circ$	35
18	Cavity Pressure Versus Height, $\delta_i = 30^\circ$, $\delta_o = 30 \pm 10^\circ$	35
19	Cavity Pressure Versus Height, $\delta_i = 40^\circ$, $\delta_o = 30 \pm 10^\circ$	36
20	Moment Versus Angle at Constant Lift, Inlet Sealed	36
21	Moment Versus Angle at Various Heights, Inlet Sealed	37
22	Moment Versus Angle at Constant Lift, Inlet Open	37
23	Moment Versus Angle at Various Heights, Inlet Open	38
24	Control Moment Versus Differential Primary Pressure When $h = 9$ Inches	40
25	Control Moment Versus Height When $\Delta P_o' = 1$ psi	40
26	Control Moment Versus Height, $\Delta\delta = 12^\circ$	41
27	Control Moment Versus Height, Vary $\Delta\delta$, $\Delta P_o' = 1$ psi	41
28	Corner Module Model.	54
29	Assembly Drawing of Corner Model	56
30	Front View of Quarter Model	57
31	Three-Quarter View of Model	57
32	Primary Airlines, Quarter Model	58
33	Instrumentation and Test Setup, Quarter Model	58
34	Comparison of Side and Corner Ejector Internal Line	60
35	Header Nomenclature and Dimensions	60
36	Header and Nozzle Locations	62
37	Area Section of Base	63
38	Area Section of Cavity	64

39	Header Calibration Test (Front View)	65
40	Header Calibration Test (Side View)	65
41	Comparison of Theoretical and Measured Mass Flow, Half-Scale Quarter Model (Corner)	68
42	Comparison of Theoretical and Measured Mass Flow, Half-Scale Quarter Model	68
43	Pressure Orifice Locations	70
44	Base Pressure Versus Flap Angle, Corner Model	73
45	Base Pressure Versus Height, Corner Model	73
46	Cavity Pressure Versus Height, Corner Model	74
47	Quarter Model Base Partition Combinations	76
48	Component Base Pressure	77
49	Component Base Pressure	77
50	Component Base Pressure	78
51	Isobar Distribution, Basic Configuration	81
52	Isobar Distribution, Basic Configuration with 3-Inch Inlet Extensions	82
53	Pressure Distribution, Side-Front Ejectors Isolated	83
54	Corner Pressure Distribution, Basic Run	84
55	Corner Pressure Distribution, Ejectors 1, 2, 3, and 4	84
56	Corner Pressure Distribution, Ejectors 1, 2, and 3	85
57	Corner Pressure Distribution, Ejectors 1 and 2	85
58	Corner Pressure Distribution, All Ejectors	86
59	\bar{P}_B versus $P_{O'}$, Inlet Extension	89
60	Surface Roughness, Ditch	89
61	Terrain Geometry	91
62	Terrain Model Geometry, Obstacle	91
63	Terrain Model, Trench, $h/\Delta H = 0.24$	92
64	Terrain Model, Trench, $h/\Delta H = 0.71$	92
65	Corner Model, Water Test, General View	94
66	Corner Model, Water Test, Operation	94
67	Compressor Map, Primary Mass Flow Versus Pressure	96
68	Compressor Map, Primary Mass Flow Versus Efficiency	96
69	Primary Mass Flow Versus Pressure	97
70	Primary Mass Flow Versus Pressure, Primary Horsepower = 10	97
71	Lift per Horsepower Versus Absolute Total Pressure of Primary Flow	99
72	Performance, Gage Base Pressure Versus Height	103
73	Power Required Versus Forward Speed	103
74	Ejector Nomenclature, Recirculation	109
75	Ejector Nomenclature, Straight	109
76	Equilibrium of Forces, Bifurcating Jet Region	117
77	Re-entrant Jet Region	119

78	Forward Speed Regimes	122
79	Leading Edge Recirculation Flow, "Transition" Regime	122
80	Leading Edge Recirculation Flow, "Super Critical" Regime.	124
81	Recirculation Flow in the "Damping" Condition.	124
82	Vehicle Control Moment	130
83	Vehicle Rolling Moment in Sideslip.	133
84	Steadiness in Yaw (GEMs and Helicopters)	137
85	Vertical Fins for Neutral Stability	137
86	Univector Control Column.	141
87	Turning Circle of Research Vehicle Versus Car and Ships.	141
88	Motion Over Short Sea (Pitch)	147
89	Motion Over Short Sea (Yaw).	148
90	Flying Height to Clear Waves, Longest and Shortest Wavelengths	150
91	Flying Height to Clear Waves; Wavelength = 2 x GEM Length.	150
92	Flying Height to Clear Waves; Wavelength = 1 x GEM Wavelength.	151
93	Signal Flow, Simplest System	158
94	Signal Flow, Rate Gyro System	161
95	Signal Flow, System Insensitive to Surface Contours	162
96	Vehicle Static Stability	163
97	Definition of Momentum Flux Components	167
98	Cushion Pressure for Example Case.	169
99	Definition of Velocities	172
100	Effect of Cavity Vorticity Upon Cushion.	172
101	Variation of Cavity Pressure with h_1/t_1	174
102	Critical Mass Ratio for Zero Cavity Pressure	175
103	Assumed Static Pressure Distributions for Thin Jet Analysis	175
104	Nozzle Exit Velocities	179
105	Variation of Mass Ratio Coefficient C_m with Mass Ratio m/m^i	187
106	Cavity with Flexible Trunk	194
107	Entrainment in a Two-Dimensional Jet	195
108	Ratio of Dynamic Pressure q Jet to Initial Value q_0 as a Function of Jet Length	198
109	Entrainment in a Partially Recirculating Jet	198
110	Free-Air Entrainment Periphery for Recirculating Jet	200
111	Cavity Zone Entrainment Loss Sketch	201
112	Theoretical Cushion and Cavity Pressure for a Recirculation Test Rig	206

113	Predicted and Measured Total Head Loss for Martin Model No. 1	206
114	Losses Due to Stable Vortex in Cavity Zone	207
115	Losses Attributable to Adverse Pressure Gradient	208
116	Simple Uniform Jet	210
117	Sketch of System Which Lowers Jet Velocity	211
118	Basic Geometry of Jet Pump	213
119	Optimum Mixing Pressure for a Static Eductor	216
120	Optimum Mixing Duct Area at Completion of Mixing	216
121	Variation of Optimum A_j/A_1 With n	217
122	Optimum Diffuser Ratios A_2/A_m With Static Eductor	217
123	Variation of Optimum Thrust Augmentation With Diffuser Efficiency η_D	218
124	Limit Augmentation Available as $n \rightarrow \infty$	218
125	Efficiency of Optimum Jet Pump Under Static Conditions	219
126	Velocities in an Eductor	220
127	Total Mixing Length Parameter as a Function of Entrainment Ratio and Diffuser Efficiency	221
128	Propulsion Unit, Assembled, Side View	237
129	Propulsion Unit, Assembled, Rear View	238
130	Propulsion Unit, Test Stand	238
131	Propulsion Unit, Compressor, Front View	239
132	Propulsion Unit, Compressor, Rear View	239
133	Primary Pressure Duct System Critical Path Stations	243
134	Jet Thrust Versus Jet Pressure ($P_{tj}/P_{sa} = 0$ to 15)	243
135	Jet Thrust Versus Jet Pressure Ratio ($P_{tj}/P_{sa} = 0$ to 7)	244
136	Improvement in GEM Performance and Cost Due to the Use of an Autopilot - No Allowance for Structural Weight Savings	259
137	Improvement in GEM Performance and Cost Due to the Use of an Autopilot - Allowing 10 Percent Reduction in Structural Weight.	259
138	Sketch of Two-Dimensional Working Model	265
139	Total Power Parameter	276
140	Lift Coefficient Versus Loading Parameter	276
141	Power Loading Versus Power Parameter	277
142	Ejectijet GEM Performance, $60,000 < W_g < 100,000$	277
143	Theoretical Cavity Pressure	278
144	Visualization of Flow.	279

TABLES

1	Weights Summary.	8
2	Summary of Maximum Possible Errors	30
3	Double Ejector Stability and Control Tests	43
4	Double Ejector Stability and Control Tests	46
5	Nozzle Alignment Effects.	55
6	Nozzle Angle Calibration.	66
7	Two- and Three-Dimensional Pressures	79
8	Effect of Sealing.	87
9	Summary of Performance Data.	101
10	P_o' Loss	242
11	"Amphibian" GEM	250
12	"Small" GEM.	251
13	"Large" GEM	242
14	"Amphibian" GEM (With Autopilot)	255
15	"Small" GEM (With Autopilot).	256
16	"Large" GEM (With Autopilot)	257
17	Cost and Payload Estimates for Inherently Stable GEMS	258

LIST OF SYMBOLS

<u>Symbol</u>	<u>Quantity</u>	<u>Dimension</u>
A	Area	ft ²
A'	Exit area of primary nozzle	ft ²
A''	Cross-sectional area of secondary stream in exit plane of primary nozzle	ft ²
A'*	Throat area of primary nozzle	ft ²
A _w	Wetted area of ejector	ft ²
a	Wetted area shape parameter	-
AR = A'/A'	Ejector area ratio	-
b	Length shape parameter	-
c	Perimeter of base area	ft
c ₁	Chord length of inlet extension (skirt)	In.
c _p	Specific heat at constant pressure	Btu/lb°R
c _v	Specific heat at constant volume	Btu/lb°R
C _D	Drag coefficient, D/qS	-
C _{D_f}	Profile drag coefficient, D _f /qS	-
C _{D_m}	Momentum drag coefficient, D _m /qS	-
C _L	Lift Coefficient, L/qS	-
D	Drag	lb
D _f	Profile drag	lb
D _m	Momentum drag	lb
\bar{D}	Vehicle effective diameter,	ft
	$\sqrt{\frac{4}{\pi} S}$	

<u>Symbol</u>	<u>Quantity</u>	<u>Dimension</u>
F	Total shear force on walls of mixing section	lb
F_H	Horizontal component of force acting on ejector ducting	lb
F_V	Vertical component of force acting on ejector ducting	lb
F_z	Lifting force in heave	lb
F_A	Force applied to ejector air	lb
h	Height of vehicle base above the ground	ft
\bar{h}	Mean height of pitched vehicle	ft
HP'	Primary horsepower, $\left(\frac{1}{2} \frac{m' V'^2}{550} \right)$	HP
I_{yy}	Moment of inertia, pitch axis	ft-lb-sec ²
J	Total momentum of tertiary flow	lb
j	Momentum of tertiary flow per unit length	lb/ft
K	Constant	-
L	Lift	lb
\mathcal{L}	Vehicle rolling moment	ft-lb
l	Length of the mixing section	ft
l	Vehicle length	ft
\mathcal{M}	Vehicle pitching moment	ft-lb
\mathcal{N}	Vehicle yawing moment	ft-lb
m	Tertiary mass flow	slugs/sec-ft, or lb/sec-ft
m'	Primary mass flow	slugs/sec-ft, or lb/sec-ft

<u>Symbol</u>	<u>Quantity</u>	<u>Dimension</u>
p	Pressure	lb/ft ²
P_o	Absolute total pressure of tertiary flow	lb/ft ²
P_o'	Total pressure of primary flow, gage	lb/in. ²
P_B	Gage base (air cushion) pressure	lb/ft ²
\bar{P}_B	Average base pressure	lb/ft ²
P_c	Gage cavity pressure, static pressure between exit and inlet under the re-circulating ejector	lb/ft ²
p_1	Gage static pressure at inlet of ejector mixing section	lb/ft ²
p_2	Gage static pressure end of mixing section of ejector	lb/ft ²
p_3	Static pressure of tertiary flow of ejector at exit	lb/ft ²
ΔP_c	Difference between forward and aft cavity pressures	lb/ft ²
P	Total installed vehicle power	HP
q_∞	Dynamic pressure of free stream in forward flight	lb/ft ²
q_j	Dynamic pressure of the jet	lb/ft ²
R	Universal gas constant	1715 ft lb/slug ^o R
sfc	Specific fuel consumption	lb/HP-hr
S	Vehicle projected planform area	ft ²
S_B	Base area	ft ²
S_c	Cavity area	ft ²
T_o	Total temperature	^o R

<u>Symbol</u>	<u>Quantity</u>	<u>Dimension</u>
t	Jet thickness	ft
τ	Time	sec
V	Free stream velocity	ft/sec
V_a	Tertiary jet average velocity at nozzle exit	ft/sec
V_f	Vehicle forward speed	mph or ft/sec
V_2	Tertiary velocity at end of mixing section	ft/sec
w	Vehicle width	ft
χ	Exponential parameter = $(t/h) (1 + \sin \theta)$	-
W	Vehicle weight	lb
W_p	Vehicle payload	lb or ton
Z	Vertical displacement in heave	ft
\dot{Z}	Time rate of change of heave	ft/sec
\ddot{Z}	Acceleration in heave	ft/sec ²
α	Pitch angle	Radians
$\dot{\alpha}$	Pitch rate	sec ⁻¹
$\ddot{\alpha}$	Angular acceleration in pitch	sec ⁻²
$\partial F_z / \partial Z$	Damping derivative	lb sec/ft
ρ	Static density	slugs/ft ³ or lb/ft ³
ρ_0	Total density	slugs/ft ³
δ_1	Exit flap angle, inner (from horizontal)	Degrees
δ_0	Exit flap angle, outer (from horizontal)	Degrees
ϵ_0	Overall recirculation efficiency	Percent
ϵ_c	Recirculation compressor efficiency	Percent

<u>Symbol</u>	<u>Quantity</u>	<u>Dimension</u>
ϵ_R	Recirculation ejector efficiency = ($m_3 V_3^2 / m' V'^2$)	Percent
η	Thrust augmentation	-
θ_1	Angle of secondary inlet measured from horizontal	Degrees
θ_2	Angle of tertiary exit measured from horizontal	Degrees
ϕ	Vehicle roll angle	Degrees
ψ	Vehicle yaw angle	Degrees
γ	Ratio of specific heats	-
m/m'	Mass augmentation	
\vec{n}	Unit vector normal to the area of integration	-
\vec{i}	Unit vector in the axial direction of the stream in the mixing section	-
ζ	Damping ratio	-
ζ_p	Damping ratio in pitch	-

Subscripts in Reference to Ejector

1 - Conditions at Station 1	(Inlet of ejector)
2 - Conditions at Station 2	(End of mixing)
3 - Conditions at Station 3	(Exit)

Superscripts in Reference to Ejector

' - Primary flow
" - Secondary flow

Note:

Any symbols not listed above are defined in the proper sections. A small arrow over a symbol is used to indicate vector quantities.

BLANK PAGE

SUMMARY

The preliminary design of a Ground Effect Machine (GEM) employing an ejector-recirculation principle for lift is presented in this report.

The scope of the work includes:

1. The modification and test of an engine-compressor unit from Government-furnished equipment (GFE),
2. Supporting component testing, both two and three dimensional, and data analysis of the improved ejector configuration;
3. The basic engineering required for the preliminary design of the vehicle configuration, controls, power-plant installation, basic structure, and performance estimates.

CONCLUSIONS

The adequacy of the primary air supply system, coupled with reliable performance data, evolved from the test and analysis accomplished in the effort reported here, assures the feasibility of constructing a full-scale operating vehicle, adequate for the environmental research and performance evaluation of the recirculation GEM.

RECOMMENDATIONS

The results of this effort have indicated, rather than established, the potential performance of an optimized vehicle design. Prior to undertaking the refinements necessary for optimum performance, it is recommended that:

1. Detailed design of the present configuration be completed and the test vehicle be constructed.
2. Tests be conducted:
 - a. To confirm the lift, stability, control, and maneuver characteristics indicated by the data.

- b. To determine the effect on performance of surface roughness, ditches, obstacles, etc.
 - c. To establish stability, control and maneuver criteria.
 - d. To determine the effect of a water and surf environment.
3. After the successful completion of the hover and low-forward-speed tests, it is recommended that the vehicle be modified for high-speed forward-flight capability. Tests could then be conducted to investigate the environmental and operational problems associated with specific missions.

VEHICLE CHARACTERISTICS

The GEM described in this report is primarily a research test vehicle which employs an ejector recirculation principle (Reference 1) to obtain lift. The vehicle is approximately 20 feet wide, 29 feet long, and 5 feet high, and weighs 2,600 pounds empty. The initial purpose of the vehicle is to investigate the hovering and low-forward-speed characteristics of this new and different concept in ground effect machines. The ultimate objective is to utilize the vehicle as a basic test bed which can be modified easily and tested over a broad range of conditions.

No attempt has been made to "optimize" the vehicle performance, as this would presuppose knowledge from the vehicle flight test program. Undoubtedly, the "optimum" vehicle will be a compromise of such factors as the hover-lift performance, forward-flight effects, stability and control, fabrication costs, and environmental and operational considerations. Certainly, the performance of the recirculating ejector is of paramount importance in determining the overall performance of the vehicle. From Reference 1, in particular section 8.3, an ejector performance which is superior to that currently obtained is predicted. More recently, as shown in a later chapter of this report, "Analytical Studies," an even more impressive improvement is predicted. However, to illustrate that the basic performance of the current configuration is entirely adequate for this phase of the research program, the following values are estimated for the high-speed forward-flight configuration:

$$\text{Figure of Merit: } \frac{h \cdot W^{3/2}}{P \cdot D^2} = 2.9 \text{ to } 3.5$$

$$\text{Vehicle Efficiency: } \frac{P \cdot sfc}{W_p \cdot V_f} \approx 1.0$$

Gross Weight to Power Ratio: 11 to 13

Payload to Power Ratio: 6 to 7

Payload to Gross Weight: 50 to 65 Percent

Height to Diameter Ratio: 0.06 to 0.09 (without skirts)

CONFIGURATION

The overall size and shape of the Martin GEM are shown in Figures 1 and 2. The basic structure is essentially a flat raft with a central superstructure which contains the driver compartment, engine, fuel, and accessory equipment. Conventional light aircraft construction techniques utilizing aluminum skin, beams, and riveted joints are employed.

In order to facilitate configuration changes and to simplify the fabrication, a modular concept is used with the ejector assemblies. Only two basic ejector assemblies are required: 8 straight units and 16 corner units. Three straight units will be attached to each side of the vehicle and one each in the front and rear. Four corner units will be attached at each of the four corners. These units can be interchanged, replaced and/or subsequently modified. In addition, the fabrication cost is significantly reduced by using this modular concept. The recirculating-ejector geometry and nomenclature are shown in Figure 3.

STRUCTURAL DESIGN

The base platform is treated as a torque box utilizing simple straight-line elements with no curved surfaces. This type of structure utilizes "soft" tooling and affords convenient modification simply by the addition of extra "cells." The additional base platform area required for the research vehicle was provided in this manner, thereby utilizing a major portion of existing structure. The addition of brackets

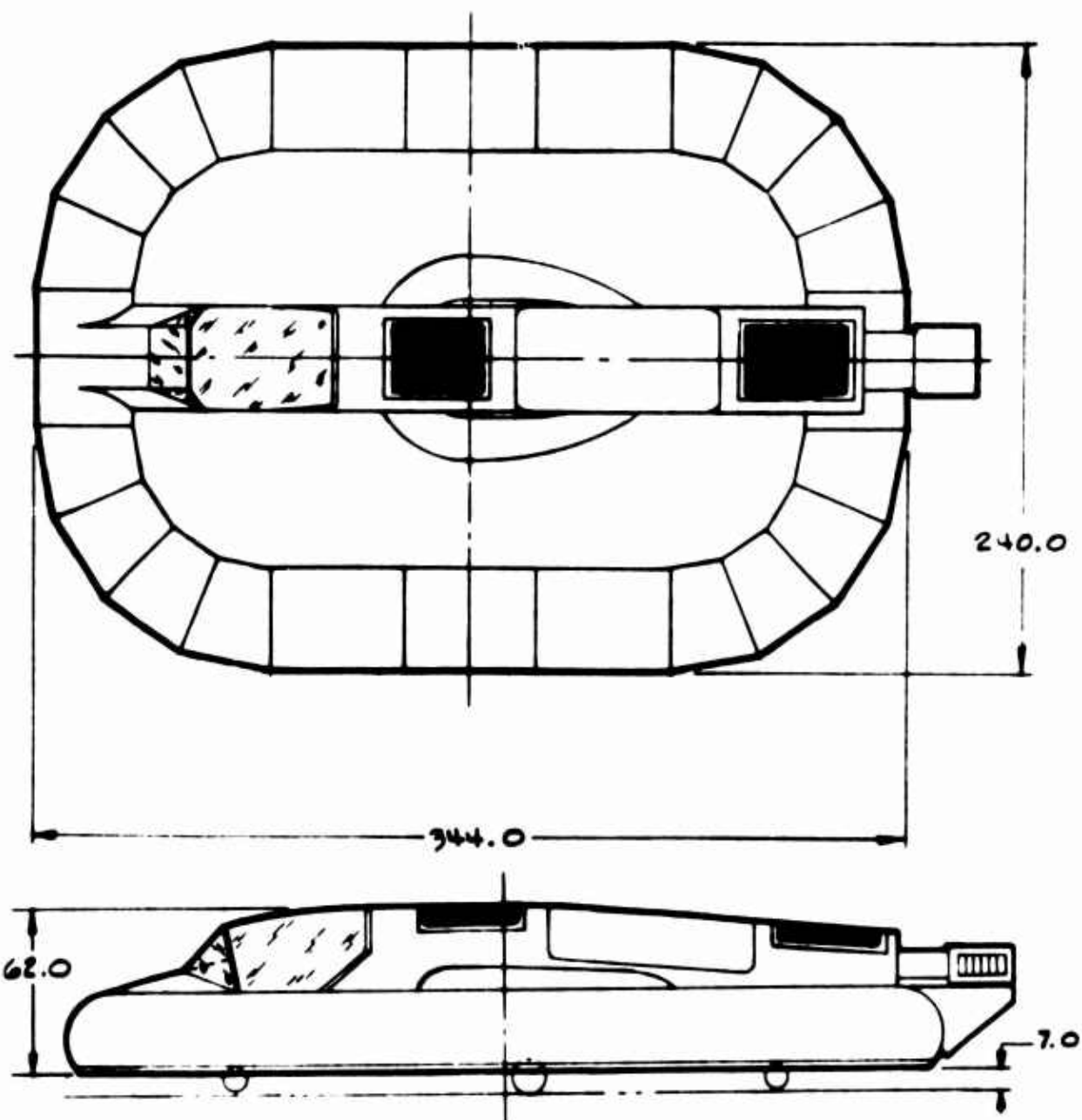


Figure 1. Research Test Vehicle, General View

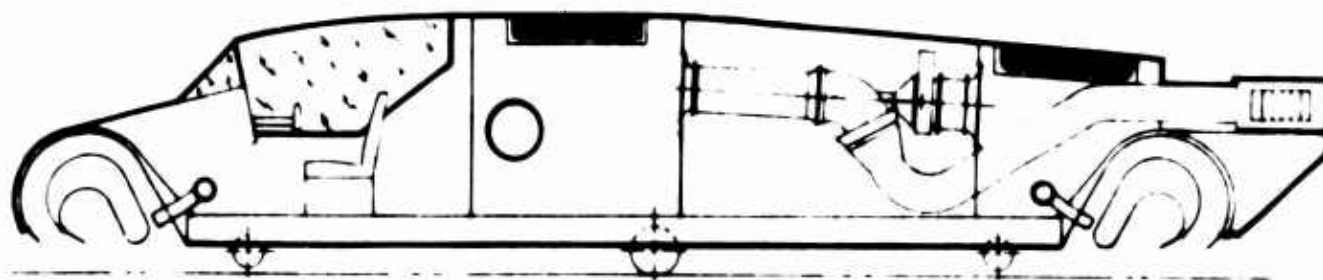


Figure 2. Research Test Vehicle, Inboard Profile

* = VARIABLE

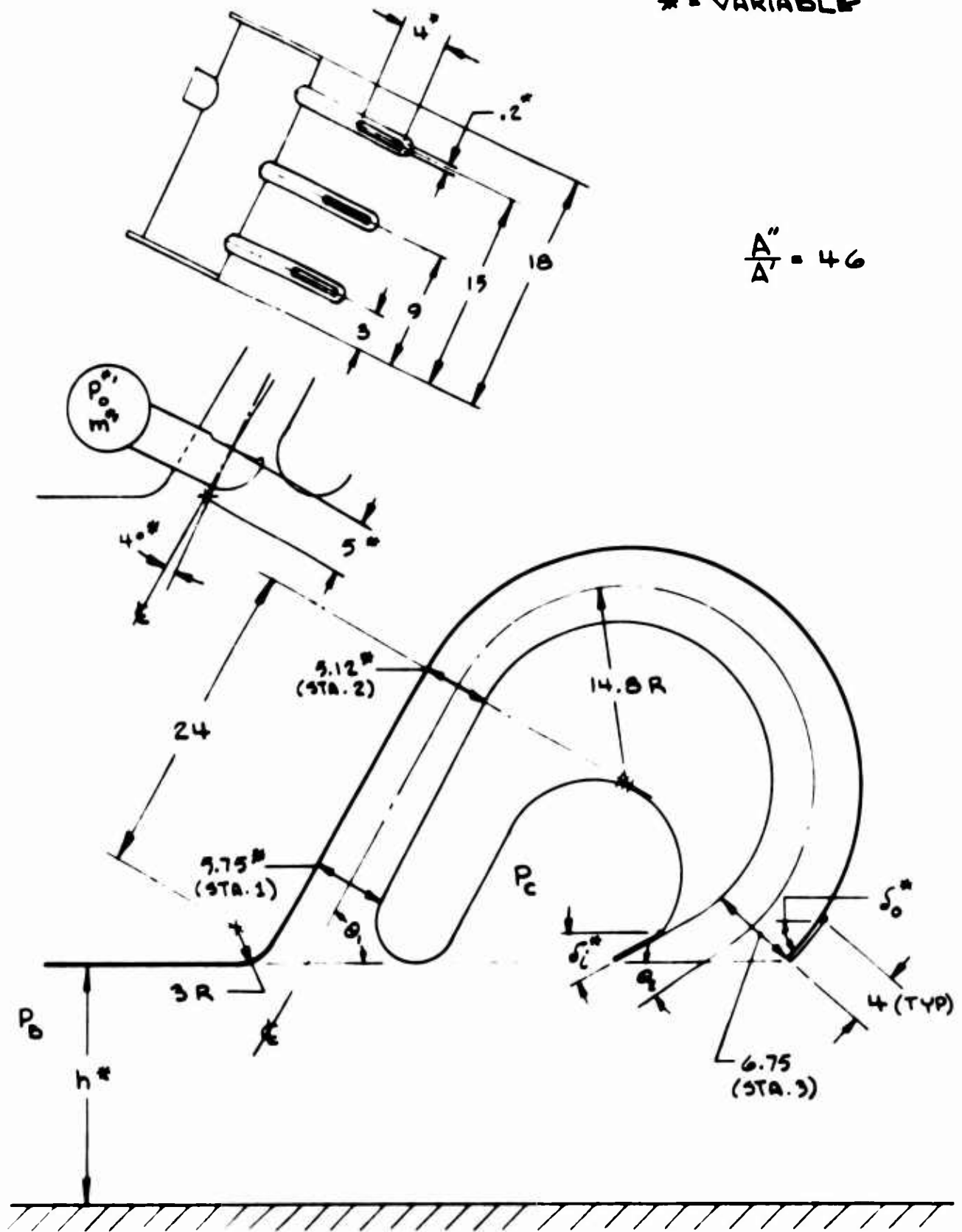


Figure 3. Ejector Geometry and Nomenclature

and mounts is also conveniently accomplished by picking up fasteners at the nearest structural member since the vehicle is essentially a grid of beams, ribs, and stringers.

The base platform structure supports the vehicle equipment and payload in addition to transmitting the base pressure to the entire vehicle. The dimensions of the platform are 248 inches by 144 inches, with beams running the long dimension and ribs running the width. This grid of beams and ribs is covered by aluminum skin to form a torque box. All skin gages are basically 0.032 inch. Six main beams extend the length of the structure and are spaced laterally at appropriate intervals to accept mounting of engines. Cap strips are placed over the flanges of the beams to provide sufficient material to carry bending loads in the beam caps. These caps also serve as skin splices in some cases. Depending upon load requirements, the cap thickness varies from 0.040 to 0.125 inch. Beam web thickness is 0.063 inch with flanged lightening holes incorporated for stiffening. Major shear loads and concentrated loads are introduced to the beams, either directly by attaching fittings or indirectly as transferred from ribs to beams. Ribs are also stiffened by flanged lightening holes. Web thickness varies from 0.032 to 0.063 inch depending upon local load requirements. Conventional round head rivets are used except in blind areas where pull-type rivets are used.

Main landing-gear wheel wells are provided in the basic structure. Landing-gear loads are transferred to main beams by means of intercostals and brackets. Nose and tail wheel equipment is attached to the base platform.

The recirculating ejector assemblies consist of a closed box beam which forms the aerodynamic configuration for the inner wall and cavity area. The beam acts as a torque box under normal loads and

is semimonocoque with 0.025 inch aluminum skin. The outer wall of 0.020 inch aluminum is attached to the torque box by means of end plates. External ribs serve to stiffen the outer wall and provide attachment to the base platform. The end plates resist any warpage which may be produced by torsional loads.

A conventional "dog-house" structure is provided aft of the driver enclosure to form the engine and compressor air intake plenum chambers and to provide a removable engine fairing.

WEIGHTS SUMMARY

A stripped (minimum equipment) vehicle will have an empty weight of 2,585 pounds distributed as shown in Table I. The anticipated weight increase for the high-speed forward-flight configuration is also shown. A vehicle having a closed cockpit, engine fairings and propulsion units that supply approximately 1,000 pounds of thrust will weigh 4,000 pounds empty. The forward propulsion units will incorporate reversible pitch propellers for braking, backing up, and down-hill maneuvering. Each propulsion unit will have a rudder mounted in the slipstream of the propellers for additional yaw control.

TABLE I

WEIGHTS SUMMARY

	Low Speed (lb)	High Speed (lb)
<u>Base Structure</u>		
Original base	525	525
Fase extensions	175	175
Back-up structure (landing gear, engine mount, lifting lugs, etc.)	<u>50</u>	<u>50</u>
	750	750

TABLE I (Cont)

	Low Speed (lb)	High Speed (lb)
<u>Ejectors</u>		
Headers	-	-
Nozzles	-	-
Outer surface	-	-
Center body	-	-
Flaps	-	-
Mounting structure	-	-
	<hr/> 800	<hr/> 800
<u>Engine and Accessories (dry)</u>		
T - 58-GE-8 Gas Turbine	285	285
J-69 compressor	75	75
Drive shaft and compressor outlet	20	20
T-58 tailpipe and vector control box	30	30
Engine mount	30	30
Starter	15	15
Oil tank and plumbing	10	10
	<hr/> 465	<hr/> 465
<u>Primary Ducting</u>		
Diffusers (2)	30	30
Plenum	40	40
Proportioning valves (2)	15	15
Rectangular ducting	20	20
Transitions (rectangular to round)(4)	20	20
Supply tubes to headers (16)	75	75
	<hr/> 200	<hr/> 200
<u>Control System</u>		
Pitch and roll wheel	10	10
Foot pedals for yaw and brakes	10	10
Ejector flap actuators (24) and servo	40	40
Cables, push rods, cranks, chain, pivots etc.	40	40
	<hr/> 100	<hr/> 100

TABLE 1 (Cont)

	Low Speed (lb)	High Speed (lb)
<u>Instruments and Electrical System</u>		
Cockpit instruments	20	30
Engine instruments	15	15
Battery	12	20
Generator	15	15
Switches, circuit breakers, panel lights, etc.	6	10
Intercomponent wiring	<u>30</u>	<u>40</u>
	98	130
<u>Driver Accommodations</u>		
Seat	12	12
Windshield wiper and washer	0	10
Seat belt	0	5
Communications equipment	<u>0</u>	<u>25</u>
	12	52
<u>Landing Gear</u>		
Main wheels	30	30
Main wheel brakes	0	10
Castoring nose and tail wheels	<u>20</u>	<u>20</u>
	50	60
<u>Miscellaneous</u>		
Plexiglas canopy	0	55
Engine compartment fairing	0	130
Air intake screens	40	24
Lights	0	20
Decking over primary air supply ducts	0	200
Inflatable bumper around vehicle	0	40
Fuel tanks (2) and plumbing	50	50
Cockpit and cowl fairing	0	30
Dashboard and consoles	20	20
Windshield and frame	<u>0</u>	<u>30</u>
	110	599

TABLE I (Cont)

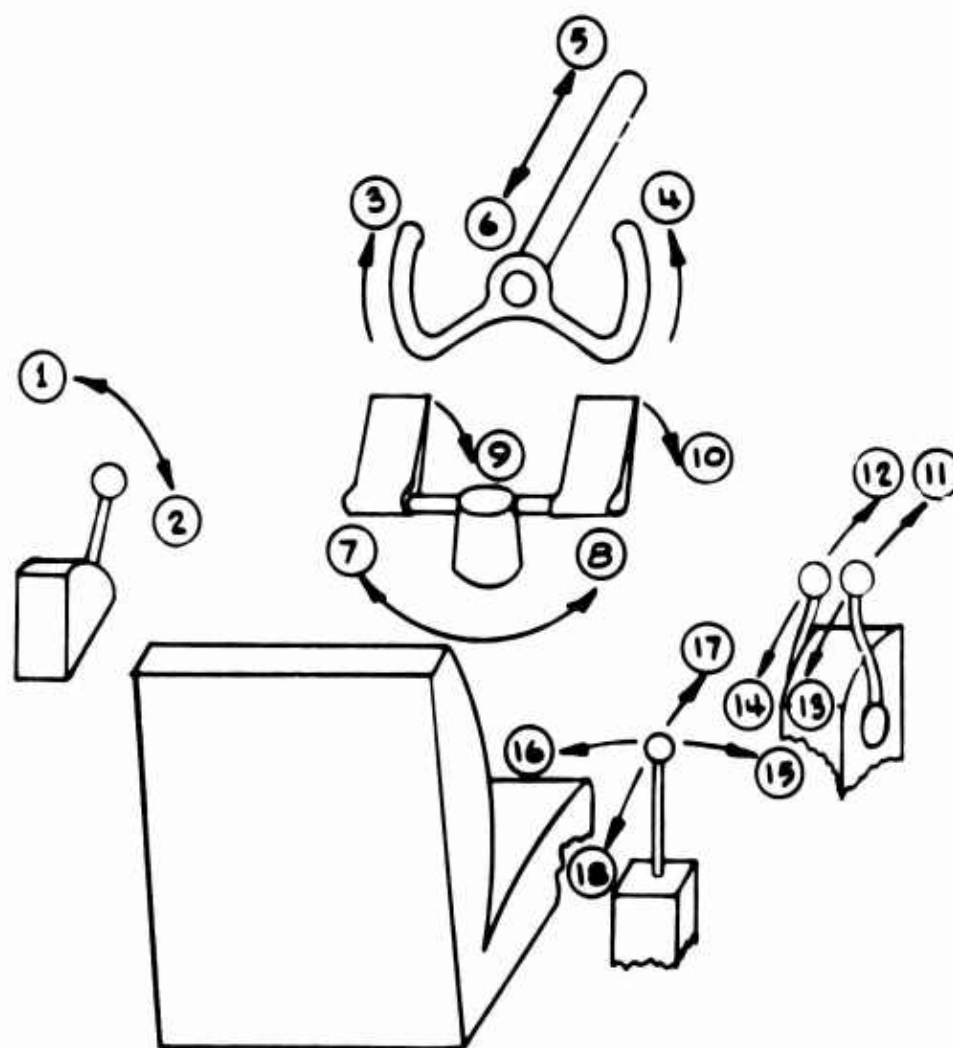
	Low Speed (lb)	High Speed (lb)
Propulsion Units (2)		
Engine, 80- to 100-hp Lycoming, Continental, Franklin	0	450
Reversible pitch propeller 54 in. dia McCauley	0	70
Engine mount	0	80
Engine cowl and spinner	0	60
Rudders (4)	0	40
Engine accessories (starter, oil cooler, tach gen, etc.)	0	40
Cockpit controls and instruments	0	30
Fuel tanks and plumbing	0	30
	<u>0</u>	<u>800</u>
Total Empty Weight	2,585	3,956

CONTROLS

In keeping with the research philosophy of the vehicle, most of the vehicle controls are presented to the driver separately. In this manner a complete evaluation can be made of the driver controls both separately and in various combinations. From these results, the final driver control system can be evolved through the elimination and/or coordination of the most effective schemes. Figure 4 is a schematic of the initial driver controls, the functions of which are described below.

Height

Moving a lever, located to the left of the driver, up and down, actuates the fuel control of the gas turbine. Full-up position affects maximum power (height), and down position idles the engine.



Key

- | | |
|--------------------------------------|--|
| 1. Turbine - Full Power | 11. Right Propulsion Unit Full Power Fwd |
| 2. Turbine - Idle | 12. Left Propulsion Unit Full Power Fwd |
| 3. Primary Control - Roll Right | 13. Right Propulsion Unit Full Power Aft |
| 4. Primary Control - Roll Left | 14. Left Propulsion Unit Full Power Aft |
| 5. Primary Control - Pitch Nose Down | 15. Trim Control - Roll Right |
| 6. Primary Control - Pitch Nose Up | 16. Trim Control - Roll Left |
| 7. Right Turn | 17. Trim Control - Pitch Nose Down |
| 8. Left Turn | 18. Trim Control - Pitch Nose Up |
| 9. Right Wheel Brake | |
| 10. Left Wheel Brake | |

Figure 4. Driver Controls, Schematic

Directional Heading (Yaw)

Foot pedals, similar to those in light aircraft, will differentially control the vanes in the exhaust of the lift engine. In this manner, the residual thrust of the gas turbine is deflected to provide a yawing moment during hover and low forward speeds. At high forward speeds, aerodynamic surfaces (rudders) will be deflected by the same driver control mechanism to provide the required yawing moment. In addition, toe pedals are provided for individual braking of the two main "landing" wheels.

Pitch and Roll (Primary Control)

As was mentioned above, various combinations of driver controls are available; this is particularly true for the pitch and roll modes. From the results of studies described elsewhere in this report, a moment may be obtained by differentially controlling the pressure in the ejector primary nozzles or by changing the exit flap angle. Initially, the primary control for pitch and roll will be accomplished by varying the pressure in the primary air lines. Figure 5 illustrates the mechanism used to proportion the primary air supply with respect to the front and rear (pitch) or sides (roll). There are two such valves which are directly controlled from the driver's steering wheel.

Movement of the wheel fore and aft will cause a change in pitching moment on the vehicle. Rotating the wheel will cause the vehicle to roll in the direction the wheel is turned.

Pitch and Roll (Trim Control)

A trim control is provided primarily to correct for a variation in the center of gravity location. A small "joy stick" is located to the right of the driver. This remotely controls the exit flap angles. The at-

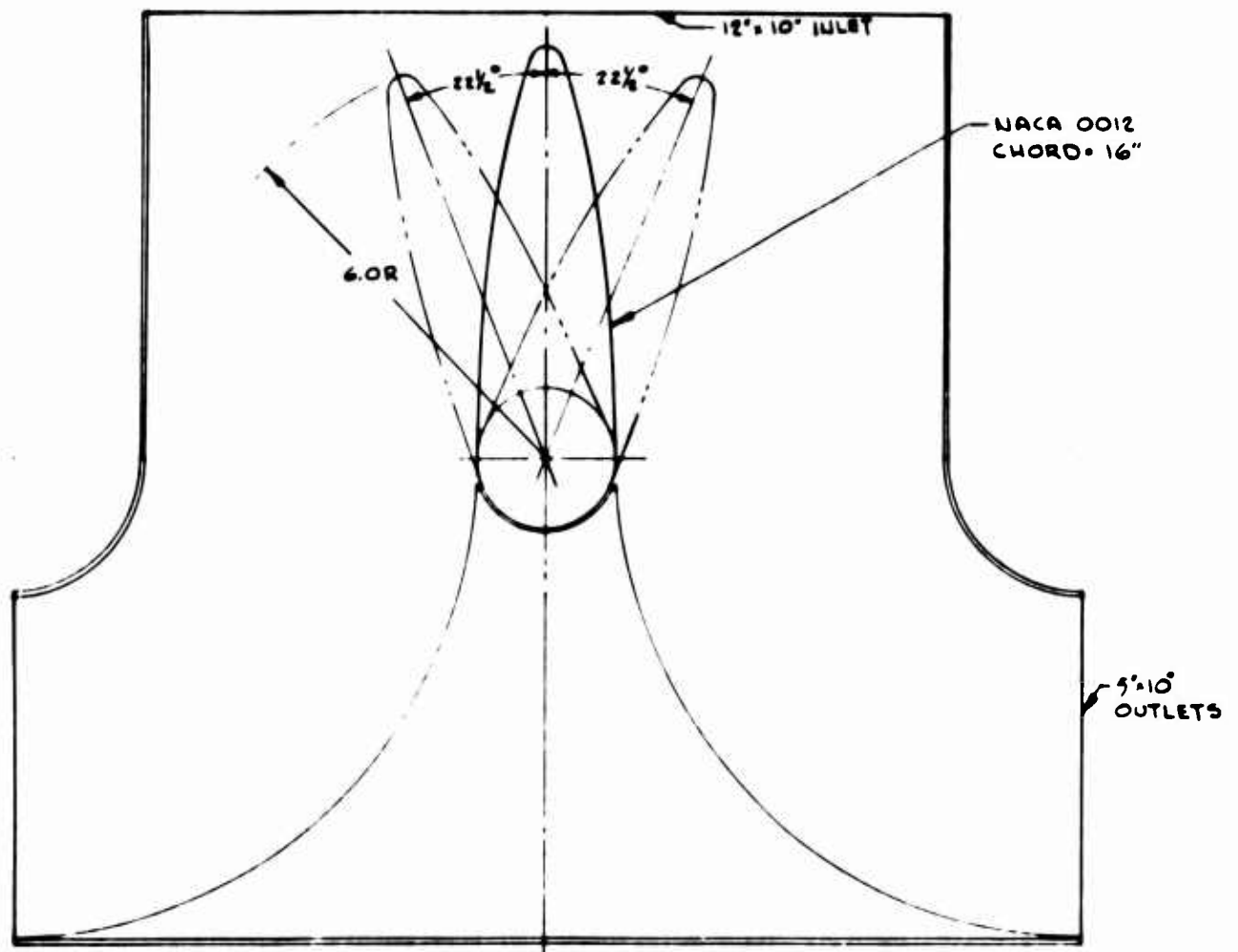


Figure 5. Primary Air Control Valve

titude (in pitch and roll) of the vehicle will be changed by a movement of the lever in the direction of the tilt required. This manual control can be replaced by an autopilot, as is discussed in detail in the following sections on "Stability" and "Analytical Studies" and in Appendix I. A sketch of the exit flap actuator is shown in Figure 6. An inner flap shown in this figure is movable, but only by prior adjustment. This flap adjustment affects performance (base pressure) rather than control and would be moved only occasionally in the research test program.

Forward Flight

During the hover and low-forward-speed flight tests, the residual thrust (125 pounds) of the gas turbine is sufficient to move the vehicle to a maximum speed of 25 mph. During the hover phase, the thrust is nulled as described earlier in the section on directional control. For high-speed forward flight, provisions have been made to accommodate separate forward-flight propulsion units.

STABILITY

The results of the two dimensional stability and control tests, shown in a later section of this report, "Component Testing", indicate that the inherent static stability will vary slightly with height and angle of tilt. It is also indicated that the configuration is slightly unstable at some combinations of height and tilt angle. It is well known that the static stability characteristics of the conventional annular jet GEM are different in the three-dimensional configuration than for the two-dimensional case. The difference invariably results in the stability properties over a broader range of height and angle of tilt than is realized in two dimensions. Similarly, the two-dimensional stability and control tests are intended only to show basic trends and order of

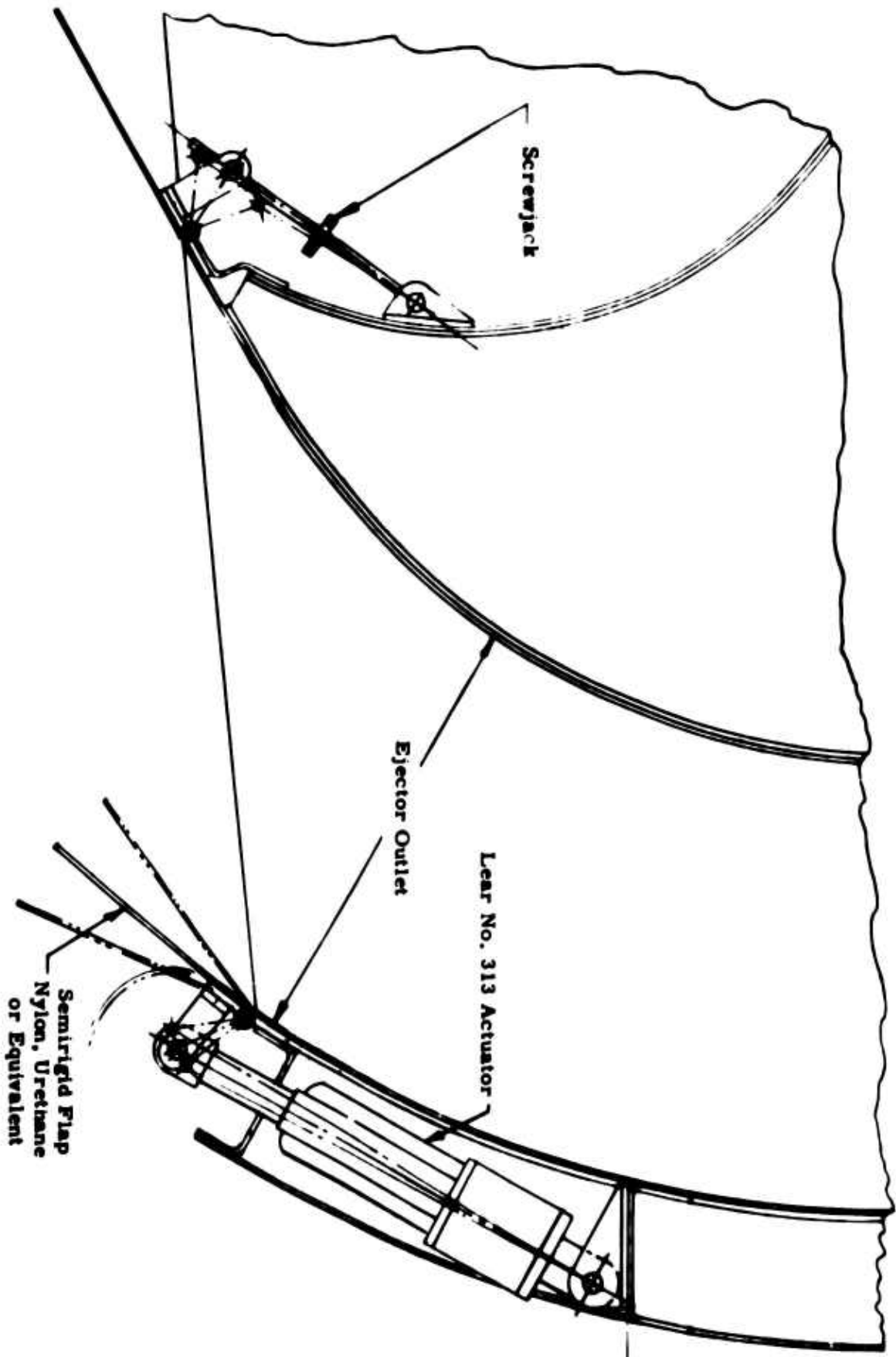


Figure 6. Exit Flap Actuator

magnitude. Based on the test results of both the two-dimensional and three-dimensional corner models and on previous tests of a small-scale three-dimensional model (Reference 2) and large-scale three-dimensional vehicle (Reference 3), it is concluded that:

1. The vehicle will, for all practical purposes, have neutral stability over the major portion of the height and tilt range and will probably have a small amount of positive static stability at a normal cruising condition (height = 18 inches, tilt = ± 3 degrees).
2. A relatively large control moment is available either by varying the primary pressure in the ejectors or by varying the exit flap angle. The relative effects of each mode of control are additive; therefore, it is proposed that each method be evaluated separately and that one method be used as a primary vehicle control and the other for a trim or stabilizing control.
3. The control moment response time is estimated to be relatively low (on the order of 50 milliseconds).
4. Serious consideration should be given the use of an autopilot in the pitch and roll planes to apply automatically the required trim moments. In a later section of this report, "Analytical Summary," and in Appendix I, the apparent advantages of an autopilot are shown to outweigh significantly the disadvantages normally associated with this type of installation. This is shown not only for the recirculation type GEM but also for the conventional annular configuration, provided large, fast-acting control moments are available.

PROPULSION (LIFT)

The power-plant installation consists of a General Electric T-58 turbine directly coupled to the first-stage compressor of a Continental J-69. This configuration was chosen because of component availability, the compatibility of the two units with regard to speed of rotation, power output, etc., and because the output of the compressor (pressure and mass flow) matches the requirements of ejector Model 1 very well. As shown in Table I the combined weight of the complete unit is only 465 pounds. This unit, as is, is capable of delivering a maximum of 650 air horsepower of primary air (820 shaft horsepower from T-58). Power is currently limited by the capacity of the J-69 compressor, but with no increase in weight the output could be increased to slightly over 1000 air horsepower (1250 shaft horsepower from T-58). This provides a power-plant installation of 0.37 pound per horsepower from essentially existing hardware.

PROPULSION (HIGH-SPEED FORWARD FLIGHT)

As a later modification, provisions have been made for two aircraft-type reciprocating engines of 80 to 100 horsepower each. These can be mounted on either side of the aft end of the vehicle for propulsion and various degrees of control. Each unit would be mounted symmetrically between two vertical fins having rudders on their aft edges, thereby allowing a propulsion package to be mounted on each side of the vehicle. A 54-inch-diameter reversible-pitch propeller will provide approximately 500 pounds of thrust given a total installed thrust of 1000 pounds, enough to allow forward speeds in excess of 60 knots, and a grade capability of 16 percent (vehicle weight at 5000 pounds).

The two propulsion units will be mounted 8 feet apart athwartship, and by operating one unit with forward pitch and the other in reverse, up to an 8000-foot-pound yawing moment can be applied to the vehicle. Operating both units in reverse will provide effective braking and control during downhill maneuvering. The fins and rudders will provide directional stability and control at higher forward speeds. Installed weight of the propulsion system including empty fuel tanks would be approximately 800 pounds, as shown in Table I.

MISCELLANEOUS CONSIDERATIONS

Noise

Reduction of turbine and compressor noise levels in the cockpit area and to the sides of the vehicle can be accomplished by installing fiberglass batts or similar material inside the engine compartment and on the bulkheads. The design of the inlet and exit is such that there is no straight-line radiated noise at ground level.

Bumper

An inflatable bumper with a semicircular cross section can be mounted around the periphery of the ejectors close to the bottom of the vehicle. This will provide protection to the structure and flap mechanism and will contribute to the flotation.

Landing Gear

Aircraft-type wheels will be mounted just aft of the CG of the vehicle approximately 7 feet apart and will contain individual brakes. Three-hundred-sixty-degree castor - type tail wheels will be mounted at the front and rear, 1 inch to 2 inches higher than the main gear. Therefore, essentially all of the weight of the vehicle is carried by the main wheels, but either end may be pushed down by a man's weight to contact one of the castor wheels for ground handling. Differential braking

on the main wheels will aid in maneuvering on the ground when not cushion borne. In addition, the use of General Motors Hovair Pads appears to complement this system very well. At low speeds on a prepared surface, the overload capability would exceed 20,000 pounds and be limited only by structural considerations of the vehicle.

Ground Handling

Lifting eyes, jack points and a tow bar lug will be provided to aid in the local moving, maintenance, and transportation of the vehicle. A boarding ladder and tether points will also be installed.

Flexible Skirts

As a part of the initial test program, flexible skirts will be attached to the under side of the vehicle base. Essentially, the skirt is an extension of the inner inlet of the recirculating ejector. It tends to reduce the turning radius of the recirculating air curtain in a manner similar to the conventional annular jet configuration.

DRAWINGS

As a part of this preliminary design effort, engineering drawings have been completed and are tabulated below:

- GMC 1302 - Research Vehicle General Arrangement
- GMC 1303 - Research Vehicle Structural Arrangement
- GMC 1304 - Research Vehicle Engine Mount
- GMC 1305 - Research Vehicle Primary Air Supply System
- GMC 1306 - Research Vehicle Schematic - Primary Air
System
- GB 2102 - Turbine and Compressor, Installation
- GB 2103 - Turbine and Compressor Mount and Connection (2
sheets)

- GB 2106 - Turbine and Compressor Instrumentation and Operation
- GB 2107 - Turbine and Compressor Drive Shaft
- GB 7005 - Half-Scale Quarter Model
- GB 7006 - Half-Scale Quarter Model Ejector Corner Lines
- GB 7015 - Half-Scale Quarter Model Pressure Tap Locations

PERFORMANCE SUMMARY

The following tabulation is a summary of the anticipated overall performance of the initial vehicle (low-speed configuration). In addition, Figure 7 shows the lift variation with height.

Height

- Normal cruise: 18 inches with 3000-pound payload
- Maximum: 24 inches, minimum gross weight
- Overload: 12 inches with 6000-pound payload
- Skirts to be installed (removable) to investigate maximum cruise height and/or minimum power at a constant height

Forward Speed

- 0 to 25 miles per hour at 18 inches height

Stability (Static)

- Heave: $\partial P_L / \partial h \geq -10$, from $h = 6$ to 24 inches

- Pitch: $\frac{\partial M / \partial \alpha}{L \times l} = \text{to } -0.010$, for $-3 \text{ deg} \leq \alpha \leq +3 \text{ deg}$
 - Roll: $\frac{\partial L / \partial \phi}{L \times w} = 0 \text{ to } -0.010$, for $-3 \text{ deg} \leq \phi \leq +3 \text{ deg}$
- } Variable by autopilot

- Yaw: Neutral stability

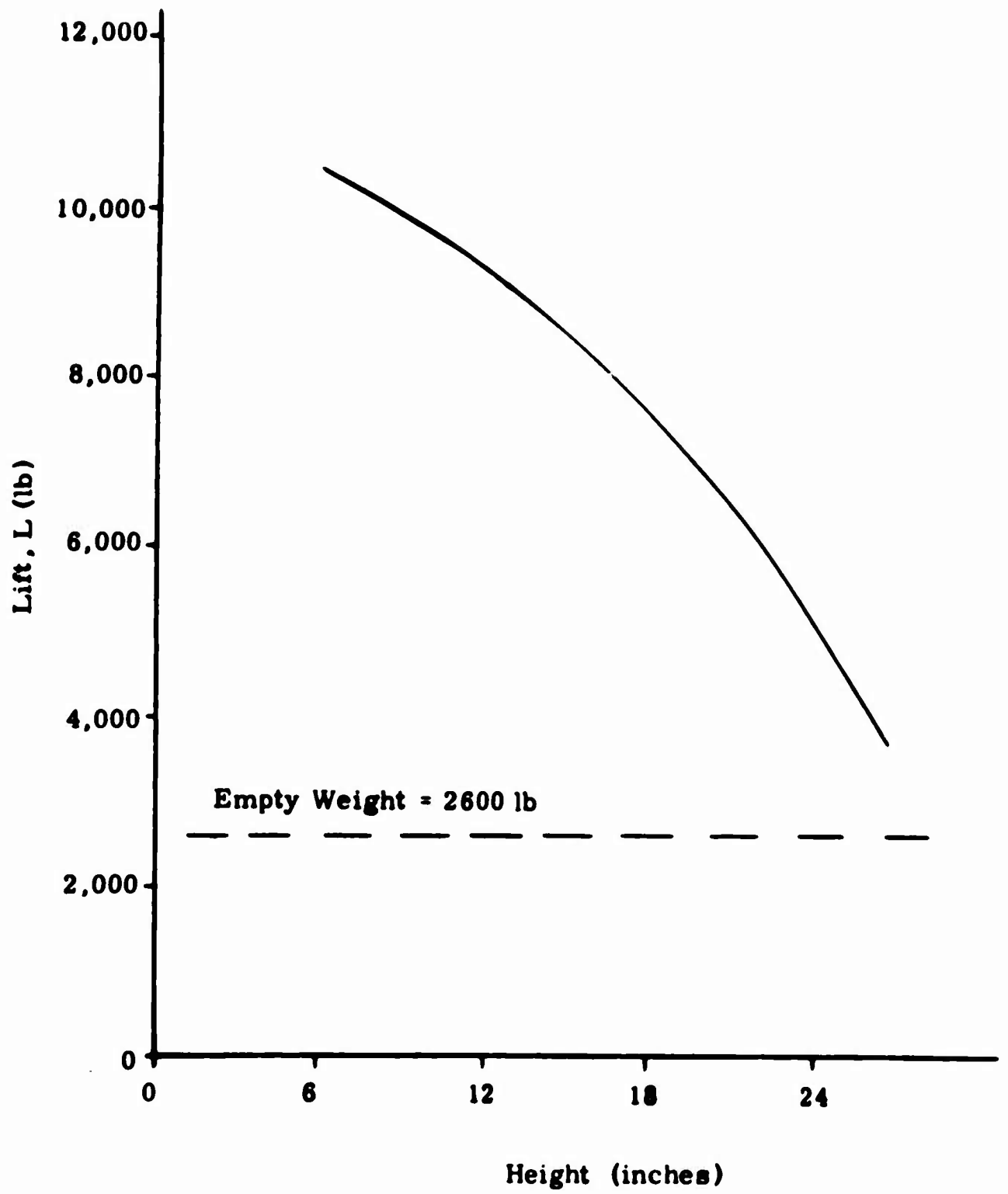


Figure 7. Performance, Lift Versus Height

Control

Pitch: $m_{\max} = 4000$ foot-pounds

Roll: $\mathcal{L}_{\max} = 1800$ foot-pounds

Yaw: $d\psi/dt^2 = \pm 0.5$ radians per second squared

Maneuver

Acceleration: 0.03g

Deceleration: 0.1g

Turning radius: 0 at $V = 0$; 800 feet at $V = 25$ miles per hour

Slope: 5 degrees from standing start

COMPONENT TESTING

In support of the preliminary design of the research vehicle, it was necessary to conduct a limited experimental investigation. Additional information was required on the stability and control characteristics and on the new vehicle corner design of the Model I ejector configuration. An existing two-dimensional stability and control tunnel was modified as per the new configuration and was tested. To determine the effect on performance of the new planform, a half-scale quarter model was designed, fabricated, and tested.

TWO-DIMENSIONAL MODEL TESTS

Description of Model and Instrumentation

The half-scale, two-dimensional stability and control model (Figures 8, 9, and 10) is to scale with the width of the research vehicle. Construction is of plywood and Plexiglas with the exception of the contoured portions of the ejector, which are sheet aluminum on plywood frames, and the primary nozzle and header assembly, which is a welded steel structure. The primary nozzle and header assembly is mounted as shown in Figure 11. This method of mounting allows freedom of nozzle location over a range of several inches and through a range of angles.

Changes in both angle and height may be simulated by adjusting the ground board. A centerboard insert has been provided to allow either complete or partial separation of the opposing ejectors.

Shop air compressors at about 100 psi supply air which is piped through two separate lines to the ejector nozzles on each side of the

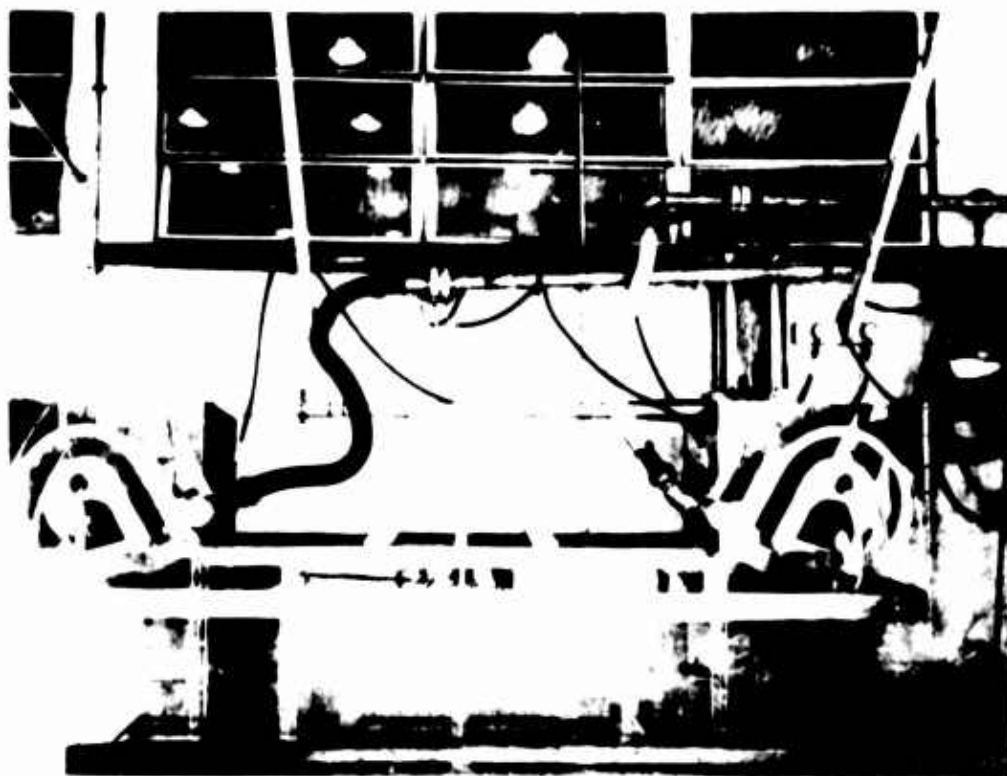


Figure 8. Two-Dimensional Stability and Control Model

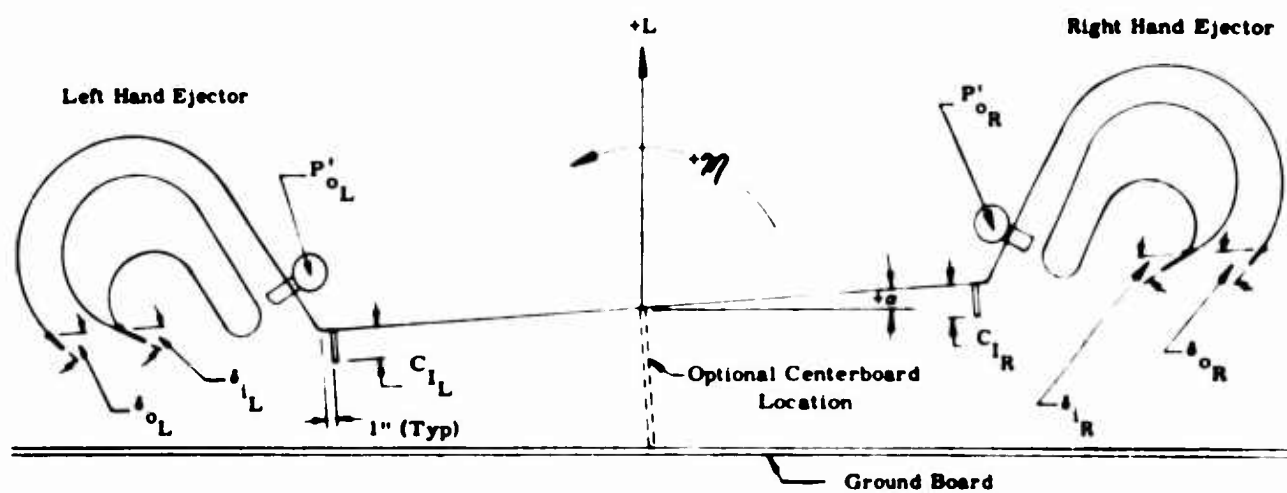


Figure 9. Stability and Control Model Geometry, Sketch

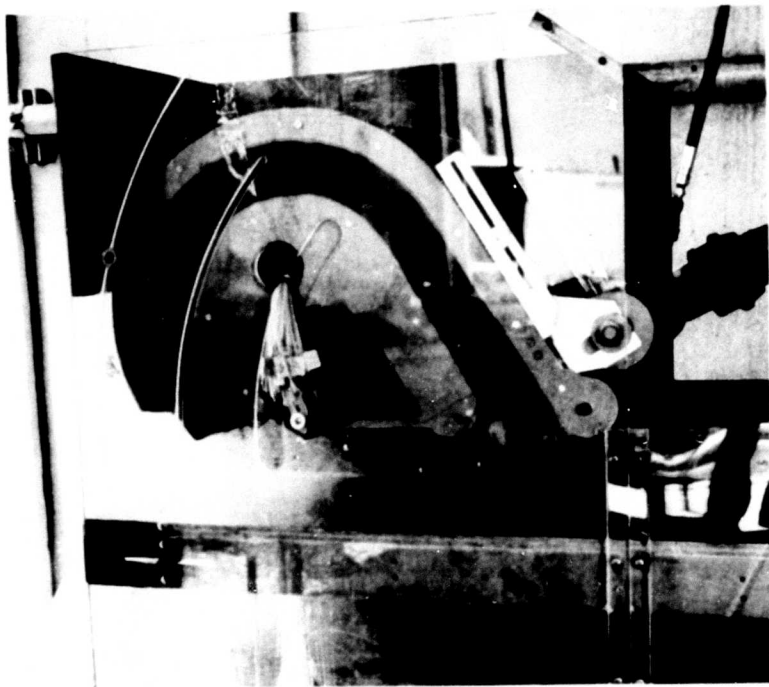


Figure 10. Ejector Configuration

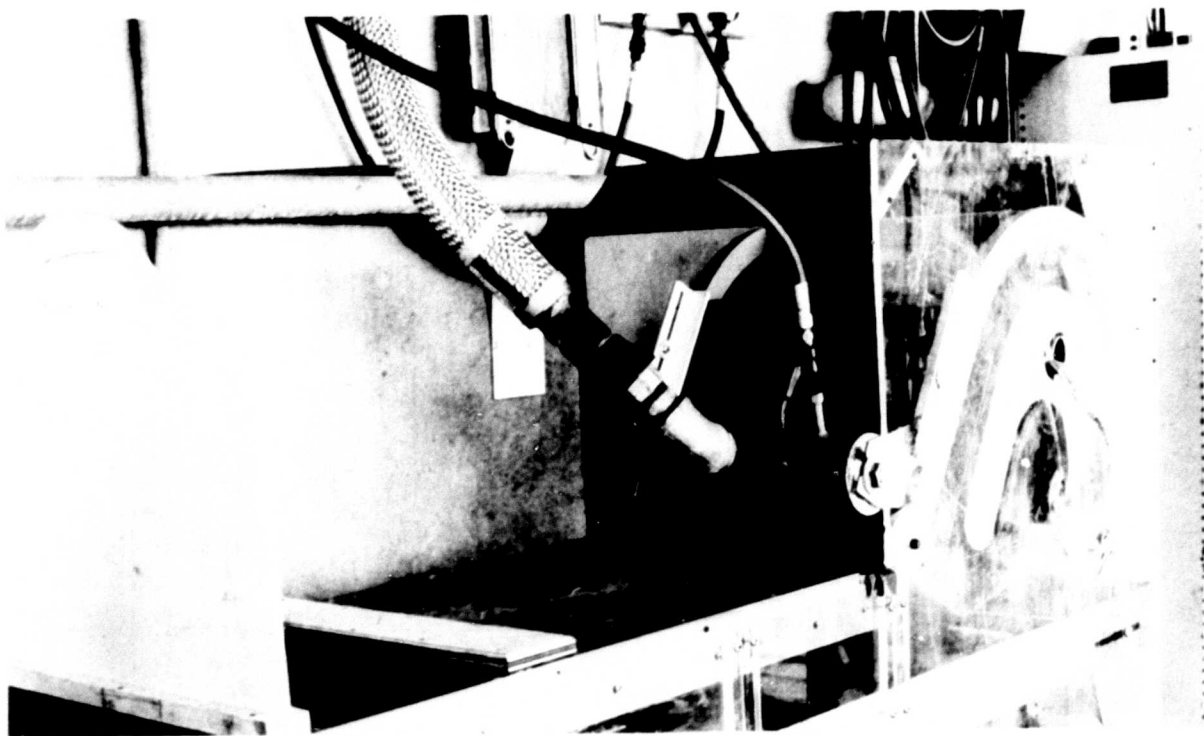


Figure 11. Primary Nozzle Installation

model. Air is regulated to the desired primary pressures of 4 to 7 psig, and an orifice meter is used to measure the mass flow.

The orifice flowmeter instrumentation consists of a mercury U-tube for measuring the pressure drop across the flowmeter, a Bourdon-type pressure gage for determining the line pressure, and a dial thermometer for measuring the line temperature. Mercury manometers are used to measure the pressure in the nozzle headers for most of the tests reported herein.

To allow the determination of forces and moments acting on the model, the instrumentation is designed to integrate the components of pressure acting on all the surfaces of the model and ground board. Pitot-static rakes are mounted in the exit flows of both ejectors. Pressure taps and the rakes are connected to a bank of inclined water manometer boards. Figure 12 shows the location of all pressure taps on the model.

Test Procedures and Data Reductions

Forces and moments were determined by a computer integration of the pressures in the separate regions of the model. Preliminary evaluation of this procedure indicated that a lateral pressure variation, principally in the mixing section of the ejector, frequently causes a significant error in the recorded moment. This occurs because the moment is determined by obtaining small differences from relatively large numbers; i.e., the difference between the integrated static pressure force on the surfaces of the two ejectors results in a moment. However, for the determination of the lift force, this condition does not exist. Correcting for a lateral pressure variation would require either fairing the pressure data prior to performing the integration or reinstrumenting the model completely. Such



Figure 12. Location of Static Pressure Taps

procedures were deemed too time consuming to fit within the testing schedule. Instead, the pressures acting on the ground board, which are the result of the vertical force acting on the model, were integrated to determine the moment. The main limitation of this procedure is that the ground board only discriminates the components normal to it, whereas integration of the pressures in the model discriminates between both normal and side forces. As a consequence, the side force vector produced in the model shifts the pressure distribution on the ground board and yields a small extraneous moment. The correction equation for side force moment is

$$\Delta \mathcal{M} = - (h \sin \alpha) L.$$

The test procedure requires setting the geometry of the model, which includes jet flap angles, nozzle location, ground board height, and angle. Thereafter, the primary pressure in the headers on either side of the model is varied. After all pressures in the model have reached a steady condition, the manometer readings are made and recorded on IBM loading forms.

An error analysis of the instrumentation, test procedure, and data recording techniques is presented in summary form in Table II.

TABLE II
SUMMARY OF MAXIMUM POSSIBLE ERRORS

Type	Range of Run Numbers	Lift (lb/ft)	Moment (ft-lb/ft)
Manometer Board	0-300	±2.5	±2.0
Resolution and Tilt			
Angle	300-500	±1.44	±1.15
Primary Pressure	0-200	±1.0	±3.75
Instrumentation	200-400	±4.3	±1.83
Instrumentation	400-500	±2.0	±0.735
Ground Board	0-200	Negl	±8.33
Misalignment	200-500	Negl	±1.5
Manometer Time			
Lag	0-500	Negl	±0.75*
Integration			
Technique	0-500	Negl	±3.0*
Side Force			
Correction	200-500	Negl	1.4 - 3.5*
Flap Angle			
Setting	0-500	Negl	±1.0

* Nominal rather than maximum values.

Discussion of Experimental Data

The purpose of this experimental program is to obtain data on stability and control for use as a design guide on the experimental vehicle.

Tables III and IV present a run schedule and summary of pertinent data for all of the stability and control tests that were performed. Figure 9 is useful for defining the geometric variables that are used in the run schedule. Comments applying to each set of entries indicate either the purpose of the run or the limitations applied to the

data. "Nozzle Sealed" indicates that the holes in the outer ejector wall through which the nozzles protrude were sealed, preventing leakage into or out of the internal passage. "Inlet Open" means that the nozzle slots were open so that they acted as vents. Early in the program, runs 1 through 156, the significance of sealing the nozzle slots was not realized, and the nozzle slots were left partially open but in an uncontrolled fashion. The effects of open nozzle slots are manifested by entraining atmospheric air into the internal flow at the higher height and by exhausting internal air at the lower height. No internal pressure data were recorded for controlled nozzle slot conditions; thus, the data for the early runs are, for the most part, qualitative in nature. However, some data taken at the 9-inch height (minimum nozzle slot effects) are used for establishing control effectiveness increments.

As a further note of explanation, the control moment and/or lift increment is defined as the difference of moment and/or lift between the condition of controls engaged and no control at comparable conditions of height and angle of attack; that is,

$$\Delta M = \mathcal{M}(\Delta\delta, \Delta P'_O, \alpha, h) - \mathcal{M}(\alpha, h)$$

$$\Delta L = L(\Delta\delta, \Delta P'_O, \alpha, h) - L(\alpha, h)$$

Figure 13 presents a typical plot of base pressure versus height for the nozzle slots sealed and open. The reduction in base pressure below a 9-inch height is considerable for the open condition. It should be emphasized that these data are plotted from the tests of a half-scale model, and linear dimensions, such as height, should be doubled to visualize the data for a full-scale machine.

Varying the exit flaps 10 degrees from the nominal setting produces the effect of base pressure shown in Figures 14 through 16. At the

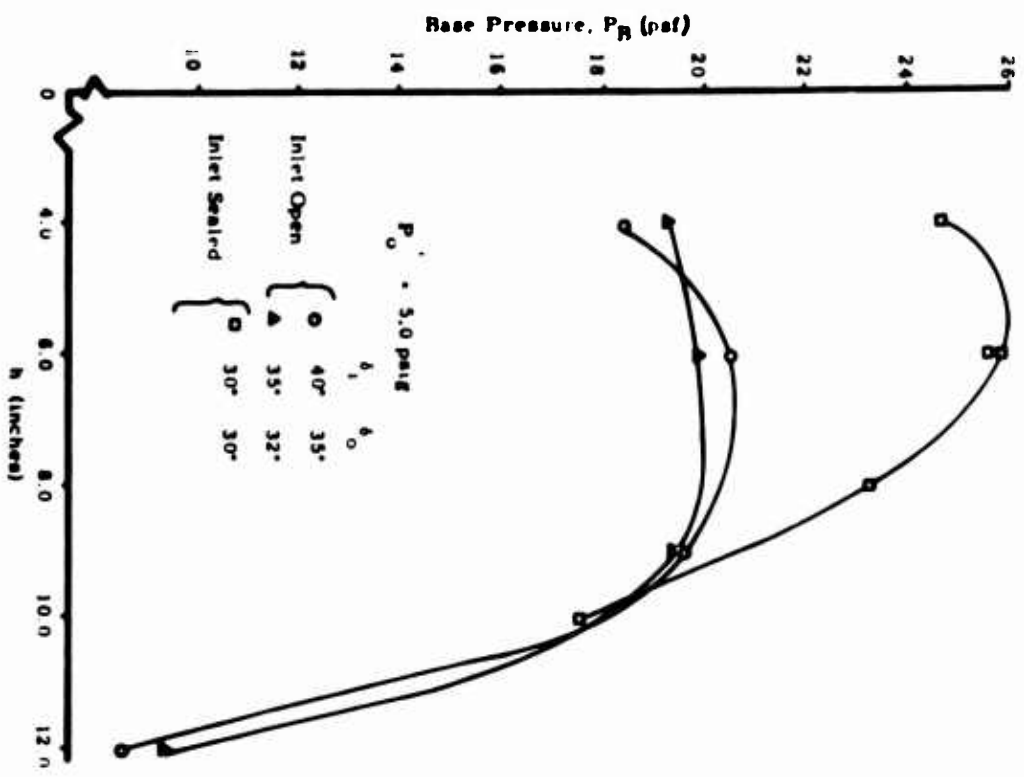


Figure 13. Base Pressure Versus Height (Half-Scale Model)

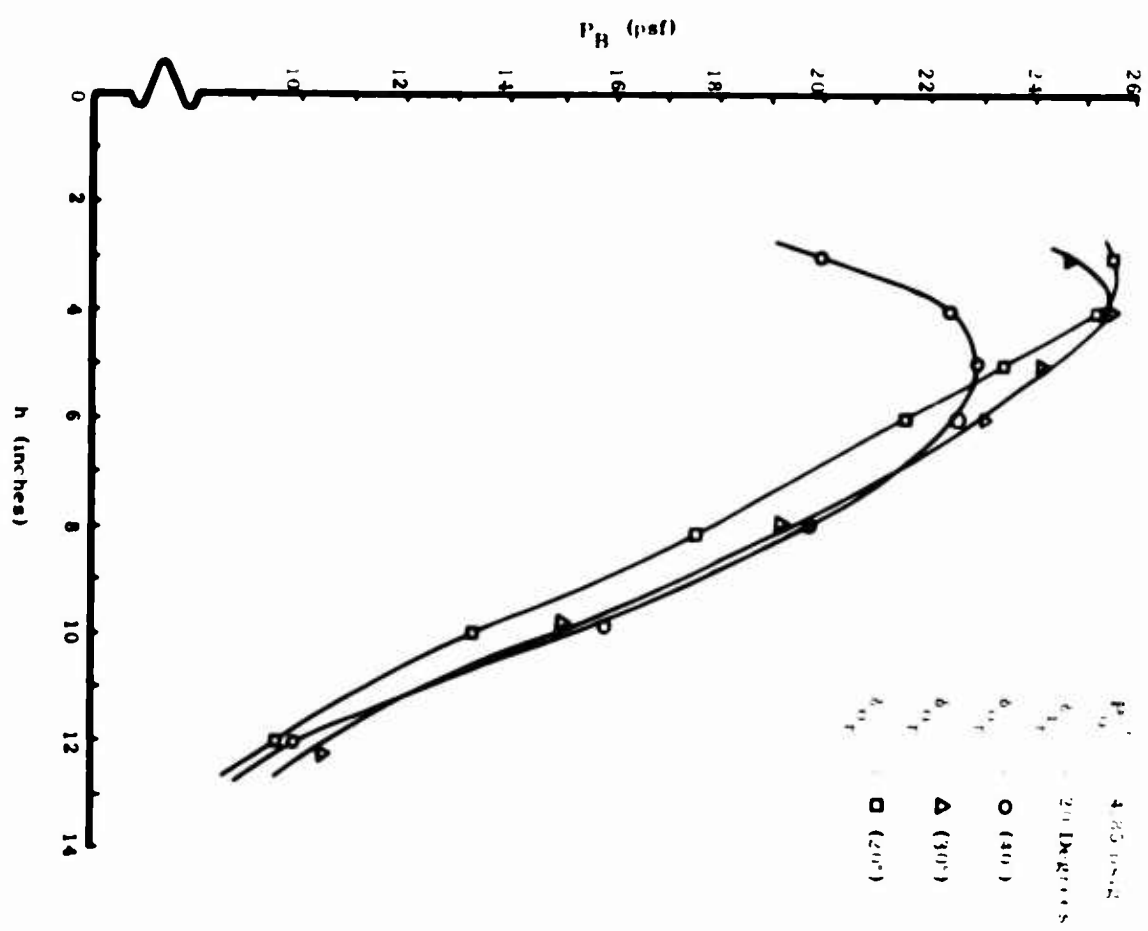


Figure 14. Base Pressure Versus Height, $\delta_1 = 20^\circ$, $\delta_0 = 30 \pm 10^\circ$

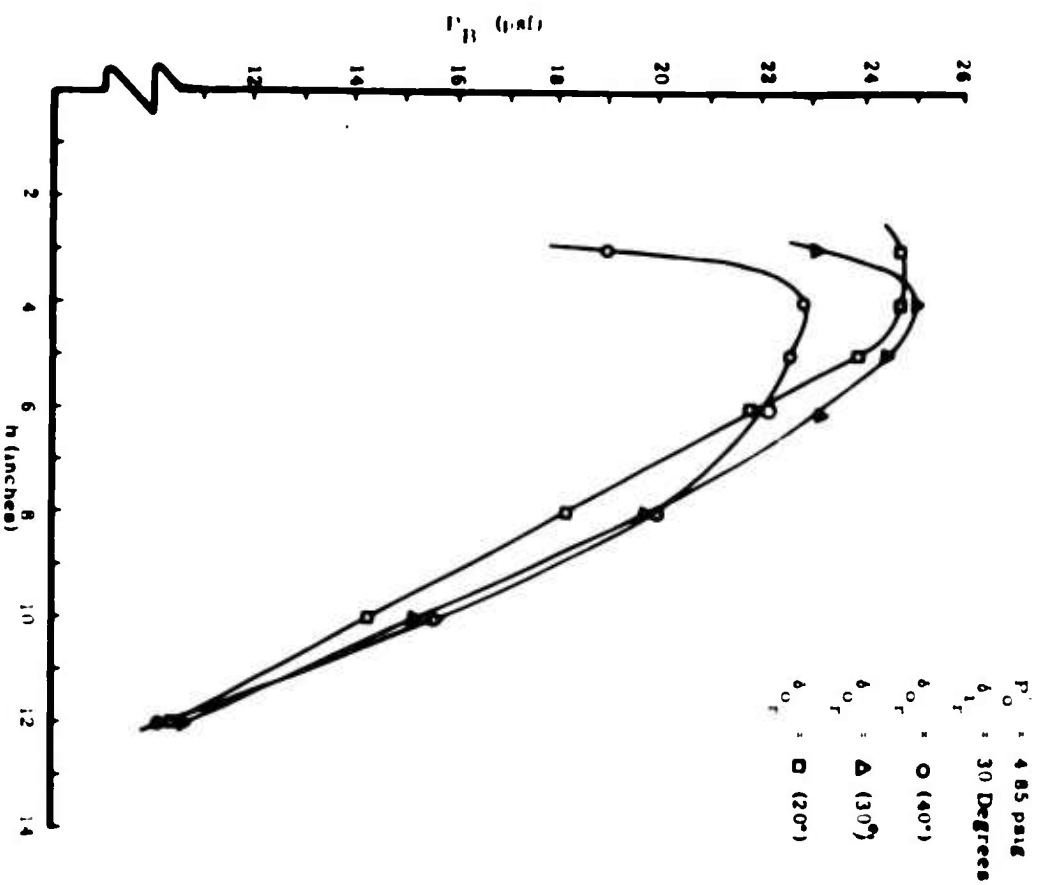


Figure 15. Base Pressure Versus Height,
 $\delta_i = 30^\circ$, $\delta_o = 30 \pm 10^\circ$

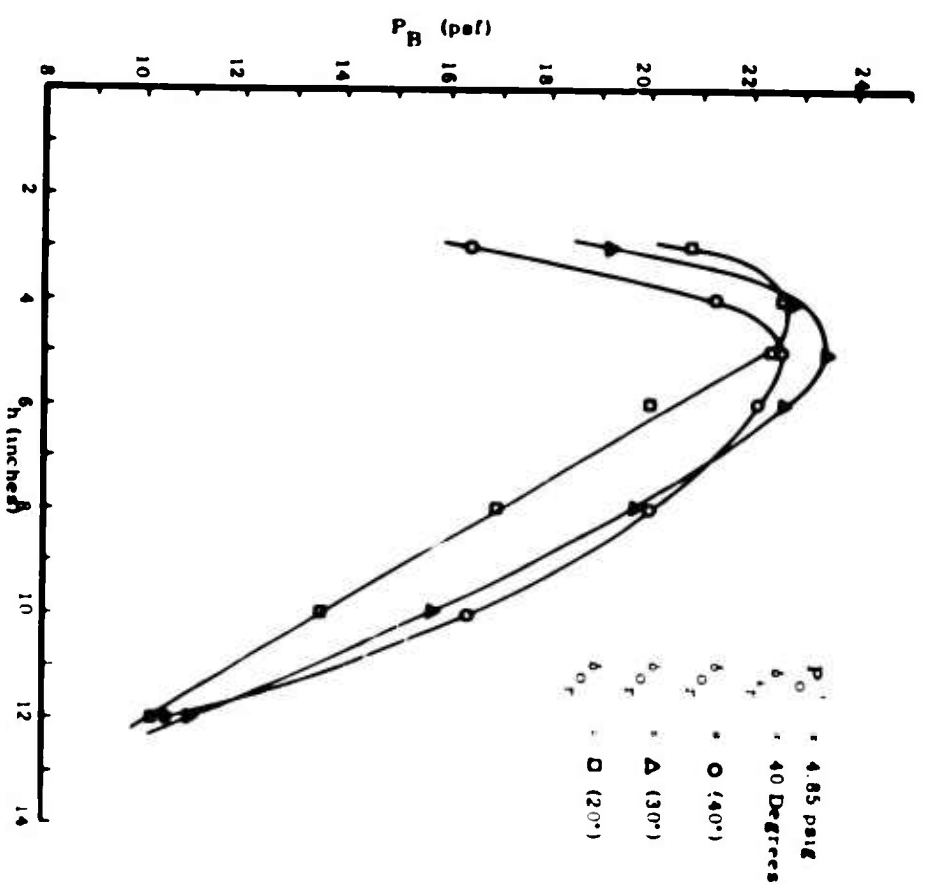


Figure 16. Base Pressure Versus Height,
 $\delta_i = 40^\circ$, $\delta_o = 30 \pm 10^\circ$

lower heights, the most obvious effect of a flap angle change appears. The base pressure curve is relatively linear over the normal operating height; however, the height at which the maximum base pressure occurs is dependent on the exit flap angle. It can be seen from Figures 17 through 19 that for a corresponding flap angle the cavity pressure is also affected. In addition to illustrating the effect of the exit flap, this series of curves (Figures 14 through 19) also indicates that the momentum flux of the recirculating curtain remains relatively constant at a given height. Across the curved jet, the static pressure gradient is a direct indication of the strength of the curtain (at a given height). It can be seen that the reduction in base pressure at the lower heights is approximately equal to the change in cavity pressure.

It appears worthwhile to speculate on the possible use that may be made of this ability to change, in effect, the slope of the lift curve (by either venting at the nozzle or varying exit flap angle). In a following chapter, "Analytical Studies", it is shown that this feature could be extremely worthwhile in forward flight. The natural frequency of the vehicle in heave is primarily a function of the slope of the lift curve. If the frequency of a forcing function occurs near the vehicle natural frequency, such as may occur over water, then the ability to alter the natural frequency of the vehicle would be an important feature. Preliminary estimates involving a range of forward speed, sea conditions, and GEM heave characteristics indicate that this is a potential problem area.

1. Stability

Figures 20 and 21 present the moment curves for the model with the inlet sealed. Figures 22 and 23 present the same data with the

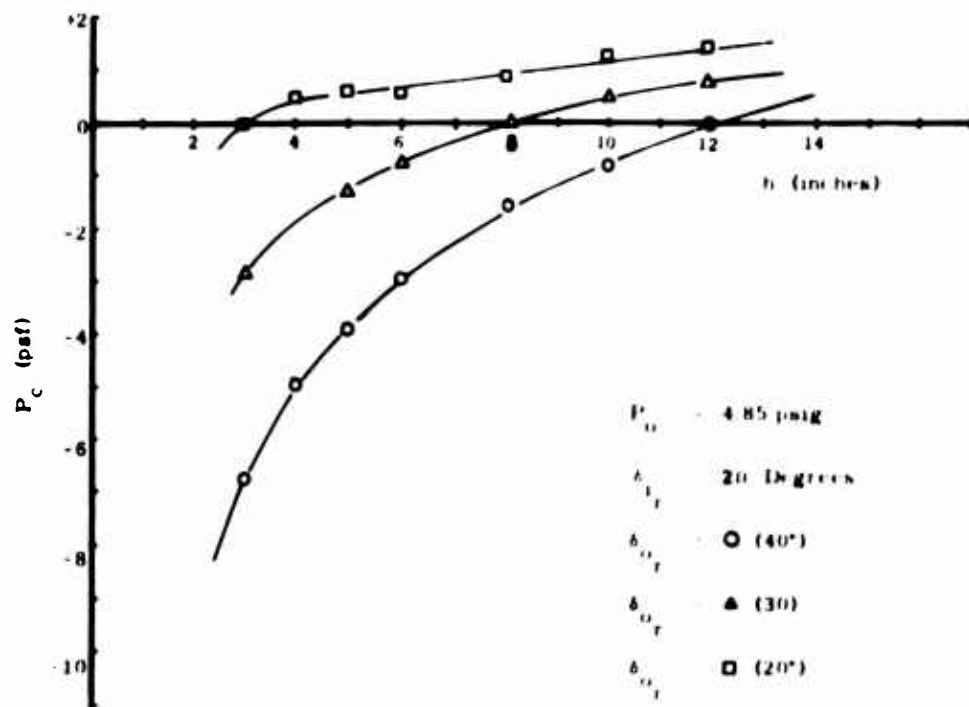


Figure 17. Cavity Pressure Versus Height,
 $\delta_i = 20^\circ$, $\delta_o = 30 \pm 10^\circ$

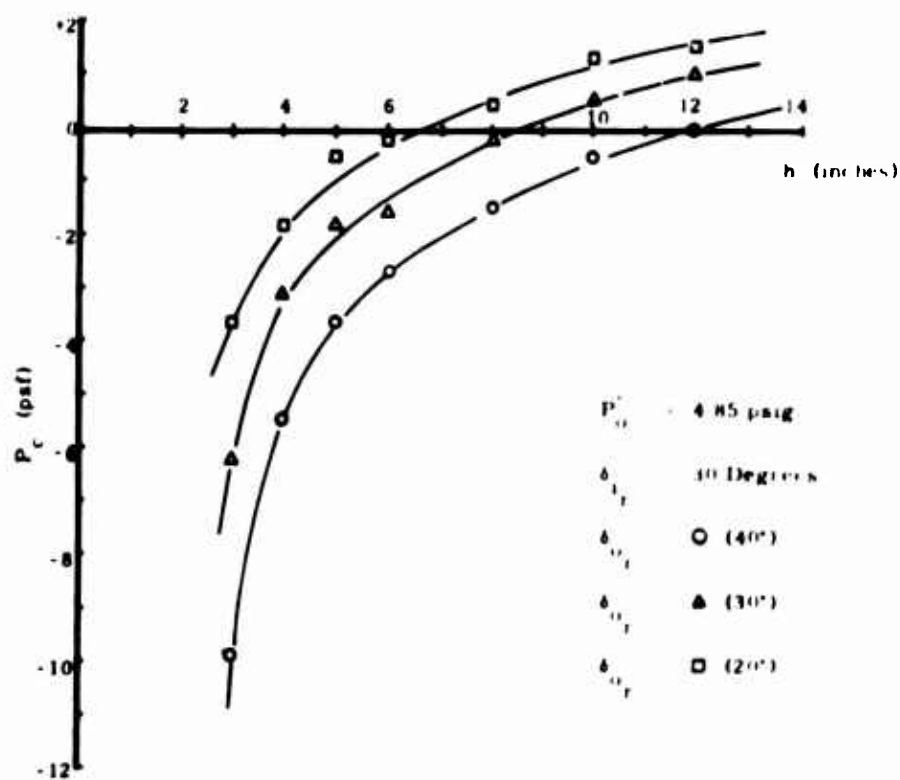


Figure 18. Cavity Pressure Versus Height,
 $\delta_i = 30^\circ$, $\delta_o = 30 \pm 10^\circ$

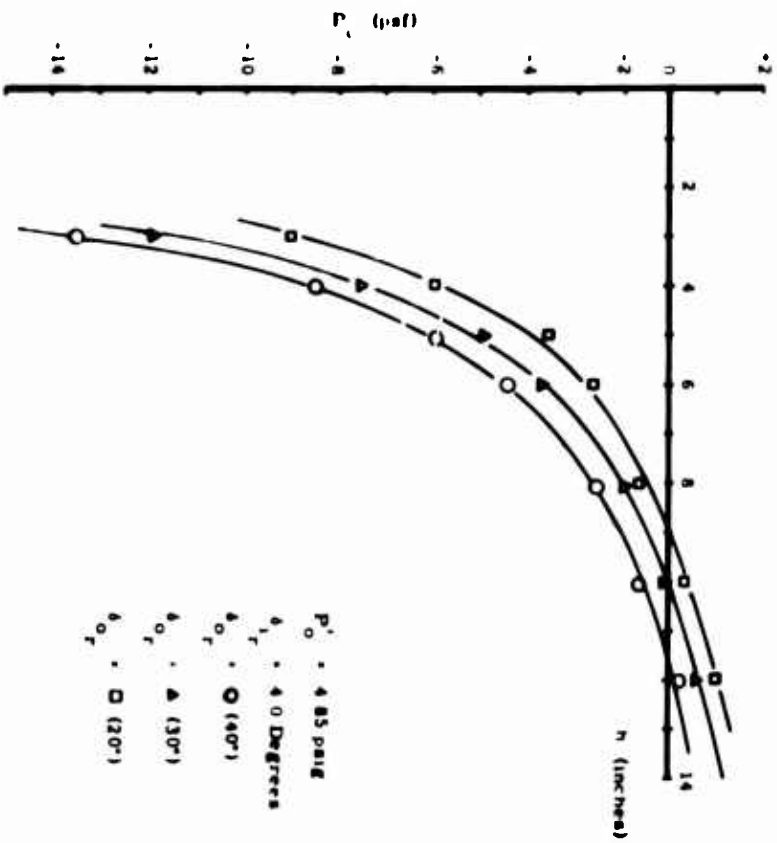


Figure 19. Cavity Pressure Versus Height.
 $\delta_i = 40^\circ$, $\delta_o = 30 \pm 10^\circ$

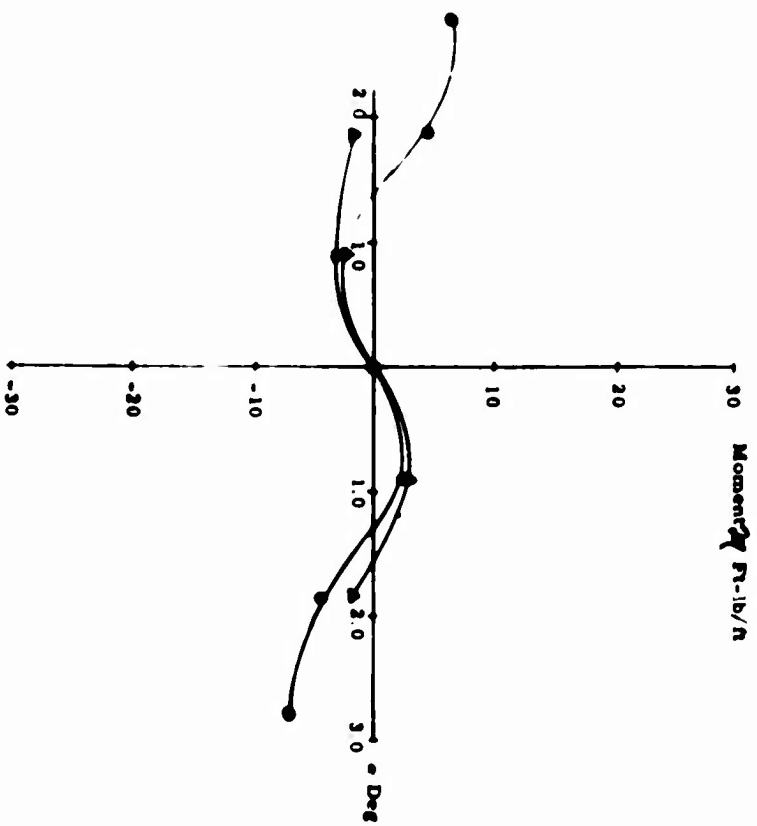


Figure 20. Moment Versus Angle at Constant
Lift, Inlet Sealed

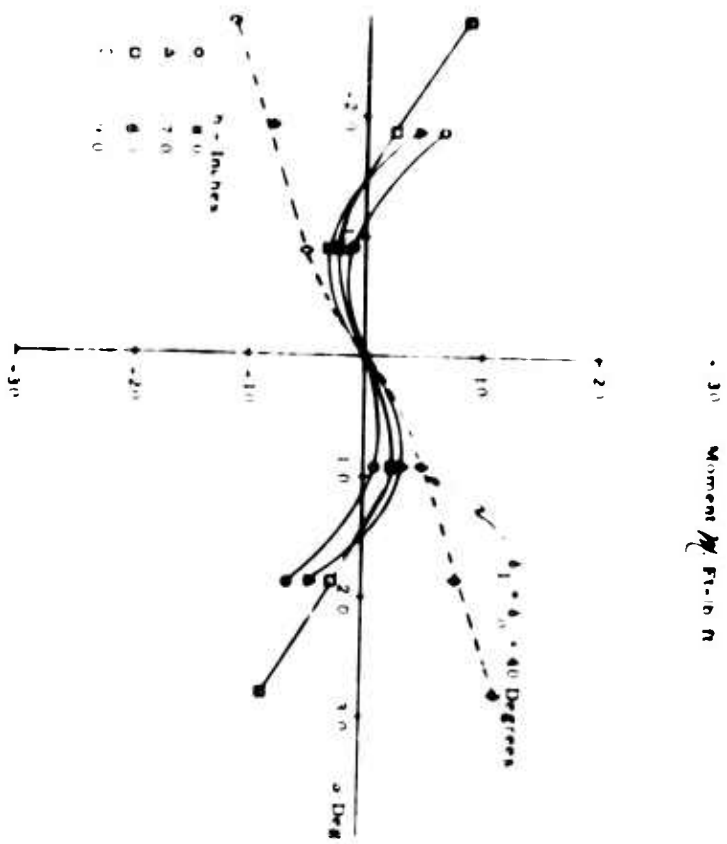


Figure 21. Moment Versus Angle at Various Heights, Inlet Sealed

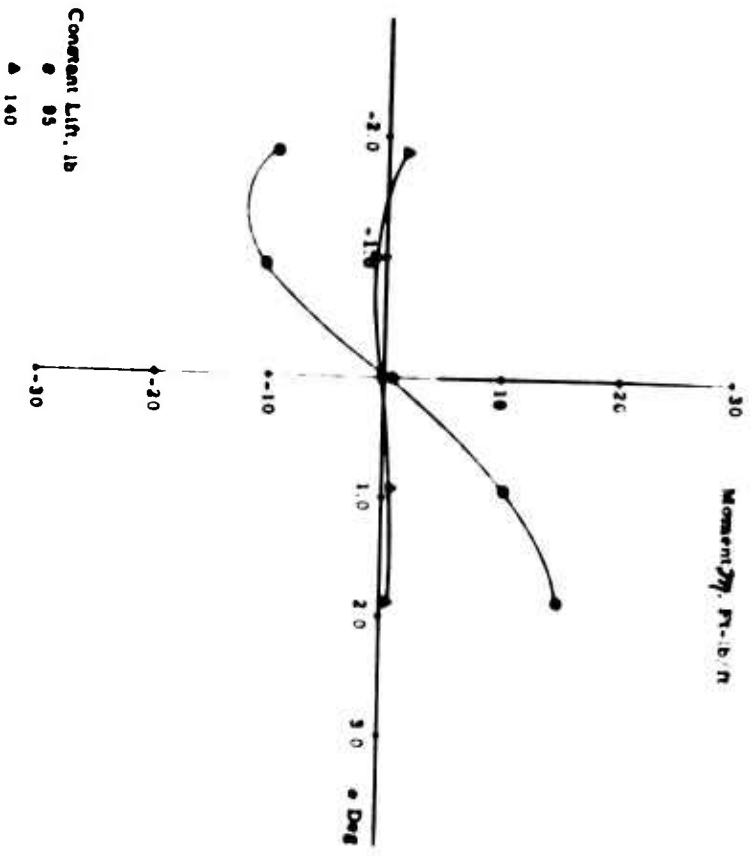


Figure 22. Moment Versus Angle at Constant Lift, Inlet Open

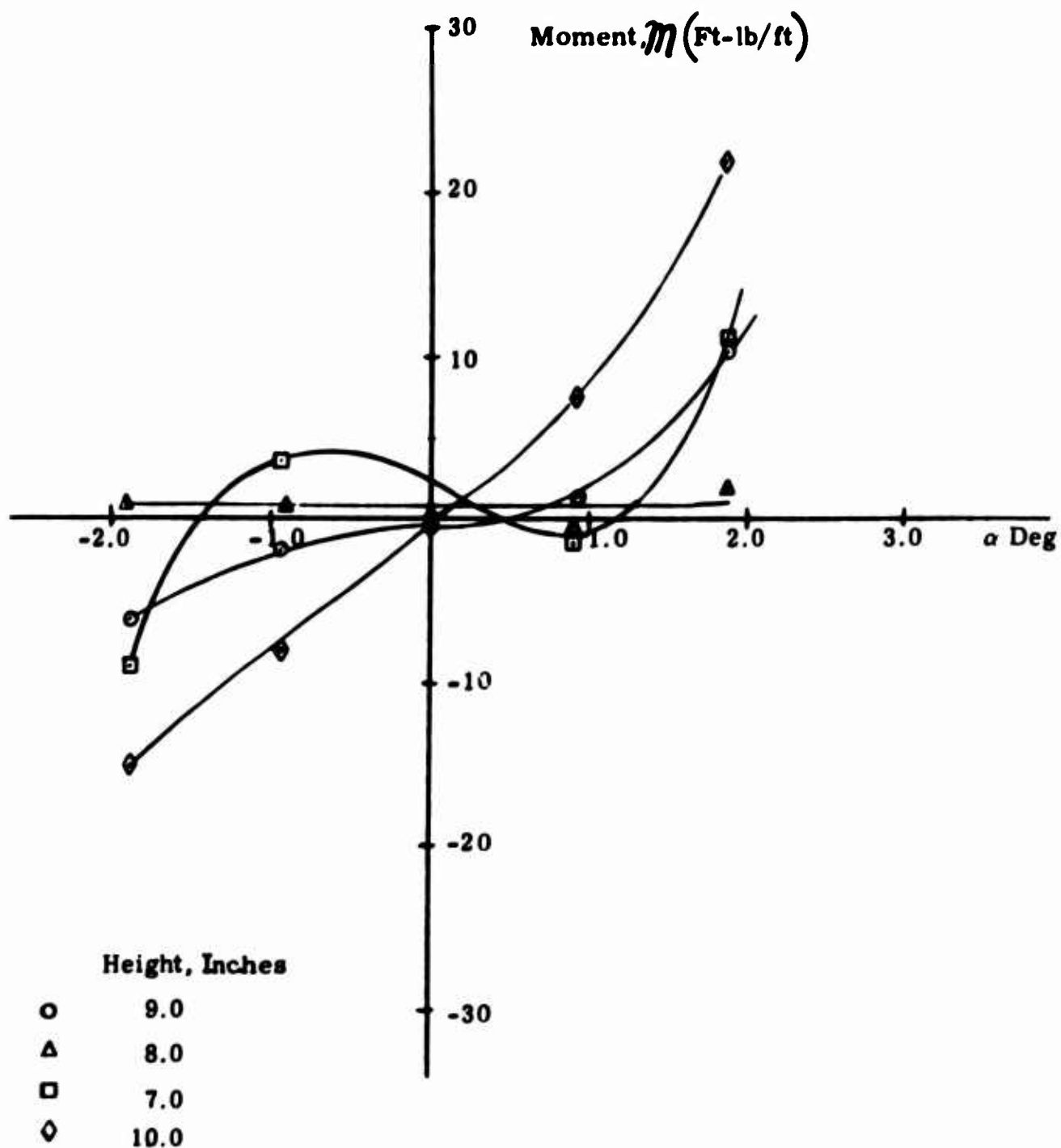


Figure 23. Moment Versus Angle at Various Heights, Inlet Open

inlet open. These moment curves are a measure of the two-dimensional static stability of the model with the usual negative moment slope, $dM/d\alpha$, indicating a stable variation. The results of this investigation indicate that the sealed two-dimensional configuration is slightly unstable at some combinations of height and tilt and slightly stable at others. Considering the amount of destabilizing moment and the accuracy of the data (probable error of approximately ± 3 foot-pounds), the configuration is considered to be, essentially, neutrally stable.

2. Control

Three control devices were evaluated: differential primary pressure, differential flap angle variations, and asymmetric inlet extension. The inlet extension control configuration consisted of varying the length of one inlet extension with respect to the other. This investigation was completed in its entirety with the nozzle slots open; therefore, the results are considered to be inconclusive. Sizeable moments were obtained but they were usually nonlinear and frequently exhibited a control reversal. This concept appears to warrant future consideration; but since the other devices investigated were very effective and mechanically simpler, the investigation was not repeated with the nozzle slots sealed.

The control moment due to differential primary pressure at various heights is shown in Figures 24 and 25. The control moment at a differential pressure of 1 psi is reasonably large, as extrapolated to the full-scale vehicle. A moment of 30 foot-pounds per foot is equivalent to a full-scale rolling moment of approximately 960 foot-pounds. This control moment was obtained by testing with one ejector at 5 psig and the other at 6 psig. Extrapolating the data to 5 and 7 psig, a maximum rolling moment of 1800 foot-pounds, full scale, would occur.

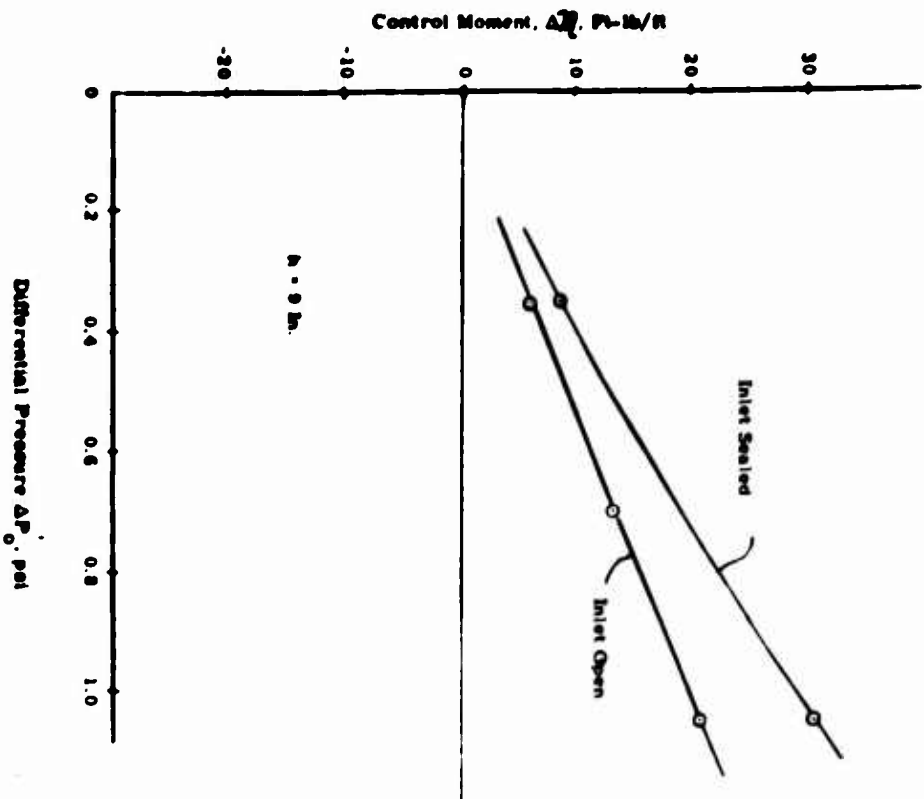


Figure 24. Control Moment Versus Differential Primary Pressure
When $h = 9$ Inches

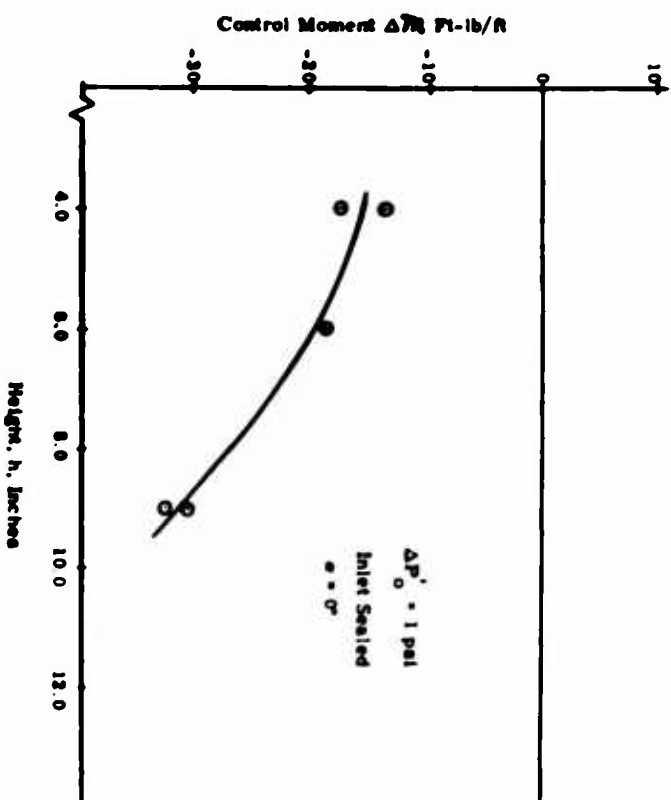


Figure 25. Control Moment Versus Height When $\Delta P_0 = 1$ psi

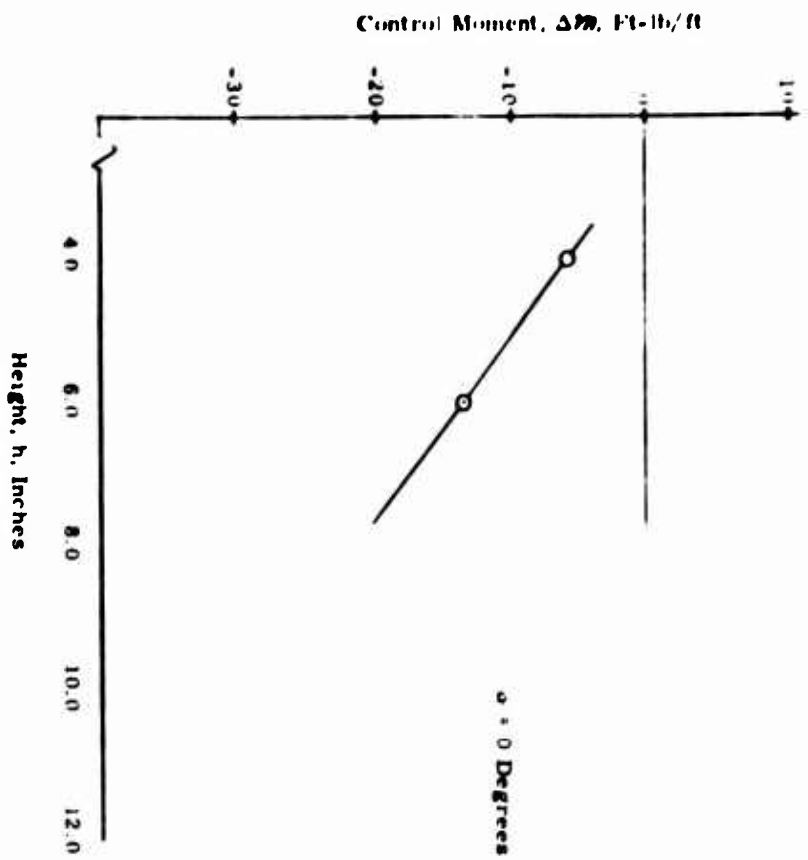


Figure 26. Control Moment Versus
Height, $\Delta\delta = 12^\circ$

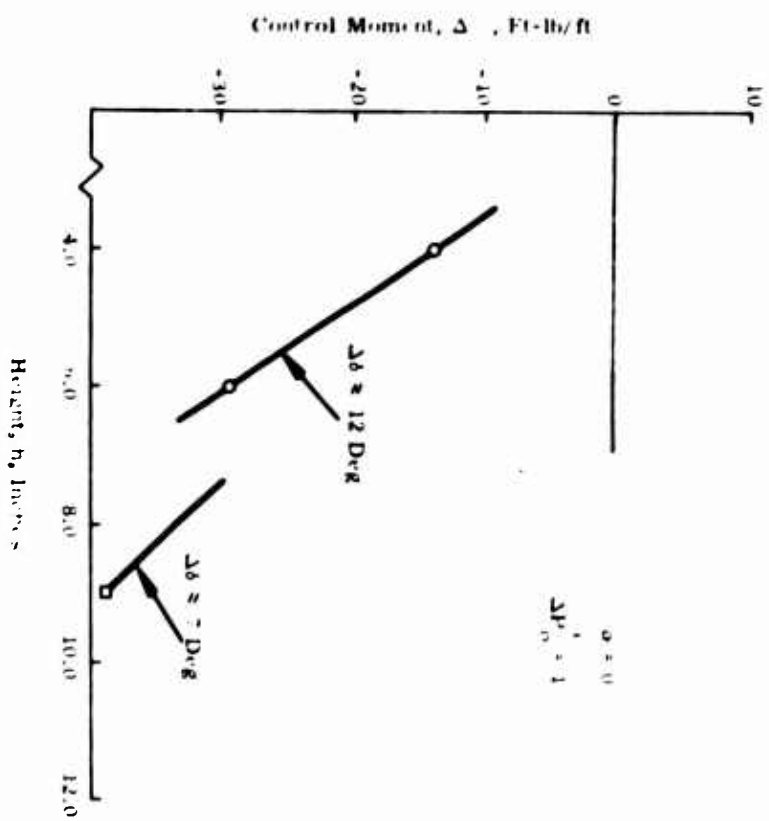


Figure 27. Control Moment Versus
Height, Vary $\Delta\delta$, $\Delta P_{O'} = 1$ psi

Control moment due to differential flaps appears in Figure 26. The trend of increasing control capability with increasing height is clearly indicated. The model was tested with a combined differential flap setting of approximately 12 degrees. It is obvious that extreme flap angles would affect the performance of the ejector, but there was no indication that the ± 15 -degree flap setting was approaching a limit except at the maximum heights. The combined effect of flap angle and differential primary pressure is shown in Figure 27.

The combination of flaps and differential primary pressure exhibited the strongest control effectiveness of all configurations tested.

Double Ejector Stability and Control Tests

[illegible]

TABLE III (Cont)

Run No.	Booster (lb)		θ (deg)	Inert Start (deg)		Exit Flap (deg)		P_c (psi)	\dot{m} (lb/sec/R)	\dot{m}^* (lb/sec/R)	P_b (psi)	P_c (psi)		Exit 1 (lb/R)		Exit 2 (lb/sec/R)		\dot{m}/\dot{m}^*	L (cm)	ETD_c (R)	R_{max} (cm)				
	γ_1	γ_2		γ_1	γ_2	γ_1	γ_2					L	R	L	R										
D-120	5	0	1.07	3	3	43	47	43	0.230	0.243	2.30	4.34	16.37	-2.17	14.4	12.0	2.10	2.06	14.1	11.7	134.31	-7.07	-11.06	2.12	1.00
D-121	5	0	1.07	3	3	43	47	43	0.102	0.235	2.30	2.67	16.07	-0.74	11.3	10.7	2.74	2.50	14.2	11.5	126.27	-12.3	-32.31	1.43	1.04
D-122	5	0	1.07	3	3	43	47	43	0.201	0.235	2.30	2.67	16.0	-5.79	10.0	12.2	2.30	2.73	14.0	12.1	142.30	17.7	-2.04	2.74	1.56
D-123	7	0	0.04	0	0	43	47	43	0.230	0.235	2.30	2.67	15.05	-0.43	12.4	11.5	2.00	2.54	12.6	11.3	131.01	-2.0	-2.315	1.00	1.31
D-124	5	0	-0.04	0	0	43	47	43	0.230	0.235	2.30	2.67	16.30	-3.50	12.2	12.0	2.02	2.04	12.7	12.6	130.02	-22.0	-26.10	1.01	1.00
D-125	5	0	-0.04	0	0	43	47	43	0.230	0.235	2.30	2.67	16.30	-7.10	12.2	12.0	2.02	2.04	12.7	12.6	130.02	-22.0	-26.10	1.01	1.00
D-126	5	0	-1.07	0	0	43	47	43	0.230	0.235	2.30	2.67	16.30	-0.43	12.2	12.0	2.02	2.04	12.7	12.6	130.02	-22.0	-26.10	1.01	1.00
D-127	5	0	-1.07	0	0	43	47	43	0.230	0.235	2.30	2.67	16.30	-0.43	12.2	12.0	2.02	2.04	12.7	12.6	130.02	-22.0	-26.10	1.01	1.00
D-128	5	0	0	0	0	43	47	43	0.230	0.235	2.30	2.67	16.30	-0.43	12.2	12.0	2.02	2.04	12.7	12.6	130.02	-22.0	-26.10	1.01	1.00
D-129	5	0	0	0	0	43	47	43	0.230	0.235	2.30	2.67	16.30	-0.43	12.2	12.0	2.02	2.04	12.7	12.6	130.02	-22.0	-26.10	1.01	1.00
D-130	5	0	0.04	0	0	43	47	43	0.230	0.235	2.30	2.67	16.30	-0.43	12.2	12.0	2.02	2.04	12.7	12.6	130.02	-22.0	-26.10	1.01	1.00
D-131	5	0	-0.04	0	0	43	47	43	0.230	0.235	2.30	2.67	16.30	-0.43	12.2	12.0	2.02	2.04	12.7	12.6	130.02	-22.0	-26.10	1.01	1.00
D-132	5	0	0	0	0	43	47	43	0.230	0.235	2.30	2.67	16.30	-0.43	12.2	12.0	2.02	2.04	12.7	12.6	130.02	-22.0	-26.10	1.01	1.00
D-133	7	0	-0.04	0	0	43	47	43	0.230	0.235	2.30	2.67	16.30	-0.43	12.2	12.0	2.02	2.04	12.7	12.6	130.02	-22.0	-26.10	1.01	1.00
D-134	5	0	-1.07	0	0	43	47	43	0.230	0.235	2.30	2.67	16.30	-0.43	12.2	12.0	2.02	2.04	12.7	12.6	130.02	-22.0	-26.10	1.01	1.00
D-135	5	0	-2.00	0	0	43	47	43	0.230	0.235	2.30	2.67	16.30	-0.43	12.2	12.0	2.02	2.04	12.7	12.6	130.02	-22.0	-26.10	1.01	1.00
D-136	5	0	-0.04	0	0	43	47	43	0.230	0.235	2.30	2.67	16.30	-0.43	12.2	12.0	2.02	2.04	12.7	12.6	130.02	-22.0	-26.10	1.01	1.00
D-137	5	0	-1.07	0	0	43	47	43	0.230	0.235	2.30	2.67	16.30	-0.43	12.2	12.0	2.02	2.04	12.7	12.6	130.02	-22.0	-26.10	1.01	1.00
D-138	5	0	-2.00	0	0	43	47	43	0.230	0.235	2.30	2.67	16.30	-0.43	12.2	12.0	2.02	2.04	12.7	12.6	130.02	-22.0	-26.10	1.01	1.00
D-139	12	12	0	0	0	43	47	43	0.230	0.235	2.30	2.67	16.30	-0.43	12.2	12.0	2.02	2.04	12.7	12.6	130.02	-22.0	-26.10	1.01	1.00
D-140	10	12	0.030	0	0	43	47	43	0.230	0.235	2.30	2.67	16.30	-0.43	12.2	12.0	2.02	2.04	12.7	12.6	130.02	-22.0	-26.10	1.01	1.00
D-141	0	12	2.000	0	0	43	47	43	0.230	0.235	2.30	2.67	16.30	-0.43	12.2	12.0	2.02	2.04	12.7	12.6	130.02	-22.0	-26.10	1.01	1.00
D-142	14	10	-0.030	0	0	43	47	43	0.230	0.235	2.30	2.67	16.30	-0.43	12.2	12.0	2.02	2.04	12.7	12.6	130.02	-22.0	-26.10	1.01	1.00
D-143	12	0	-2.000	0	0	43	47	43	0.230	0.235	2.30	2.67	16.30	-0.43	12.2	12.0	2.02	2.04	12.7	12.6	130.02	-22.0	-26.10	1.01	1.00
D-144	0	0	0	0	0	43	47	43	0.230	0.235	2.30	2.67	16.30	-0.43	12.2	12.0	2.02	2.04	12.7	12.6	130.02	-22.0	-26.10	1.01	1.00
D-145	5	0	-0.04	0	0	43	47	43	0.230	0.235	2.30	2.67	16.30	-0.43	12.2	12.0	2.02	2.04	12.7	12.6	130.02	-22.0	-26.10	1.01	1.00
D-146	7	0	-0.04	0	0	43	47	43	0.230	0.235	2.30	2.67	16.30	-0.43	12.2	12.0	2.02	2.04	12.7	12.6	130.02	-22.0	-26.10	1.01	1.00
D-147	3	0	-2.00	0	0	43	47	43	0.230	0.235	2.30	2.67	16.30	-0.43	12.2	12.0	2.02	2.04	12.7	12.6	130.02	-22.0	-26.10	1.01	1.00
D-148	0	0	-0.04	0	0	43	47	43	0.230	0.235	2.30	2.67	16.30	-0.43	12.2	12.0	2.02	2.04	12.7	12.6	130.02	-22.0	-26.10	1.01	1.00
D-149	0	0	-2.00	0	0	43	47	43	0.230	0.235	2.30	2.67	16.30	-0.43	12.2	12.0	2.02	2.04	12.7	12.6	130.02	-22.0	-26.10	1.01	1.00
D-150	0	0	-2.00	0	0	43	47	43	0.230	0.235	2.30	2.67	16.30	-0.43	12.2	12.0	2.02	2.04	12.7	12.6	130.02	-22.0	-26.10	1.01	1.00
D-151	5	0	-1.07	0	0	43	47	43	0.230	0.235	2.30	2.67	16.30	-0.43	12.2	12.0	2.02	2.04	12.7	12.6	130.02	-22.0	-26.10	1.01	1.00
D-152	0	0	-1.07	0	0	43	47	43	0.230	0.235	2.30	2.67	16.30	-0.43	12.2	12.0	2.02	2.04	12.7	12.6	130.02	-22.0	-26.10	1.01	1.00
D-153	7	0	-0.04	0	0	43	47	43	0.230	0.235	2.30	2.67	16.30	-0.43	12.2	12.0	2.02	2.04	12.7	12.6	130.02	-22.0	-26.10	1.01	1.00
D-154	0	0	-2.00	0	0	43	47	43	0.230	0.235	2.30	2.67	16.30	-0.43	12.2	12.0	2.02	2.04	12.7	12.6	130.02	-22.0	-26.10	1.01	1.00
D-155	0	0	-0.04	0	0	43	47	43	0.230	0.235	2.30	2.67	16.30	-0.43	12.2	12.0	2.02	2.04	12.7	12.6	130.02	-22.0	-26.10	1.01	1.00
D-156	3	0	-2.00	0	0	43	47	43	0.230	0.235	2.30	2.67	16.30	-0.43	12.2	12.0	2.02	2.04	12.7	12.6	130.02	-22.0	-26.10	1.01	1.00
D-157	7	0	-0.04	0	0	43	47	43	0.230	0.235	2.30	2.67	16.30	-0.43	12.2	12.0	2.02	2.04	12.7	12.6	130.02	-22.0	-26.10	1.01	1.00
D-158	0	0	-2.00	0	0	43	47	43	0.230	0.235	2.30	2.67	16.30	-0.43	12.2	12.0	2.02	2.04	12.7	12.6	130.02	-22.0	-26.10	1.01	1.00

TABLE IV

DOUBLE EJECTOR STABILITY AND CONTROL TESTS

Stability Model
200 Series Data Summary
Inlet Open

Run No.	h_L (in.)	h_R (in.)	α (deg)	Center Board	δ_{L_i} (deg)	δ_{L_o} (deg)	δ_{R_i} (deg)	δ_{R_o} (deg)	P'_{oL} (psi)	P'_{oR} (psi)	\bar{P}_B (psf)	L (lb/ft)	\mathcal{M} (ft-lb/ft)
D-201	9	9	0	In	40	36	40	34	5.0	5.0	19.8	154.0	-1.37
202	9	7	-0.935	In	40	36	40	34	5.0	5.0	20.6	164.0	+4.62
203	9	5	-1.870	In	40	36	40	34	5.0	5.0	20.6	157.1	-2.40
204	9	3	-2.805	In	40	36	40	34	5.0	5.0	19.8	133.9	-3.41
205	7	9	0.935	In	40	36	40	34	5.0	5.0	20.6	163.5	-5.25
206	5	9	1.870	In	40	36	40	34	5.0	5.0	20.8	160.0	+3.70
207	3	9	2.805	In	40	36	40	34	5.0	5.0	19.1	130.0	+3.22
208	9	9	0	Out	40	36	40	34	5.0	5.0	19.5	151.1	-0.76
209	9	7	-0.935	Out	40	36	40	34	5.0	5.0	20.7	160.5	+0.88
210	9	5	-1.870	Out	40	36	40	34	5.0	5.0	20.5	158.0	+7.00
211	9	3	-2.805	Out	40	36	40	34	5.0	5.0	17.9	132.2	-6.71
212	7	9	0.935	Out	40	36	40	34	5.0	5.0	20.7	161.8	-0.73
213	5	9	1.870	Out	40	36	40	34	5.0	5.0	20.0	155.6	-4.50
214	3	9	2.805	Out	40	36	40	34	5.0	5.0	17.6	130.8	+2.06
215	12	12	0	In	40	36	40	34	5.0	5.0	8.4	63.6	-2.36
216	12	12	0	Out	40	36	40	34	5.0	5.0	8.5	63.9	2.62
217	10	10	0.935	Out	40	36	40	34	5.0	5.0	9.9	74.5	25.50
218	8	10	1.870	Out	40	36	40	34	5.0	5.0	10.2	78.4	22.06
219	12	10	-0.935	Out	40	36	40	34	5.0	5.0	9.3	68.5	-20.50
220	12	8	-1.870	Out	40	36	40	34	5.0	5.0	9.9	74.9	-14.18
221	9	8	-1.870	In	40	36	40	34	5.0	5.0	9.6	116.8	-7.71
222	6	6	0	In	40	36	40	34	5.0	5.0	20.7	159.2	+0.06
223	6	6	0	Out	40	36	40	34	5.0	5.0	20.5	158.0	+4.47

TABLE IV (Cont)

Run No.	h_L (in.)	h_R (in.)	α (deg)	Center Board	δ_{L_i} (deg)	δ_{L_o} (deg)	δ_{R_i} (deg)	δ_{R_o} (deg)	P'_{oL} (psi)	P'_{oR} (psi)	\bar{P}_B (psf)	L (lb/ft)	m (ft-lb/ft)
D-224	6	4	-0.935	Out	40	36	40	34	5.0	5.0	19.3	143.9	-3.44
225	4	6	+0.935	Out	40	36	40	34	5.0	5.0	19.3	142.9	+6.27
226	4	4	0	Out	35	33	35	31	5.0	5.0	18.3	131.8	+1.05
227	9	9	0	In	35	33	35	31	5.0	5.0	19.6	150.7	27.40
228	1	3	0	Out	35	33	35	31	5.0	5.0	19.4	148.9	2.77
229	7	7	-0.935	Out	35	33	35	31	5.0	5.0	19.9	154.2	3.33
230	7	5	-1.870	Out	35	33	35	31	5.0	5.0	20.8	160.2	6.61
231	7	9	0.935	Out	35	33	35	31	5.0	5.0	20.8	157.1	-8.98
232	5	9	1.870	Out	35	33	35	31	5.0	5.0	20.7	159.0	-14.63
233	6	6	0	In	35	33	35	31	5.0	5.0	20.7	156.1	-3.28
234	6	6	0	Out	35	33	35	31	5.0	5.0	19.9	153.5	-7.90
235	6	4	-0.935	Out	35	33	35	31	5.0	5.0	19.2	143.3	-15.82
236	4	6	+0.935	Out	35	33	35	31	5.0	5.0	19.2	137.4	-17.21
237	12	12	0	Out	40	36	40	34	5.0	5.36	9.3	70.4	3.90
238	12	12	0	In	40	36	40	34	5.0	5.36	9.3	69.2	10.00
239	12	12	0	Out	40	36	40	34	5.0	5.36	9.1	69.1	-2.91
240	12	12	0	In	40	36	40	34	5.0	5.36	9.1	69.4	-0.09
241	9	9	0	In	40	36	40	34	5.4	4.7	9.5	67.3	-9.85
242	9	9	0	Out	40	36	40	34	5.4	4.7	9.0	67.1	+19.86
243	9	9	0	Out	40	36	40	34	5.4	4.7	19.8	154.2	6.27
244	9	9	0	Out	40	36	40	34	5.7	5.0	19.9	156.5	13.19
245	9	9	0	Out	40	36	40	34	5.0	5.4	19.9	154.3	-5.67
246	9	9	0	Out	40	36	40	34	5.0	5.7	20.3	159.1	-14.60
247	9	9	0	Out	40	36	40	34	4.7	5.0	18.4	143.6	-5.00
248	9	9	0	Out	40	36	40	34	4.7	5.4	18.9	147.6	-13.56
249	9	9	-0.935	Out	40	36	40	34	5.4	5.0	21.2	166.7	4.46
250	9	9	-0.935	Out	40	36	40	34	5.7	5.0	22.4	174.6	11.51

TABLE IV (Cont)

Run No.	h_L (in.)	h_R (in.)	α (deg)	Center Board	δ_{L_i} (deg)	δ_{L_o} (deg)	δ_{R_i} (deg)	δ_{R_o} (deg)	P'_{oL} (psi)	P'_{oR} (psi)	\bar{P}_B (psf)	L (lb/ft)	M (ft-lb/ft)
D-251	9	7	-0.935	Out	40	36	40	34	5.4	4.7	20.6	160.4	10.20
252	↓	↓	↓	In	↓	↓	↓	↓	5.4	5.0	20.7	163.9	-3.67
253	↓	↓	↓	Out	↓	↓	↓	↓	5.7	4.7	21.2	165.5	15.65
254	↓	5	-1.870	↓	↓	↓	↓	↓	5.7	4.7	21.1	164.4	20.14
255	↓	↓	-1.870	↓	↓	↓	↓	↓	5.4	4.7	20.3	158.2	16.73
256	↓	↓	-1.870	↓	↓	↓	↓	↓	5.4	4.3	19.8	154.0	20.20
257	6	6	0	↓	↓	↓	↓	↓	5.4	4.7	19.8	154.3	8.84
258	↓	↓	↓	↓	↓	↓	↓	↓	5.7	5.0	21.2	164.7	8.47
259	↓	↓	↓	In	30	30	40	34	5.0	5.0	18.4	142.7	1.82
260	↓	↓	↓	In	30	30	40	34	↓	↓	18.9	142.1	16.25
261	↓	↓	↓	Out	40	35	30	30	↓	↓	19.4	148.4	-0.53
262	↓	↓	↓	In	42	42	40	34	↓	↓	20.2	154.8	-0.33
263	↓	↓	↓	Out	42	42	40	34	↓	↓	20.0	152.8	-4.27
264	↓	4	-0.935	↓	42	42	40	34	↓	↓	18.9	140.7	-10.79
265	9	9	0	In	40	35	30	30	↓	↓	18.4	142.1	6.29
266	9	9	0	↓	↓	↓	↓	↓	↓	↓	19.0	143.3	-9.53
267	9	3	-2.805	Out	↓	↓	↓	↓	↓	↓	19.7	146.9	-8.11
268	9	9	0	Out	↓	↓	↓	↓	↓	↓	16.2	127.5	24.45

TABLE IV (Cont)
Stability Model
300 Series Data Summary
Inlet Sealed

Run No.	h_L (in.)	h_R (in.)	α (deg)	δ_{L_i} (deg)	δ_{L_o} (deg)	δ_{R_i} (deg)	δ_{R_o} (deg)	P'_{oL} (psi)	P'_{oR} (psi)	\bar{P}_B (psf)	L (lb/ft)	M (ft-lb/ft)
D-301	4	3	-0.467	31	31	30	30	5	5	26.1	204.4	14.63
302	4	4	0	31	31	30	30	5	5	26.7	206.8	-0.11
303	5	5	0	31	31	30	30	5	5	28.3	224.2	8.37
304	6	6	0	31	31	30	30	5	5	26.5	210.4	3.74
305	8	8	0	31	31	30	30	5	5	23.2	181.0	2.19
306	10	6	-1.870	31	31	30	30	5	5	17.5	137.8	6.49
307	9	7	-0.935	31	31	30	30	5	5	20.5	159.9	-0.56
308	9	5	-1.870	31	31	30	30	5	5	22.6	176.8	4.90
309	9	3	-2.805	31	31	30	30	5	5	23.0	178.6	8.74
310	3	9	+2.805	31	31	30	30	5	5	23.4	182.5	1.48
311	6	4	-0.935	31	31	30	35	5	5	26.7	211.4	11.29
312	8	8	0	30	30	30	35	5	5	22.5	177.2	7.37
313	8	6	-0.935	30	30	30	35	5	5	23.8	188.3	10.48
314	8	4	-1.870	30	30	30	40	5	5	24.9	196.7	16.70
315	8	8	0	30	30	30	40	5	5	21.8	170.9	12.64
316	8	6	-0.935	30	30	30	25	5	5	23.5	184.6	15.88
317	8	4	-1.870	30	30	30	25	5	5	23.9	185.9	4.74
318	8	8	0	30	30	30	40	5	5	22.5	174.4	6.07
319	9	9	0	40	40	40	40	5	5	19.4	149.7	6.89
320	9	7	-0.935	40	40	40	35	5	5	20.7	163.1	1.75
321	9	3	-2.805	40	40	40	35	5	5	21.0	165.4	11.19
322	9	7	-0.935	40	40	40	45	5	5	21.6	169.5	-8.67
323	9	7	-0.935	40	40	40	45	5	5	20.7	163.5	14.04
324	9	9	0	40	40	40	40	5	6	19.2	149.8	-23.58

TABLE IV (Cont)

Run No.	h_L (in.)	h_R (in.)	α (deg)	δ_{L_i} (deg)	δ_{L_o} (deg)	δ_{R_i} (deg)	δ_{R_o} (deg)	P'_{oL} (psi)	P'_{oR} (psi)	\bar{P}_B (psf)	L (lb/ft)	M (ft-lb/ft)
D-325	9	9	0	40	40	40	35	5	5	19.4	150.6	-25.03
326	9	9	0	40	40	40	45	5	5	18.1	141.5	15.37
327	6	6	0	40	40	40	40	5	6	26.0	207.2	-13.75
328	6	6	0	40	40	40	45	5	5	22.3	177.6	20.02
329	6	4	-0.935	40	40	40	45	40	40	22.5	178.4	17.78
330	6	4	-0.935	36	36	36	36	40	40	24.1	190.7	7.76
331	9	9	0	36	36	36	36	40	40	20.6	159.8	-0.24
332	6	6	0	36	36	36	36	40	40	25.1	198.6	18.80
333	5	5	0	36	36	36	36	40	40	26.0	208.3	12.06
334	4	4	0	36	36	36	36	40	40	24.9	193.0	-2.21

TABLE IV (Cont)
Stability Model
400 Series Data Summary
Inlet Sealed

Run No.	h_L (in.)	h_R (in.)	α (deg)	δ_{L_i} (deg)	δ_{L_o} (deg)	δ_{R_i} (deg)	δ_{R_o} (deg)	P_{oL} (psi)	P_{oR} (psi)	P'_{oL} (psf)	P'_{oR} (psf)	\bar{P}_o (psf)	L (lb/ft)	m (ft-lb/ft)
D-401	4	4	0	31	31	30	30	5	5	-2.08	-2.85	27.2	214.3	-1.51
402	↓	↓	↓	31	31	30	30	5	6	+0.52	-5.84	30.0	236.8	-18.70
403	↓	↓	↓	31	40	30	15	5	6	+1.55	-3.37	26.9	204.3	-15.38
404	↓	↓	↓	31	40	30	15	5	5	-1.82	-0.65	25.6	193.5	-7.39
405	3	5	0.935	31	31	30	30	↓	↓	-3.63	-2.85	26.9	207.9	-15.70
406	6	6	0	↓	↓	↓	↓	↓	↓	+0.52	-0.78	25.6	203.6	-1.24
407	↓	↓	↓	↓	↓	↓	↓	↓	6	2.59	-2.47	27.9	220.7	-19.87
408	↓	↓	↓	31	40	30	15	↓	6	2.08	-0.52	24.0	189.0	-30.57
409	↓	↓	↓	31	40	30	15	↓	5	-0.26	+0.78	23.1	182.4	-14.69
410	5	7	0.935	31	31	30	30	↓	↓	-1.17	+0.52	25.6	202.7	2.35
411	4	8	1.870	↓	↓	↓	↓	↓	↓	-3.10	+1.30	25.0	195.6	-2.72
412	3	9	2.805	↓	↓	↓	↓	↓	↓	-6.22	+1.43	22.6	176.8	1.72
413	9	9	0	40	39	40	39	↓	↓	+0.26	-0.13	19.4	150.4	5.01
414	↓	↓	↓	40	39	40	39	↓	6	+4.15	-3.76	18.8	147.5	-27.59
415	↓	↓	↓	40	43	40	25	↓	6	+3.11	-1.94	17.1	131.9	-33.71
416	↓	↓	↓	40	43	40	25	↓	5	-0.52	+0.52	18.1	138.0	-0.02
417	8	10	0.935	40	39	40	39	↓	6	+1.30	-0.73	21.0	161.9	-15.28
418	8	10	0.935	↓	↓	↓	↓	↓	5	-2.08	+1.56	17.0	133.7	8.99
419	7	11	1.870	↓	↓	↓	↓	↓	5	-4.54	+2.73	14.0	110.3	15.04
420	7	11	1.870	↓	↓	↓	↓	↓	6	-3.38	+1.95	16.8	130.6	6.67
421	6	12	2.805	↓	↓	↓	↓	↓	6	-5.45	+2.59	14.9	117.0	12.59
422	↓	↓	↓	40	43	40	25	↓	5	-6.35	+3.12	12.4	98.43	18.43
423	↓	↓	↓	40	43	40	25	↓	5	-6.10	+4.28	13.0	102.5	12.95
424	↓	↓	↓	40	43	40	25	↓	6	-4.80	+3.50	15.9	123.2	1.08

THREE-DIMENSIONAL MODEL TESTS

Previous investigations (References 2, 3, and 4) have shown that particular attention should be given to the design of the corner configuration of the recirculation concept, because losses in the overall lifting capability, ranging from 1 to 20 percent, have occurred, depending on the corner design. In arriving at a final configuration, consideration was given not only to the internal and external aerodynamics of the air curtain but also to fabrication techniques, to vehicle control devices and planform, and to probable future modifications (such as for over water and for high-speed forward flight).

A corner configuration was designed and a brief experimental investigation was conducted to determine the anticipated full-scale three-dimensional performance. There are some obvious limitations to the interpretation of these data from the test, because the model is not a true three-dimensional model. The recorded lift, as a function of height, primary pressure, and exit flap angle is valid and requires no correction. However, the complete three-dimensional effects of variables, such as different inlet extension sizes and shapes, surface roughness, and over-water operation on vehicle performance must be determined from the full-size test vehicle.

Description of Models and Instrumentation

1. Module Corner Model

As mentioned above, the basic design of the corner configuration involves numerous considerations. The detail design involves not only the vehicle planform but the internal dimensions of the ejector as well. In order to maintain the proper performance in the ejector, certain area ratios, such as the relationship between the area at the inlet, the end of the mixing section, and the exit, must be maintained.

Obviously, the characteristic width of the corner ejector will increase radially; therefore, the thickness must be reduced proportionally. This results in an exit air curtain which is relatively thin in comparison to the flow from the sides, front, and rear ejectors. For these reasons, and those mentioned above, a modular form of construction was used. This permitted fabricating and testing one of the units prior to the commitment of the design to all units.

The module corner model was designed, fabricated in the existing two-dimensional tunnel, and tested. The results were incorporated in the design of the remaining units. Figure 28 shows the side and top views of this model. Special features such as the individual alignment of the primary nozzles, static pressure taps throughout, and exit rakes were provided in the original unit.

The primary objective of this test was to determine the basic feasibility of the design and to provide detail design information, such as the required individual nozzle flow angle and exit flap angle. For the most part, the tests were conducted at one primary pressure (5 psig) and one height (equivalent to 18 inches full scale). The results, shown in Table IV, indicate that the performance is adequate and that the effect of nozzle alignment is important. No separate data were recorded on the effect of the exit flap since the optimum flap angle did not change with respect to nozzle alignment. The configuration chosen for the corner model is shown in Table V as Run No. 4. At a primary pressure of 5 psi and a height of 9 inches, with the pressure survey rakes removed from the exit flow, the base pressure received was 12.8 psf. This corresponds to a base pressure of 15.3 psf obtained from the normal two-dimensional configuration under similar test conditions.

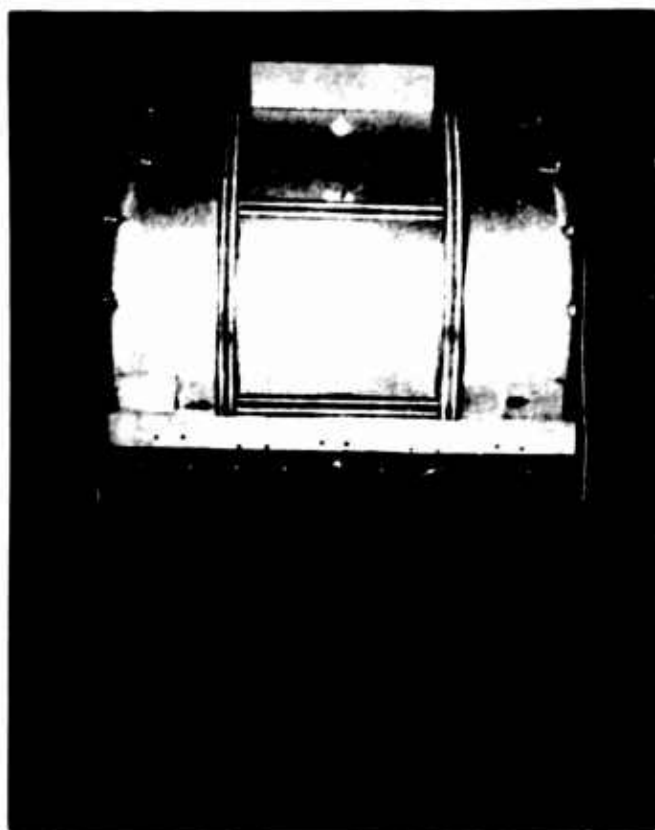


Figure 28. Corner Module Model

TABLE V
NOZZLE ALIGNMENT EFFECTS

Flow Angle (degrees)						
Run No.	Nozzle No. 1	Nozzle No. 2	Nozzle No. 3	Nozzle No. 4	\bar{P}_B	\bar{P}_c
1	0	0	0	0	11.3	-0.45
2	+2	0	0	-2	11.8	-0.45
3	3	1	-1	-3	11.3	-0.45
4	4	2	-2	-4	11.9	0
5	6	3	-3	-6	12.1	0
6	10	5	-5	-10	11.7	0
7	12	6	-6	-12	11.7	0
8	+1	+1	+1	+1	10.8	-0.45
9	+2	+2	+2	+2	10.6	0
10	+4	+4	+4	+4	10.6	0
11	+8	+8	+8	+8	9.2	0
12	10	10	10	10	8.8	0

Note: a) $P_o' = 5.0$ psig
b) $m' = 0.343$ lb/sec-ft
c) $\delta_i = 38^\circ$, $\delta_o = 45^\circ$
d) Pressure survey rakes in exit flow.

2. Half-Scale Quarter Model

The corner model is a 1/2-scale quarter section of the research vehicle. Figure 29 is the 1/2-scale quarter model assembly drawing. Figures 30 through 33 are photographs of the model and support equipment. Plywood, aluminum, and steel are the principal materials used in the fabrication of the model and its associated equipment. The model is adjustable to 3-, 6-, 9-, 12-, and 18-inch heights; and the attitude of the header assembly is completely adjustable. The following paragraphs describe the model and its equipment more fully.

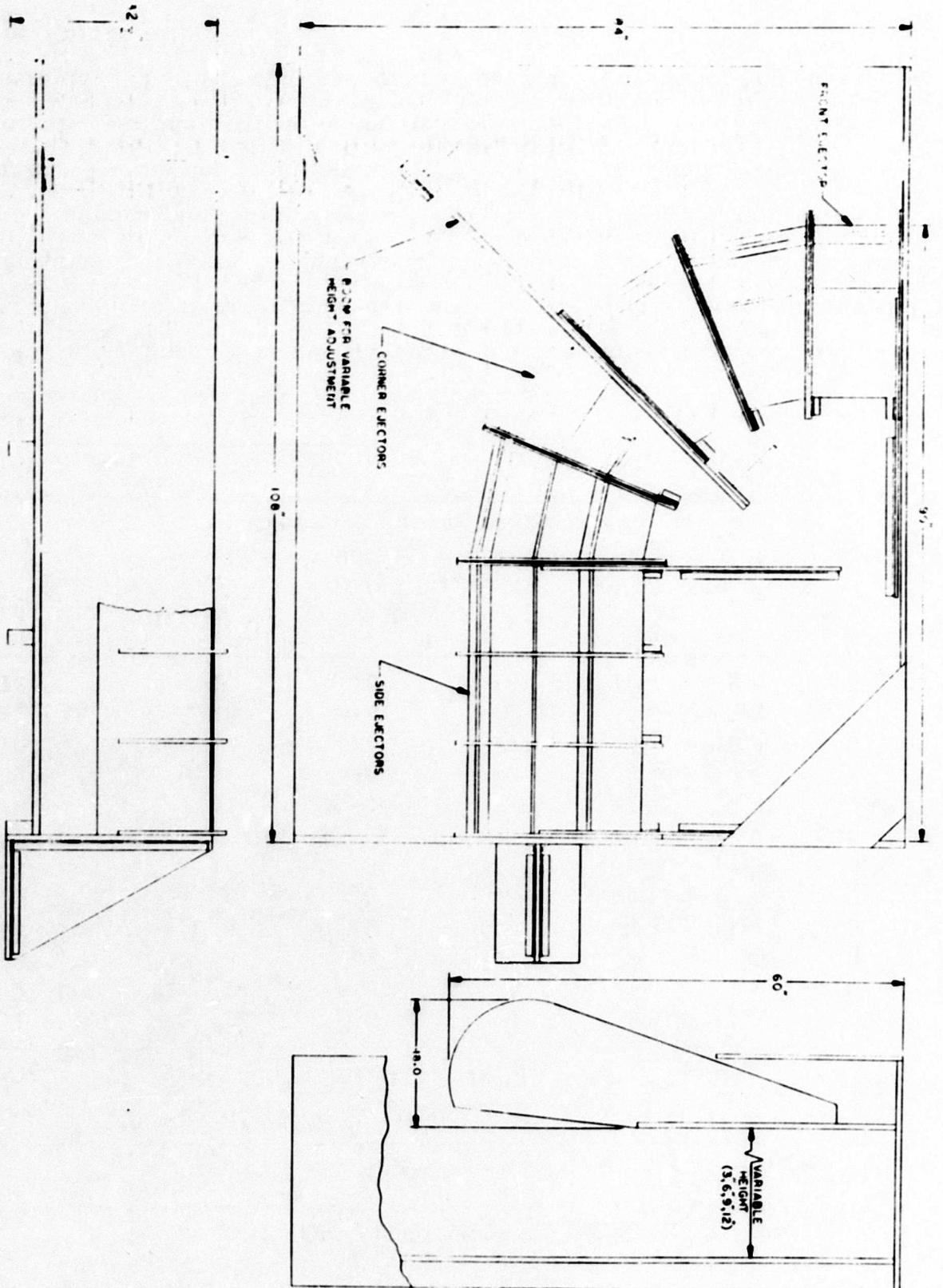


Figure 29. Assembly Drawing on Corner Model



Figure 30. Front View of Quarter Model

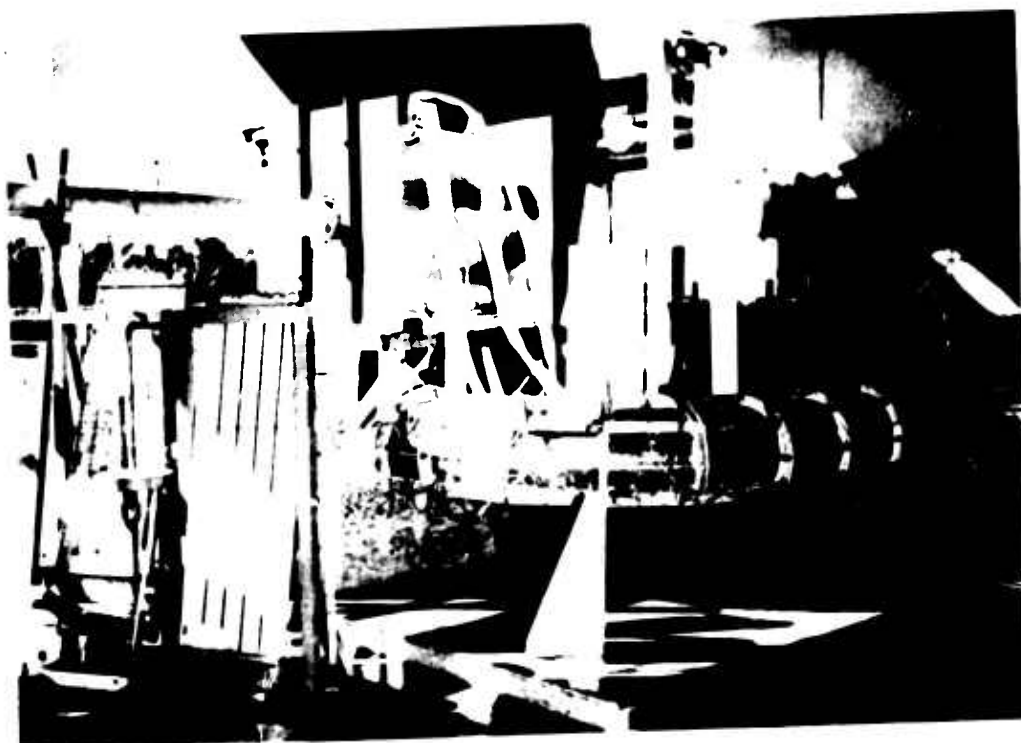
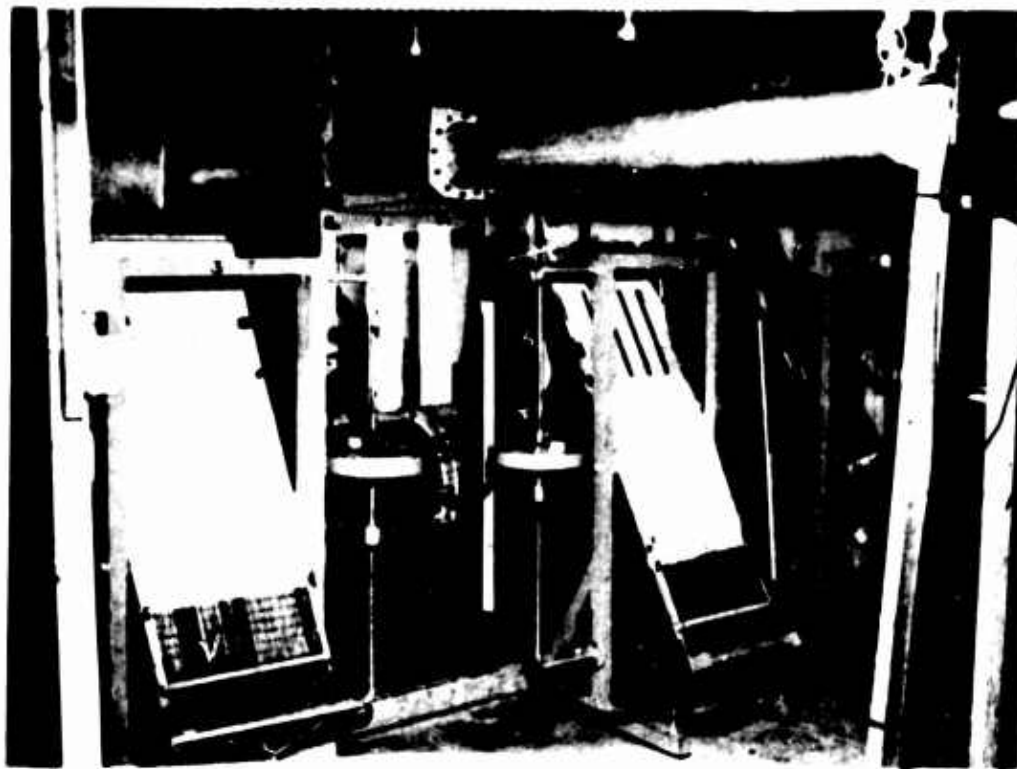


Figure 31. Three-Quarter View of Model



Figure 32. Primary Airlines, Quarter Model



**Figure 33. Instrumentation and Test Setup,
Quarter Model**

The support structure consists of a rectangular platform and two vertical center boards, $84\frac{3}{4}$ inches wide, $108\frac{3}{4}$ inches long, and $4\frac{3}{8}$ inches high. The platform is plywood-covered to ensure smooth terrain for test purposes. Vertical centerboards replace the planes of symmetry and also provide support for the model.

The 1/2-scale quarter corner model consists of the base, the ejectors, and the header assembly. The model base is a 36-inch by 62.09-inch rectangle with one corner modified by a series of chords of four equal arcs totaling 90 degrees. Recirculating ejectors are attached to the base.

Ejector internal lines for the side, front, and corner sections are shown in Figure 34. Lines for the side and front ejectors were scaled from earlier ejectors. The corner ejector lines are also from earlier ejectors but are to maintain a constant internal area for the expanding corner planform. The inlet dimensions of each ejector reflect an $AR = 47.6$ ($AR = \text{area of ejector inlet/exit area of nozzles}$). Made from aluminum sheet, the internal air passage is formed to the required contour. Surfaces of the passages were painted and sanded to provide a uniform, smooth surface.

The different ejector sections are shown in Figure 34. Outer surface dimensions of the corner ejectors were identical to the other ejectors. This provided a continuous, smooth, outer-exit jet surface. Exit flaps were located on the inner and outer surfaces of each ejector section.

Header nomenclature and dimensions are presented in Figure 35. The header nozzle configuration used in this test was based on a header design which was developed during previous test programs. Separate header assemblies were used to ensure an even distribution

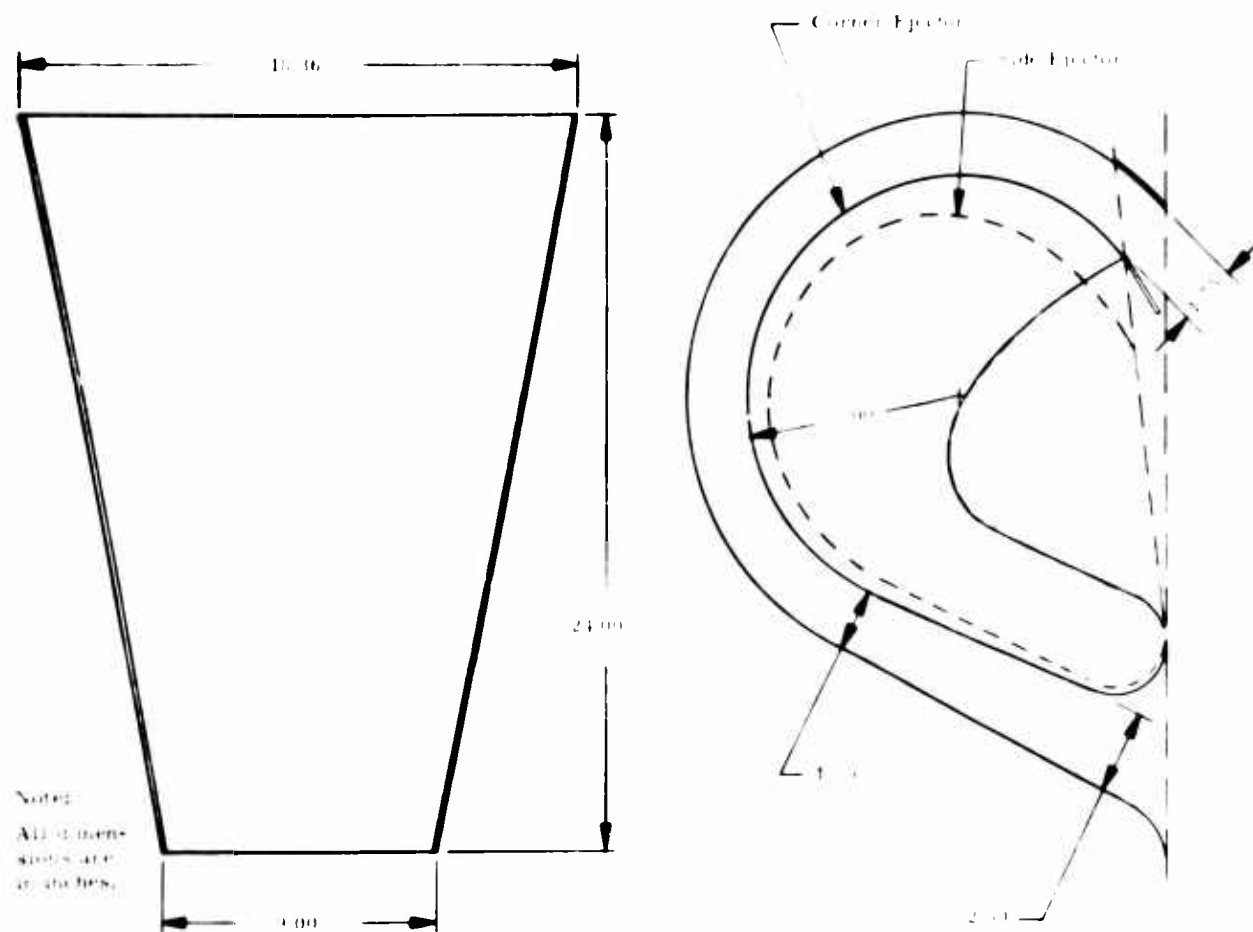


Figure 34. Comparison of Side and Corner Ejector Internal Line

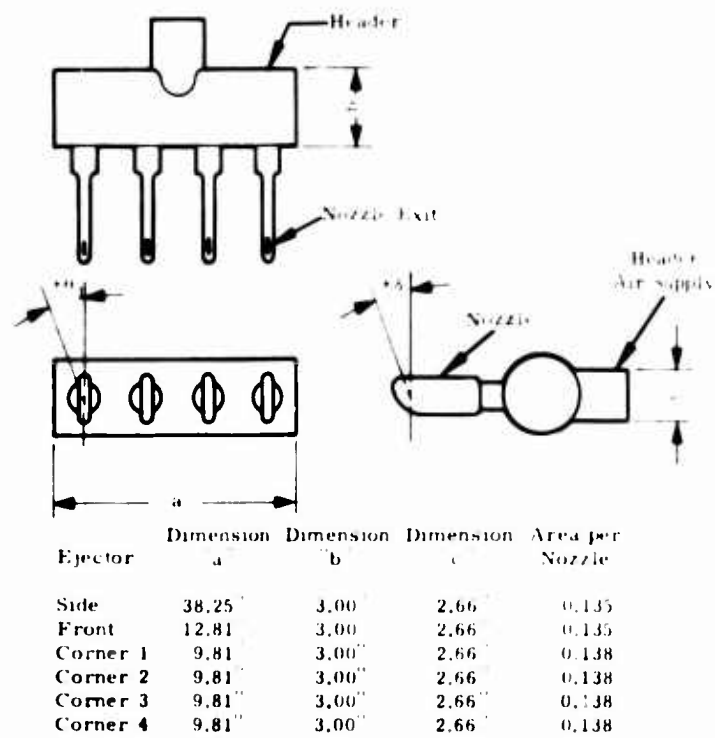


Figure 35. Header Nomenclature and Dimensions

of pressure and mass flow to each nozzle. This allowed flexibility in the choice of primary (header) pressure, P_0' , to provide for alternate header location with respect to the ejector inlet, and to facilitate header fabrication and assembly. Each nozzle of the corner headers, as shown in Figure 36, has a prescribed angular orientation based on test data from the module corner model.

Angular orientation of the nozzles is shown in Figure 35. Orientation of the primary flow for the side, front, and rear ejectors is directed parallel with the walls of the mixing section.

Test Procedures and Data Reduction

1. Model Calibration

The quarter model was instrumented with approximately 300 pressure orifices to measure the base, inlet, exit, and internal-flow static pressures and the total pressures in the flow. Additional instrumentation measured the header pressures, pressure drop of flowmeter, and the plenum tank pressure. These pressures were measured on multiple tube manometer boards and U-tubes. The manometer boards were adjusted to a 30-degree tilt from the vertical and used water as a working fluid. The primary air temperature was measured by a dial thermometer. Figures 37 and 38 present the pressure tube locations.

The individual primary nozzle sections were calibrated for mass flow, total pressure at the nozzle exit, and exit flow angularity.

The flow angularity test consisted of pumping water into the header supply pipe and measuring the resulting flow angles. Table VI summarizes the flow angularity test results, and Figures 39 and 40 are photographs of this calibration. From these data, it can be seen that

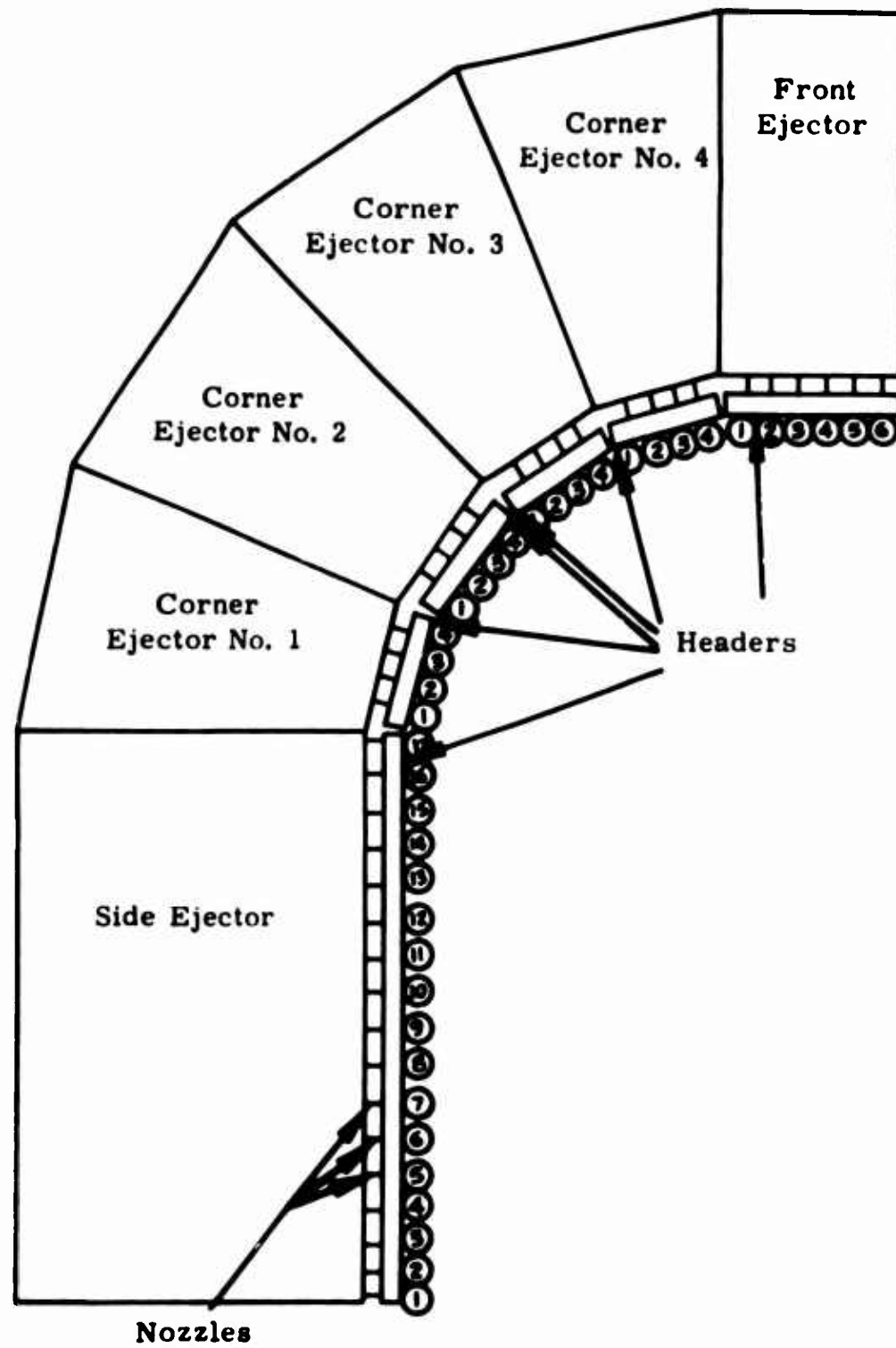


Figure 36. Header and Nozzle Locations

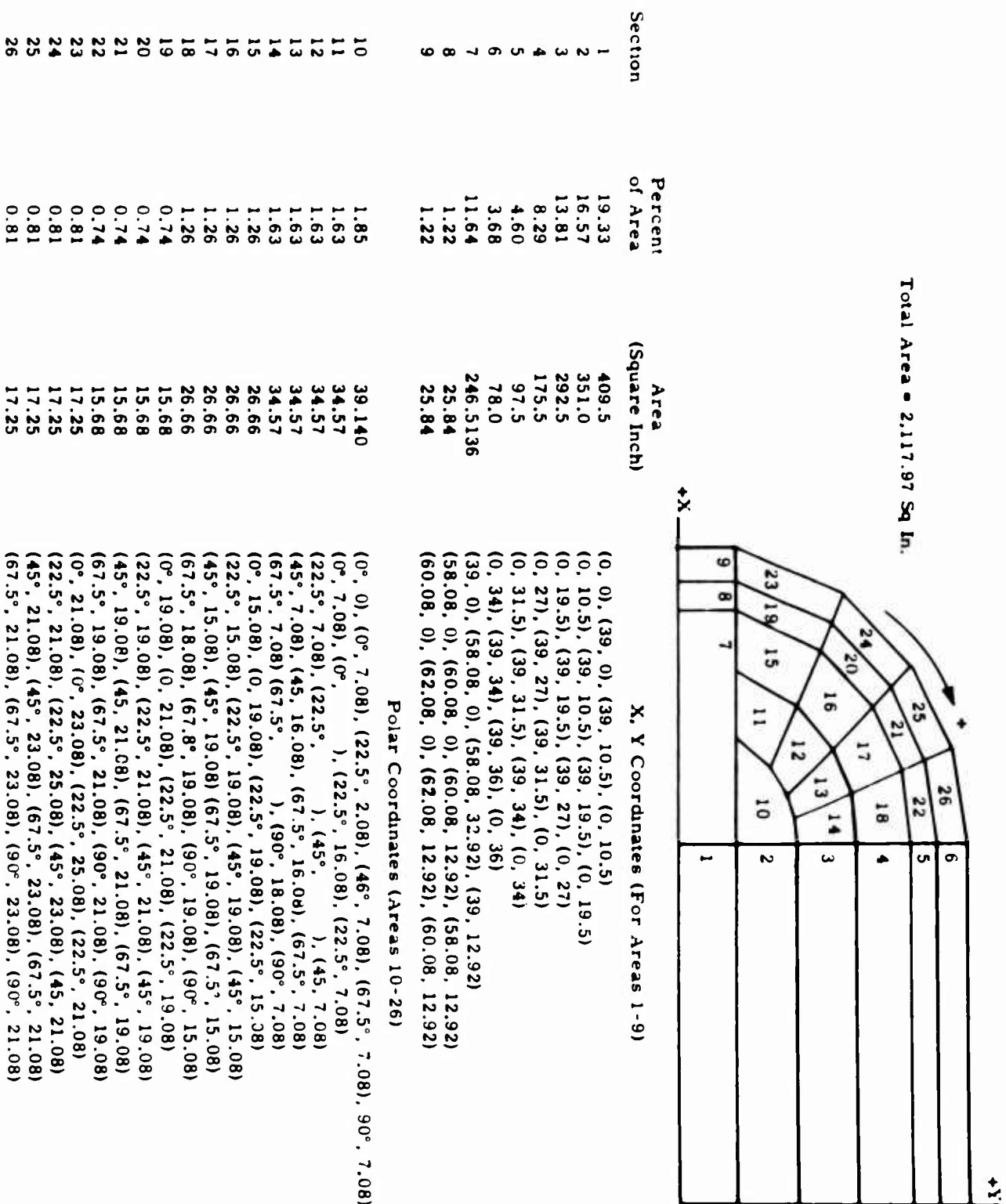
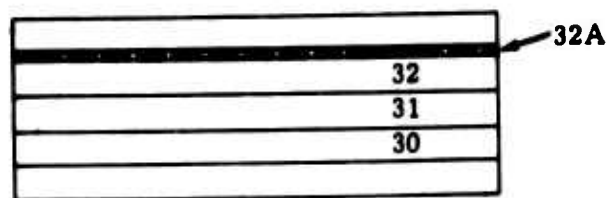


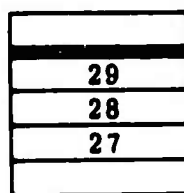
Figure 37. Area Section of Base

Section	Area (Square Inch)	Percent of Area
27	34.4	6.33
28	41.3	7.60
29	48.1	8.85
29A	10.9	2.01
30	103.8	19.1
31	124.8	23.0
32	145.0	26.7
32A	32.8	6.04
33-1	47.1	5.93
34-1	45.4	5.72
35-1	56.9	7.17
36-1	49.6	6.25
33-2	47.1	5.93
34-2	45.4	5.72
35-2	56.9	7.17
36-2	49.6	6.25
33-3	47.1	5.93
34-3	45.4	5.72
35-3	56.9	7.17
36-3	49.6	6.25
33-4	47.1	5.93
34-4	45.4	5.72
35-4	56.9	7.17
36-4	49.6	6.25

Top View
Side Ejector



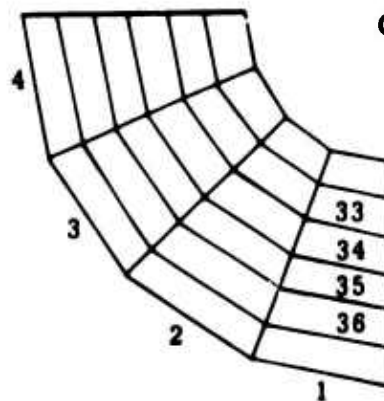
Front Ejector



Total Area

541.1 square in. (side - front)
 (ejector only)
 507.4 square in. W/O 29A and 32A

Corner Ejectors
Top View



Total Area

796.0 square in. (corner ejector only)

Figure 38. Area Section of Cavity



Figure 39. Header Calibration Test
(Front View)



Figure 40. Header Calibration
Test (Side View)

none of the corner ejectors has the desired flow angle distribution as determined from the module corner model tests.

TABLE VI
NOZZLE ANGLE CALIBRATION

Header Assembly	Nozzle Number	Azimuth Flow Angle		Elevation Flow Angle (deg)
		Measured (deg)	Desired (deg)	
Side	1	+0	0	+4.0
	2	-0	0	+4.0
	3	-1.0	0	+4.0
	4	-3.5	0	+4.0
	5	-1.0	0	+4.0
	6	-1.0	0	+4.0
	7	-2.5	0	+4.0
	8	-2.5	0	+4.0
	9	0.0	0	+4.0
	10	-3.5	0	+4.0
	11	0.5	0	+4.0
	12	-1.0	0	+4.0
	13	-1.0	0	+4.0
	14	-3.0	0	+4.0
	15	+3.5	0	+4.0
	16	-1.5	0	+4.0
	17	0.0	0	+4.0
Front	1	0.0	0	5.0
	2	3.0	0	5.0
	3	0.0	0	5.0
	4	1.0	0	5.0
	5	1.0	0	5.0
	6	0.0	0	5.0
No. 1	1	+6.0	+0	8.5
	2	-3.25	+2	8.5
	3	-1.0	-2	8.5
	4	+4.0	-4	8.5

TABLE VI (Cont)

Header Assembly	Nozzle Number	Azimuth Flow Angle		Elevation Flow Angle (deg)
		Measured (deg)	Desired (deg)	
No. 2	1	2.5	+4	4.5
	2	0.0	+2	4.0
	3	0.0	-2	4.0
	4	2.0	-4	4.0
No. 3	1	-3.5	+4	7.0
	2	-3.0	+2	7.0
	3	-3.5	-2	7.0
	4	-2.5	-4	7.0
No. 4	1	5.0	+4	7.0
	2	5.0	+2	7.0
	3	4.0	-2	7.0
	4	-1.5	-4	7.0

Calibration of the header mass flow characteristics and measurement of the individual nozzle total pressure was conducted at value of header pressure of $P_O' = 4, 5, \text{ and } 6$ psig. Figures 41 and 42 present a comparison of the measured mass flow with the theoretical value. The average effective area of the nozzles is about 50 percent of the geometric area.

Simultaneously with the mass flow calibration, the total pressure at each nozzle exit plane was recorded. The measured total pressure values were relatively uniform except for the nozzles located directly opposite the header supply pipe. It was concluded that the inlet to the primary headers should be oriented at 90 degrees to the nozzle axis rather than directly opposite, thereby preventing an uneven pressure distribution.

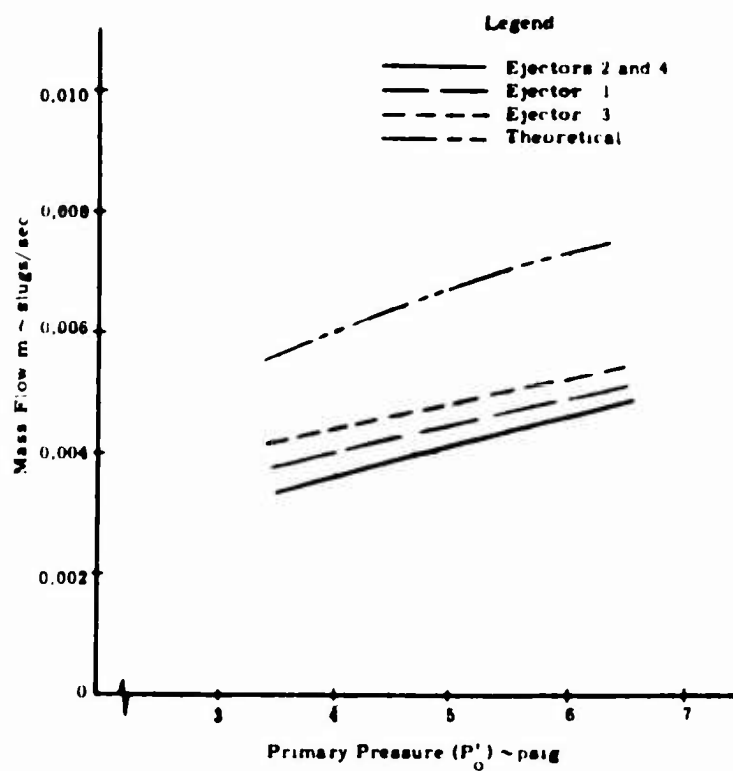


Figure 41. Comparison of Theoretical and Measured Mass Flow, Half-Scale Quarter Model (Cornier)

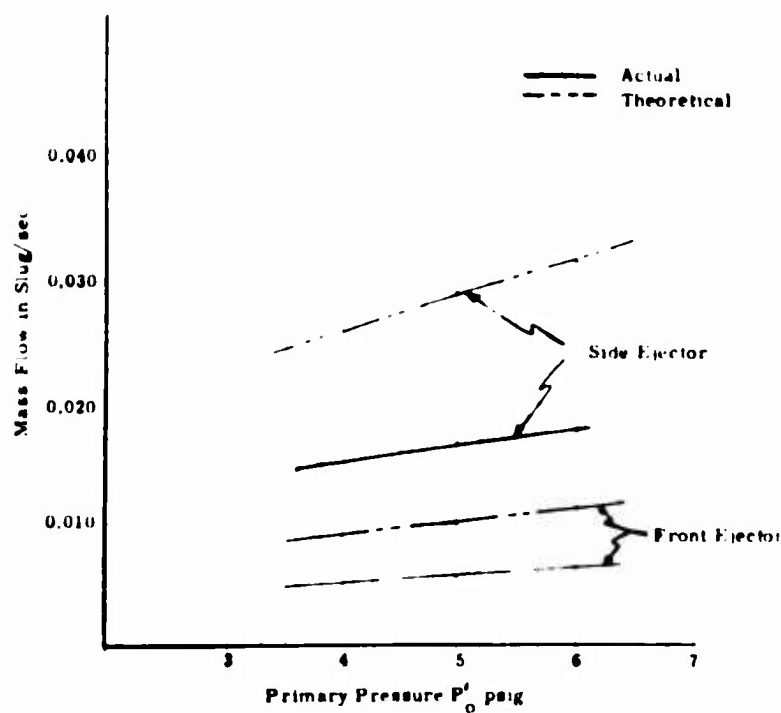


Figure 42. Comparison of Theoretical and Measured Mass Flow, Half-Scale Quarter Model

2. Test Program

The objectives of the test program for the corner model were as follows:

- a. The determination of the general performance of the model at varying heights, primary pressures, and exit flap angles.
- b. The effect of an inlet extension (skirt).
- c. The determination of the model performance over simulated surface roughness.
- d. The determination of the model performance over water.

The general test procedures were concerned with adjusting the flap angles and setting and maintaining the header pressure for a particular model configuration; adjustment of the inner and outer exit flaps was accomplished by setting a tooling jig on a flat surface parallel to the model base and by adjusting the flap angles to the reference surface. This procedure produced uniform and repeatable flap angle settings. A review of the nozzle total pressure calibration data showed that operation of the model at constant primary pressure at the plenum resulted in a significant pressure variation between header assemblies. This did not reflect a realistic operating condition for the full-scale vehicle. Therefore, the model was tested at a uniform nozzle exit total pressure by maintaining a total head in the plenum at a higher value than was required, and then adjusting each header pressure to its assigned value.

3. Data Reduction

The pressure orifice locations for this corner model are shown in Figure 43. The base pressure orifices were located so that each orifice represented an area. In the regions of rapid pressure

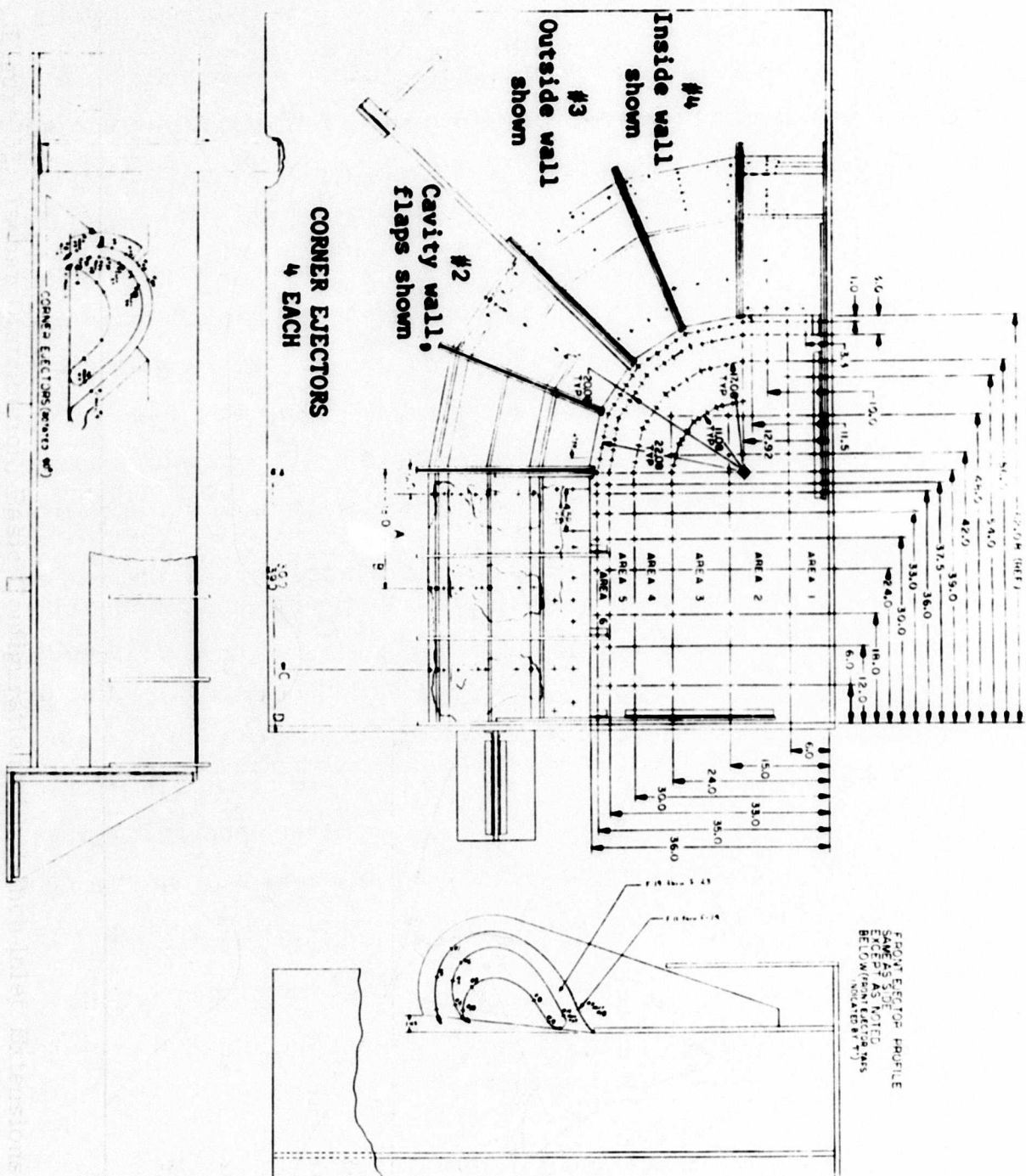


Figure 43. Pressure Orifice Locations

changes the orifices were located closer together. The cavity orifices were located in a similar fashion. Figures 37 and 38 show the division of the base and cavity areas.

The corner model performance data are presented as an average base pressure and/or average cavity pressure versus either height or primary header pressure (P'_0).

To establish the performance of the corner model, static pressures representing pressures in the base, in the cavity, in the exit and inlet of the internal-flow ducting, and on the exit flaps were recorded. The total and static pressures of the exit flow were recorded by means of a rake located in the exit flow just upstream of the exit flap hinge lines. Additional recorded pressures provided data for header primary pressure mass flow measurements and calculations.

The average base pressure is determined in the following manner:

The average base pressure for each section is calculated from

$$P_{b_n} = \frac{\sum_{1}^{\chi} P_{b_n}}{\chi}$$

where n designates the section and χ is the number of orifices in the section.

This is corrected to reflect the reference area $A_r = 2,118 \text{ in.}^2$ which is the total base area for the 1/2-scale quarter model.

$$\bar{P}_{b_n} = P_{b_n} \frac{A_n}{A_r}.$$

The base pressure of each section is added to give the average base pressure (\bar{P}_b) referenced to the base area.

$$\bar{P}_b = \frac{\sum_{n=1}^{n=26} \bar{P}_{b_n}}{n}$$

The average cavity pressure is determined in a similar fashion. The total cavity area of 1303.4 in² is the reference area used to correct each cavity section contribution. The side and front ejector area of sections 29A and 32A (the area within the reflex of the cavity) is not included in the reference area.

Discussion of Experimental Data

1. Basic Corner Model

The performance data represent a sealed configuration as described in the previous section on two-dimensional tests unless otherwise noted. Figure 44 presents the base pressure variation with flap angle for the design height. The optimum setting of 35 degrees for inner and 38 degrees for outer flaps reflects a 1 percent higher average base pressure than for the flap setting used at the 4-inch height testing. The optimum flap angles for the other heights were determined in a similar manner.

Figure 45 summarizes the base pressure variation with height for primary pressures of 4, 5, and 6 psig for the corner model. The dotted portion of the primary pressure curve for $P'_0 = 6$ psig near the 6-inch test height is an extrapolated curve because the data for this test point were not considered as representative.

Figure 46 presents the cavity pressure variation with height for $P'_0 = 4, 5,$ and 6 psig respectively. Again, the dotted curve is extrapolated from the data at $h = 6$ inches and $P'_0 = 6$ psig. At all test conditions, the cavity pressure is positive; furthermore, the cavity pressure has a stable variation with height. This trend indicates

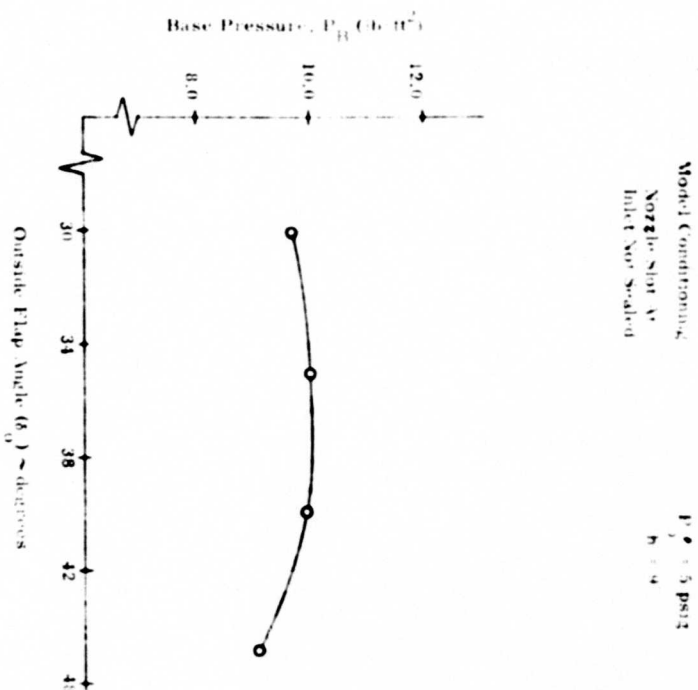


Figure 44. Base Pressure Versus Flap Angle, Corner Model

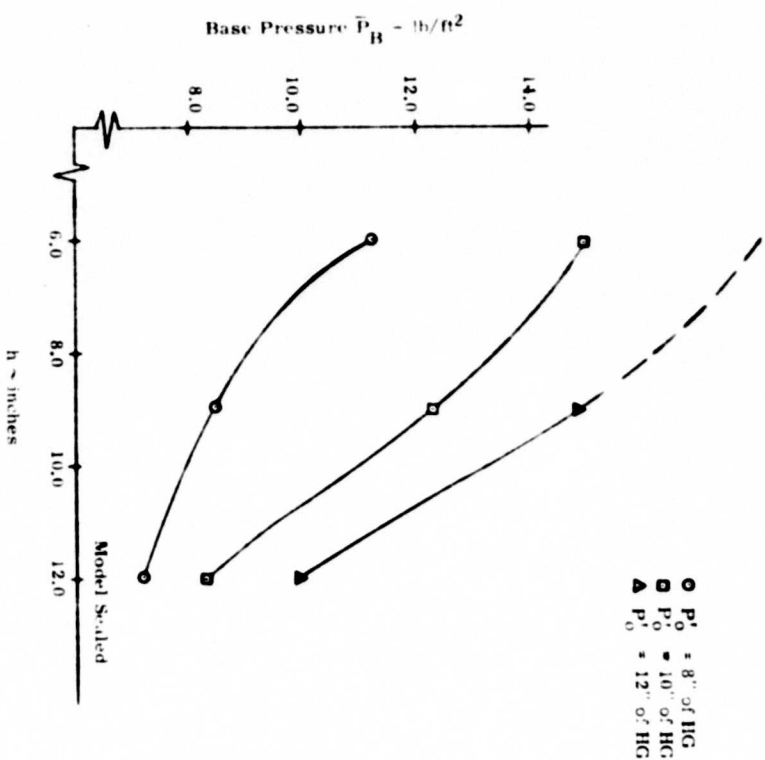


Figure 45. Base Pressure Versus Height, Corner Model

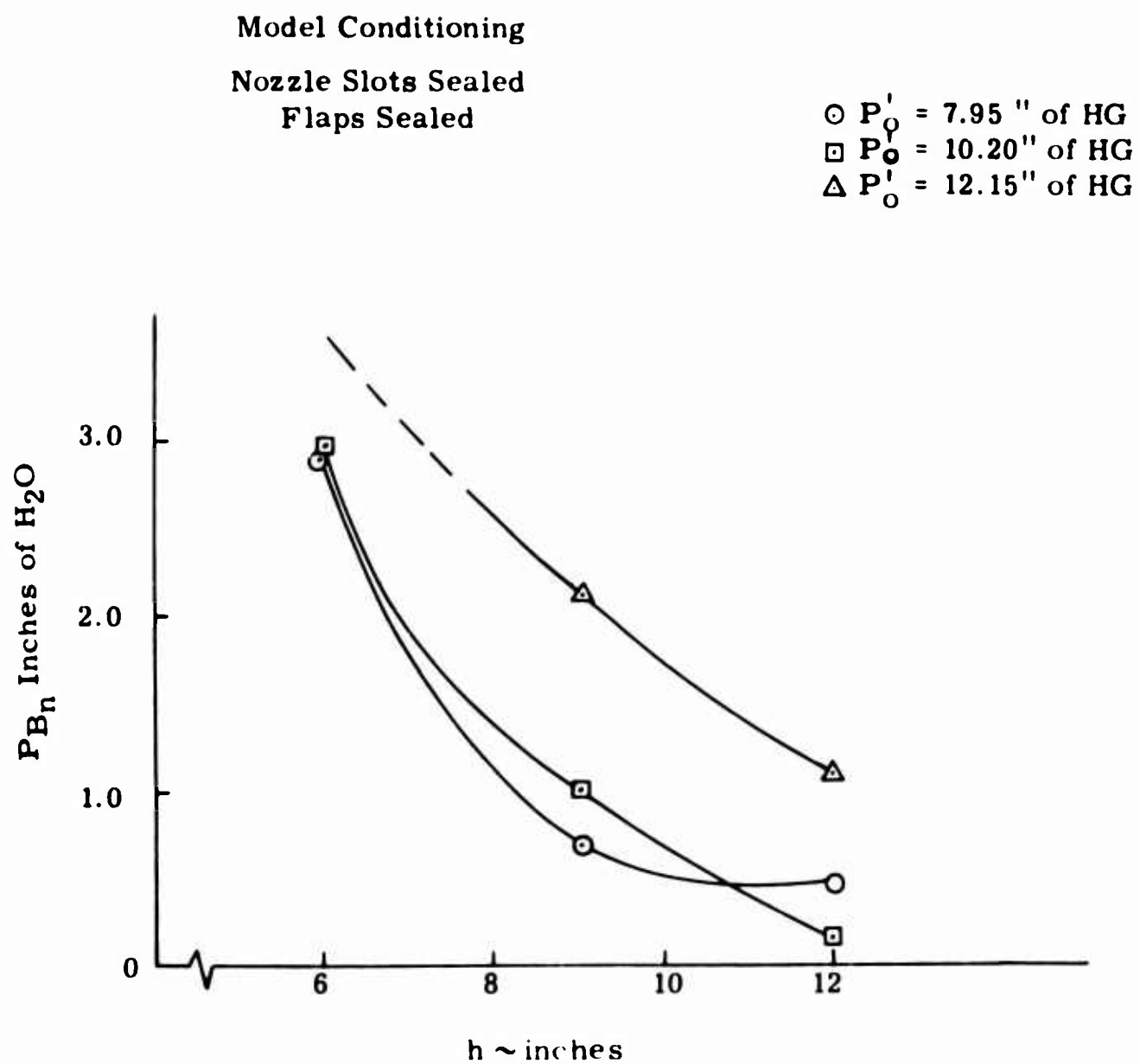


Figure 46. Cavity Pressure Versus Height, Corner Model

that the inherent static stability properties of the three-dimensional vehicle will be superior to the predicted characteristics based on two-dimensional tests as discussed in the previous section, "Two-Dimensional Model Tests".

The corner ejectors were tested as separate units and in combination with each other. Figure 47 identifies the various combinations tested. A summary and comparison of the corner data are presented in Figures 48, 49, and 50. The general trend indicates that as the corners are more and more isolated, the lower the average base pressure becomes. In Figure 49 a comparison of the relative ejector strength for the isolated combination of corners is made. It is seen, for example, that ejector No. 1 operates best when combined with all of the ejectors and poorest when combined with ejectors 2-3 (combination 1-2-3). It is paradoxical that whenever ejector 3 is included in the combination of 1-2-3 it (No. 3) has very poor base pressure; yet with the addition of ejector 4, in a combination of 1-2-3-4, ejector 3 has the highest base pressure. Again the difference in base pressure levels in Figure 49 is a measure of the interaction and support supplied by the individual ejectors. In Figure 50 a comparison between ejectors for the individual and combined cases shows that in every instance the individual ejector performance is lower.

In Figure 48 it is seen that the original two-dimensional corner ejector provided the highest base pressure. The difference in performance between this ejector unit and the individual corner units of the corner model appears to be in direct relationship to the alignment of the primary nozzles. This was shown in the previous section on "Model Calibration", where the alignment is not critical but

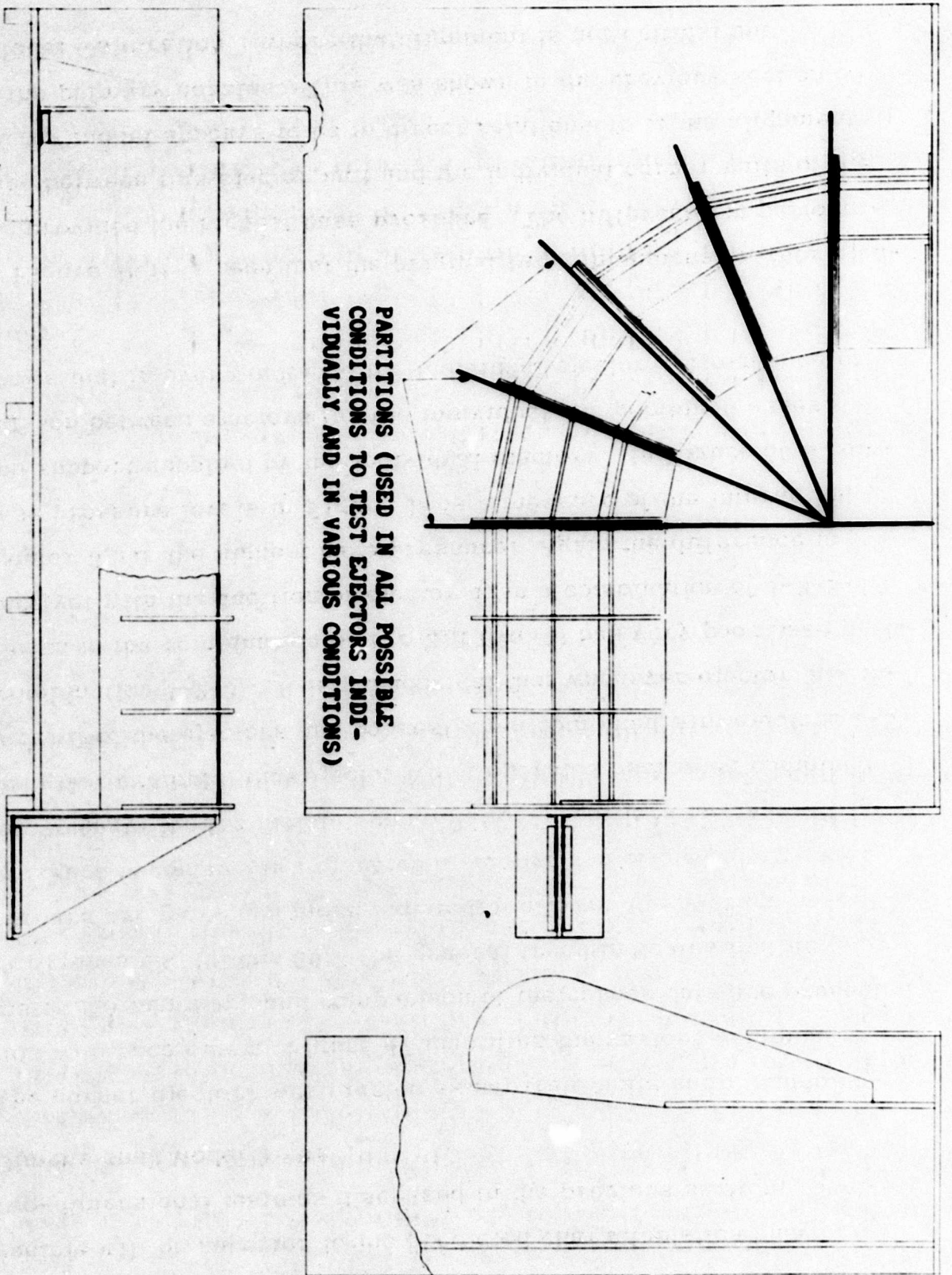


Figure 47. Quarter Model Base Partition Combinations

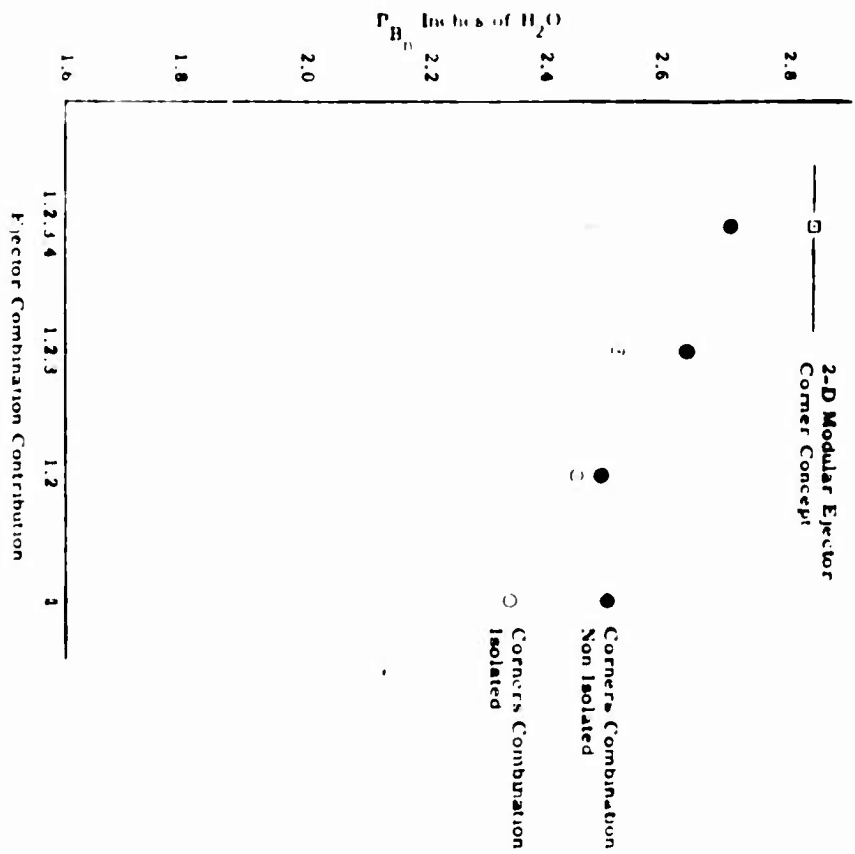


Figure 48. Component Base Pressure

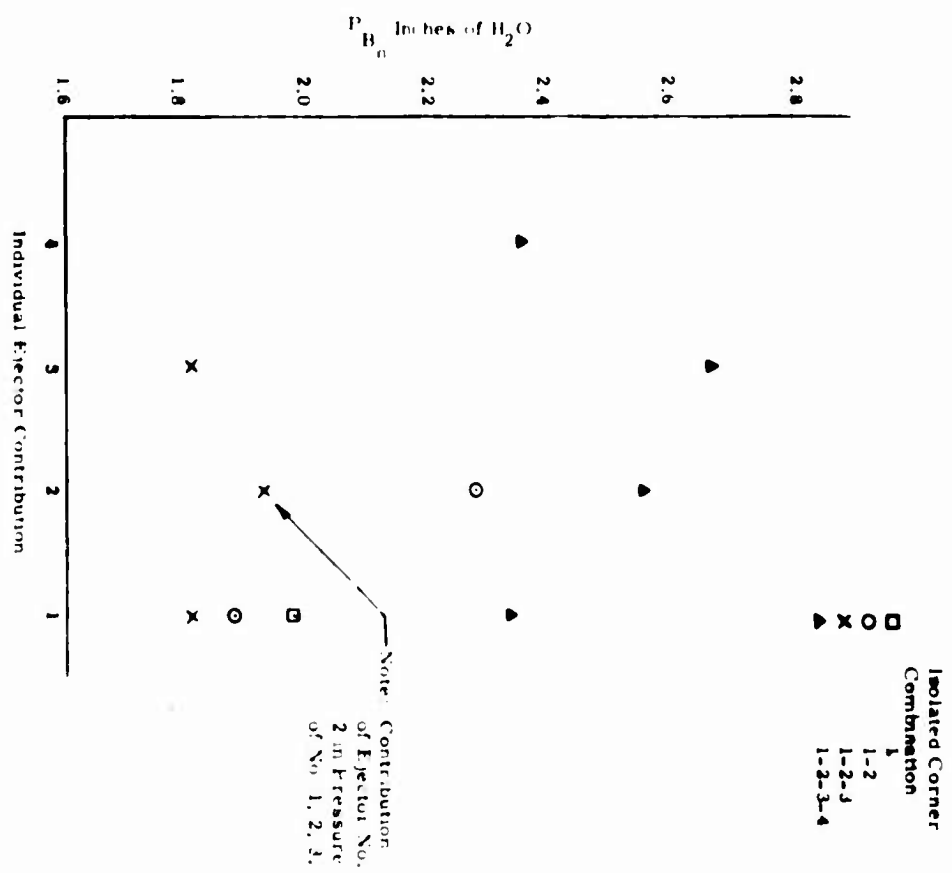


Figure 49. Component Base Pressure

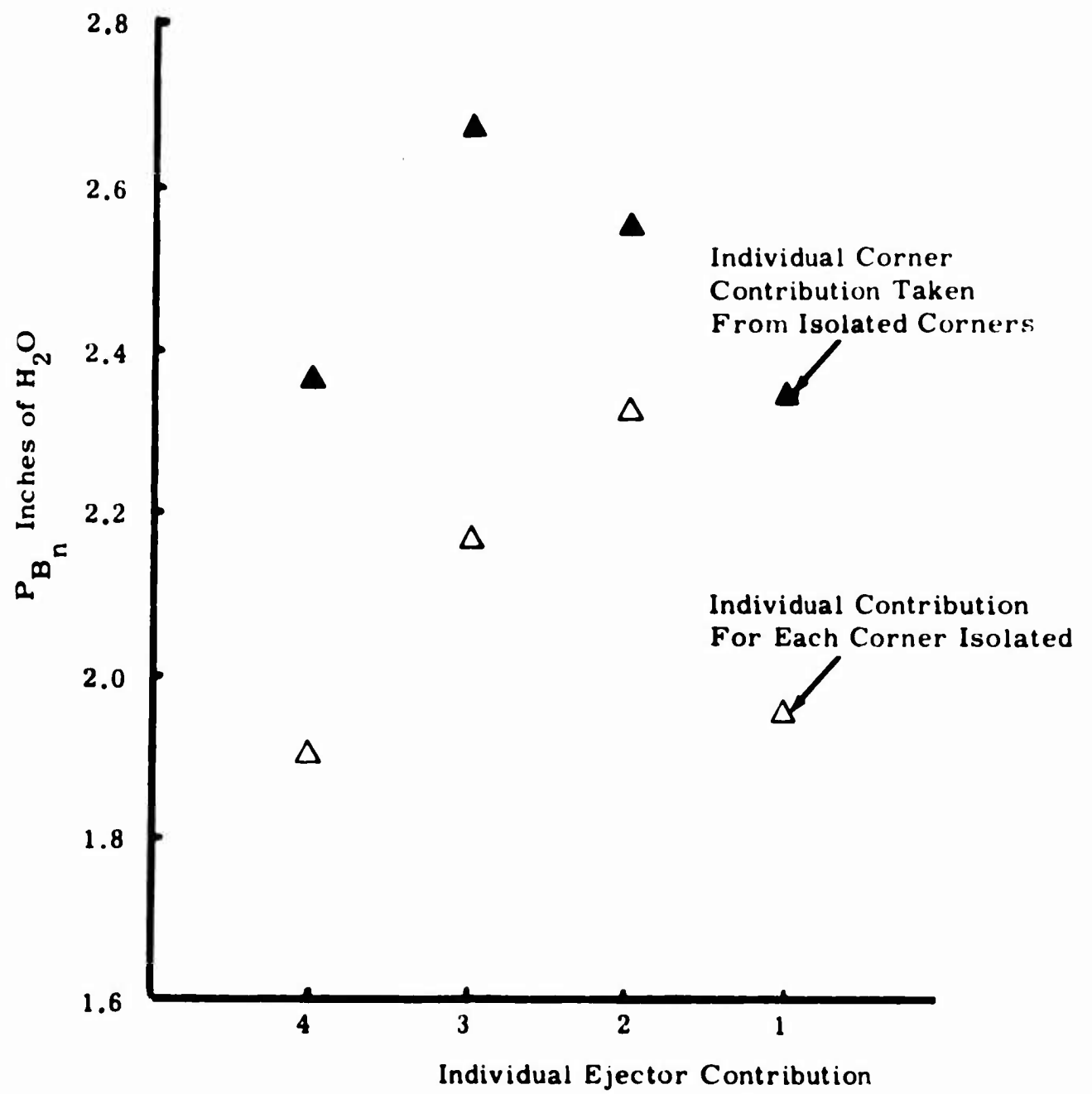


Figure 50. Component Base Pressure

certainly very important (a manufacturing tolerance of ± 1 degree must be maintained in future work).

Typical two- and three-dimensional base pressure data for areas of the model are tabulated in Table VII. The two-dimensional values were taken from the isolated corner test data and the three-dimensional values from data with no sectioning. A comparison of these values indicates that the more efficient side ejector provides three-dimensional base pressure support for the other sections of the model. The amount of the support is also tabulated.

TABLE VII
TWO- AND THREE-DIMENSIONAL PRESSURES

(Pressures in inches of water)

Section	2-D*	3-D*	Interference	3-D*	2-D**
Side	3.8	2.9	-0.9	1.93	2.52
Front	2.4	2.78	+0.38	0.41	0.36
2-D					
Corners	Individual Combination				
No. 1	2.00	2.34	2.5	+0.50/+0.16	0.12 0.117
No. 2	2.32	2.56	2.5	+0.18/-0.06	0.12 0.128
No. 3	2.16	2.68	2.64	+0.48/-0.04	0.13 0.134
No. 4	1.90	2.36	2.70	+0.80/+0.34	0.13 0.123

* Based on each section's own base area

** Based on total base area

In Table VII, the 2-D* column reflects data taken with the sectioning panels in place to give two-dimension values. The 3-D* column reflects data with no sectioning but averages the base pressures over the equivalent area of the 2-D* data. The interference was calculated

by subtracting the 3-D* from the 2-D* data. The 3-D** and 2-D** columns are merely the 2-D* and 3-D* data corrected to reflect the reference area (base).

The above values emphasize the overall penalty paid for a poorly operating ejector. The manner in which the pressure adjusts between sections becomes apparent as shown in Table VII. The different pressure levels cause a flow from the strong side ejector section toward the weaker corners. This was confirmed by tuft studies of the base.

Figure 51 presents a typical base pressure distribution by means of isobars. Figures 52 through 58 are plots of the base pressure distribution for the other configurations tested. Reviewing the individual isolated corner isobar plot, Figure 58, it is seen that this plot is different from the others, as the circular isobar distribution indicates the presence of a strong standing vortex flow. The adverse pressure distribution also covers a larger portion of the base area, which indicates the extent of the disturbance. This effect was undoubtedly the result of the way in which the individual corner ejectors were isolated from one another. The base was partitioned into relatively small pie-shaped areas such that each corner ejector would be independent of the other. In this manner the relative performance of each could be compared. However, the absolute value of performance cannot be determined from this test because of the adverse flow conditions which were created in the separate base regions.

The base pressure distribution for two-dimension models has been shown to be relatively constant across the base of the model. It is clear that none of the pressure distributions shown in Figures 49 through 56 resemble the characteristic two-dimension distribution.

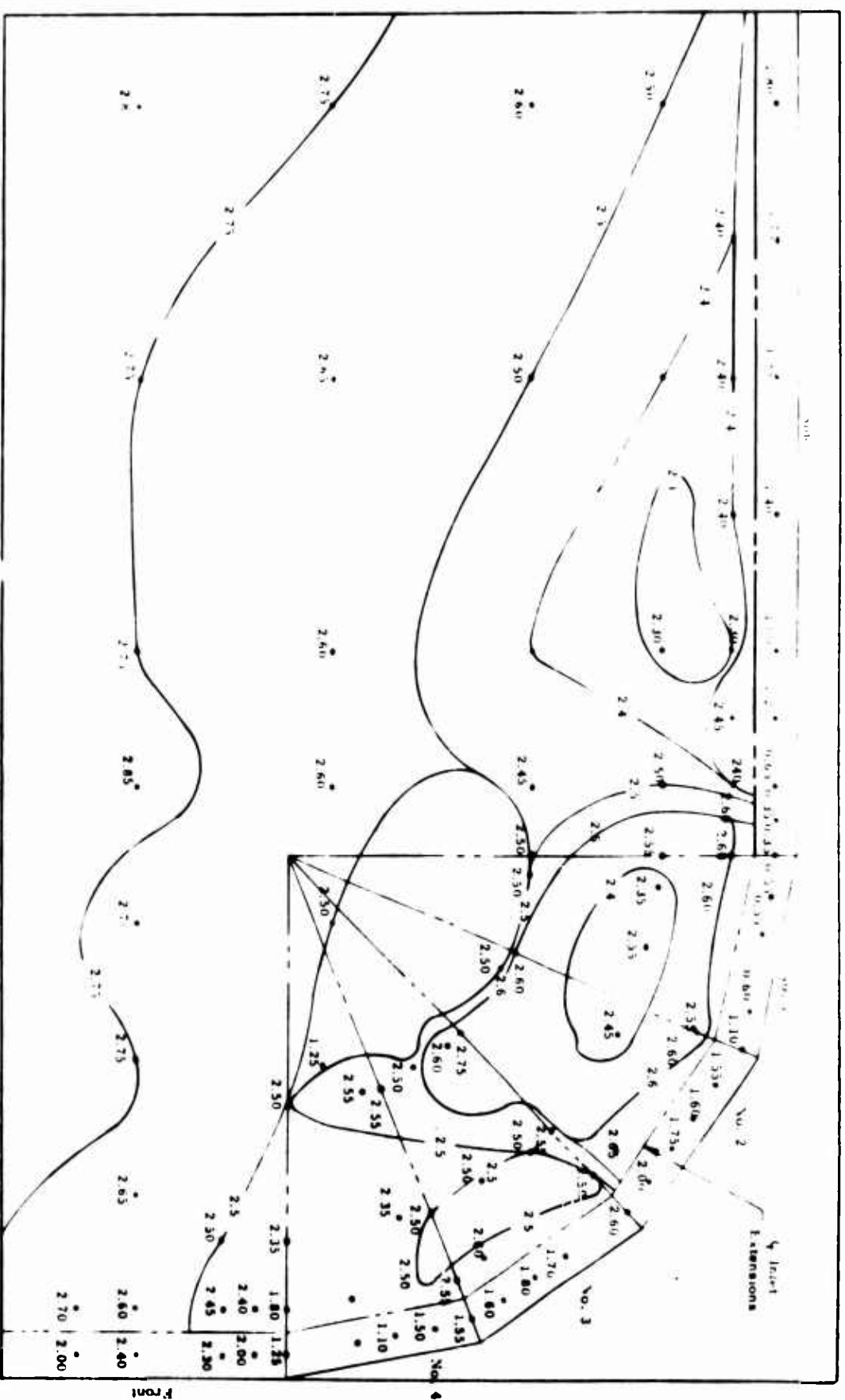


Figure 52. Isobar Distribution, Basic Configuration with 3-Inch Inlet Extensions

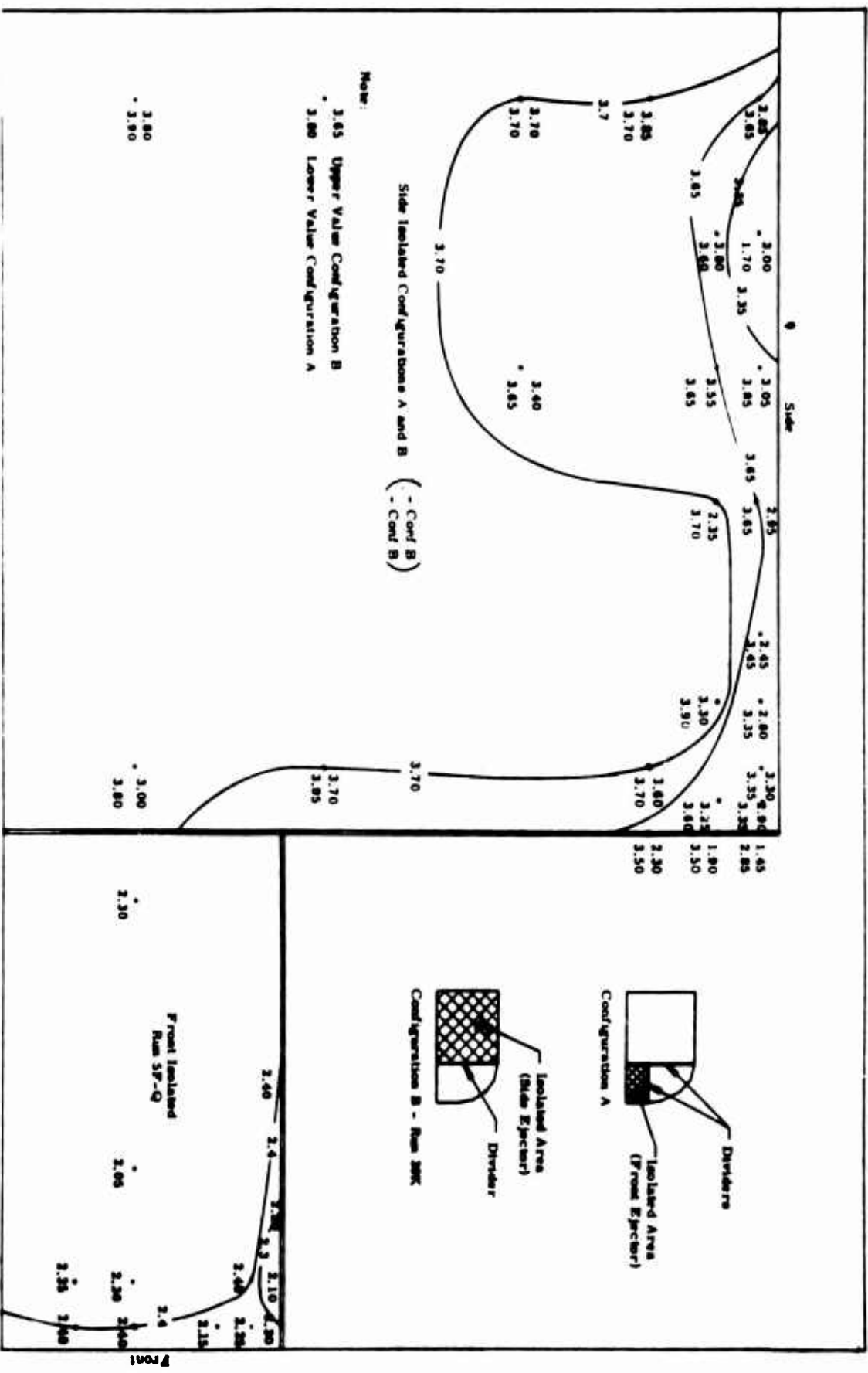


Figure 53. Pressure Distribution, Side-Front Ejectors Isolated

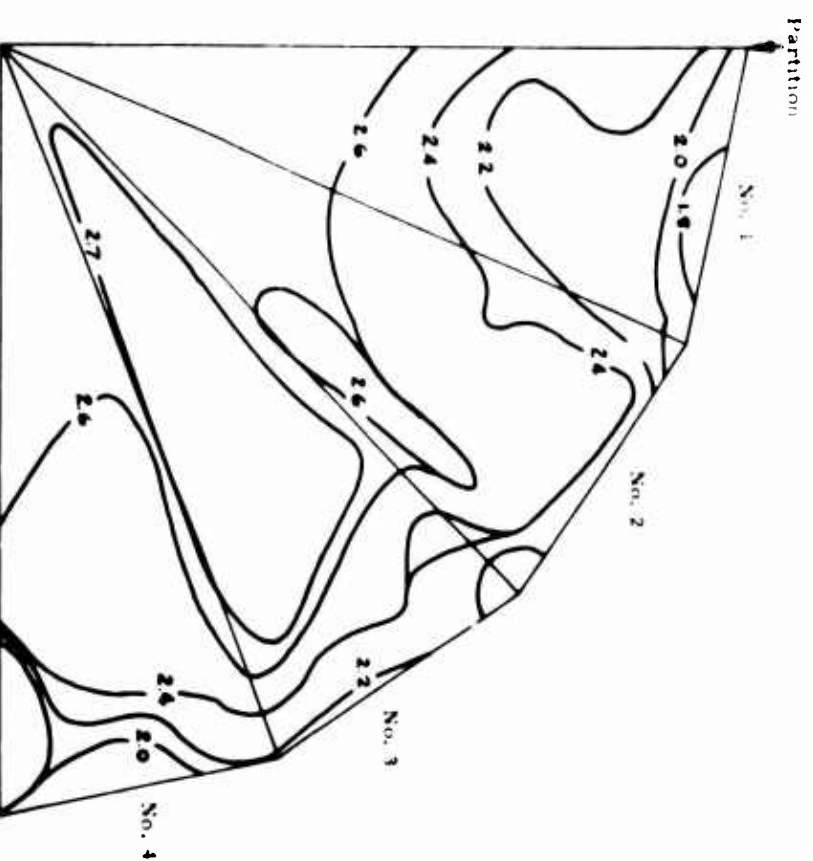
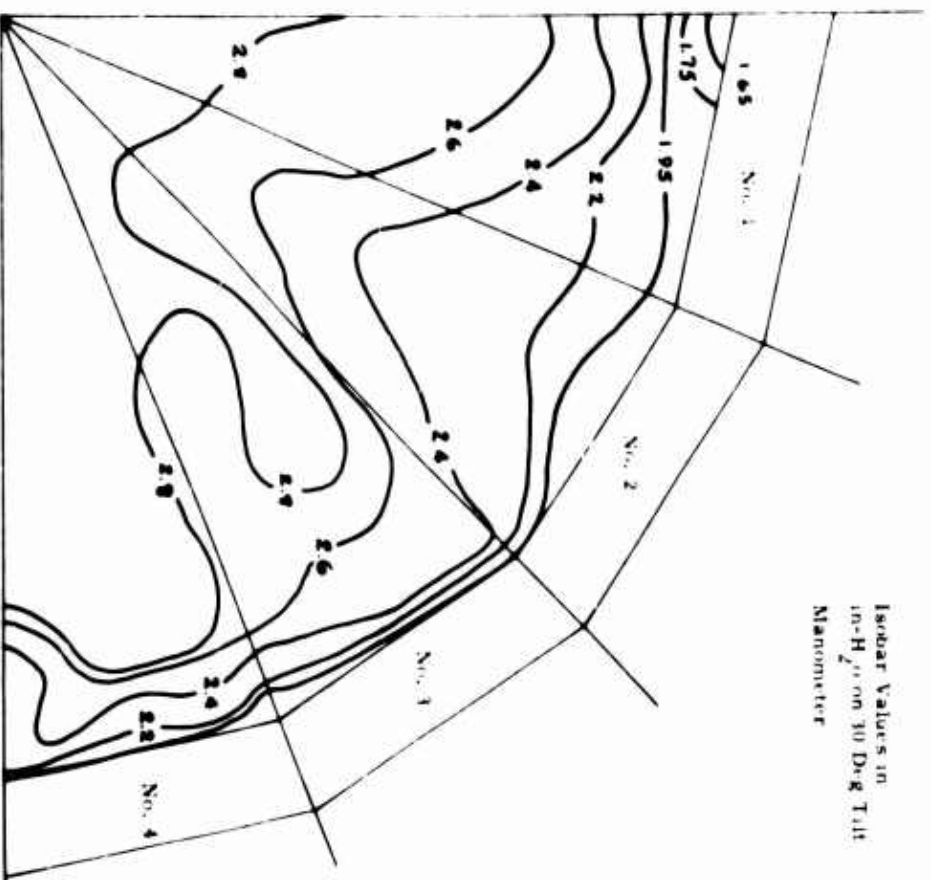


Figure 54. Corner Pressure Distribution,
Basic Run

Figure 55. Corner Pressure Distribution,
Ejectors 1, 2, 3, and 4

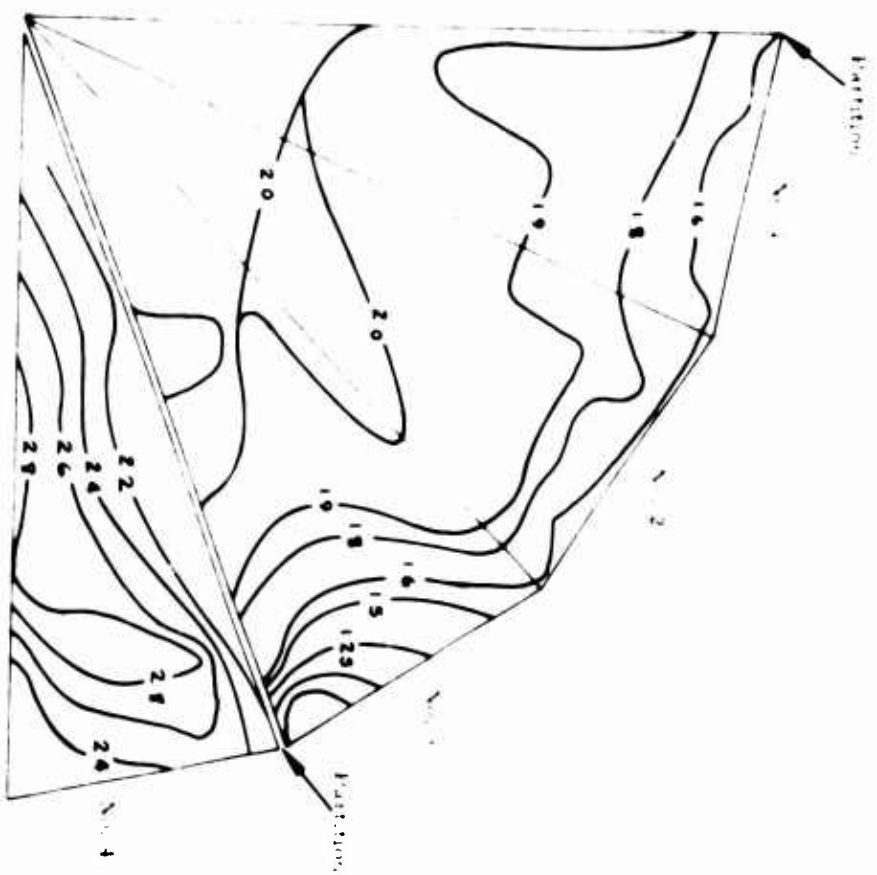


Figure 56. Corner Pressure Distribution,
Ejectors 1, 2, and 3

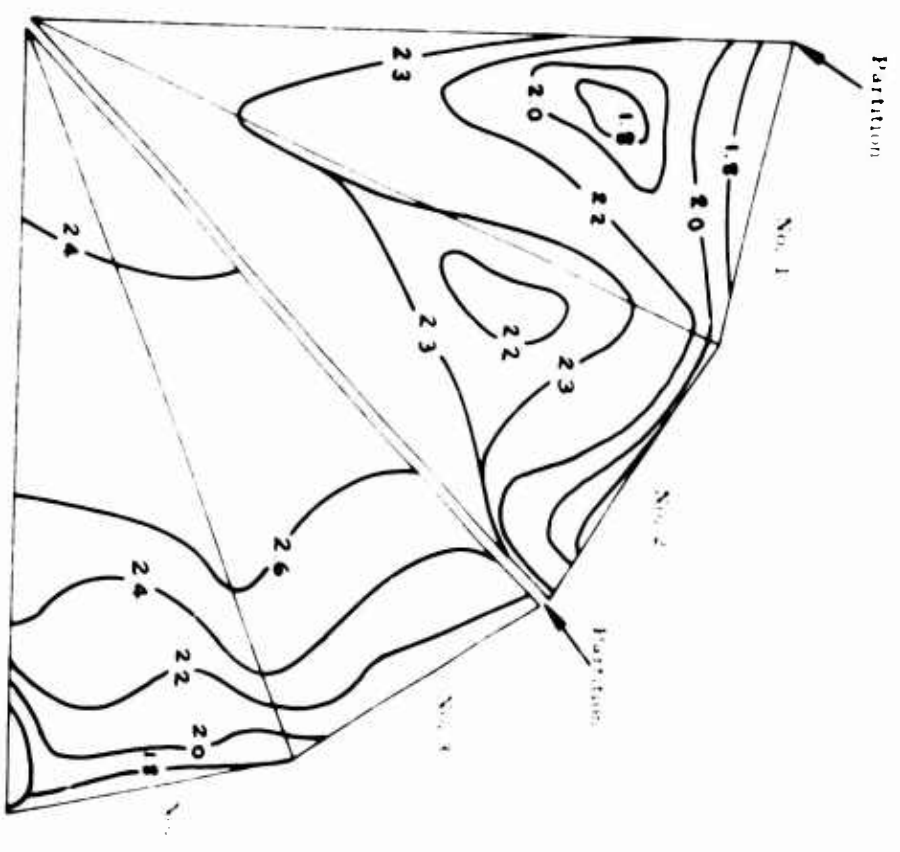
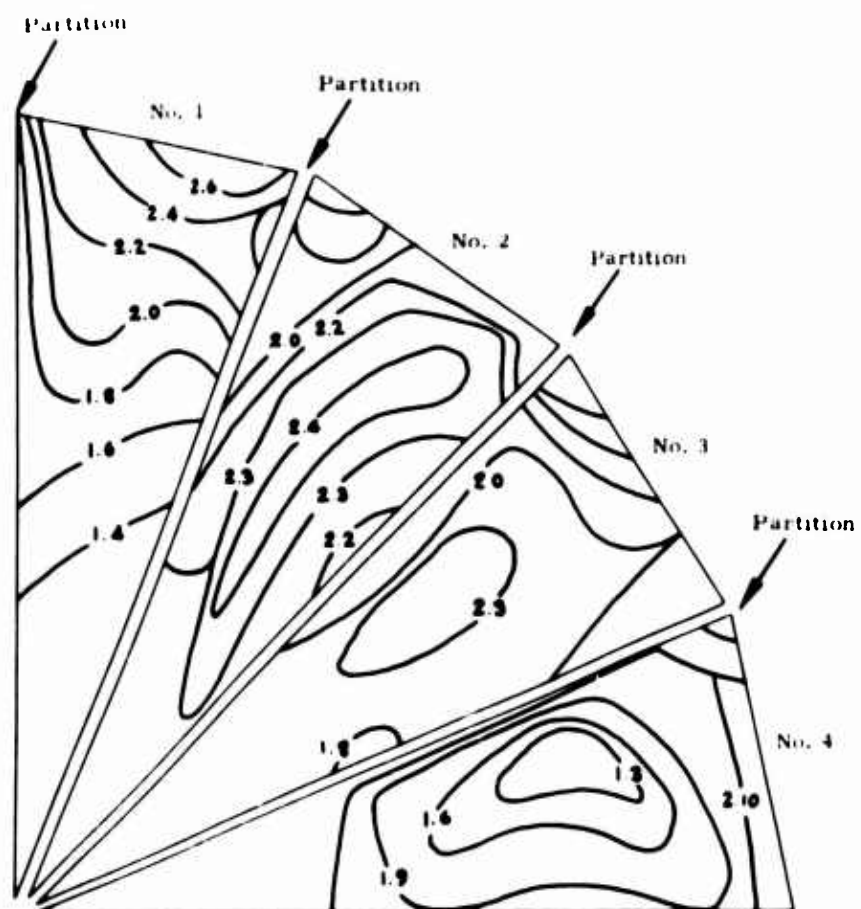


Figure 57. Corner Pressure Distribution,
Ejectors 1 and 2



**Figure 58. Corner Pressure Distribution,
All Ejectors**

This is caused by the interaction between the individual ejectors as a result of a considerable variation in ejector performance. This mismatching is primarily due to the nozzle misalignment as shown previously in Table VI, but it is also caused by a variation in the primary mass flow, shown in Figures 41 and 42. Since the primary nozzles are of welded construction, it was not possible to realign or modify them during this investigation.

Data taken with the model unsealed are compared with data of the sealed model in Table VIII. An increase of 12 percent in base pressure for the flap hinges and gaps being sealed is shown; sealing the inlet nozzle slots is shown to improve the base pressure by 5 percent over the unsealed condition. The 17-percent improvement in base pressure makes it necessary to provide seals for these items in the full-scale design.

TABLE VIII
EFFECT OF SEALING

Condition of Model ($P'_o = 5$ psi)	Flaps In/Out	Base Pressure \bar{P}_B Lb/ft ²
Unsealed Model	30/35	10.2
	30/40	10.2
Flap Hinges Sealed	30/40	11.25
Flap Hinges and Gaps between Flaps Sealed	30/40	11.8
Nozzle Slots Sealed		12.3

2. Inlet Extension (Skirts)

A comparison of the base pressure values with and without an inlet extension for varying primary pressure is shown in Figure 59. The particular extension tested had no effect at $P'_0 = 4$ psig, except to cause a reduction in base pressure at the higher primary pressures. The decrease in base pressure values with the addition of the inlet extensions (3-inch chord mounted perpendicular to the base) is contrary to the effect previously experienced. The effects of inlet extensions were to reduce the effective turning radius of the curtain and to extend the constant base pressure distribution to the extensions. This leveling-off trend of the base pressure is seen from a comparison of the pressure distributions shown in Figures 51 and 52. However, the base pressures ahead of the inlet extensions are lower than those with the inlet extension on. Since only one configuration (size, shape, and location) was tested, and because of the asymmetry in the performance of the individual ejectors, this phase of the investigation is considered to be inconclusive.

3. Surface Roughness

Two basic types of terrain are provided for testing. Figure 60 is a photograph showing the test setup of a simulated ditch consisting of two pieces of 2-by-4-inch joist covered by heavy cardboard. The two separate pieces could be taped together to simulate smooth terrain or could be separated at various distances, thereby simulating a trench of fixed depth but of varying width. Another trench depth was tested by placing the two 2-by-4-inch joists on their sides. The other type of terrain simulated was an obstacle. This consisted of two 2-by-4-inch joists covered with a board 9 inches wide. Here, again, two heights were tested by rotating the 2 by 4.

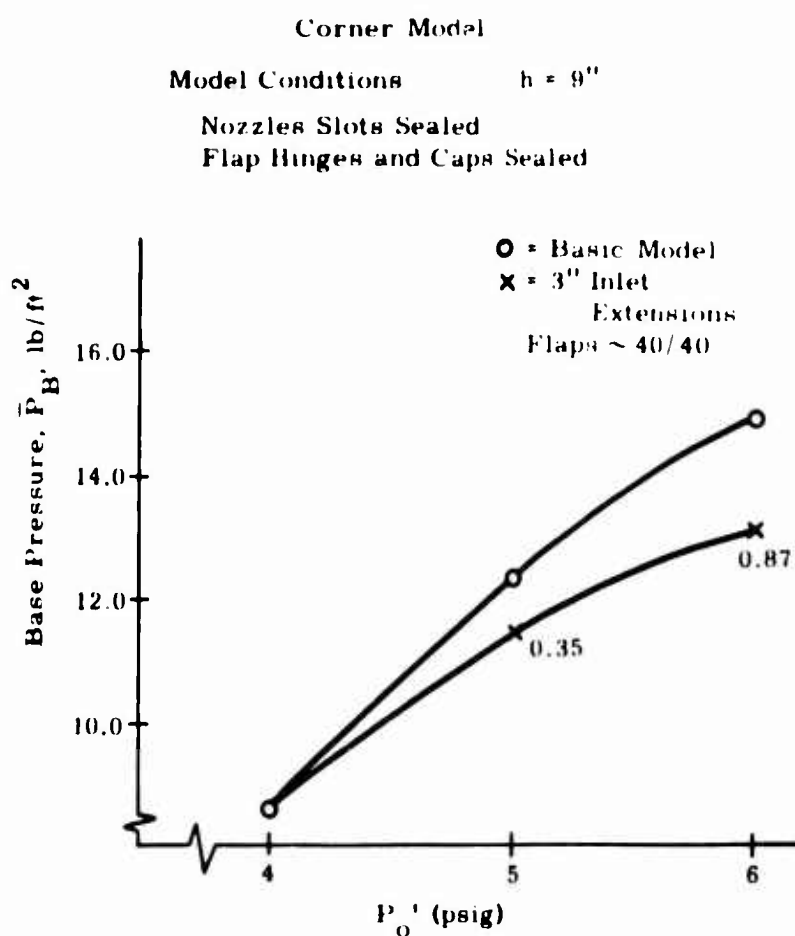


Figure 59. \bar{P}_B versus P_O' , Inlet Extension

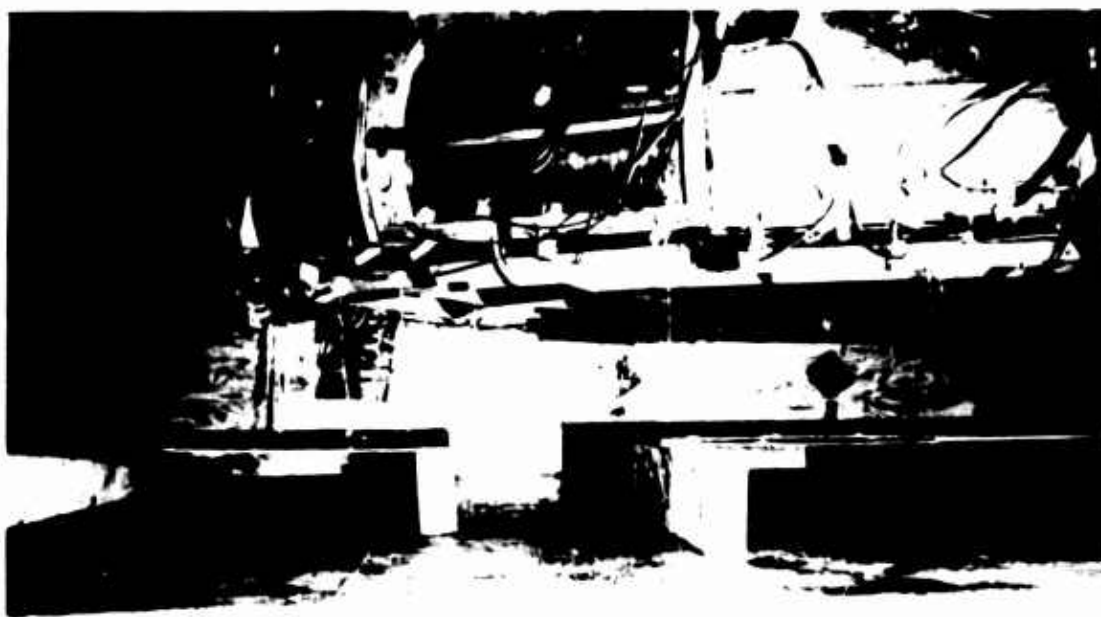


Figure 60. Surface Roughness, Ditch

The choice of basic models reflects an effort to minimize the terrain model complexity to facilitate analysis of the data. Figure 61 defines the terrain model geometry as well as the test locations. The results are presented for the variation of the base pressure ratio with obstacle geometry and position with respect to the model.

The base pressure ratio is defined as the ratio of the average base pressure in the presence of terrain to the average base pressure for a smooth surface, P_{BT}/P_B . This is plotted for an obstacle of two sizes in Figure 62. It is seen that the higher obstacle causes a greater decrease in P_{BT}/P_B . The rapid decrease in \bar{P}_{BT}/\bar{P}_B as the obstacle is moved from $X/L = 0.9$ toward $X/L = 0.8$ simulates the passage of the obstacle through the front exit jet curtain.

Figures 63 and 64 present the results of the trench terrain test. The results of this test seem at least partially contradictory. The deeper trench causes the larger maximum loss in lifting efficiency; as expected, however, for varying trench width, the middle width ($2\Delta X$) causes a greater decrease than the larger width ($3\Delta X$). The rapid loss in lifting efficiency as the trench passes the front stagnation point is similar to the loss reported for the obstacle model. A comparison of the data for the two terrain models shows that the trench caused a larger decrease in lifting efficiency.

During terrain testing it was observed that the trench provided a natural path for air to escape from under the vehicle, and it was decided to determine the effect of sealing off the trench or, in other words, to limit the span of the trench with respect to the model width. Qualitative results indicate a rapid decrease in base pressure as the span (width) of the ditch increases to a point outside the stagnation point of the side exit curtain. Variation of span inside

Figure 62. Terrain Model Geometry, Obstacle

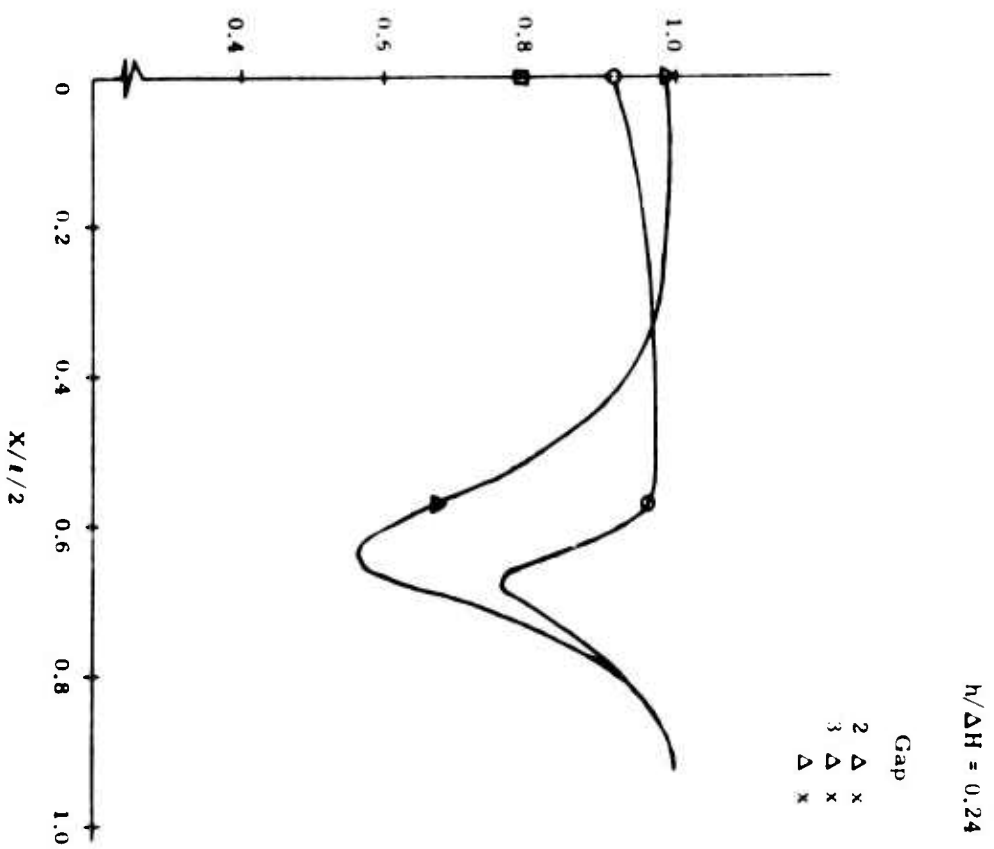


Figure 63. Terrain Model, Trench, $h/\Delta H = 0.24$

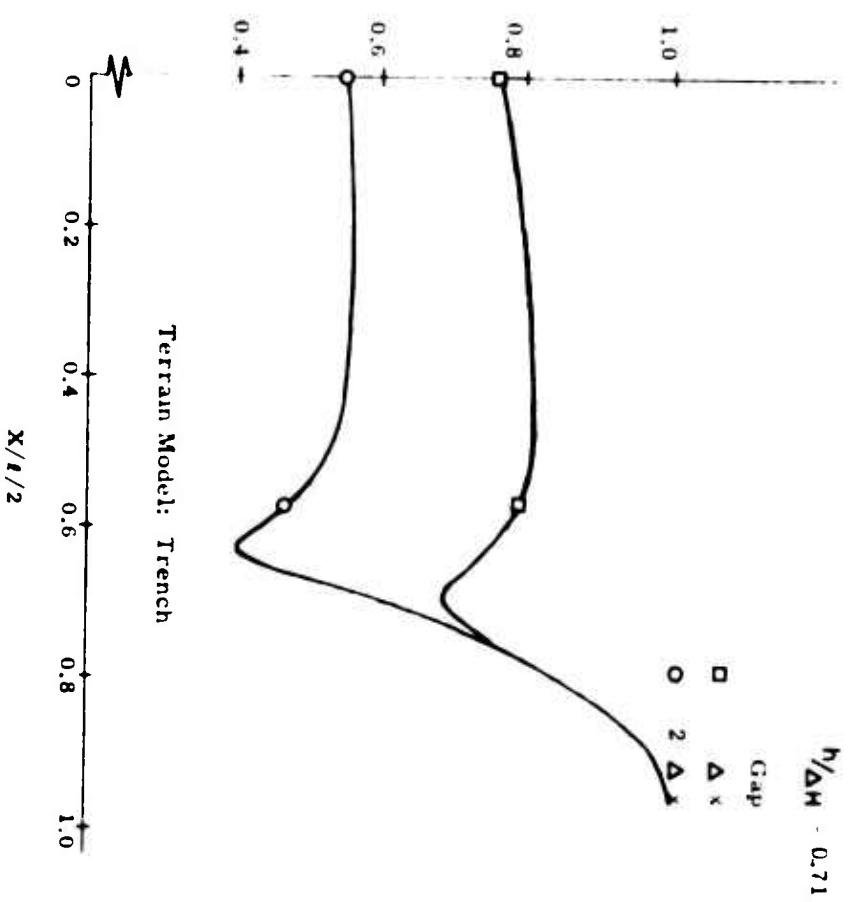


Figure 64. Terrain Model, Trench, $h/\Delta H = 0.71$

this stagnation and behind the front jet curtain has no effect on base pressure.

4. Over-Water Operation

The water test was the last item on the test program. Figures 65 and 66 are photographs of the model and water test. The data recorded were necessarily qualitative in nature - the base pressure orifices became blocked with water almost immediately, and the accuracy of measuring water displacement in the tank was difficult because of the wave motion.

Test runs were made at heights of 9 and 3 inches and for primary pressures of 4, 5, and 6 psig. For the 9-inch height and $P_o = 5$ psig, a displacement of 2.6 inches of water was observed as compared with 2.84 for the same operating conditions on a smooth surface. The 3-inch height run produced a water displacement which was too difficult to measure.

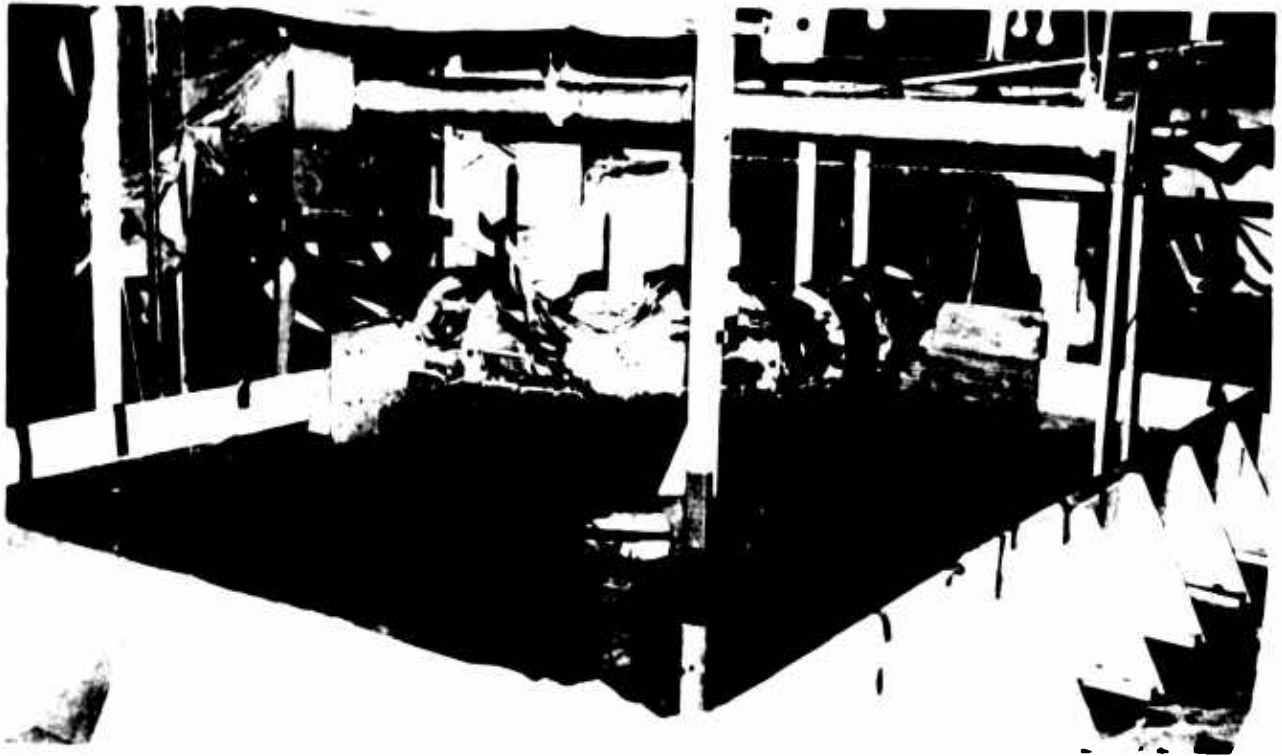


Figure 65. Corner Model, Water Test, General View

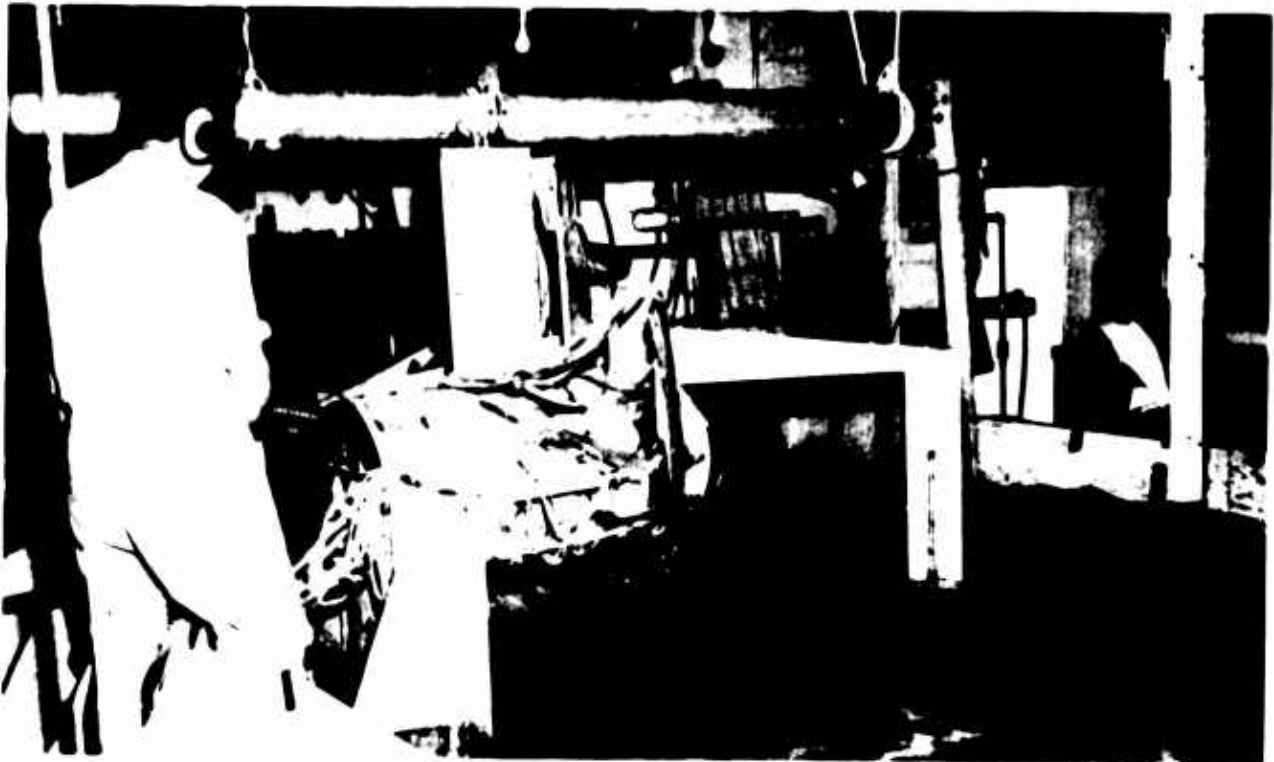


Figure 66. Corner Model, Water Test, Operation

ANALYTICAL STUDIES

The analysis presented in this section refers to any effort not directly involved in conducting an experimental investigation. As such, it falls into two broad categories:

1. The application of the theoretical and experimental data to the design and performance estimates of the vehicle;
2. The basic theory involving the fundamentals of the flow phenomenon.

BASIC PERFORMANCE ESTIMATES

1. Hover

In determining the anticipated performance of the full-size vehicle, it must first be established what the engine-compressor unit is capable of delivering. Previous investigations and the results of a later section, "Propulsion Investigation," indicate that the output of the T-58 engine and J-69 compressor matches the ejector requirements reasonably well. Figures 67 and 68 show this output in terms of speed (rpm), pressure ratio and compressor efficiency. The output, at a maximum operating speed of 21,460 rpm, is plotted in Figure 69 in terms of primary pressure at the ejector nozzle and mass flow per foot of primary header length. It is determined in a later section, "Propulsion Investigation," that a total head loss through the primary in lines of 0.5 psi can be expected. The vertical scale, P_0' of Figure 69, reflects this consideration. It has also been determined that the total length of the primary headers will be 58.75 feet. The horizontal scale of Figure 69 is plotted accordingly in pounds per second per foot of header length. From Figure 70, a cross plot of lines of constant horsepower per foot was superimposed on Figure 69. For reference purposes, the range

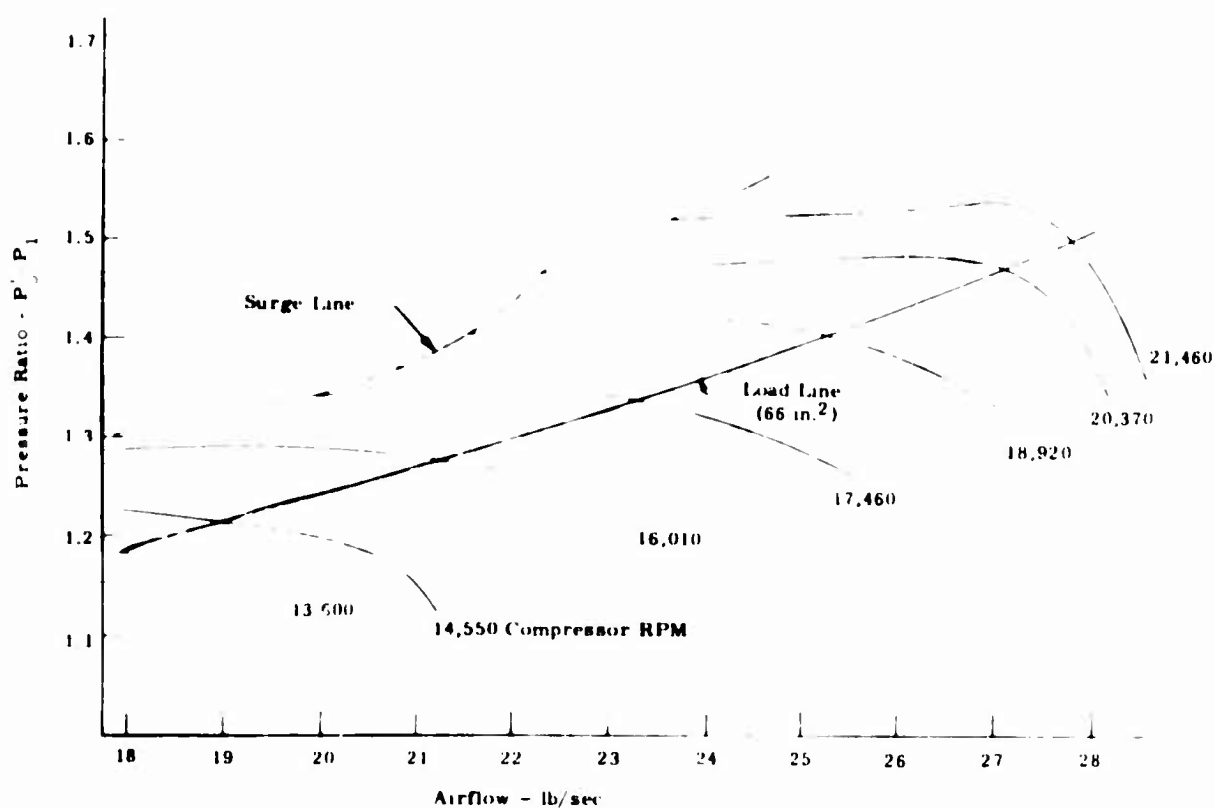


Figure 67. Compressor Map, Primary Mass Flow Versus Pressure

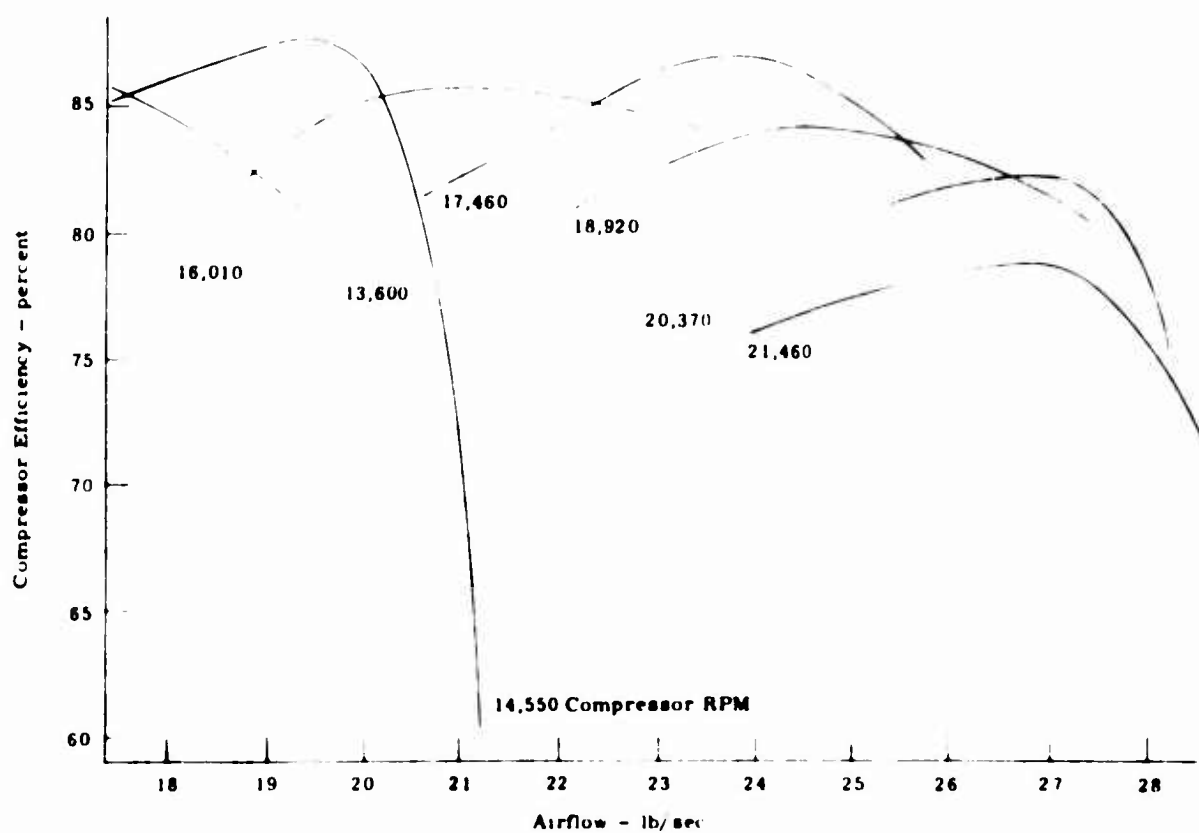


Figure 68. Compressor Map, Primary Mass Flow Versus Efficiency

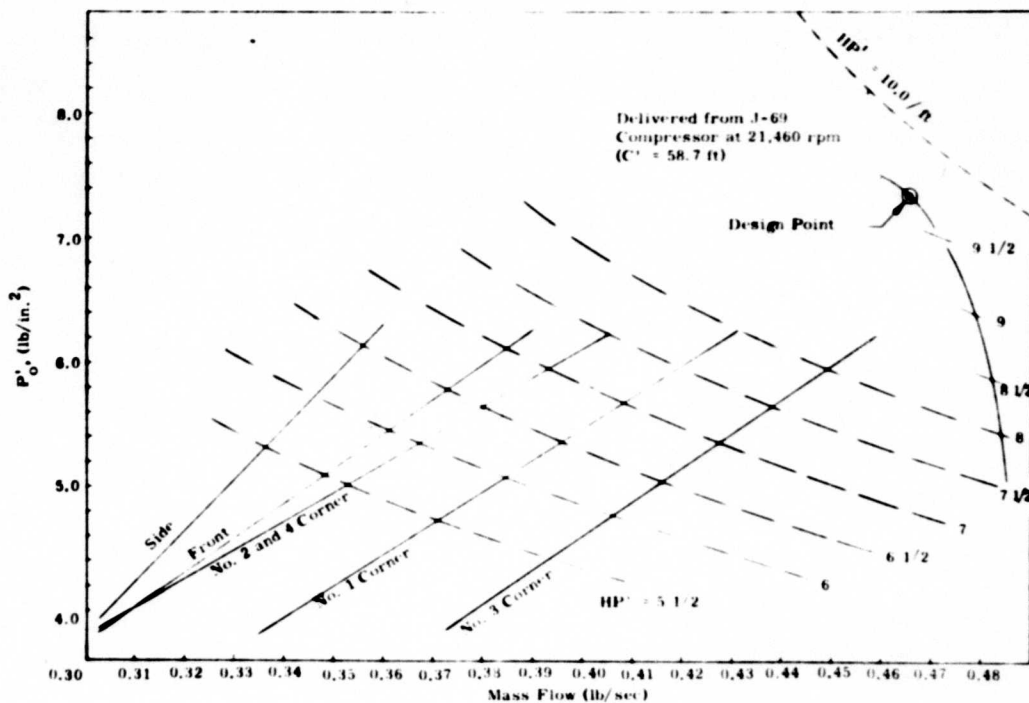


Figure 69. Primary Mass Flow Versus Pressure

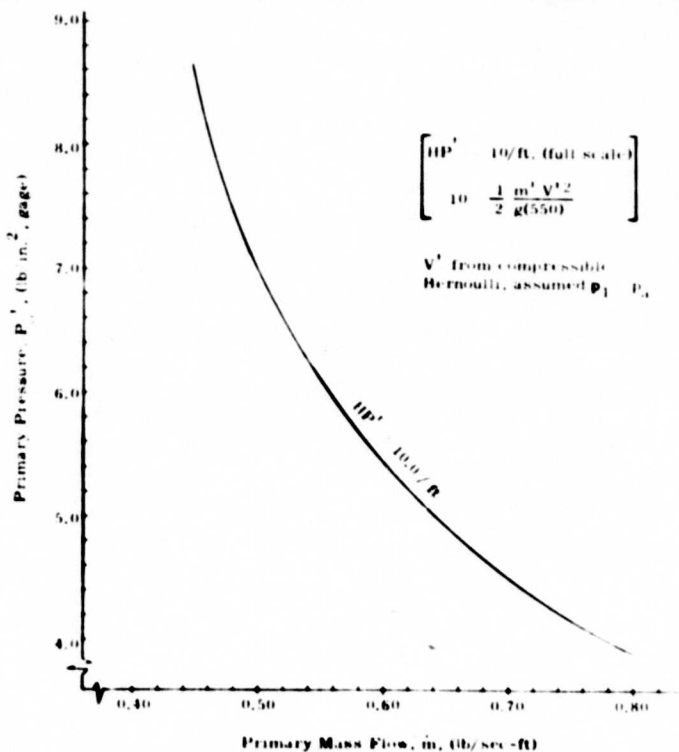


Figure 70. Primary Mass Flow Versus Pressure, Primary Horsepower = 10

over which the corner model ejectors were tested is also shown (see "Component Testing, Three-Dimensional Model Testing"). It can be seen that maximum output of the compressor, as delivered to the primary nozzles, varies from

$$m' = 0.485 \text{ lb/sec-ft}$$

$$P_o' = 4.90 \text{ lb/in.}^2$$

$$HP' = 7.75 \text{ HP/ft}$$

to

$$m' = 0.460 \text{ lb/sec-ft}$$

$$P_o' = 7.50 \text{ lb/in.}^2$$

$$HP' = 9.7 \text{ HP/ft.}$$

Second, it must be determined what combination of the above will provide the best results. The criterion will be maximum lift per horsepower. It has been established that for a given ejector configuration at a constant height, the lift will vary linearly with primary pressure (over the range of pressures being considered). Figure 71 shows the variation of lift per horsepower (actually plotted as P_o' / HP') versus primary pressure. The primary air line loss and variation in compressor efficiency (Figure 68) has been included. It is shown that the lift per horsepower steadily increases with primary pressure until the limitation of the compressor pressure ratio is reached. The design point for maximum performance is chosen at a primary pressure of 7.35 psi, as shown in Figure 71. This value is transferred back to Figure 69, and it can be seen that the design condition will be:

$$P_o' = 7.35 \text{ psig}$$

$$m' = 0.466 \text{ lb/sec-ft}$$

$$HP' / \text{ft} = 9.6 \text{ HP/ft (delivered)}$$

$$HP'_{\text{total}} = 720 \text{ HP (required from T-58).}$$

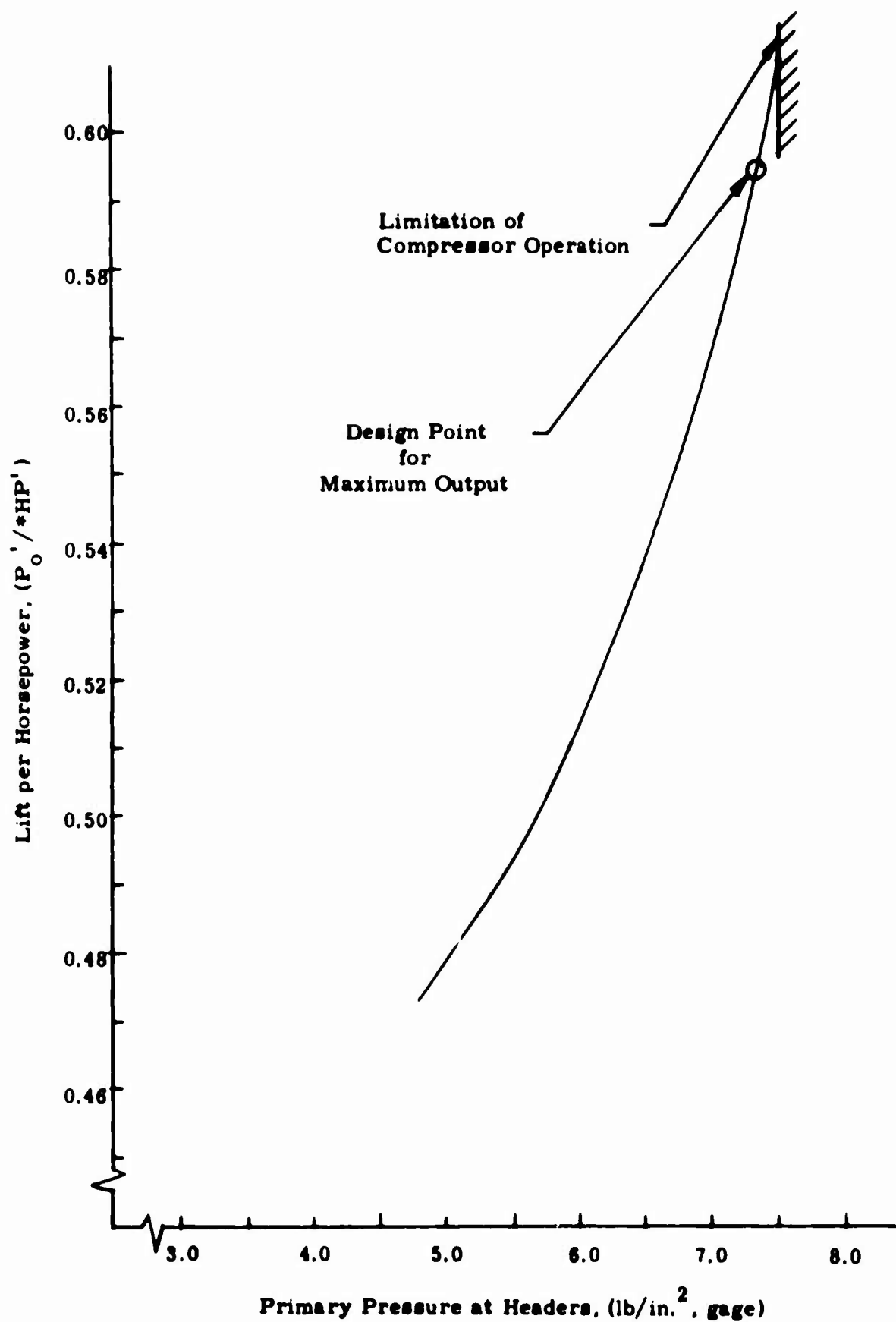


Figure 71. Lift per Horsepower Versus Absolute Total Pressure of Primary Flow

Third, from this design condition the base pressure and total lift can now be determined. A brief summary of the performance data is shown in Table IX. It can be seen that there are no experimental data at the exact design conditions determined previously. The following equation has been developed for the interpolation of data under varying conditions of the primary air flow from the ejectors:

$$P_{B_n} = P_{B_1} \sqrt{\frac{P'_{o_n}}{P'_{o_1}}} \left[\frac{m'_n}{m'_1} \right] \quad (1)$$

In using this relationship, the configuration must remain fixed, i.e., height, flap angles, and ejector dimensions. In other words, if the base pressure is known for a given configuration and test condition, and if only the primary mass flow and pressure are changed, the new base pressure can be determined. The accuracy of this estimate, as shown in the right column under \bar{P}_B in Table IX, is generally accurate to within ± 2 percent.

From the data presented in Table IX and the above equation, the relationships for the vehicle design condition between the "2-D" base pressure and height is shown in Figure 72. Also from the data, the performance of the 2-D corner module and 3-D quarter models is plotted at an 18-inch height. It was shown in a previous section, "Component Testing, Three-Dimensional Model Tests", that the performance of the 3-D quarter model was substandard because of severe nozzle misalignment. It was also shown that the 3-D performance will be less than the highest performing ejector unit and greater than the weakest. (The weaker units draw from the stronger and the result is an average between the two limits.) If the quarter model nozzles had been aligned properly the test point shown at an 18-inch height in Figure 72 would have been below the

TABLE IX
SUMMARY OF PERFORMANCE DATA

Model	Run No.	h	P _o '	m'/ft	HP'/ft	P _B	
						Experi- mental Data	Esti- mate
<u>2-D Single</u>	112	6	5.26	0.352		23.9	-
	110	9	5.26	0.352		22.1	-
	107	12	5.26	0.352		21.2	-
	66	12	8.8	0.429		36.0	33.4
	67	12	11.5	0.480		50.5	42.7
	79	18	5.26	0.352		18.0	-
	78	18	9.67	0.438		32.2	30.5
	101	24	5.26	0.352		10.6	-
(Design Point Est)		18	7.35	0.466	9.6	-	28.2
<u>2-D Double</u>	D-208	*18	5.0	0.444		19.5	20.2
	D-227	↓	↓	↓		19.6	
	D-319	↓	↓	↓		19.4	
	D-413	↓	↓	↓		19.4	
	D-304	*12	5.0	0.444		26.5	24.0
	D-332	↓	↓	↓		25.1	
	D-406	↓	↓	↓		25.6	
	D-302	*8	5.0	0.444		26.7	12.0
	D-401	8	5.0	0.444		27.2	
	D-237	*24	5.0	0.444		9.3	
	D-239	24	5.0	0.444		9.1	
(Design Point Est)		18	7.35	0.466	9.6	-	24.8
<u>2-D Corner Module</u>		*18	5.0	0.343		12.8	-
		↓	5.4	0.350		13.5	13.6
			7.1	0.402		18.0	17.9
			9.2			22.5	
(Design Point Est)		18	7.35	0.466	9.6	-	21.5

TABLE IX (Cont)

						\overline{P}_B	
Model	Run No.	h	P_o'	m'/ft	HP'/ft	Experi- mental Data	Esti- mate
<u>3-D Quarter</u>							
Full Corner		18	4.9	0.346		12.3	-
				(avg)			
Full Corner			5.9	0.380		14.9	14.8
				(avg)			
Side Only			4.9	0.326		17.1	
Front Only				0.341		10.8	
Corner No. 1				0.378		10.5	
Only							
Corner No. 2				0.348		11.5	
Only							
Corner No. 3				0.411		12.1	
Only							
Corner No. 4				0.348		10.6	
Only							
(Design Point Est)		↓ 18	↓ 7.35	0.466	9.6	-	20.3

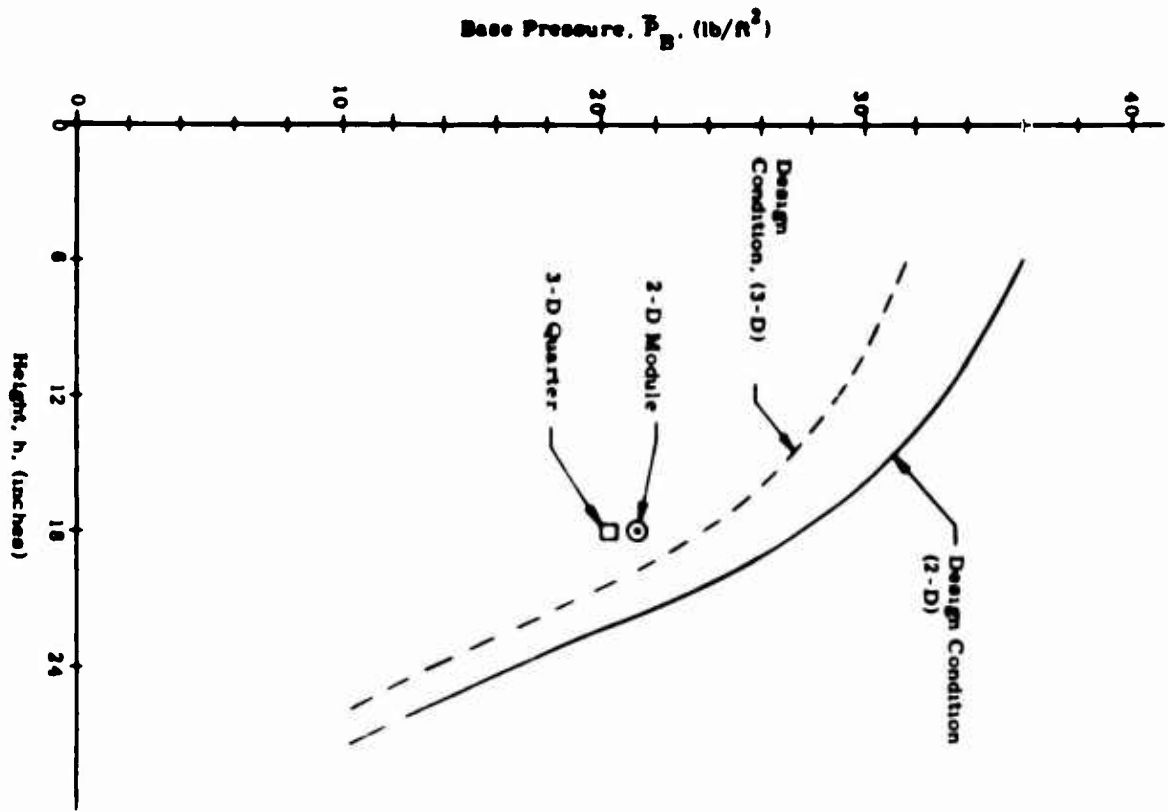


Figure 72. Performance, Gage Base Pressure Versus Height

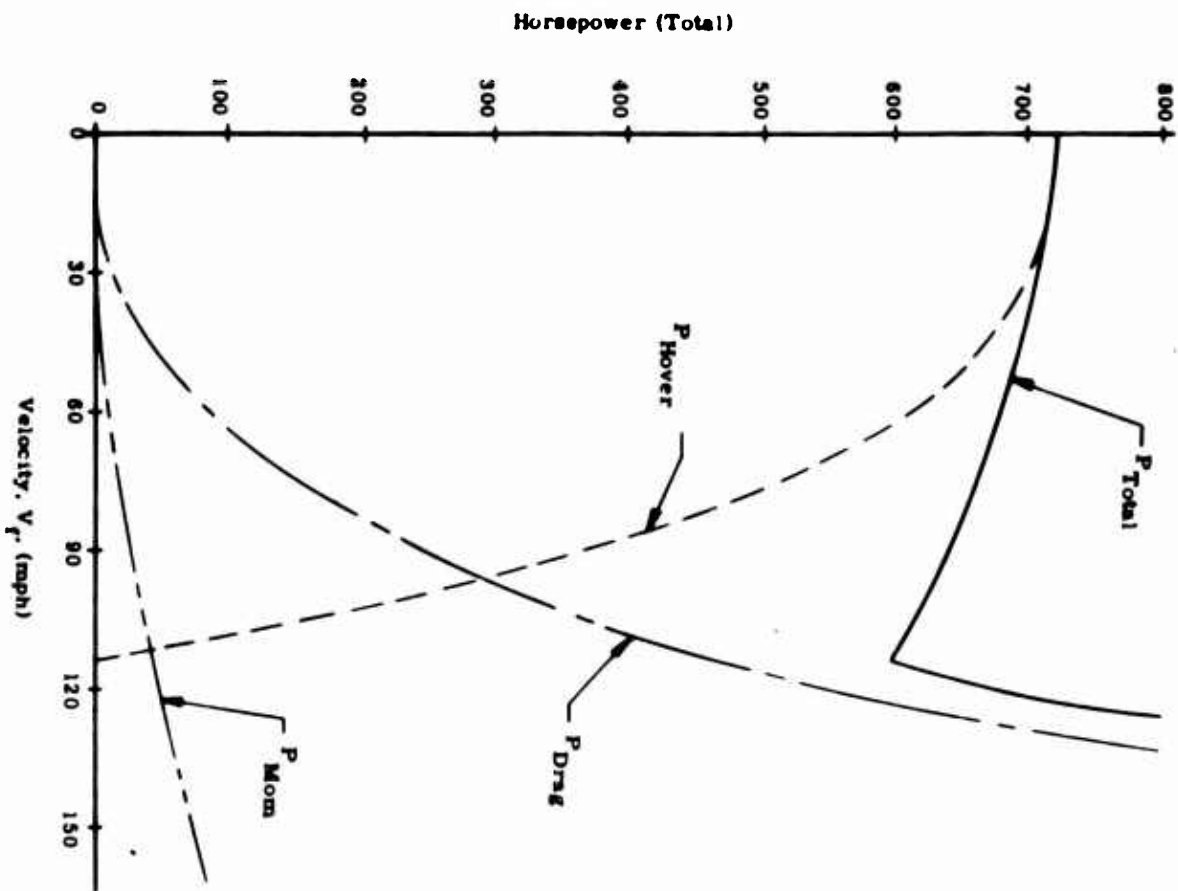


Figure 73. Power Required Versus Forward Speed

dotted curve (Design Condition, 2-D) and above the test point labeled 2-D Module.

In estimating the design condition performance, an average is taken between the straight side, the front and rear ejectors, and the corner ejectors. The resulting base pressure is weighed according to the relative length of the units as shown below:

$$P_B = \frac{(21.5 \text{ lb/ft}^2)(24 \text{ ft}) + (28.2)(34.75)}{24 + 34.75}$$

$$P_B = 25.5 \text{ lb/ft}^2, \text{ at } h = 18 \text{ inches.}$$

In addition to the lift from the base pressure, a significant lifting force is obtained from the ejector proper. The force, a change in momentum flux between the entering and exiting air, is shown in Table IV as the difference between the total lift (L) and the base pressure lift ($P_B \times 6.3'$). The total lift of the full-scale vehicle is shown in Figure 7.

2. Forward Flight

A rigorous and fairly generalized analysis of the forward flight condition is shown in Appendix III. However, a simplified analysis is shown here in order to illustrate a characteristic of this particular vehicle--the total required power steadily decreases with increasing forward speed until very high speeds are obtained. This trend is shown in Figure 73 and is derived from the following calculation; the total required power is the sum of the power required for lift, momentum, drag and profile drag.

$$P_T = P_{\text{Lift}} + P_{\text{Momentum}} + P_{\text{Drag}} \quad (2)$$

The lift power is reduced in forward flight because of the aerodynamic lift on the top surface of the vehicle, or

$$P_{\text{Lift}} = P_{\text{Hover}} - K \frac{LV}{550}$$

$$P_{\text{Hover}} = 720$$

Assuming that

$$L = 7000 = C_L q S$$

where,

$$C_L = 0.5$$

$$S = 520.$$

Then,

$$L = 0.31V^2.$$

K is evaluated by considering that at some forward speed the vehicle will be completely airborne and the initial hover power will be reduced to zero. For the assumed conditions, this velocity is

$$V = \sqrt{\frac{L}{0.31}} = \sqrt{\frac{7,000}{0.31}}$$

$$V = 150 \text{ ft/sec}$$

Therefore,

$$K = \frac{(720)(550)}{(7,000)(150)}$$

$$K = 0.378$$

and

$$P_{\text{Lift}} = 720 - \frac{(0.378)(0.31V^2)V}{550}$$

$$P_{\text{Lift}} = 720 - 0.0001540V^3 \quad (3)$$

Next, the power chargeable to the momentum drag is

$$P_{\text{Momentum}} = \frac{m' V^2}{2 (550)}$$

$$m' = 27.4 \text{ lb/sec, (from J-69 compressor)}$$

$$P_{\text{Momentum}} = \frac{m' V^2}{(32.2) (550)}$$

$$P_{\text{Momentum}} = 0.001546 V^2. \quad (4)$$

Finally, the profile drag power is found from

$$P_{\text{Drag}} = \frac{C_D q S V}{550}$$

$$= \frac{(0.12) (0.0012) (520)}{550} V^3$$

$$P_{\text{Drag}} = 0.000136 V^3 \quad (5)$$

Combining Equations (3), (4) and (5) into Equation (2), the total power is shown to vary with forward speed, V.

$$P_T = (720 - 0.0002130 V^3) + 0.001546 V^2 + 0.000136 V^3. \quad (6)$$

This equation is shown plotted in Figure 73 and correlates well with more rigorous analysis in Appendix III.

CRITIQUE OF THE MARTIN RECIRCULATION EJECTOR THEORY*

Introduction

A theory of the recirculating ejector was derived at Martin Orlando in 1960. A simplified theoretical treatment of the aerodynamics of the circulating peripheral jet developed by the Martin Company was given in 1962. Both theories are discussed in detail in Reference 1.

*By Dr. G. D. Boehler, Aerophysics Company, Washington, D.C.

The purpose of the following discussion is to re-examine critically these previously-developed internal and external-flow theories and to update them as necessary. The scope of the discussion is limited to two-dimensional flow considerations, as described in Reference 1. This does not imply a criticism of the earlier work, which is confirmed to be sound, but an extension of it. The two- and three-dimensional ejector test results discussed earlier in this report are satisfactory to predict the performance of the proposed Martin research vehicle. However, they pertain to only one basic configuration (Model 1). It is of interest to have a parametric analysis available to pave the way for further optimization, using other ejector configurations.

It is also of interest to obtain some insight into the stability of the ejector flow, since it contributes to the overall stability of the vehicle. While the analysis in Reference 1 assumes the flow conditions and gives the geometry of the ejector and of the internal duct which is compatible with these flow conditions, the present discussion also considers the reverse problem: the determination of the flow corresponding to a given ejector geometry and ejector primary flow.

The external-flow characteristics of the recirculation ejector are less well known than the internal-flow characteristics. A speculation into a prediction of the base pressure, as a function of the ejector flow characteristics, which differs from the theory of Reference 1, points the way to further research. An attempt was made towards finding the simplest possible solution. In particular, it is no longer felt, as it was at the time that Reference 1 was written, that recourse to a conformal flow mapping solution of the flow is warranted.

Internal-Flow Analysis

A complete two-dimensional recirculating ejector analysis is presented in Reference 1. The compressible, inviscid theory is first discussed,

then a viscous solution is presented, for which the solution of the equations can be found by iteration, starting from the results of the inviscid solution.

The symbols and subscripts used here are generally the same as those in Reference 1, except as shown in Figure 74, where ① corresponds to the inlet, ② to the end of the mixing section, ③ to the nozzle exit, and ④ to the beginning of the curved jet region through which the base pressure is sustained. Losses due to diffusion and turning are assumed to take place between Stations ② and ③ and are lumped together. A schematic of the ejector and external-flow field is shown in Figure 75.

It is shown in Reference 1 that if one specifies a given exit mass flow, \dot{m} (delivered against a total head P_{O_3} and a static head p_3), resulting from a primary flow defined by Γ_0' and ρ_0' and from a secondary flow by P_0'' and ρ_0'' , there is an infinite number of possible area ratios, A''/A' (ejector configurations), which deliver the required flow from the given reservoir conditions. Each configuration corresponds to a particular mixing section pressure p_1 .

Note here that the mixing section pressure p_1 is assumed to be uniform. This is a close approximation only but must be kept at this time. Thus, the following eight quantities completely define the geometry of the ejectors:

$$P_0', \rho_0', P_0'', \rho_0'', p_1, P_{O_2}, p_3, m_3.$$

As part of the work reported in Reference 1, a computer program was prepared to accept the above quantities as input and to solve for the other flow quantities and areas as output. The above quantities are not varied at random but in such a fashion as to represent the features

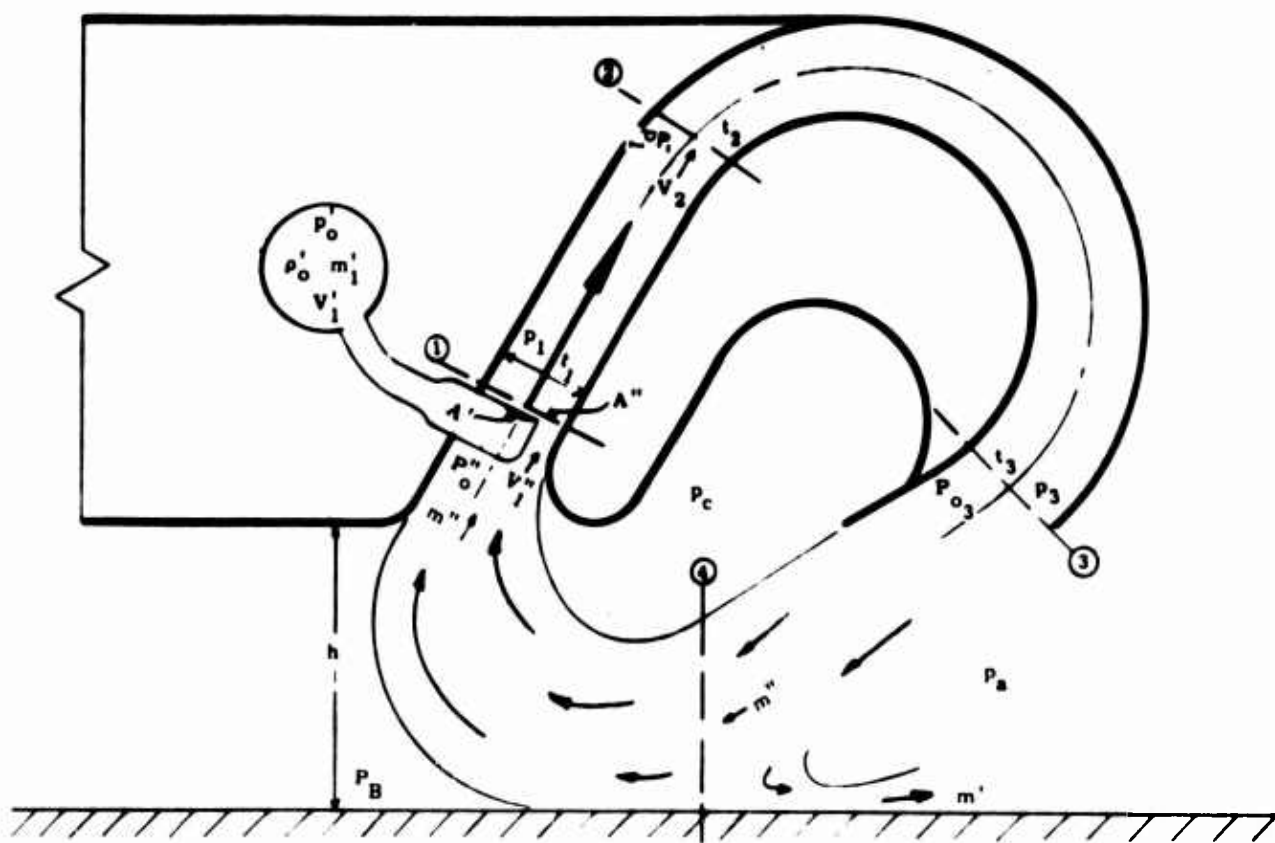


Figure 74. Ejector Nomenclature, Recirculation

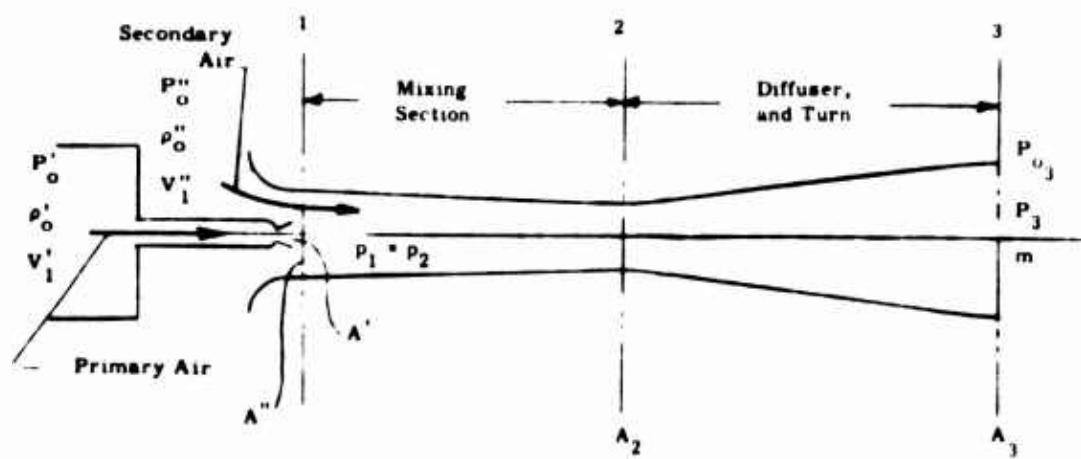


Figure 75. Ejector Nomenclature, Straight

of a recirculating ejector. The first feature of a recirculating ejector is that the secondary total pressure P_0'' is not atmospheric but is related to the tertiary total pressure P_{03} . The ratio of these two pressures is called the pressure recovery,

$$PR = \frac{P_0''}{P_{03}}. \quad (7)$$

The second feature is that the ejector is assumed to diffuse to atmospheric pressure at Station (3). As seen in Figure 74, the true static pressure (gage) at exit $P_c/2$ is small. Hence $p_3 \approx p_{at}$. Third, the loss in total pressure between Stations (2) and (3) due to diffuser and turn is called ΔP_0 . Hence,

$$P_{02} = P_{03} + \Delta P_0. \quad (8)$$

The results of the program are plotted in Reference 1, where the power ratio ϵ , as defined below, is used as the efficiency criterion.

$$\epsilon = \frac{m_3 V_3^2}{m' V_1'^2}. \quad (9)$$

This is not necessarily a good criterion for the efficiency of a ground effect machine using recirculation. The criterion is to maximize the base pressure P_B for a given primary pressure P_0' . As will be seen in the next section, the base pressure is related to the momentum or to the total pressure of the jet at Station (3). Further, the base pressure depends upon the secondary mass flow, not the tertiary mass flow. Therefore, it appears that the following is a better criterion than ϵ :

$$\eta = \frac{m'' V_3}{m' V_1'}. \quad (10)$$

Flow Characteristics of the Ejector With a Fixed Geometry

The computer program must be used for the design of a recirculating ejector system. However, it is of further interest, for a given ejector of fixed geometry to have an analytical method to study the effect of some flow ejector quantities on others. For example, a tilt of the base of the machine will cause a change in the operation of the ejector. Also, a promising way to control the MCTV is by differential changes of the primary pressure. One may want to find out, for example, the effect of a change in P_o' from 5 to 6 psig on the secondary momentum of the system. Hence, the following section. In the left column are the eight quantities which were assumed known, and in the right column are shown the corresponding eight quantities assumed known for the analysis of this section:

P_o'	P_o'
ρ_o'	ρ_o'
P_o''	A'
ρ_o''	A''
P_1	P_1
P_3	P_3
m_3	A_2
P_{o_2}	A_3

It must be shown that, if the eight quantities in the column on the right are known, the problem can be solved. First, if one knows P_o' , ρ_o' , A' , and p_1 , the primary velocity, V_1' , and the primary mass flow, m_1 , can be calculated from the following quantities:

$$V_1' = \sqrt{\frac{2\gamma}{\gamma-1} \left(\frac{P_{01}'}{\rho_{01}'} \right) \left[1 - \left(\frac{p_1}{P_{01}'} \right)^{\frac{\gamma-1}{\gamma}} \right]} \quad (11)$$

$$\rho_1' = \rho_{01}' \left(\frac{p_1}{P_{01}'} \right)^{1/\gamma} \quad (12)$$

$$m' = \rho_1' A_1' V_1' \quad (13)$$

The list of the right-hand column is not entirely satisfactory: it is known that, given an ejector geometry, a certain primary flow, and values for the duct losses and the pressure recovery, only one flow can be obtained. However, if p_1 (mixing section static pressure) is an input to the problem, for each value of p_1 , one will have a different flow. Therefore, p_1 cannot be an independent input but must be calculated in terms of the other inputs.

There are 12 unknowns:

$$\rho_{01}'', P_{01}'', V_1'', m''$$

$$\rho_{02}', \rho_2', P_{02}', V_2$$

$$\rho_{03}', \rho_3', P_{03}', V_3$$

One finds that there are 13 equations. Hence, Equation (26) must be used to find p_1 . These equations are as follows:

$$m' V_1' + m'' V_1'' = (m' + m'') V_2 \quad (14)$$

$$m'' = \rho_{01}'' \left(\frac{p_1}{P_{01}''} \right)^{1/\gamma} (A_1' V_1'') \quad (15)$$

$$V_1'' = \sqrt{\frac{2\gamma}{\gamma-1} \left(\frac{P_{o_1}''}{\rho_{o_1}''} \right) \left[1 - \left(\frac{p_1}{P_{o_1}''} \right)^{\frac{\gamma-1}{\gamma}} \right]} \quad (16)$$

$$\left(\frac{\gamma}{\gamma-1} \right) \left[\frac{m' P_{o_1}'}{\rho_{o_1}'} + \frac{m'' P_{o_1}''}{\rho_{o_1}''} \right] = (m' + m'') \left[\left(\frac{\gamma}{\gamma-1} \right) \frac{p_2}{\rho_2} + \frac{V_2^2}{2} \right] \quad (17)$$

$$V_2 = \sqrt{\left(\frac{2\gamma}{\gamma-1} \right) \frac{P_{o_2}}{\rho_{o_2}} \left[1 - \left(\frac{p_2}{P_{o_2}} \right)^{\frac{\gamma-1}{\gamma}} \right]} \quad (18)$$

$$\frac{p_2}{P_{o_2}} = \left(\frac{\rho_2}{\rho_{o_2}} \right)^\gamma \quad (19)$$

$$m' + m'' = \rho_2 A_2 V_2 \quad (20)$$

$$m' + m'' = \rho_3 A_3 V_3 \quad (21)$$

$$\rho_3 = \rho_{o_3} \left(\frac{p_3}{P_{o_3}} \right)^{\frac{1}{\gamma}} \quad (22)$$

$$\frac{P_{o_2}}{\rho_{o_2}} = \frac{P_{o_3}}{\rho_{o_3}} \quad (23)$$

$$V_3 = \sqrt{\frac{2\gamma}{\gamma-1} \left(\frac{P_{o_3}}{\rho_{o_3}} \right) \left[1 - \left(\frac{p_3}{P_{o_3}} \right)^{\frac{\gamma-1}{\gamma}} \right]} \quad (24)$$

$$P_{o_3} = P_{o_2} - \Delta P_o \quad (25)$$

$$P_o'' = (PR) P_{o_3} \quad (26)$$

These equations can be solved for the viscous case, $F \neq 0$, in Equation (5) on a digital computer by iteration. They can also be differentiated and the effect of a change in one variable on the others can be found. In the next paragraph, it will be shown that, for incompressible flow, one can find an approximate solution for p_1 .

Incompressible Flow of Recirculating Ejector of Fixed Geometry

The equations for incompressible flow of a recirculating ejector are as follows:

$$p_1 + \frac{1}{2} \rho V_1'^2 = P_o' \quad (27)$$

$$m' = \rho A' V_1' \quad (28)$$

$$m' V_1' + m'' V_1'' = (m' + m'') V_2 \quad (29)$$

$$m'' = \rho A'' V_1'' \quad (30)$$

$$p_1 + \frac{1}{2} \rho V_1''^2 = P_o'' \quad (31)$$

$$p_1 + \frac{1}{2} \rho V_2^2 = P_{o_2} \quad (32)$$

$$m' + m'' = \rho A_2 V_2 \quad (33)$$

$$m' + m'' = \rho A_3 V_3 \quad (34)$$

$$p_3 + \frac{1}{2} \rho V_3^2 = P_{o_3} \quad (35)$$

$$P_{o_3} = P_{o_2} - \Delta P_o \quad (36)$$

$$P_o'' = (PR) P_{o_3} \quad (37)$$

Substituting Equations (28), (30) and (33) into Equation (19) yields:

$$\rho A' V_1'^2 + \rho A'' V_1''^2 = \rho A_2 V_2^2 \quad (38)$$

From Equation (27)

$$\rho V_1'^2 = 2 (P_o' - p_1); \quad (39)$$

and from Equations (31) and (37),

$$\rho V_1''^2 = 2 (PR) P_{o_3} - p_1. \quad (40)$$

Combining Equations (33) and (34),

$$V_3 = \frac{A_2}{A_3} V_2. \quad (41)$$

Combining Equations (32), (35), and (36),

$$p_3 - p_1 = \frac{1}{2} \rho (V_2^2 - V_3^2) - \Delta P_o. \quad (42)$$

Substituting Equation (41) into (42),

$$\rho V_2^2 = \frac{2 (p_3 - p_1 + \Delta P_o)}{(1 - A_2/A_3)^2} \quad (43)$$

One more transformation is needed for Equation (40):

$$\rho V_1''^2 = 2 (PR) P_{o_3} - 2p_1$$

$$\rho V_1'^2 = 2 (PR) (p_1 + \frac{1}{2} \rho V_2^2 - \Delta P_o) - 2 p_1. \quad (44)$$

Substituting Equations (39), (43) and (44) into Equation (28),

$$2 A' (P_o' - p_1) + 2 A'' (PR) (p_1 + \frac{1}{2} \rho V_2^2 - \Delta P_o) - 2 A'' p_1 = \rho A_2 V_2^2$$

or

$$2 A' (P_o' - p_1) + 2 A'' (PR) (p_1 - \Delta P_o) - 2 A'' p_1 = \rho V_2^2 [A_2 - A' (PR)].$$

Finally,

$$2 A' (P_o' - p_1) + 2 A'' (PR) (p_1 - \Delta P_o) - 2 A'' p_1 = \frac{2 (p_3 - p_1 + \Delta P_o) [A_2 - A' (PR)]}{\left[1 - \frac{A_2}{A_3}\right]^2}. \quad (45)$$

The last equation is a linear equation in p_1 , which can be solved for p_1 as a function of the input quantities.

EXTERNAL-FLOW ANALYSIS

Bifurcating Jet Region

The bifurcating jet region is described in Reference 1 in terms of the equilibrium of forces shown in Figure 76.

The momentum flux of the tertiary flow is given by:

$$j_3 = 2 (P_{o_3} - p_3) t_3 / \text{unit length}. \quad (46)$$

Assuming a linear variation of static pressure across the nozzle, from P_c to zero,

$$j_3 = 2 \left(P_{o_3} - \frac{P_c}{2} \right) t_3. \quad (47)$$

This equation disregards viscous mixing. It appears unobjectionable, except that the pressure P_c probably should be considered as acting over a dimension of $(h-t_3)$ rather than the height h .

The term j_3 , as used in Equation (46), was defined in Equation (45). An important consideration, though, is that the total pressure, P_{o3} , is far from being constant across the duct. Since the flow emerges just after completing a turn in the duct, the velocity on the outside wall is much larger than the velocity on the inside wall (typically, it is three times as large).

Using Reference 5, the total pressure of the jet should be defined as a mean total pressure of the annular jet exhausting towards the right and a mean total pressure of the recirculating branch of the jet. The mean total pressure of the recirculating jet is defined as follows:

$$\bar{P}_{o3} = \frac{1}{2t_3} \int_0^{t_3'} v^2 dy + \frac{P_c}{2}. \quad (50)$$

Under these conditions, Equations (45) and (46) appear to be correct. Substituting Equation (45) into Equation (46), one finds

$$P_c = -\frac{2t_3}{h} \left[P_{o3} - \frac{P_c}{2} \right] \left[1 - \frac{2}{m/m'} - \cos \theta_3 \right].$$

Rearranging, it becomes

$$P_c = \frac{2 P_{o3} \frac{t_3}{h} \left[\frac{2}{m/m'} + \cos \theta_3 - 1 \right]}{1 - \frac{t_3}{h} \left[1 - \frac{2}{m/m'} - \cos \theta_3 \right]} \quad (51)$$

The important consequence of the non-uniformity of the total pressure at the jet exit is this: in Ejector Configuration 1-a (defined in Reference 4), the maximum velocity is always towards the outside, the

minimum velocity is always towards the inside. Therefore, the mean total pressure of the annular jet exhausting towards the right is much larger than the mean total pressure of the re-entrant jet. If the velocity distribution were reversed (maximum velocity on the inside wall), the converse would be true; i.e., for the same total jet momentum the base pressure P_B would be increased. However, to have a stronger annular jet means a larger P_c' , and this may be important for stability. The force equilibrium shown in Figure 76 appears correct, but really is not, unless it is interpreted properly.

It is possible that an ejector duct configuration with a uniform exit velocity distribution would be desirable. This would not be difficult to achieve.

Re-entrant Jet Region (Figure 77)

A prediction of the base pressure, P_B , is much more hazardous than that of the cavity pressure, P_c , as was already noticed in Reference 1.

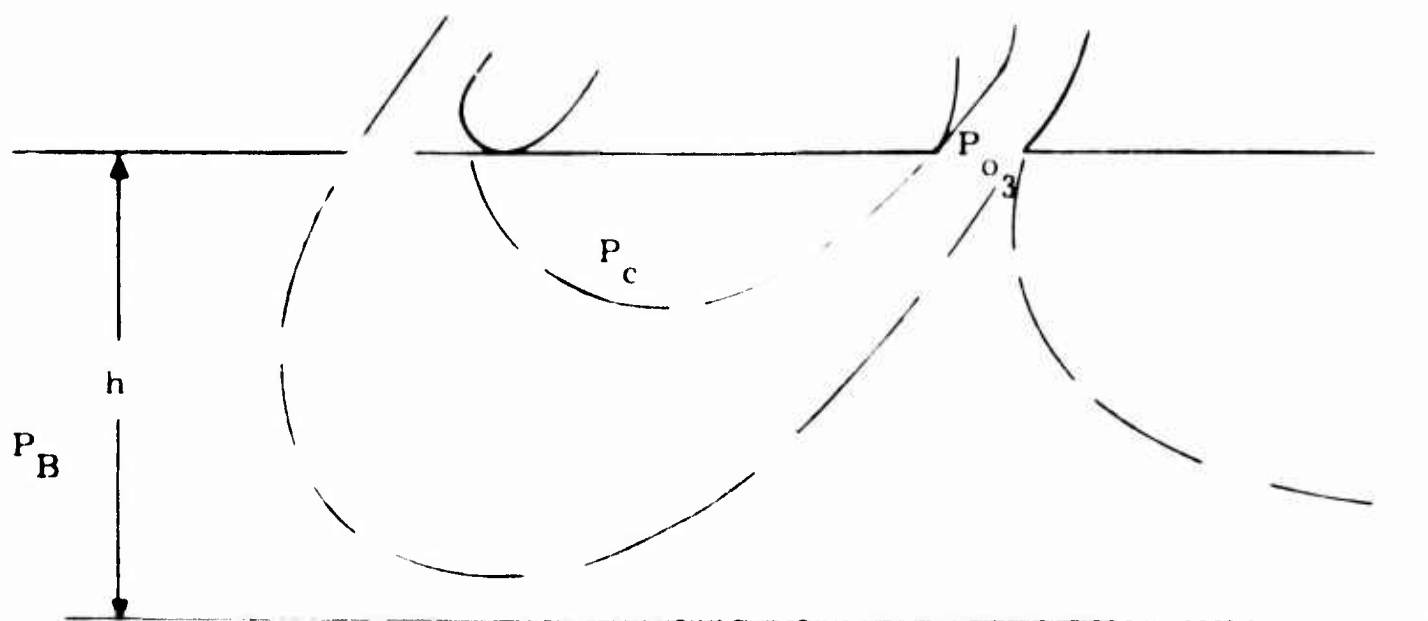


Figure 77. Re-entrant Jet Region

There is little doubt that the base pressure, P_B , is related to the tertiary flow total pressure, as it was defined from Equation (47). Possibly, the best physical representation of this jet total pressure is given by the stagnation pressure on the ground board.

One can attempt to apply either momentum or exponential theory to the re-entrant curved jet. This was done in Reference 1 with limited success. In a more recent effort, the exponential theory was modified by noting that the static pressure in the mixing region of the ejector is lower than atmospheric and that this must "strengthen" the re-entrant jet and, hence, increase P_B . Unfortunately, this approach cannot be justified at the present time.

The difficulty in setting up a theory for the external flow comes from the lack of static and total pressure measurements for this external flow. The important point which needs clarification is that of the magnitude of the pressure recovery P_0''/P_{O3} . There appears to be no physical reason why a high pressure recovery cannot be obtained. Again, a proper definition of P_{O3} is essential.

*STABILITY, CONTROL AND MANEUVER CHARACTERISTICS OF THE MARTIN RESEARCH VEHICLE

The Martin Research Vehicle is the first experimental GEM to use the ejector recirculating flow principle to generate the base pressure. This machine has certain characteristics which differ from those of the normal annular jet machine. In addition, it has certain capabilities which enhance its value as a test vehicle. The fundamental properties of the annular jet machine and those of the Martin GEM are the same. Both are large inert objects of high density, which have no contact with the ground and are sustained and maneuvered by aerodynamic forces.

*By Norman K. Walker and Staff, Norman K. Walker Associates, Inc., Bethesda, Maryland.

Aerodynamic Flow Regimes

As described on several occasions, see Reference 6, the normal GEM passes through three distinct flow regimes as it accelerates from rest; similar flow regimes appear in the case of the recirculating GEM (Figure 78).

1. Subcritical

At very low speeds the jet flow is predominant, and a GEM is surrounded by a cloud of eddies. In the case of the Martin recirculating machine, the actual primary flow, which is ejected from the machine, is much smaller than in the case of the annular jet GEM; hence, the subcritical regime can be observed only at very low speeds and is almost non-existent.

2. Transitional

At higher speeds, the excess air (primary flow) is ejected ahead of the machine, but is then forced to flow back over the surface of the machine. In turning back, the primary flow leaves a dead-air region or separation bubble ahead of the machine. This generates what appears to be a characteristic bow wave in front of the machine.

The bow wave is actually two lines: a stagnation line where the recirculating jet splits to release the primary flow, and a separation line where the forward-flowing primary air leaves the surface to curve back over the GEM. As the vehicle speed is increased, an increasing proportion of the primary air flow is forced to flow back into the base. This flow probably separates from the recirculating flow at the entry to the recirculating duct (Figure 79).

3. Supercritical

In the supercritical region the entire primary air supply is forced back under the machine. External air also flows under the base. Flow

Subcritical



Transition



Super Critical



Figure 78. Forward Speed Regimes

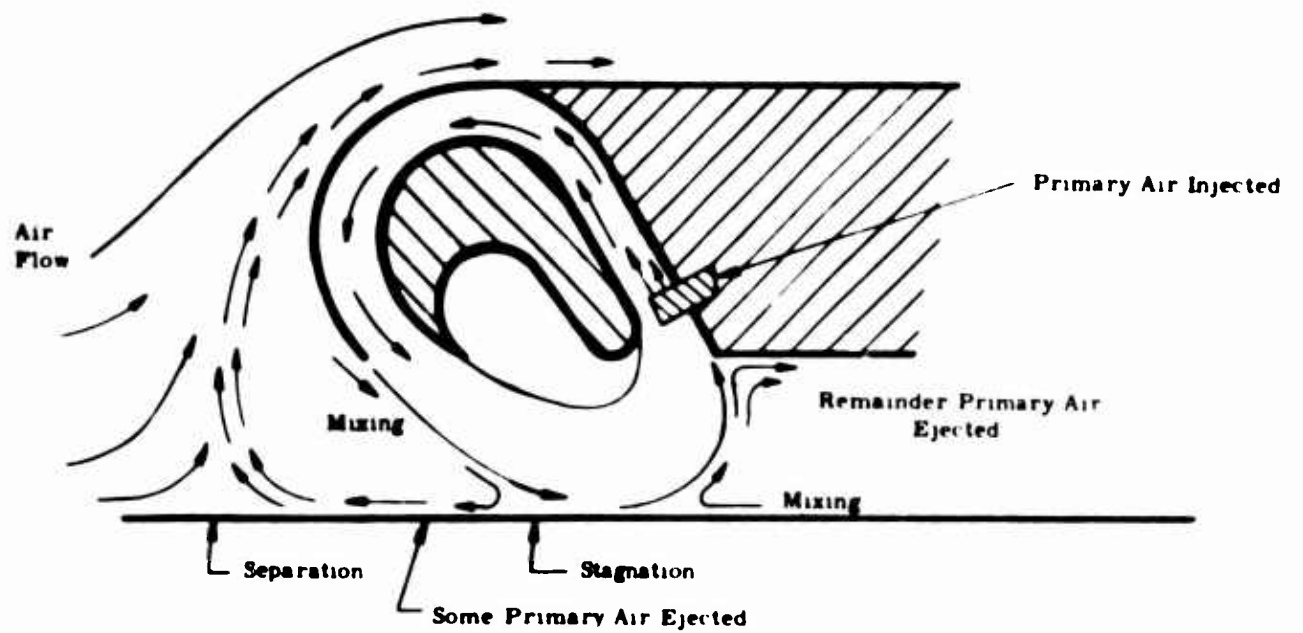


Figure 79. Leading Edge Recirculation Flow, "Transition" Regime

conditions in this regime have not been studied, but are probably as shown in Figure 80, with a greatly reduced volume of secondary air circulating and spillage of all the primary air occurring at the entrance to the ejector duct.

The results of wind-tunnel tests made by Martin on an early wind-tunnel model of the research vehicle show that the conditions in this region are largely associated with the total volume of circulating air flow in the recirculation system. These results correlate well with the results for an annular jet (see Reference 2).

For the research vehicle at 18 inches altitude, the second critical velocity, at which the external air flow passes under the machine, occurs roughly when $q = 0.4 P_{t_i}$ where P_{t_i} = total head of the circulating flow. Since the velocity of the circulating flow is in excess of 200 feet per second, it follows that the second critical velocity is in excess of 126 feet per second. Hence, the initial flight trials with the research vehicle, where the maximum speed expected is less than 40 feet per second, will not approach the second critical region.

The great majority of tests will be made in the transitional region, where the lift and drag are comparable with those for a "mound" of the same shape as the GEM, but with the air cushion replaced by a solid body. The various stability derivatives may be assumed to be the sum of those due to static conditions plus those due to the aerodynamic forces (Reference 7).

Heave Stability

1. Hover

The GEM is supported on a cushion of air contained by a recirculating curtain. The motion in the vertical plane is assumed to consist of a damped simple harmonic motion, the frequency of which is controlled by the variation of lift with altitude (Figure 7).

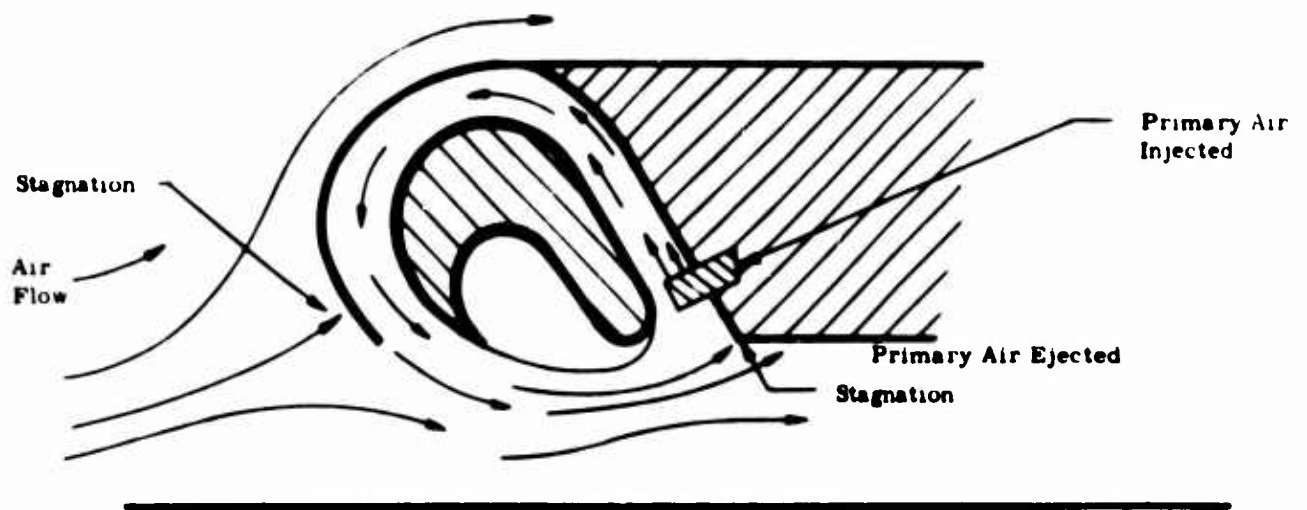


Figure 80. Leading Edge Recirculation Flow, "Super Critical" Regime

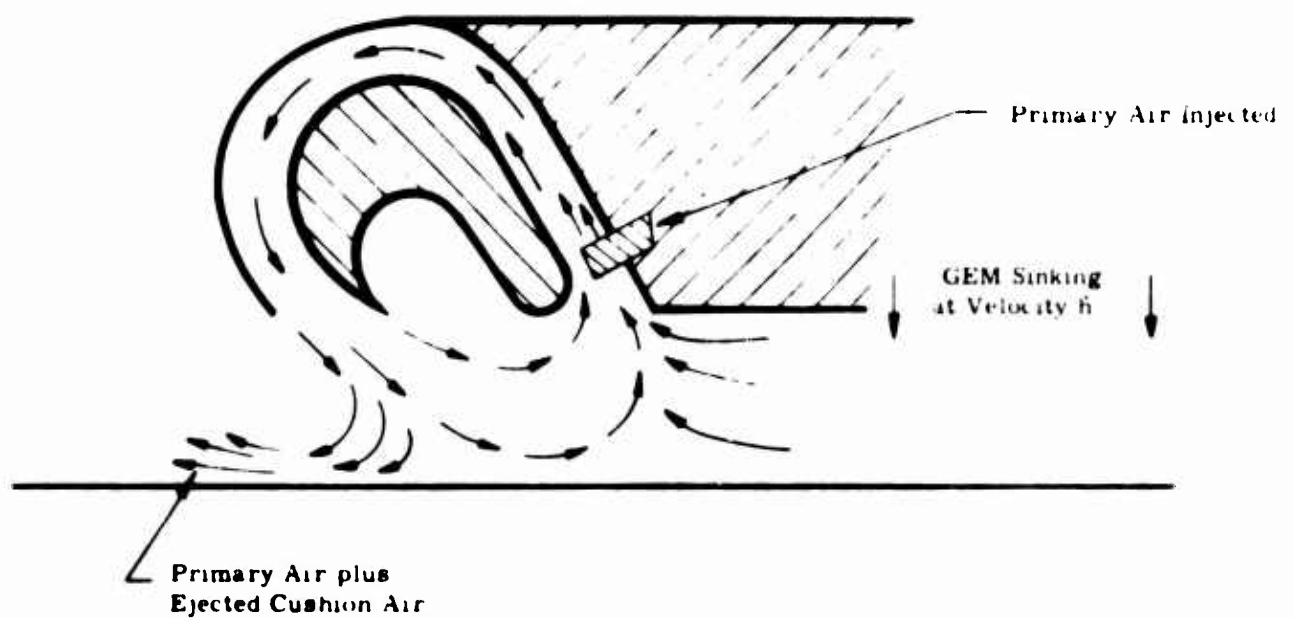


Figure 81. Recirculation Flow in the "Damping" Condition

This curve has a slope of 4000 pounds per foot, hence the undamped natural frequency is given by $\omega_0 = \sqrt{g \ k/w}$ radians per second between 12 inches and 25 inches in altitude. For the unloaded machine ($w = 3000$ pounds) and f_0 is 1.04 cycles per second. For the heavily loaded machine, ($w = 7000$ pounds), f_0 is 0.68 cycles per second.

Damping was studied in the Martin report on the earlier test vehicle, Reference 1, but it is believed that the estimates given are unreliable. A downward displacement of the machine does not cause air to flow out below the recirculating jet as is normally assumed for the annular jet case, but instead increases the mass flow of air in the ejector duct. This additional mass flow is then spilled with the primary flow outside the machine (Figure 81).

So far, this phenomenon has not been studied in detail, but results with the three-dimensional model suggest that heave damping will be appreciable, at least 20 percent critical and probably much more.

At low altitudes the research vehicle will be unstable if the slope of the curve of lift versus altitude becomes positive. This regime will be avoided by the use of a rudimentary undercarriage, but can also be controlled by changing the flap angle at the exit of the recirculating duct.

2. Forward Flight

In forward flight, the research vehicle will experience a lift coefficient on the order of 0.35, which at a forward speed of 40 feet per second will generate a total lift of about 390 pounds. This is quite small in relation to the total lift on the machine; therefore, it is not to be expected that the aerodynamic forces due to forward speed will modify the heave characteristics significantly during the initial trials.

Stability and Control in Pitch and Roll

The static stability properties of the new vehicle configuration are not accurately known at this time. Taking the worst indication, as shown in the two-dimensional double ejector tests, the vehicle should be mildly unstable. Considering the two-dimensional single ejector tests and the simulated three-dimensional corner model tests, the vehicle will exhibit a small amount of positive inherent static stability. Since there was no indication of a strong moment in either case (either stabilizing or destabilizing) the vehicle is normally assumed to be neutrally stable. However, in the following analyses if an unstable moment appears to be a factor which must be considered, then the vehicle is conservatively assumed to be unstable.

The stability characteristics can be effected by detailed redesign of the ejector, or by the addition of such auxiliary devices as secondary air stabilizing jets. It is recommended that advantage be taken of the excellent control characteristics of the Martin GEM to experiment with various forms of inexpensive, simple autopilots. The development of such a device would also benefit other types of GEM's.

1. Advantages of a Simple Autopilot

To date, most ground effect machines have featured inherent static stability in roll and pitch, since this seemed to ease the pilot's control problem and was in any case easy to achieve. However, when attempts were made to lay down realistic criteria for stability based on response to shifts of CG, etc., it was found that the additional lift power required for the stabilizing jets was expensive and that sufficient control to override the inherent stability was difficult to obtain (Reference 8).

It was suggested in Office of Naval Research (ONR) Report ACR/NAR-26, Reference 9, that many advantages accrued from the use of a simple

autopilot to control the GEM in pitch and roll, and from leaving the heave mode (in any case the most well behaved) uncontrolled.

The following advantages were claimed for such a system.

- a. Considerable savings in cost could result, since the major item of cost in a GEM is the cost of the engines, and the lift power would need to be increased by 15 or 20 percent if stabilizing jets were fitted. It is shown in Appendix I that, using the assumptions of ONR Report ACR/NAR-26, the cost of an annular jet GEM with trunks is reduced at least 10 percent for a given payload by fitting the machine with a simple autopilot, even after allowing generously for the cost of the autopilot. Insufficient data exist for a similar comparison for the Martin vehicle, but the costs are probably similar.
- b. The machine would not be so greatly affected by waves since the pitch response could be excited only through static stability. If the machine had negligible static stability and a pitch angle autopilot, then there would be no pitch response and the waves could affect the machine only through the heave response. This point has been examined in detail later in "Motion Over a Wave Surface," where it is assumed that the heave and pitch frequencies and damping ratios are much the same (as is normally the case) and where it is shown that for most frequencies and wavelengths encountered, the hover height required to clear waves without impact is 50 percent greater for the machines which are free to pitch.
(Note: Impact may occur at bow or stern.)
- c. At high speed the normal GEM is likely to be troubled by a combined rolling and yawing oscillation akin to the "Dutch Roll" of

an airplane. It is hard to eliminate this effect aerodynamically, but a suitably designed autopilot could provide a complete cure.

- d. Over a hard surface the normal GEM tends to follow the lowest contour. In addition, traversing even a slight slope will demand either continuous roll control to hold the machine level and hence cancel the effect of the slope, or continuous side force to hold the banked machine on its course. Both of these are expensive in power, since continuous control requires just as much power as the stability power it is overcoming. The autopilot GEM wastes no power to promote stability. It, therefore, uses little power to maintain its orientation.
- e. In the case of an amphibious lighter GEM, maneuvering onto or near a well deck ship or other amphibious shipping, it would be unaffected by the roll of the ship or of the water surface. This would make operations much easier in a seaway, especially if the GEM were operated at speed and the ship had a dry well deck and flexible trail mat as proposed in Reference 9.
- f. The hump drag over water would be appreciably reduced at some sacrifice of height.

2. Application of the Autopilot

Most GEMs are deficient in lateral and pitch control and sometimes suffer from a long lag in the control system, which makes it difficult to use a really simple autopilot.

The lift of the Martin machine is controlled by the power of the ejector jets, and these, being operated by air at fairly high pressure, provide a rapid response. Response to a sudden change in air pressure has not been measured, but estimates are that the change in rolling moment due

to the change in secondary flow momentum and to the change in cavity pressure is obtained within 20 milliseconds. This is followed by a somewhat slower readjustment of the base pressure which does not in any case give the major component of control moment.

Hence, if the lateral jets are coupled transversely, a valve can be installed which will increase the flow to one side and decrease that to the other without greatly affecting the total flow. Such a valve needs only a very small hinge moment (on the order of 20 pound-inches or so at the maximum, and possibly much less).

3. Control Power

Control power available, as compared to that required to overcome the slight static instability at small angles is shown in Figure 82. This shows that with only a 1-psi pressure differential and a 10-degree exit-flap angle, a maximum moment of 1600 foot-pounds is available. Since the injectors actually run at 5 to 7 psi, a much lower differential can be used. In practice, the result will probably be doubled, giving 2680 foot-pounds, or $\mathcal{L}/Lw = 0.027$.

The margin of control power is ample to cope with the possibility of any unstable rolling moments, until the limiting angle of 2.1 degrees is reached. At that point the clearance on the low side is half the hover height. If it is assumed that no variation of lift with roll angle occurs, then the machine can roll

$$\phi_{\max} = \tan^{-1} 18 \text{ in.} \times 2/20 \text{ ft} = 8.5 \text{ degrees.}$$

If we assume that the hover height is only preserved at the upper edge, the maximum roll angle is 4.3 degrees. The true maximum roll angle is probably between the two, say, 6.5 degrees.

(Results shown are for ± 1 psi pressure differential and 10° flap deflection)

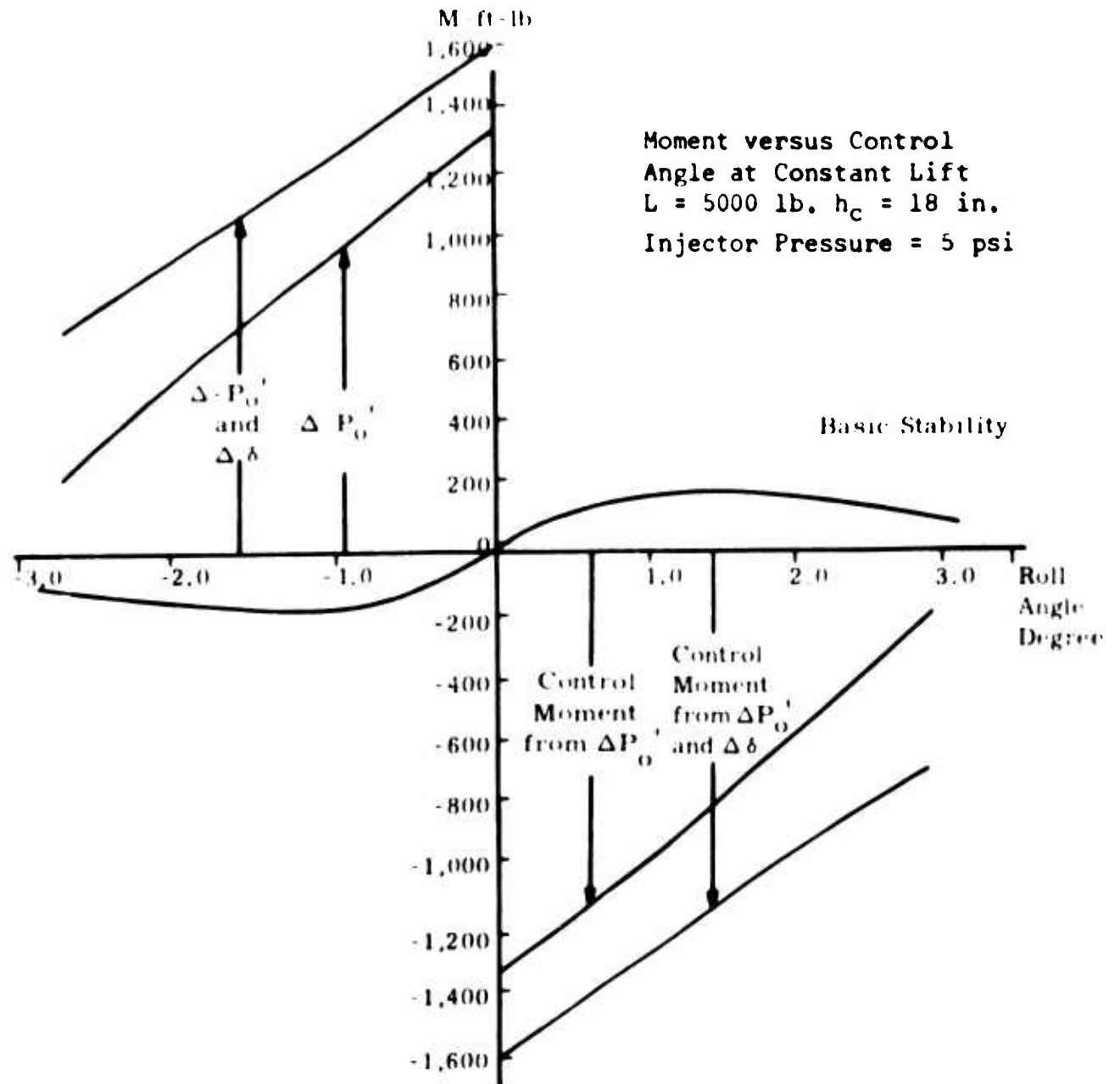


Figure 82. Vehicle Control Moment

It was suggested in References 8 and 9 that a useful GEM should possess a margin of control power to cope with asymmetric loading of the cargo. The detailed study of possible cargoes made in these references showed that early estimates were excessive, since normally cargoes consisted of one large item mounted centrally in the loading bay, and partial off loadings were very unlikely.

Assuming that a 20-foot-wide GEM might have a cargo bay 10 feet wide and that typical loads would be 8 feet wide, a load could scarcely be laterally off center by more than 4 inches (i.e., double gap one side). Assuming a payload of 2000 pounds for a 5000-pound machine, this implies a maximum moment of 670 foot-pounds. This is well within the capability of the control, especially if it is assumed that the pilot would use the exit flap angle as an auxiliary trim.

Allowance must also be made for aerodynamic effects due to sideslip. There is a large aerodynamic moment resulting from sideslip at high speeds for most GEM's (Reference 7). This is due partly to side forces on the body and fins, but mainly to the offset aerodynamic lift which is prompted by body depth. The low silhouette of the Martin research vehicle will minimize this effect. For preliminary trials an allowance must be made for the 390-pound aerodynamic lift to shift laterally almost to the 1/4-beam point at 90-degree sideslip. For a more normal 30-degree sideslip, this would imply a moment of 390×3 foot-pounds = 1170 foot-pounds.

This could be serious, but fortunately the Martin machine features a central "spine" housing the pilot and engine. When the machine sideslips, the pressure distribution on the spine is reflected onto the lifting body, tending to roll the windward side down. It is estimated that this tendency will roughly halve the value of the rolling moment due to

sideslip (Figure 83). Hence, the research vehicle possesses sufficient control power in roll to fill all possible requirements and has an adequate margin if the exit flaps are used to help trim.

It is suggested that the autopilot should control the whole of the pressure differential to the nozzles (1300 to 2600 foot-pounds), but that this should be done through a force feedback actuator so that direct manual override is possible if desired. In addition, the pilot would have control over the exit-flap angles as trim devices.

In pitch the requirements are broadly similar, except that control power may be somewhat less in proportion. There will be no requirements for control in pitch due to sideslip, but the aerodynamic lift acting on the body will give a nose-up moment of about 2900 foot-pounds at the maximum speed of 40 feet per second. Since this moment will increase steadily with the speed, it is suggested that the machine be trimmed nose heavy, to the extent of 1500 foot-pounds or so, by adjusting the CG position, and that it be balanced for level flight by offsetting the exit flaps. As the speed increases, the exit flaps can be returned to a symmetrical position and then reversed. Since this is a very slow change, the autopilot will not be required to cope with it. The very large nose-up trim due to the effect of the intake will be minimized with the Martin research vehicle, since the primary airflow is so much less than the jet flow of the annular type machine.

4. Major Features of the Stabilization System

The major requirement for a GEM roll and pitch stabilization system is that it be capable of holding the GEM level. This implies that the autopilot must provide a restoring moment, proportional to angular displacement, sufficient to overcome moments resulting from a CG shift, wind gusts, and the inherent instability of the Martin vehicle.

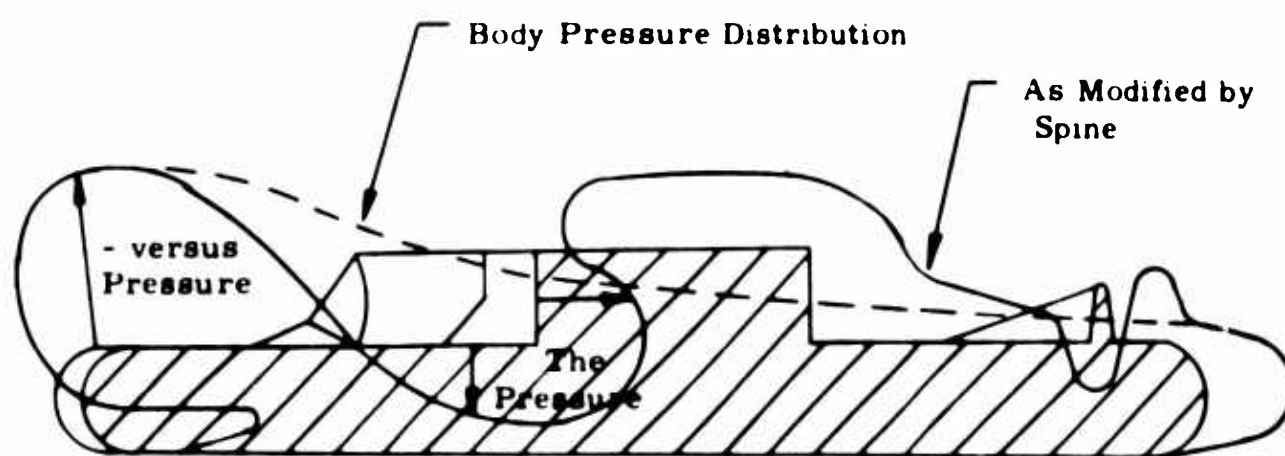
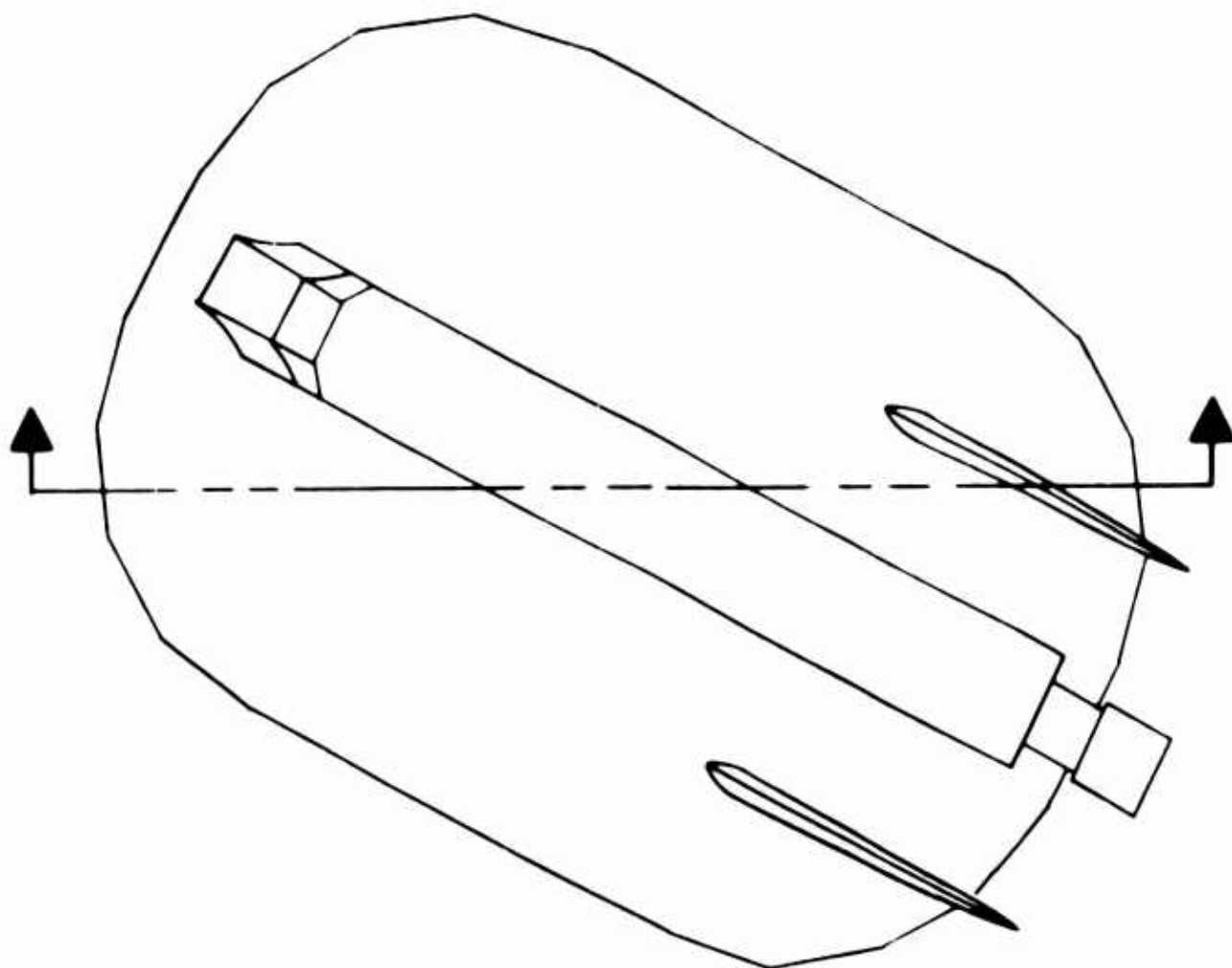


Figure 83. Vehicle Rolling Moment in Sideslip

The resolution of the system must be sufficient to detect errors as small as $1/4$ degree.

A suitably simple pitch and stabilization system has been studied and is described later in "A Preliminary Assessment of the Basic Autopilot Characteristics." This system would result in a machine having much the same frequency and damping characteristics as a stable GEM, except that the response to surface waves will be reversed in direction. Furthermore, since the unstable moments (if present) will be small in magnitude, the response of the machine to a rising slope of 5 degrees will still not exceed minus $1/2$ degree. Therefore, even this simple autopilot gives a considerable improvement in behavior as compared to an inherently stable GEM which will follow the surface contour. This system is recommended for experiments to study the behavior in artificially stabilized GEM and includes additional components, a rate gyro, and rate servo. This system gives:

- a. Greatly reduced response to surface waves;
- b. Damping necessary to eliminate wave resonance;
- c. Excellent high-speed characteristics;
- d. Resistance to CG shift and the ability to park on a slope.

A sudden application of a rolling moment of 700 foot-pounds will result in a partial roll displacement of 1 degree and a lateral displacement of 1 foot.

For experimental work all necessary components would be guided missile components and various systems would be investigated by the use of DC computing techniques and a single "patch-panel" permitting any desired components or assembly of the components to be tested. Since the required units are all in "quantity production", a complete set of parts for roll, pitch, and yaw control will not cost more than \$10,000 or weigh more than 75 pounds.

Once the various systems have been evaluated in the flight test program, it will be possible to investigate the use of commercial light aircraft autopilot components such as are marketed by Tactair, Mitchell, and Lear. Such systems can be purchased at a cost of about \$1000 per channel complete. The weight per channel will be less than 10 pounds. There is no doubt that these commercial components could be used to assemble the first system, but in comparison with the more versatile components described above, the test results would be very restrictive.

The economic studies of Appendix I assumed that an autopilot employing commercial components could be built, but the savings are so great in the overall cost of the research vehicle that the cost of the autopilot itself is quite minor.

5. Manual Override

The angular acceleration available for manual override of autopilot control system is about $1/2$ radian per second² or 500 mils per second² with full control in roll. If the pilot were to use simple bang-bang control, in an emergency he could maintain flight. According to recent experiments, he could control within a limit of approximately ± 15 mils or ± 1 degree (see Reference 10). In fact, these measurements were made with a pilot simply acting as an observer, and tests at APL/JHU on a controller seated in a controlled object show that the accuracy is increased several times by kinesthetic feedback (see Reference 11). Therefore, in case of a failure of the autopilot controls, the pilot would be able to control the machine satisfactorily. Certainly, the problem of GEM control is no more complex than that of the helicopter. There are also simple systems of control described later in the section, "Alternate Forms of Control" which permit direct manual operation.

Stability and Control in Yaw

The Martin GEM is a large unwieldy object with no yaw stability and very little damping. The angular acceleration provided by the engine efflux is $\pm 1/2$ radian per second². Comparison of this acceleration with the results for helicopters (see Figure 84 and Reference 12) suggests that it would feel sluggish. This acceleration is appreciably less than the value of 1.26 radians/second² for GEM III, even allowing for the increased length.

Control would be greatly improved by a simple autopilot capable of providing a weak heading reference and sufficient damping to give a velocity time constant of 1 second in the absence of the heading signal. The pilot could then override the heading signal for gross maneuvers and still have the facility of heading reference control during long runs.

The components necessary for this purpose are available in many light aircraft autopilots. It is proposed to assemble a breadboard system to explore pilot preferences, since the GEM is a new form of transportation and there is little previous background experience concerning it.

At high speeds the GEM will be directionally unstable at small angles, to the extent of roughly 1500 foot-pounds at $1/2$ radian sideslip. This is the maximum that can be controlled, but a better solution would be to add small low-aspect-ratio fins at the rear as shown in Figure 85.

Alternate Forms of Control

1. Univector Control

Univector control, a very simple system of control which eliminates the autopilot, but produces similar results under suitable conditions, was invented by Walker several years ago. This system has never

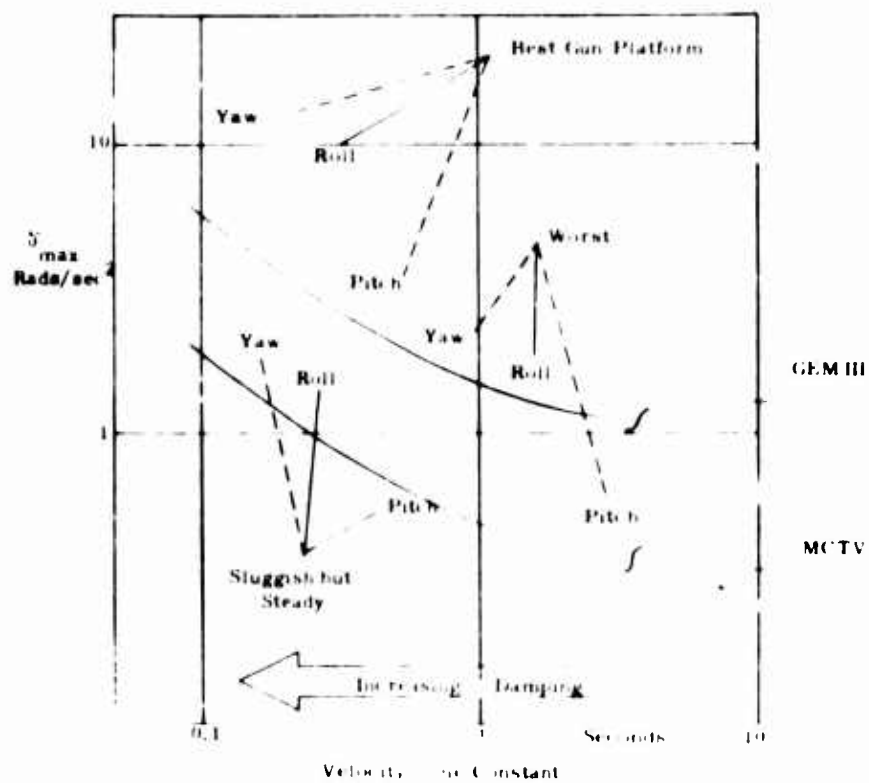


Figure 84. Stability in Yaw
(GEMs and Helicopters)

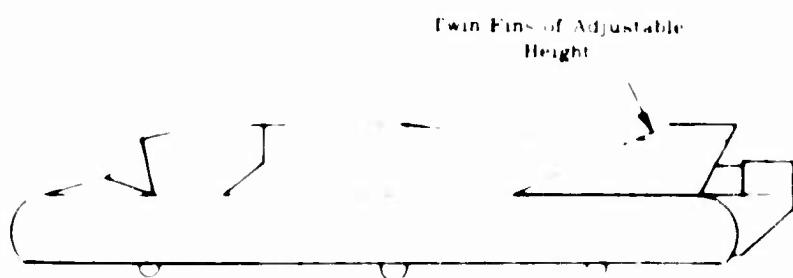
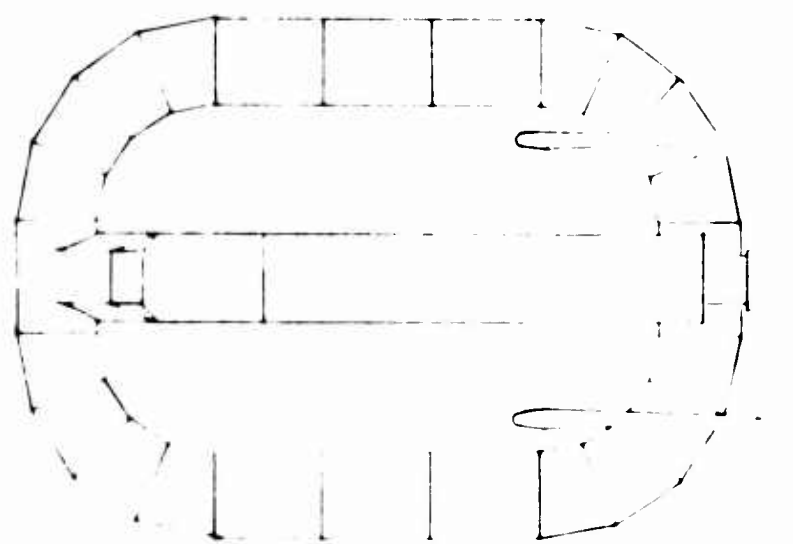


Figure 85. Vertical Fins for Neutral Stability

been tested because of the lack of a suitable test vehicle with good control response.

In this system the pilot does not directly control the machine; he aims a simple sight at the point on the horizon he wishes to reach. At the same time, he holds a cross wire level with the horizon (Figure 86).

It is obvious that this procedure establishes a direction reference, a roll reference, and a pitch reference all with no drift, relative to the craft itself. Quite appreciable forces could be withdrawn from the sight to operate control valves directly if desired. Indeed, a combination of springs and dampers could be used to generate artificial damping. However, it would be simpler at first, on a test vehicle, to generate these signals electrically and to operate through electrical servos.

Steering would be simplified by mounting the compass on the sight itself. Then maneuvering could be accomplished by banking, with or without a change of heading.

This system is particularly suitable for controlling the Martin research vehicle since the aerodynamic side forces will not complicate maneuver appreciably.

2. Pendulum Control

Many attempts have been made to use pendulums for control in simple autopilots. The mathematics are very difficult because of the large effect of the acceleration terms. Once it is realized that the dynamics of the pendulum must be related to those of the GEM and control achieved from the pendulum transient, a solution is possible.

A pendulum could be used to control the transient behavior of the research vehicle provided that the periods of oscillation were long and

undamped. This could be achieved very simply using an air bearing, and the research vehicle would be a very suitable platform on which to test the device.

In 1960, experiments were made with a ball mounted in a set of air bearings as a reference device. From these experiments it was decided that the scheme was feasible. Such a device is presented here only to show the possibility of the research vehicle as a test bed for new and attractive ideas. The use of a simple standard three-axis autopilot with electric pickoffs is favored as the initial step in any such evaluation program.

Maneuverability

Since the low speeds available for the flight test program rule out aerodynamic control, maneuver must generally be accomplished by biasing the autopilot to tilt the machine. The research machine will be very docile, since the steady-state condition will be one of rest with no deflection in roll or pitch.

1. General Considerations

With the proposed autopilot, the pilot could leave his seat and walk around the machine, yet the maximum displacement would be only a few feet. Assuming that 6-degree tilt is permitted, the research vehicle would generate 0.10g, giving a 425-foot turning circle at 25 miles per hour. This is rather poor compared to a car, and appreciably worse than most displacement craft. It would seem best to experiment with the land undercarriage over the ground by adjusting the lift until about 10 percent is carried on the wheels. Tests conducted in England by Folland and Vickers have shown that this leads to very effective control and maneuver at low speeds.

However, the GEM does have one great advantage over other craft. At lower speeds the lateral maneuverability is still the same and there is no lower limit to the turning circle. Figure 87 shows that if the various craft are compared on the basis of turning-circle radius per unit length, the Martin research vehicle is as good as a car at high speeds, and much better than ship or car below 10 miles per hour. The apparent ease of maneuver in a car is due to the use of banked turns by our highway engineers. The apparent poor precision of GEM maneuvering is due to the use of inadequate and sluggish controls and to the complication of the control systems. The proposed autopilots should go a long way toward correcting these deficiencies.

3. The Effect of Wind

In the hover condition the most serious effects of wind will be sideforce. Assuming that a wind of 25 miles per hour blows on the machine from the beam, it will generate a force due to a sideforce coefficient of 1.0 acting roughly on the entire side area. The side area is about 170 square feet allowing for the fins; the result is a maximum sideforce of 100 pounds. This can be nullified by banking the machine through $100/5000$ radians or 1.15 degrees. Since at a 90-degree sideslip the machine will be almost neutrally stable, the yawing moments will be very small and easily controlled.

In forward flight a 15-mile-per-hour wind gust directly across the course will generate a transient sideslip angle of $\tan^{-1} 15/25$ or 31 degrees. There will be little disturbance in yaw if the fins are correctly sized, but there will be a transient rolling moment of about 50 percent of the capacity of the autopilot, and a transient roll of about 1 degree downwind.

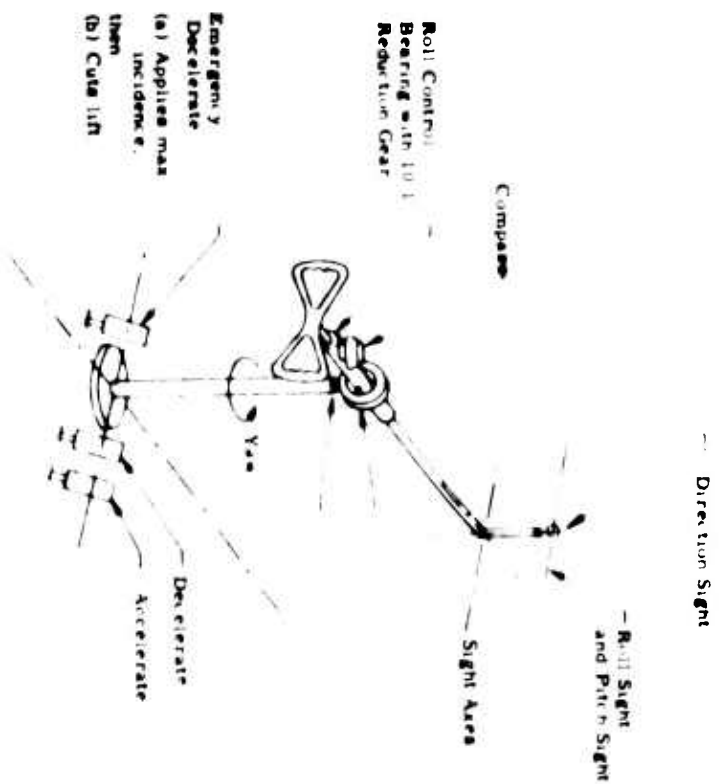
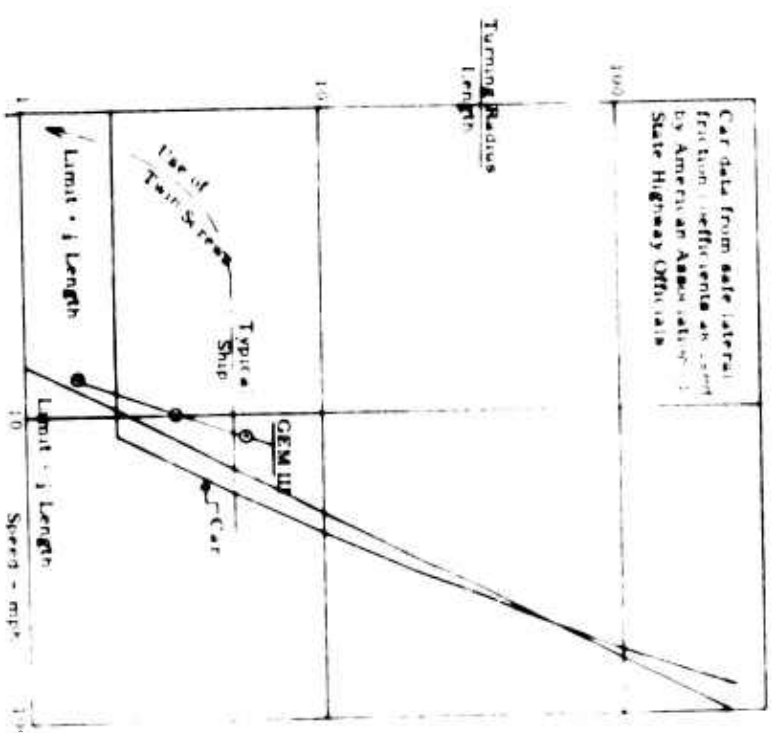


Figure 86. Univector Control Column



These results suggest that the research vehicle will be able to perform trials successfully in steady or gusty winds of up to 15 miles per hour, which is a very considerable proportion of the available forward speed. In contrast, the tests on the annular GEM III at Langley AFB were abandoned when the wind velocity exceeded 7 miles per hour. However, GEM III has about the same side area, for a gross weight of only 1850 pounds, or 37 percent of that of the research vehicle, and is probably too stable in yaw for comfortable handling, References 13 and 14.

Human Engineering of the Control System

It is most desirable that the control system of a new form of transport such as the GEM should be engineered to agree with long-held conventions, and also should, if possible, be consistent. Two basic conventions are current at present:

1. Conventional

In conventional control, the operator assumes that he is seated on a fixed point in space and applies force or moment to the machine to urge it in the direction he wishes it to go. The steering of a bicycle and the banking of an airplane are examples of conventionally coupled controls.

2. Kinesthetic

In kinesthetic control the operator strives to maintain his equilibrium in a moving environment by assuming that he is at fault. On a lifting platform, if the nose rises, the operator leans forward to keep his own position fixed. In this concept, control signals are sometimes the reverse of conventional.

3. General Considerations

Some controls are unsound but are so well established that nothing can be done to prevent their being used. The best example is that of the

n
,
l.
n-
rudder pedals in an aircraft, or the footbrake of a car. The former system is best avoided for GEM's, but the latter is very commonly used and understood.

For the GEM, it is assumed that the conventional system is best, and angular displacements will be corrected by moving some control as if it were rigidly connected to the machine. Similarly, in general, displacements should be effected by displacement of a control.

A great simplification of the research vehicle is the elimination of a separate sideforce control. The pilot can easily learn to treat roll as both roll angle and also as rate of change of heading. This will ease his problem and those of the designers considerably.

15 The suggested Univector control, shown in Figure 86, meets these requirements. A rotation of the control unit nose down produces a nose-down trim change, a rotation to the right produces a bank to the right, and a rotation to the left about the vertical column produces a rotation of the machine to follow.
e

The usual car accelerator is so well understood that from a human factors standpoint it cannot be bettered. It is, in any case, a conventional control. Similarly, the footbrake is well understood, although theoretically poor. An emergency brake pedal might be provided for the left foot which would first give full nose-up trim, and then, through a detent, cut the lift engine.

Vertical altitude will surely be controlled by the speed of the main engine, and exit-flap angles. These could be simple trim controls.

Lateral force is unnecessary and not available. The main side force will be provided by a bank angle, with trim for skid, and special training or other devices will be needed to enable the pilot to make the best use of it.

The results with the Air Research Simulator show that directing a GEM accurately is not easy. Here again, the use of an electric autopilot with electric control will facilitate experiment with unorthodox combinations of controls.

Motion Over a Wave Surface

As compared to annular jet and plenum chamber GEMs of the same size and weight, this recirculation GEM exhibits the interesting feature of having a rather low stiffness to angular displacement in pitch and roll, relative to the surface over which it is flying. This is in combination with fairly powerful sources of available control moment. Therefore, the Martin GEM offers the possibility of experimentally investigating the means and merits of attitude stabilization in pitch and roll.

The question arises, does stabilizing in pitch improve the sea-keeping qualities of the machine? Some insight into the behavior of a GEM in a fully developed sea can be obtained by examining the simpler case of the GEM operating over a heavy swell. By this we mean a sea with a single component of wavelength and height. Such a sea will have a unique wave celerity associated with the wavelength, but relative to the GEM the velocity of the waves will be compounded of the wave velocity and the GEM speed. The frequency of encounter will be dependent on the latter. Therefore, the GEM should be considered as operating over a waving surface whose frequency and wavelength are independent of each other.

A preliminary consideration will be the response of the GEM in heave alone when flying over a heaving surface, that is, one that is rising and falling in a regular periodic manner. Many authors have discussed the heave motion of GEMs over a fixed surface and derived a differential

equation of the third order with constant coefficients. By rejecting the highest frequencies as being of little interest to a GEM, this is reduced to a second order equation. It then relates to a single mode of damped oscillation as the GEM returns to its equilibrium position after a disturbance in height.

Thus,

$$(D^2 + 2\zeta\omega D + \omega^2) Z = 0 \quad (52)$$

where

ω = natural frequency with zero damping

ζ = damping ratio.

This has the complementary function

$$Z = Z_0 e^{-\zeta\omega t} \cos \left[\omega \sqrt{1 - \zeta^2} t + \alpha \right] . \quad (53)$$

If the surface is moving vertically, its velocity and position will add to the GEM's velocity and height in generating force on the mass of the machine.

Thus, we have

$$D^2 Z = - (2\zeta\omega D + \omega^2) y \quad (54)$$

where y is the height relative to the surface.

That is,

$$(D^2 + 2\zeta\omega D + \omega^2) y = D^2 h \quad (55)$$

where h is the height of the surface.

Then the Particular Integral is

$$y = \frac{D^2 h}{D^2 + 2\zeta\omega D + \omega^2}. \quad (56)$$

Adding the Complementary Function, after the transient has subsided,

$$y = y_o + \frac{D^2 h}{D^2 + 2\zeta\omega D + \omega^2} \quad (57)$$

That is,

$$y = Z_o + \frac{D^2 h}{D^2 + 2\zeta\omega D + \omega^2} \quad (57)$$

Let the surface be moving up and down in a regular cyclic manner

$$h = \frac{H}{2} (\sin \mu t). \quad (58)$$

Then,

$$\begin{aligned} y &= Z_o + \frac{D^2}{D^2 + 2\zeta\omega D + \omega^2} \cdot \frac{H}{2} (\sin \mu t) \\ &= Z_o + \frac{H}{2} \cdot \frac{\phi^2}{T} \sin (\mu t + \xi) \end{aligned} \quad (59)$$

where

$$T^2 = 4\zeta^2 \phi^2 + \phi^2 - 1^2 \quad (60)$$

$$\tan \xi = \frac{2\zeta\phi}{(\phi^2 - 1)}, \text{ and } \phi = \frac{\mu}{\omega}. \quad (61)$$

This applies, of course, only to the motion over a sea whose wave-length is long compared to the GEM.

The motion over a relatively short sea may be examined by considering the GEM to be formed of two compartments, front and rear, each having the characteristics of the GEM in heave when working together, but modified by an efficiency factor when working differently. This factor may be applied to the nominal distance between the two compartments, thus affecting the pitching moment only (Figure 88).

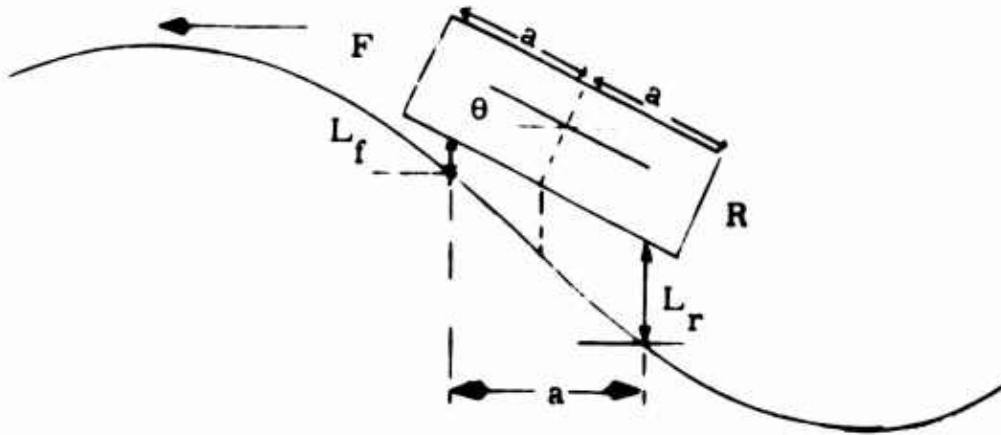


Figure 88. Motion Over Short Sea (Pitch)

Thus if L_f , L_r are the vertical forces acting on the front and rear halves respectively,

$$\text{Heave lift} = L_f + L_r$$

$$\text{Pitching moment} = (L_f - L_r) a \eta$$

where η is the efficiency factor referred to above.

Let the sea have a wavelength λ , and let the height of the sea above its mean height be

$$h_s = \frac{H}{2} (\sin \mu t) \text{ amidships of the GEM.} \quad (62)$$

Then the phase difference between the front and rear is

$$2\pi a/\lambda = 2\epsilon. \quad (63)$$

Considering only heave motion, and supposing the pitch to be stabilized, (Figure 89).

$$h \text{ front} = \frac{H}{2} \cdot \sin \overline{\mu t + \epsilon}$$

$$h \text{ rear} = \frac{H}{2} \cdot \sin \overline{\mu t - \epsilon}$$

$$h \text{ mean} = \frac{1}{2} (h \text{ front} + h \text{ rear})$$

$$= \frac{H}{2} \cdot \cos \epsilon \cdot \sin \mu t.$$

Therefore, using the result of Equation (59),

$$y \text{ mean} = Z_0 + \frac{H}{2} \cos \epsilon \cdot \frac{\phi^2}{T} \sin (\mu t + \xi) \quad (64)$$

(y mean is the mean height, front and rear, relative to the mean sea height, front and rear).

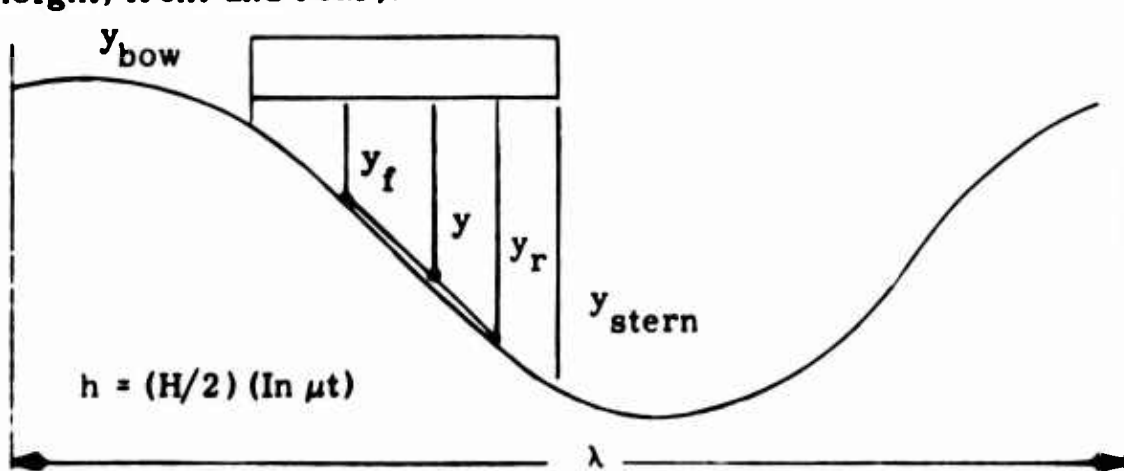


Figure 89. Motion Over Short Sea (Heave)

The bow clearance is given by

$$y \text{ bow} = y \text{ mean} + h \text{ mean} - h \text{ bow}$$

$$= y \text{ mean} + \left(\frac{H}{2}\right) \cos t \cdot \sin \mu t - \left(\frac{H}{2}\right) \sin \overline{\mu t - 2\epsilon} \quad (65)$$

and

$$y_{\text{stern}} = y_{\text{mean}} + \left(\frac{H}{2}\right) \cos \epsilon \cdot \sin \mu t - \left(\frac{H}{2}\right) \sin \overline{\mu t + 2\epsilon} . \quad (66)$$

That is,

$$\begin{aligned} \Delta y_{\text{stern}}^{\text{bow}} &= Z_o + \left(\frac{H}{2}\right) \cos \epsilon \cdot \left(\frac{\phi^2}{T}\right) \sin \mu t + \xi \\ &\quad + \left(\frac{H}{2}\right) \cos \epsilon \cdot \sin \mu t - \left(\frac{H}{2}\right) \sin \mu t + 2\epsilon \\ &= Z_o + \left(\frac{H}{2}\right) \cdot B \sin \mu t + \gamma \end{aligned} \quad (67)$$

where B is determinable from the preceding expressions.

The GEM will just touch the waves at bow or stern if

$$\left[\frac{Z_o}{\frac{H}{2}} \right] = B^2 . \quad (68)$$

B has been evaluated for $\xi = 0.2$, $\epsilon = 0, \pi/4$ and $\pi/2$ and the results are plotted in Figures 90, 91 and 92.

The pitching moment applied to the GEM is

$$I \frac{\ddot{\theta}}{g} = (L_f - L_r) a \eta \quad (69)$$

$$\begin{aligned} \ddot{\theta} &= \frac{ga\eta}{I} (L_f - L_r) \\ &= \frac{ga\eta}{I} \cdot \frac{\omega}{g} \cdot (2\zeta\omega D + \omega^2) (y_f - y_r) \\ &= \frac{a^2}{k^2} \cdot \eta \cdot (2\zeta\omega D + \omega^2) \theta \text{ relative to sea} \\ &= (2\zeta_p \omega_p D + \omega_p^2) \theta \text{ relative to sea} \end{aligned} \quad (70)$$

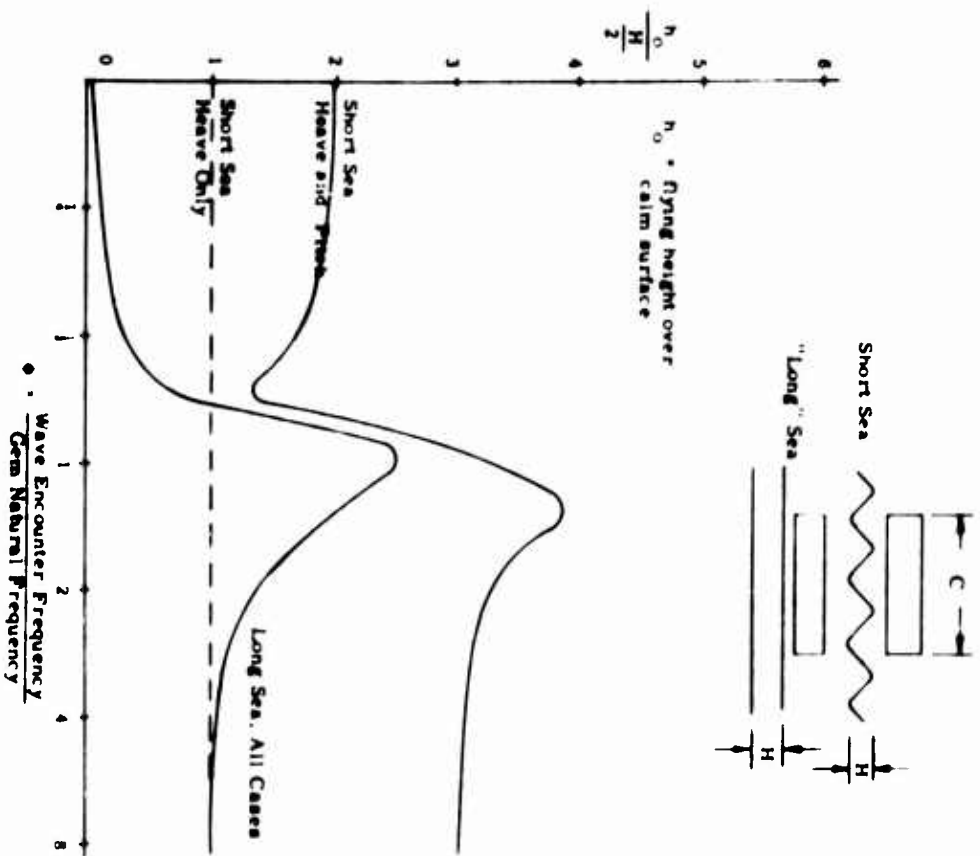


Figure 90. Flying Height to Clear Waves,
Longest and Shortest Wavelengths

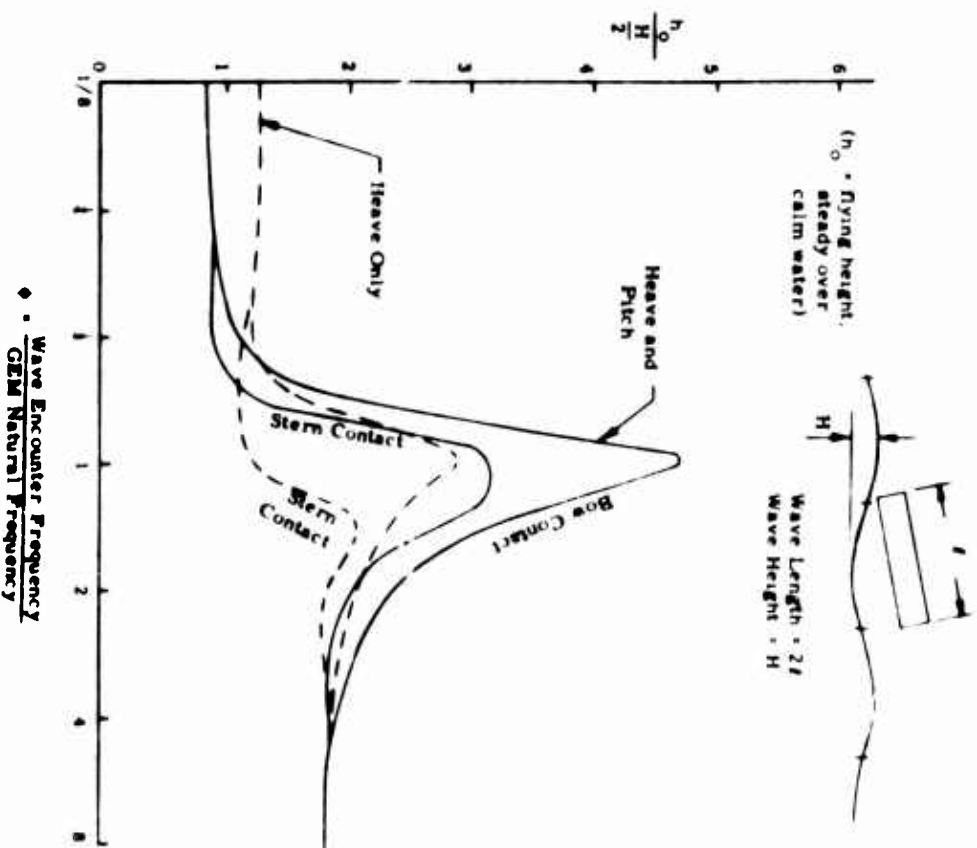


Figure 91. Flying Height to Clear Waves;
Wavelength = 2 x GEM Length

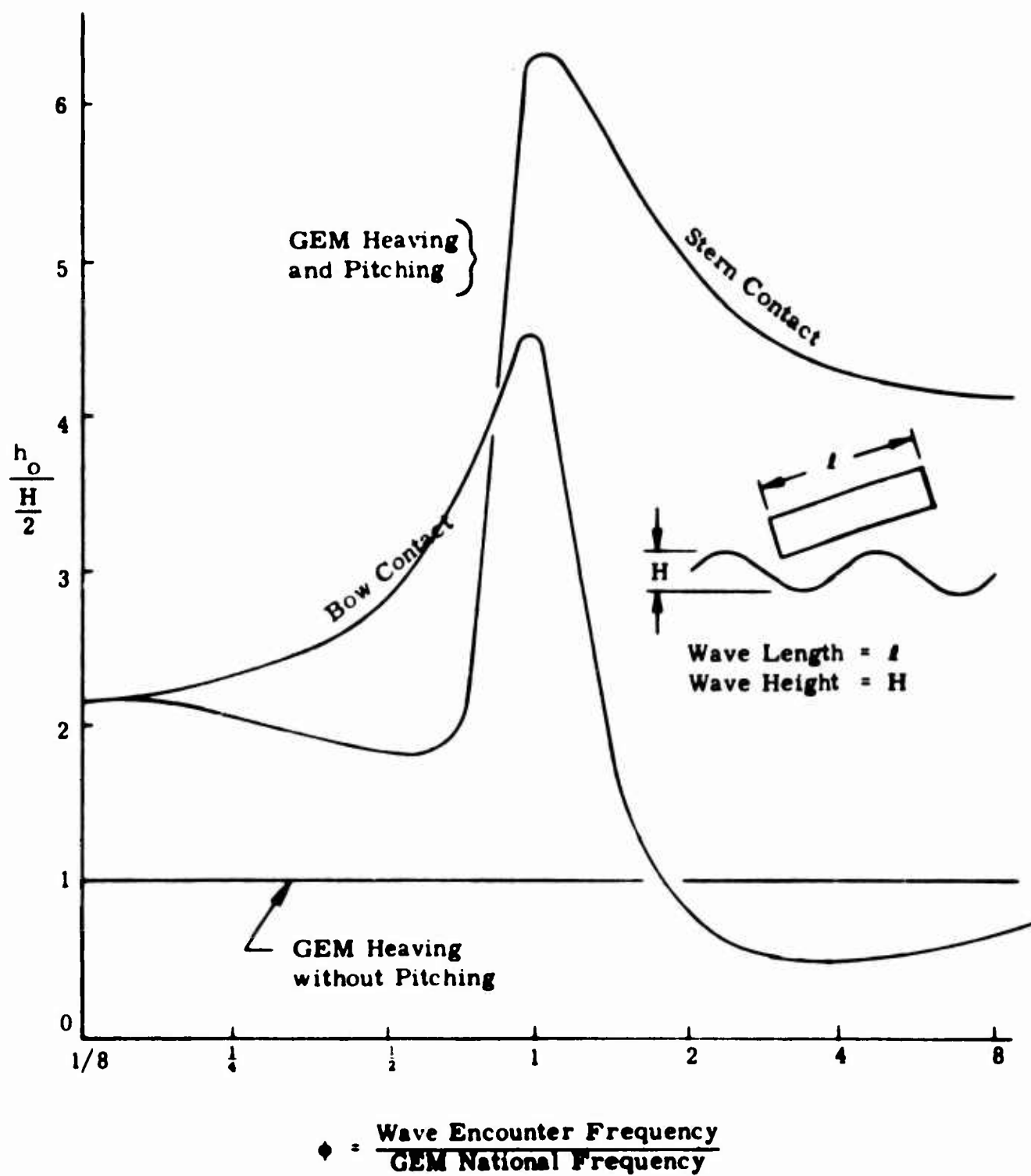


Figure 92. Flying Height to Clear Waves;
Wavelength = 1 x GEM Wavelength

$$\theta_{rel\ sea} = \frac{D^2}{D^2 + 2\zeta_p D + \frac{2}{p}} \cdot \theta_{sea} \quad (71)$$

and

$$\begin{aligned} \theta_{sea} &= \frac{h_f - h_r}{a} = \frac{H}{2a} (\sin \overline{\mu t + \epsilon} - \sin \overline{\mu t - \epsilon}) \\ &= \frac{H}{a} \sin \epsilon \sin (\mu t + \frac{\pi}{2}) \end{aligned} \quad (72)$$

Therefore, using the result of Equation (61),

$$\theta_{rel\ sea} = \theta_{o\ rel\ sea} + \frac{H}{a} \sin \epsilon \left(\frac{\phi^2}{T} \right)_p \sin (\mu t + \xi_p + \frac{\pi}{2}) \quad (73)$$

Therefore,

$$\theta = \frac{H}{a} \sin \epsilon \left(\frac{\phi^2}{T} \right)_p \cos \overline{\mu t + \xi_p} - \frac{H}{a} \sin \epsilon \cos \mu t \quad (74)$$

where suffix $(\theta/T)_p^2$ denotes values of ζ, ω appropriate to pitching

The effect of pitching on the bow and stern wave clearance may be written at once as

$$\Delta y_{stern}^{bow} \text{ pitching and heaving} = \Delta y_{stern}^{bow} \text{ heaving} \pm a\theta \quad (75)$$

and substituting the above results.

This gives

$$\Delta y_{stern}^{bow} = Z_o + \left(\frac{H}{2} \right) B_1 \sin \overline{\mu t + \gamma} \quad (76)$$

The GEM will just touch the waves at bow or stern if

$$\left[\frac{Z_o}{\frac{H}{2}} \right]^2 = B_1^2 . \quad (77)$$

This has been evaluated for the simplified case when $\zeta_p = \zeta = 0.2$, $\omega_p = \omega$ and is plotted in Figures 90, 91 and 92.

The results of this analysis are, of course, no more valid than the initial assumptions. Nevertheless they suggest strongly that there is much benefit to be derived from stabilizing a GEM in pitch if avoiding contact with waves is desired. The stabilized GEM stays out of the water better at all speeds and wavelengths except when wallowing (left side of Figure 91) where it seems beneficial to let the nose come up as the wave comes beneath the ship.

The curves should not be pressed too hard at the right-hand side. The Martin GEM has a natural frequency around 0.8 cycle per second so that speed over the sea is $\phi \times 0.8 \times \text{wavelength}$. In Figure 85 where wave length = $2l = 80$ feet, $\phi = 2$ represents a speed of 128 feet per second over the waves. At more moderate speeds and shorter wave lengths, $\phi > 2$ is straining the mathematical model of lift, since it is a function only of compartment center height.

Pitch stabilization seems to have its most dramatic effect in quelling the troublesome resonance at $\phi = 1$ (Figure 92) at wavelengths equal to the length of the craft. At longer seas (twice the craft length) the reduction is only about 1/3. If the residue is tiresome, it may be possible to avoid this by varying the natural frequency of the machine, since the troublesome condition is restricted to a narrow frequency band by the pitch stabilization.

The case of the "long" sea, as considered, is somewhat more artificial than the others, because it postulates that the surface is flat beneath the GEM. Actually the case describes the GEM motion, pitch stabilized, over a heaving raft or deck rather than over water.

THE EFFECT OF CONTROL OF THE HEAVE CHARACTERISTICS

It is shown in the previous section, "Motion Over a Wave Surface," that the use of control pitch and roll substantially reduces the response of a GEM to surface waves and permits operation in more arduous conditions. If such a simple pitch and roll autopilot is installed, the main factors affecting the response of the machine are the heave characteristics, and it is of interest to inquire whether these also can be appreciably improved.

Certain deductions can be made at once:

1. Since the machine is designed to fly at a given lift and a given distance from the surface, any attempt to control the altitude variations must imply that the lift can be raised, and this presumably implies that the power of the lift engine must vary.

Unless the engine has some "power accumulator" to absorb this excess power, it follows that power must be dissipated in some other form than lift when the surface is rising and that additional power must be available to supply additional lift when the surface is sinking. Hence, there must be excess power available, and over an undulating surface the power used will be considerably increased (unless the excess power can be directly fed into the propulsion units).

2. Since the control system must control the whole lift of the machine, the end organs (servos and controls) required will be of considerable

size and probably of excessive lag. The same applies, of course, to the design of an autopilot for a fully immersed hydrofoil, but in this case the main control can be drawn from hydrodynamic surfaces which are immersed in water and hydrodynamically balanced. In such case, the response time lag and activating power are minimized.

3. Some difficulties could be overcome by using a space reference inertial autopilot with a GEM designed to give a lift independent of altitude from the surface, but this would be a very complex and expensive piece of equipment.

The above remarks are true whether the autopilot is designed to modify the static stability (heave frequency) or the damping of the GEM. It was also shown previously that in regular seas little improvement results from major modifications to the variables. Indeed, a modest damping ratio of 0.1 to 0.2 is probably as good as any, particularly if the region of resonance can be avoided.

It may therefore be concluded that no simple autopilot will make any worthwhile modification to the surface resonance characteristics of a GEM and that there is no advantage to be gained from massive increases in damping, since the damping is relative to the surface. The pilot can appreciably improve results by taking care to avoid the critical encounter frequencies and this can be done by changing course or speed relative to the waves; this procedure was adopted on several occasions during the recent rough-water trials of the SRN 2 in England. However, this may not always be convenient or possible, and the Martin research vehicle does present an alternative possibility which is worth investigating.

By altering the angle of the exit flaps and the jet pressure, the pilot can appreciably change the inherent variation of lift with height, hence, altering the natural frequency in heave. He can therefore adjust the machine characteristics while in flight to avoid any resonance condition encountered. Full-scale experiments would be required to evaluate the effectiveness of this procedure as compared to a change of course, or speed, but in a military operation the latter alternatives might not always be permissible.

A Preliminary Assessment of the Basic Autopilot Characteristics

It is shown in Appendix I that a considerable improvement in performance and handling qualities of any GEM can result from the use of artificial stabilization of pitch and roll attitude using a simple autopilot. A difficulty with most available machines is that the roll and pitch controls are inadequate and sluggish; but the Martin vehicle does possess adequate control power, and the time lags in generating control movement are likely to be acceptable.

1. Properties of the Vehicle

It is assumed that the characteristics of the vehicle can be adequately represented by:

- a. A linear variation of roll moment with roll angle to the surface to the extent of 600 foot-pounds/degree which is unstable.
- b. A damping moment proportional to rate of roll relative to the surface of approximately 35 foot-pounds/degree-second. This is sufficient in most cases to give a damping ratio of about 0.1.
- c. A roll inertia of 3500 foot-pounds per second².
- d. A control moment which is proportional to some control displacement and which has a maximum value of 4000 foot-pounds.

- e. The maximum roll angle is unspecified, since the apparent unstable static moment reaches a maximum at a 1- or 2-degree roll-angle displacement. Any system which is acceptable over the first 2 degrees of roll is, therefore, certainly better for large oscillations even if the control moment is the limiting factor.

2. Requirements

- a. The vehicle may be slightly statically unstable. A system is needed to provide positive static stability on space axes. What limitation on control lag can such a system accept?
- b. The damping of the vehicle, which is derived from aerodynamic damping plus the jet flow damping, is positive but small. Improved overwater results might be obtained if additional damping on space axes could be provided by the autopilot.
- c. It is desirable to minimize the response of the vehicle to waves. This could be achieved by designing for neutral static stability. If static stability or instability is present, what is the additional penalty for designing the autopilot to minimize surface response?
- d. If the vehicle operates over land with zero static stability, it will be unaffected by ground contours. Suppose that static instability is present, what characteristic of the autopilot will eliminate the effect and permit vehicle to hover on a slope, or to accept a shift in CG position?

3. Properties of Various Systems

- a. Simplest System (Provides roll stabilization without additional damping):

The signal flow diagram for the simplest type of system (no additional control damping included) is given in Figure 93.

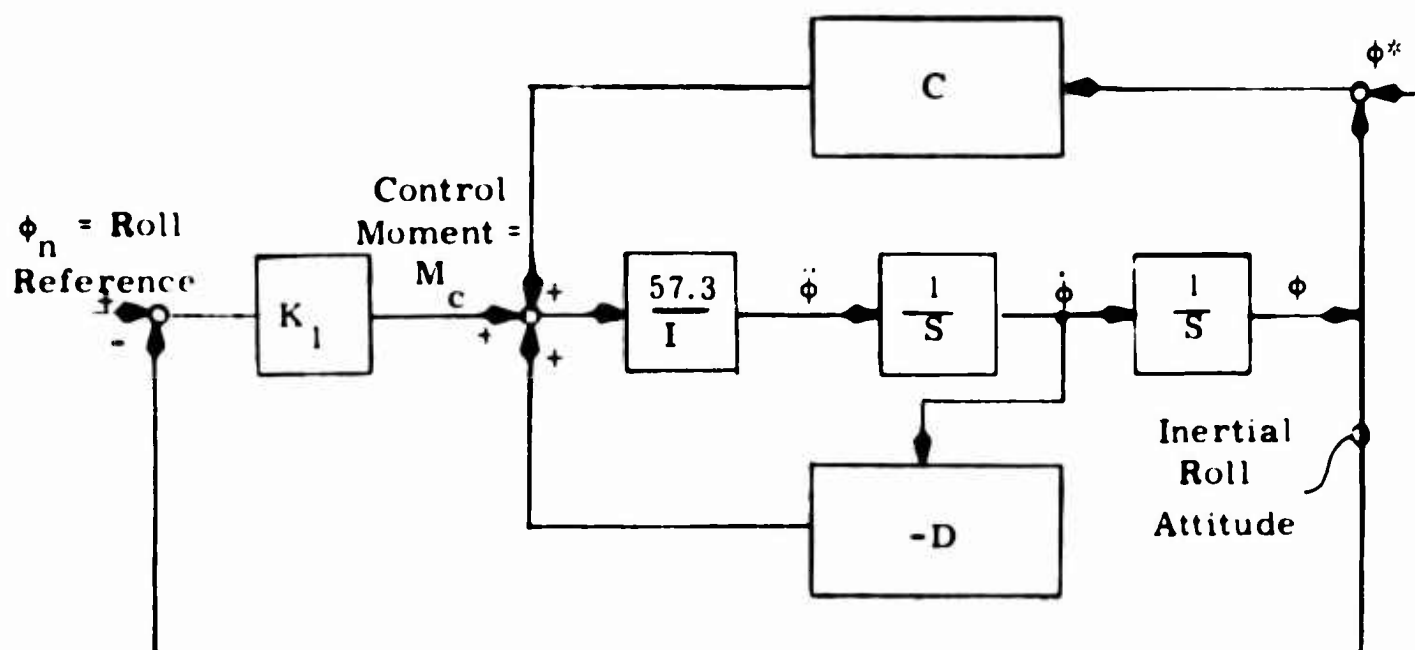


Figure 93. Signal Flow, Simplest System

In this figure, as shown, the signs of static stability derivatives $+C$ and damping $-D$ are selected to correspond to the assumption of static instability and stabilizing damping. The input to the static stability derivative C is $\phi + \phi^*$, the sum of the inertial roll and effective roll due to surface variations. Dimensions are as defined earlier.

For this system the loop characteristic equation is

$$\Delta = S^2 \cdot \frac{I}{(K_1 - C) 57.3} + S \cdot \frac{D}{(K_1 - C)} + 1. \quad (78)$$

Assuming that the value of D is sufficiently large, control stability is still only obtained for $K_1 - C$ positive. A value of $K_1 = 2C_{\max} = 1200$ foot-pounds/degree is about the minimum allowable to provide adequate design margin for the moderately smooth surface contour case. Thus under this assumption the controlled roll frequency is shown as follows:

$$\omega_n = \left[\frac{(K_1 - C) 57.3}{I} \right]^{\frac{1}{2}} = \left[\frac{(1200 - 600) 57.3}{3,500} \right]^{\frac{1}{2}} = 3.15 \text{ radians/sec} \quad (79)$$

In order to achieve this sort of control band width, the extraneous control servo lags, etc., at frequencies near 3 radians must be minimized. A control servo-second order band pass of 12 radians per second or about 2 cps should be adequate. This implies that a first-order equivalent lag of about 160 milliseconds is acceptable. (Unfortunately a fluid flow control system of this type includes considerable "transport" lag, thus, the acceptable lag is appreciably lower in this case than the first-order lag.)

There should be no difficulty in building a system of this type since the lags are unlikely to reach these limits.

This system is roughly comparable in its characteristics to the behavior of an inherently stable GEM with a stable static roll moment of 600 foot-pounds/degree except that the response to waves will be of the opposite sign.

For the system as shown, the roll output ϕ due to a surface variation ϕ^* is given by

$$\frac{\phi}{\phi^*} = \frac{C}{K_1 - C} \left[\frac{1}{S^2 \left[\frac{I}{(K_1 - C) 57.3} \right] + S \left[\frac{D}{K_1 - C} \right] + 1} \right] \quad (80)$$

and in the limit $\phi/\phi^* = 1$, for $K_1 = 2C$ and inherent stability and no autopilot $\phi/\phi^* = -1$, for $K_1 = 0$.

This system may well be acceptable, since the actual static instability is small compared to the heave frequency and, in any case, is limited to approximately 500 foot-pounds.

b. Modifications to Provide Reduced Surface Response

Since the surface response of this system can be reduced by simply reducing the static moment coefficient "C" toward the limit of $C = 0$, then

the surface response "C" also can be varied to some extent by adjustments of flap angle and jet pressure.

An alternative conventional technique is to increase the gain factor of the autopilot K_1 . An acceptable variation of output with input might well be 20 percent. Hence,

$$\frac{C}{(K_1 - C)} = \frac{1}{5},$$

and the roll stabilization band width for system A becomes

$$\omega_n = \left(\frac{K_1 - C}{I} \times 57.3 \right)^{\frac{1}{2}} = 7 \text{ radians/second.} \quad (81)$$

The roll loop damping varies inversely as ω_n ; thus, even if the damping, D , were adequate for the first case, it might not be so for the higher control band width. Furthermore, the phase margin due to the damping, D , at loop resonance, ω_n , is reduced about in proportion to ω_n , while the allowable additional servo lag which can be tolerated at this frequency must also be reduced proportionately. Accordingly, the ratio of servo band width to ω_n must be greater than the factor of 4 assumed for the previous case; a factor of 8 is now more nearly correct. Thus, the required second-order servo band width is about $8 \times 7 = 56$ radians/per second or about 9 cps, which implies a total acceptable first order control lag of about 36 milliseconds.

c. Improved System To Give Artificial Damping

The inherent damping of the vehicle may be insufficient. If additional damping is, in fact, required, it can be achieved by using either a simple lead network or an additional rate gyro. While the lead network itself is simpler and cheaper in fabrication, its use imposes a requirement for dc signal processing. Furthermore, fairly stringent requirements

are also imposed on the resolution, dynamic range, and vibration sensitivity of the roll attitude gyro. The tradeoff in this area can be assessed only by careful evaluation of both techniques and by simulations involving non-linear effects of servo amplifier and servo rate saturation.

The signal flow diagram for the rate gyro system is given in Figure 94.

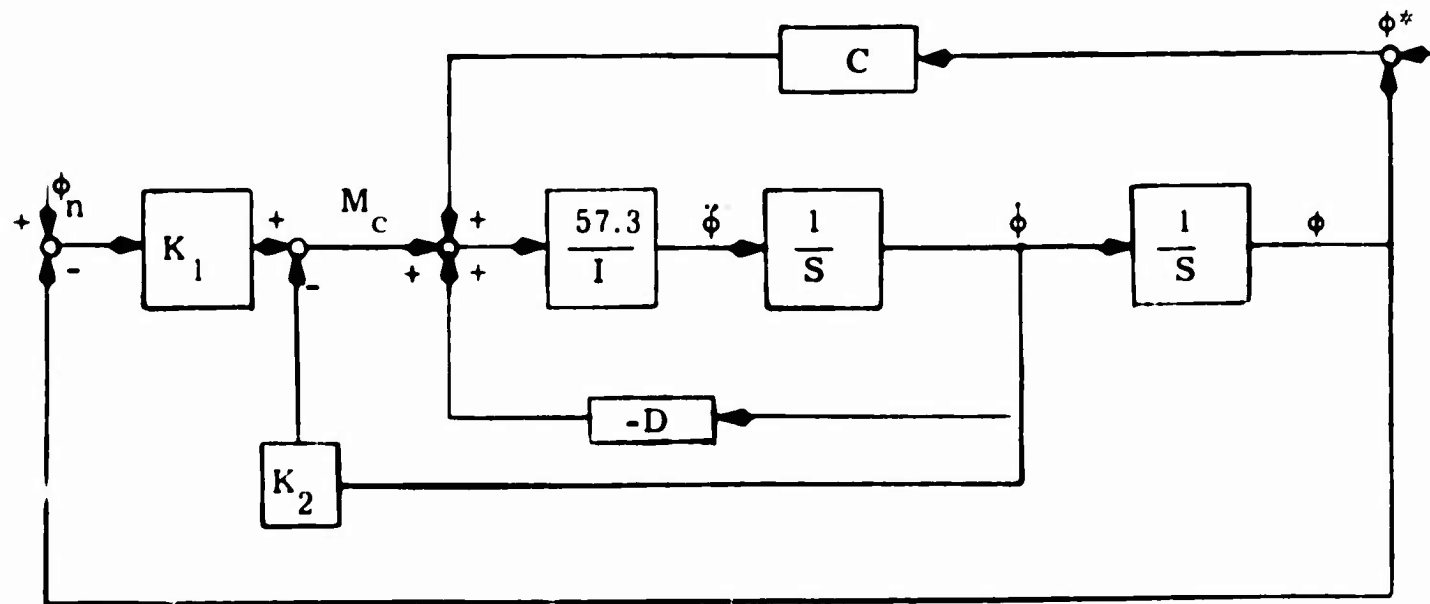


Figure 94. Signal Flow, Rate Gyro System

This circuit is identical to the one shown in Figure 93, except for the addition of the rate feedback term through the gain K_2 . The characteristic equation is

$$\Delta = S^2 \cdot \frac{1}{(K_1 - C) 57.3} + S \cdot \frac{D + K_2}{K_1 - C} + 1. \quad (82)$$

Note that the term K_2 merely adds to the inherent damping D . However, in this case the stability requirements of the rate loop dictate a somewhat wider band width servo, since the rate gyro itself introduces some additional lag. The use of a lead network in place of the rate gyro leads to an even more stringent design restraint. Servo band widths of 5 to 6

and 8 to 9 cps respectively are required, corresponding to first order control lags of 60 milliseconds and 36 milliseconds.

d. Improved System To Give Zero Error Over An Inclined Surface

Static insensitivity to surface contours or to fixed moments due to CG shift can be achieved by adding an additional feedback of integrated error. In this way the roll error required to generate a control moment to nullify the static moment is eliminated during the transient.

A convenient way to achieve this result is to employ a rate servo rather than a position servo. This is indicated by introducing another integral term, $1/s$, into the system ahead of M_C as shown in Figure 95.

The additional term K_3S , which is required to provide the loop stability, can be achieved by proper selection of servo input mixing components if dc signal shaping is used.

Here again the required servo band width is 8 to 9 cps. However, this mode of operation can not be achieved with a lead network; a rate gyro is required. A system with control damping gyro and rate servo to provide static insensitivity to surface is shown below.

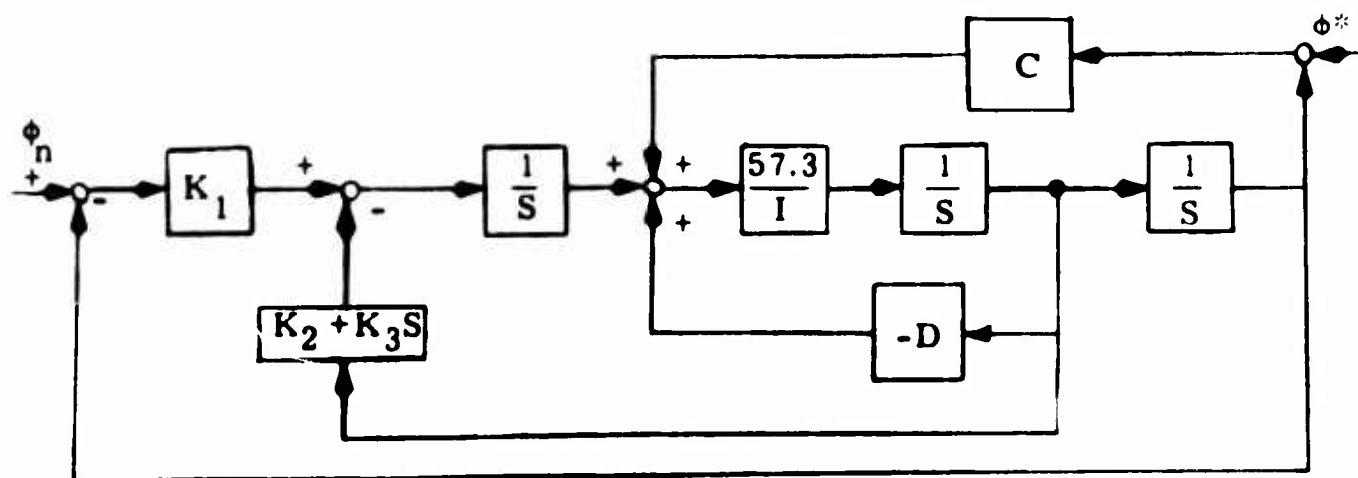


Figure 95. Signal Flow, System Insensitive to Surface Contours

4. Effect of Non-Linearities in the Aerodynamics

The assumed variation of static roll moment with angle is unstable and linear, with a slope of 600 foot-pound/degree. Figure 20 shows that the actual variation may be much less than this, if it is assumed that the machine loses altitude slightly as it rolls due to the loss of lift. In any case the maximum roll moment does not exceed 500 foot-pounds. It is shown in a previous section, "Component Tests" that the unstable trend resulted from the two-dimensional test results. To be conservative, this trend is assumed to exist for the full-size vehicle; however, there is strong evidence that the vehicle will actually have a small amount of positive inherent stability.

The response to surface irregularities will be greatly reduced, and the system gain of 1200 foot-pounds/degree may well be satisfactory. For large angles of 3 degrees, the moment applied to the machine will be 100 to 500 foot-pounds, and this can be cancelled by a deflection of the GEM in roll of only $1/12$ degree to $5/12$ degree.

Similarly, a limit cycle oscillation of $\pm 1/2$ degree would probably be acceptable to the pilot at the frequencies involved, and this would increase the tolerance of the system.

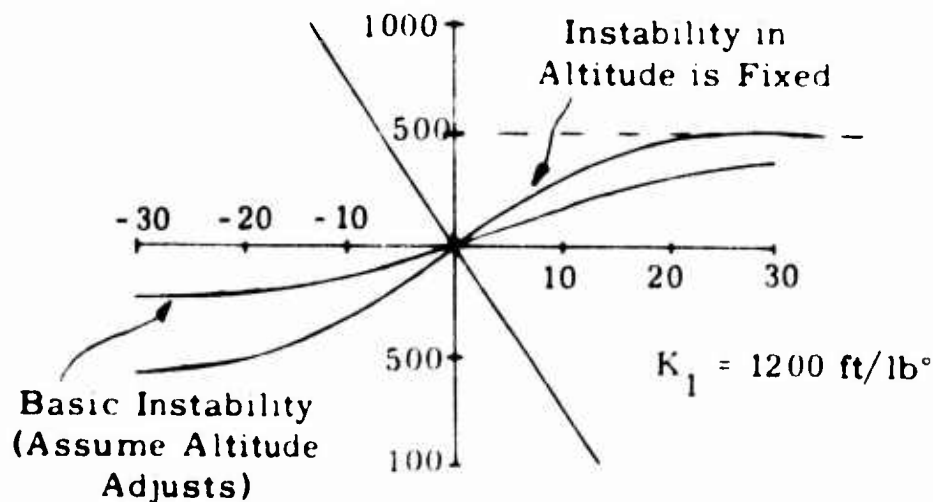


Figure 96. Vehicle Static Stability

CONCLUSIONS

The Martin research vehicle possesses a unique combination of fast powerful roll and pitch controls, with a low silhouette and a good ground clearance. It is therefore an excellent test vehicle to explore the results of various simple autopilot systems, as compared to inherent pitch and roll stability (which can be obtained, if desired, by utilizing the waste compressor exhaust to drive a compartmenting jet). Initial experiments should be conducted at low forward speed (up to 25 miles per hour), but the good payload and flat upper deck permit the installation of any desired combination of forward propulsion and maneuvering engines. The flat deck also permits use of aerodynamic control and maneuver surfaces as fitted to the VA3.

A simple autopilot system using a position gyro can be designed which will stabilize the vehicle against an assumed unstable static moment of 600 foot-pound/degree, but will provide no added damping. The general response of the system will be similar to that of a normal inherently stable GEM, but the response to waves will be reversed in sign. Since the assumed unstable moment limits at 100 to 500 foot-pounds, the response to surface irregularities will not exceed $1/2$ degree in roll, even for slopes of 5 degrees or so. This behavior may well be acceptable. Such a system will use simple components and can accept a total equivalent first-order control lag of up to 160 milliseconds, which is well within current estimates.

An improved system giving artificial damping can be devised by adding a shaping network. This will imply the use of dc computation, and also require that the total equivalent first-order control lag be limited to 36 to 40 milliseconds. A somewhat less demanding way of adding damping is to use a rate gyro in addition to the position gyro. In this case, ac

pickoffs may still be used, and a 5 to 6 cps bandwidth is acceptable, implying a total permissible first-order control lag of 50 to 60 milliseconds.

A much better system results from the use of a rate gyro, a position gyro, and an integrating device such as a rate servo. In this case the response to waves can be reduced by 80 percent, and the vehicle will adjust to zero roll within 1 second after a sudden shift of the CG or a change of slope and hence will "park" on slopes; any reasonable desired degree of damping could be added. Such a system would require a servo bandwidth of 8 to 9 cps, implying a maximum permissible first-order lag of 36 to 40 milliseconds, which may be difficult to achieve.

Advantage could be taken of the nonlinearity of the aerodynamics to reduce the required system gain by a factor of 4. This would give slightly improved response to waves and the simplest system with adequate damping to resist even the resonant condition. The machine would adjust to zero roll on a slope, or following a CG shift, within 2 seconds. This would still be adequate, since a sudden application of a 700 foot-pound moment would give a transient roll of only 1 degree, which would be eliminated in 2 seconds giving a lateral displacement of about 1 foot. Such a system would permit a total first order control lag of 100 to 120 milliseconds. The quickest and most expedient way to achieve a working system will be to make use of standard off-the-shelf missile-type components, to use dc signal processing, and to engineer the system with patchboard connections at the input of the servo amplifier. Such a system will present no development problems other than those inherent in the control characteristics of the MCTV itself. All the necessary components are available as stock items, and the cost of the components for a pitch and roll system would be on the

order of \$8000 for the combined system, which weighs approximately 60 pounds. With those components, any of the systems described could be hooked up on the patch panel. Once the system has been engineered and tested, it would be possible to examine the use of light aircraft autopilot components for a production system.

SOME CONSIDERATIONS OF THE AERODYNAMICS OF THE MARTIN EJECTOR RECIRCULATION CONCEPT*

A Thin Jet Theory Analysis of Two Dimensional Partially Recirculating Flow

1. Basic Assumptions

In the theory of annular jets, if the height of the vehicle above the ground plane exceeds about three jet thicknesses, then the static pressure of the jet varies in an approximately linear manner across its thickness. Thus acceptably accurate results can be obtained by assuming that the static pressure of the jet is equal to the mean of the static pressures on either side of it. This is the so-called "thin-jet theory" approach, and the equations resulting from this assumption are often easier to handle than the more precise "layered-jet theory" approach, such as that given in Reference 14, for example. Provided that the restriction on height is observed, then, the thin jet theory will give acceptable agreement with experiment, at least for the purposes of a preliminary investigation; in cases where such agreement is not obtained, we can reasonably expect a defect in the analysis rather than in the "thin-jet" assumptions.

*By Peter R. Payne, Frost Engineering Development Corporation,
Englewood, Colorado

2. Assessment of Previous Work

The problem of partially recirculating flow has been previously analyzed in Reference 1, and in other Martin publications ; the assumptions of constant momentum flux along the jet and zero vorticity in the cavity region and the conventional "thin-jet" theory assumptions were used. The equations derived from this analysis were found by Martin to give good agreement with the static pressure measured in the vortex region (Region B of Figure 97), but to overestimate the cushion pressure. The reason for this was the assumption of constant momentum flux. The Martin theory assumed

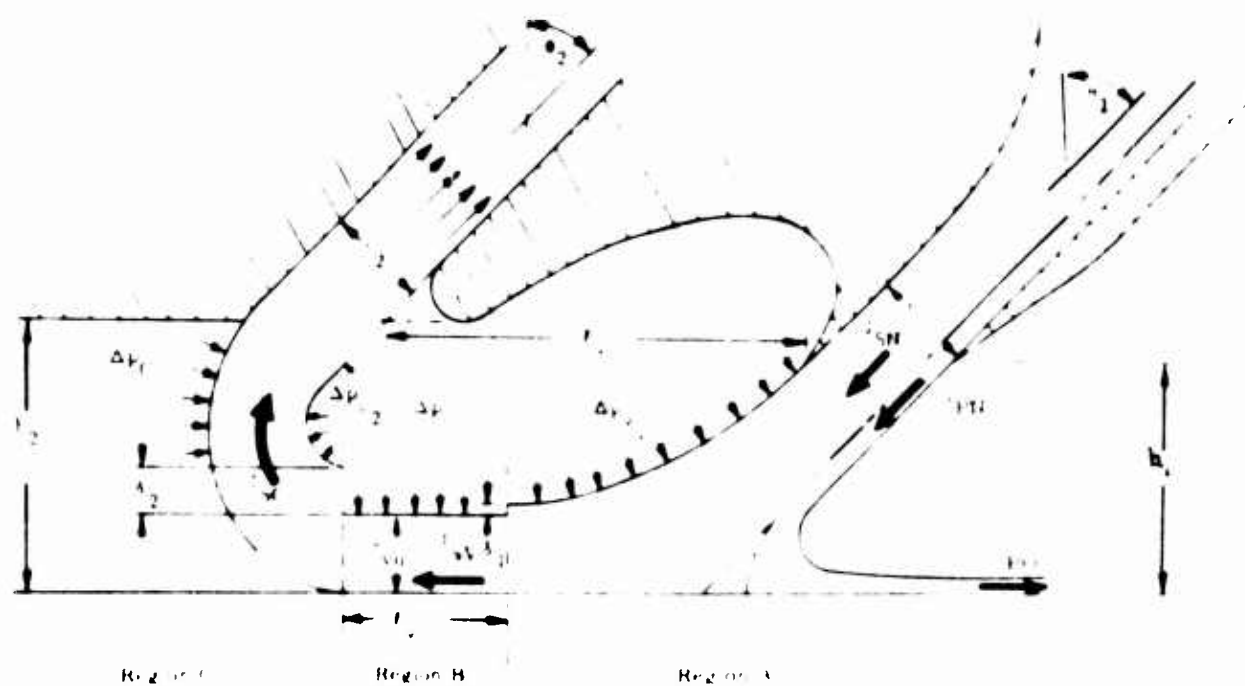


Figure 97. Definition of Momentum Flux Components

$J_{SC} = J_{SN}$, which would only be true if the static pressure were the same everywhere (see Figure 97). In practice, even if total head is conserved throughout the jet, the velocity in region C will be much less than in region A, because of the higher static pressure, and thus the momentum flux will be less. This correction has been made in this section.

The Martin theory was then modified by utilizing the "layered jet" theory in region C while retaining the thin jet assumptions in region A. Since layered jet theory is based upon total pressure rather than momentum flux, this automatically corrected the error made in the earlier analysis, but introduced two others.

In the first place, the mixture of two fundamentally different theoretical approaches destroyed the balance of the equations. At low hover heights, thin jet theory gives a cushion or cavity pressure which is twice the correct value, while layered jet theory gives the correct result. Thus, as the hover height was reduced, the cavity pressure given by the revised Martin theory increased (in a negative manner) much more rapidly than the calculated (positive) pressure rise across the re-entrant jet. This resulted in the prediction of negative cushion stiffness at low hover heights (see Figure 98). Since negative cushion stiffness actually occurs in practice (for other reasons), this theoretical result was apparently regarded as indicating the essential correctness of the initial assumptions. In fact, it is merely a mathematical accident, but one which may prove

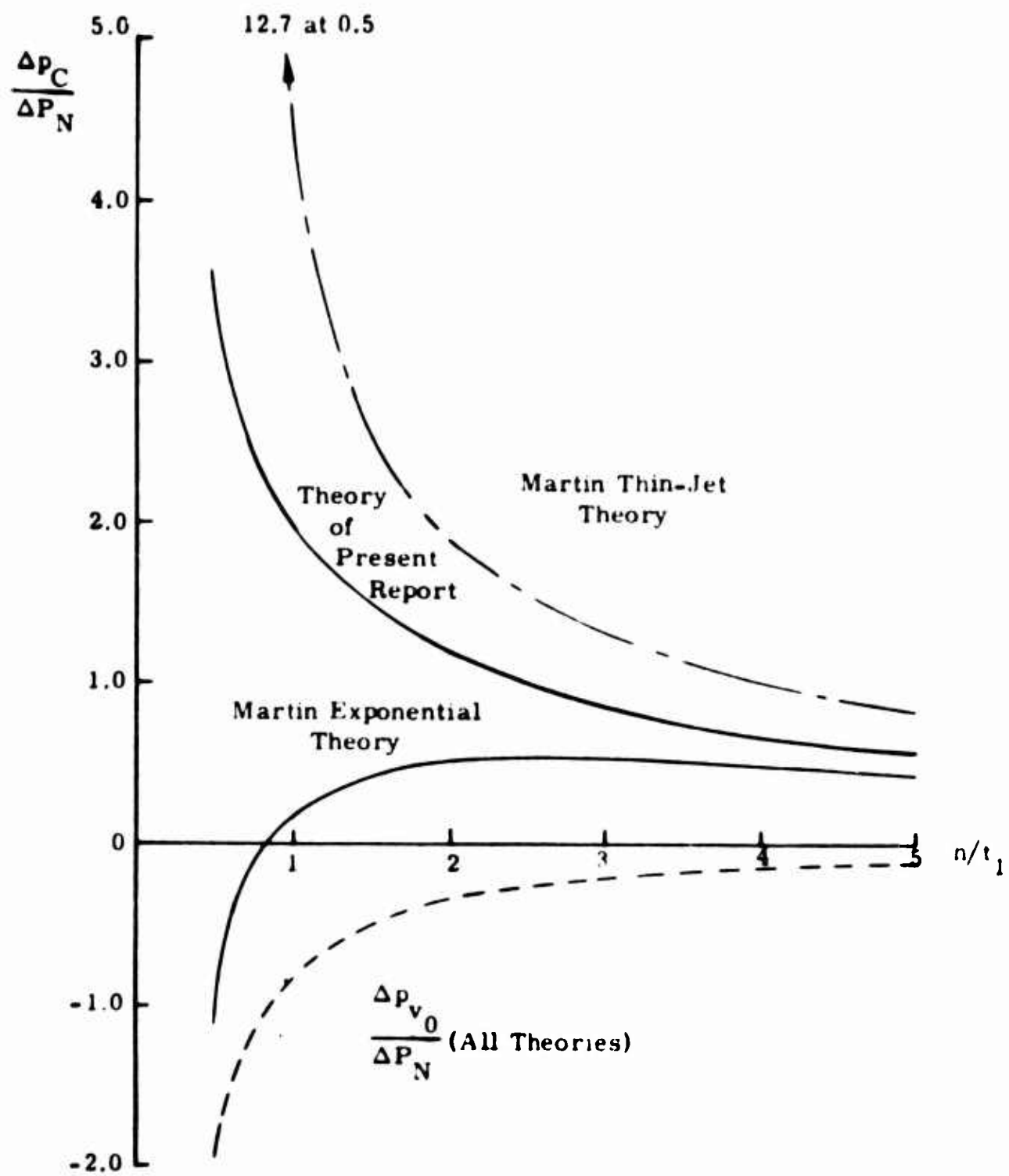


Figure 98. Cushion Pressure for Example Case

dangerous, in that it has masked the urgency of the need to find (and rectify) the true cause of negative cushion stiffness and the large energy losses associated with it.

The second error in the revised Martin theory was much less serious, in that it resulted only in an underestimate of the cushion pressure (vehicle base pressure). If the layered jet theory is to be applied to the reentrant jet, then the jet thickness (t) in the exponential parameter,

$$\chi = \frac{t}{h} (1 + \sin \theta), \quad (83)$$

must be the actual jet thickness in the reentrant region and not its thickness at the exit nozzle. Because of the higher static pressure in region C, the jet thickness will obviously be greater than at the exit nozzle because of its lower velocity, and hence the parameter (χ) will be larger. When the Martin exponential theory is corrected for this, it predicts larger cushion pressures in the middle height range, as indeed occurs experimentally.

3. Influence of the Cavity Region

The Martin theory assumed zero flow in the cavity region, so that within it, the static pressure is everywhere the same. In practice this condition could be realized only by placing a flexible, vented diaphragm in this region, which would physically separate the jet and cavity-zone flows. However, cavity vorticity can be neglected also if the cavity vortex is cylindrical and experiences no serious pressure losses due to diffusion, since in this case the static pressure at the jet/vortex interface is also constant, although, of course, larger than the value at the center of the region. In this case the vortex can be regarded as a sort of aerodynamic roller bearing.

Unfortunately, the present cavity zone configurations are of such a shape that very large losses can occur; and since the basic momentum flux of the cavity vortex is comparable with that of the jet, this obviously results in low pressure recovery ratios. The work so far is primarily concerned with a description of cushion cavity pressures. It should be noted, however, that, based on present theory, energy loss in the recirculating jet can be reduced by increasing jet thickness at the expense of the cavity zone volume, irrespective of how adverse is the cavity zone profile.

The most probable "worst case" from the point of view of cavity vortex flow on cushion pressure generation is given by

$$\begin{aligned}v_1 &= 0 \\v_2 &= v_{S_2}\end{aligned}$$

in Figure 99. This implies that the vortex flow has negligible energy when it encounters the exiting jet, due to diffusion losses, but has been accelerated to the jet speed by the time zone C is reached. As shown in Figure 100, this assumption results in a substantial reduction in calculated cushion pressure.

Apart from the relatively minor task of using layered theory to describe cushion and cavity pressures, it would seem that, so far as the external-flow field is concerned, the most important problem is the flow in the cavity zone. This problem is rendered complex by the magnitude of the losses involved, if the losses were restricted to friction and mixing losses alone, it would be relatively simple. Moreover, a detailed analysis of a high-loss system is of doubtful utility, because our major concern is to develop a cavity-zone geometry which will cause only small energy losses.

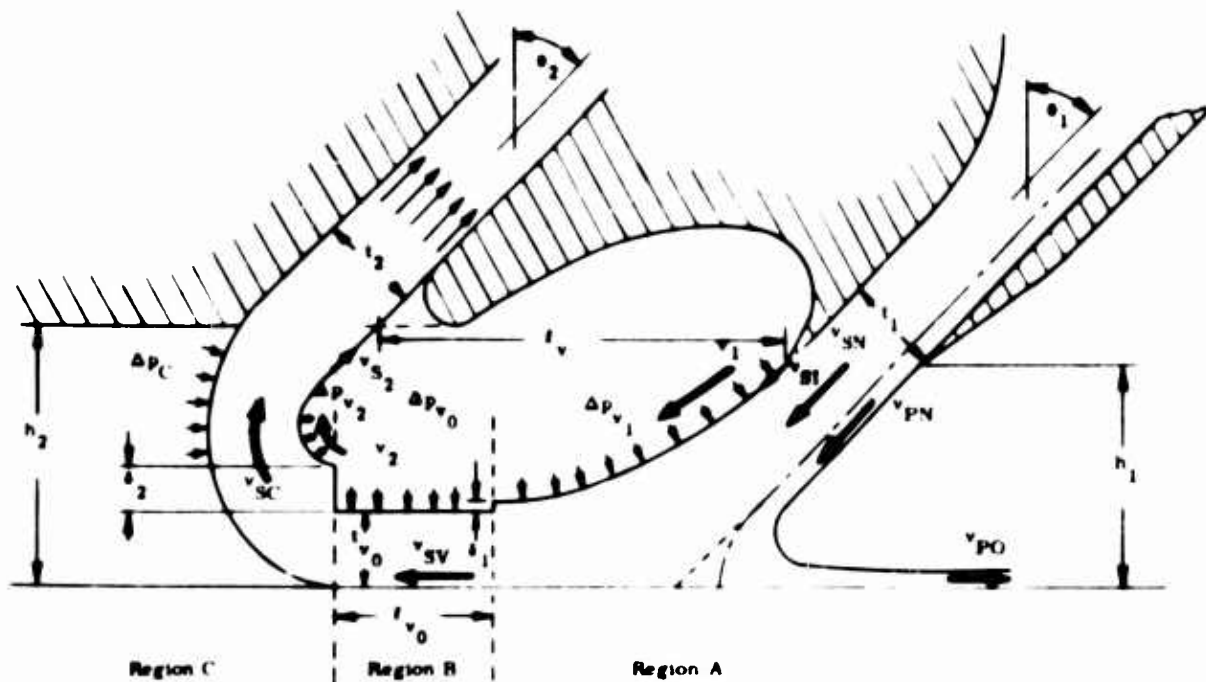


Figure 99. Definition of Velocities

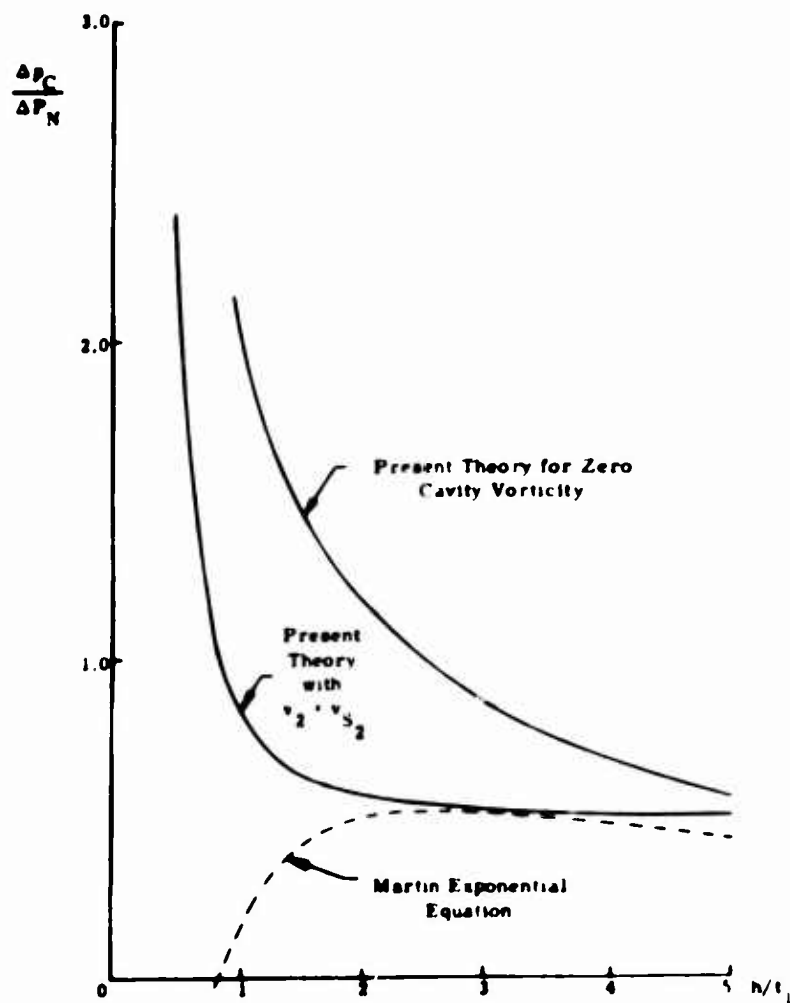


Figure 100. Effect of Cavity Vorticity upon Cushion

4. Free Air Entrainment Losses

In contrast to the 100-percent recirculation case, free air entrainment is relatively unimportant for partial recirculation, because that portion of the jet with which it mixes is in any case exhausted to ambient. Losses due to vortex generation in the cushion region are also likely to be much less than the (already small) losses which occur with an annular jet, because of the lower velocity of the reentrant jet.

5. Jet Diffusion Losses

With one fixed and one free boundary, the recirculating jet experiences a static pressure rise as it passes from zone B to zone C in Figure 97. It is felt that this can be achieved with negligible energy loss because of the free boundary at the jet/cavity vortex interface, but this assumption needs to be examined experimentally, as a matter of high priority.

6. Cavity Zone Pressure

Unless the mass augmentation is quite small, the cavity zone static pressure will usually be negative (Figure 101), a condition which will result in an adverse effect on overall performance in many practical configurations. Cavity pressure can be increased by increasing θ_1 , the angle at which the existing jet is pointed inwards from the vertical, as shown in Figure 102. We assume that the inner boundaries of the jet in regions A and C (Figure 103) approximate to circular arcs, so that the static pressure for solid rotations is

$$\Delta P_N = \Delta p_{v_0} + \frac{1}{2} \rho v_N^2 \quad (84)$$

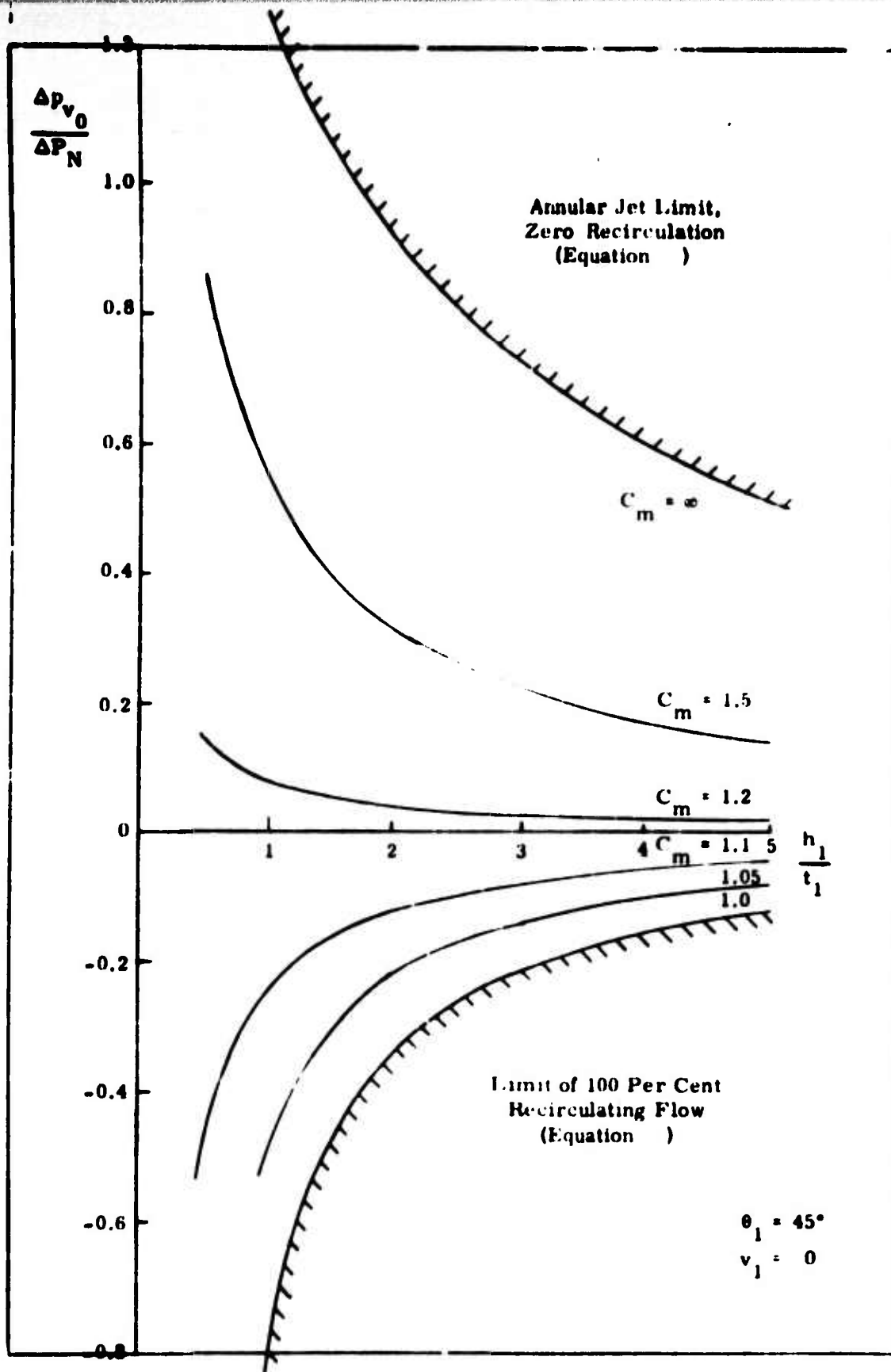


Figure 101. Variation of Cavity Pressure with h_1/t_1

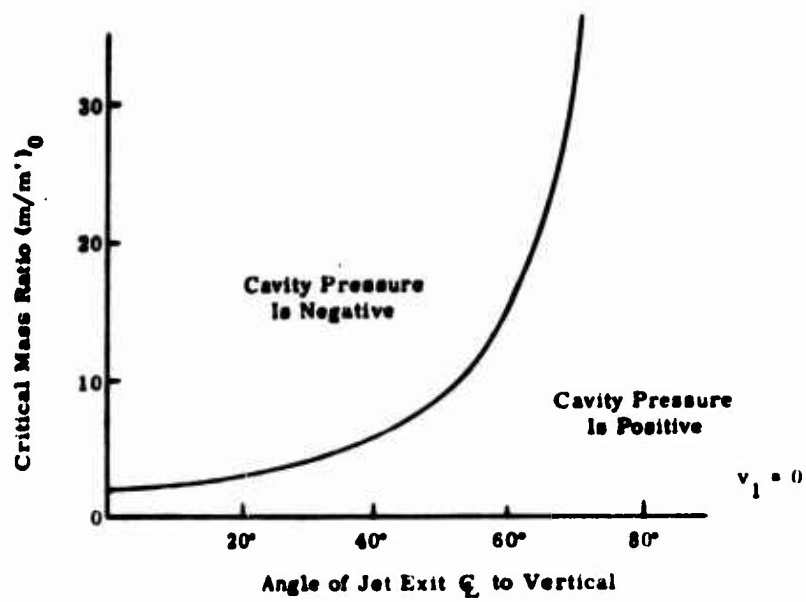


Figure 102. Critical Mass Ratio for Zero Cavity Pressure

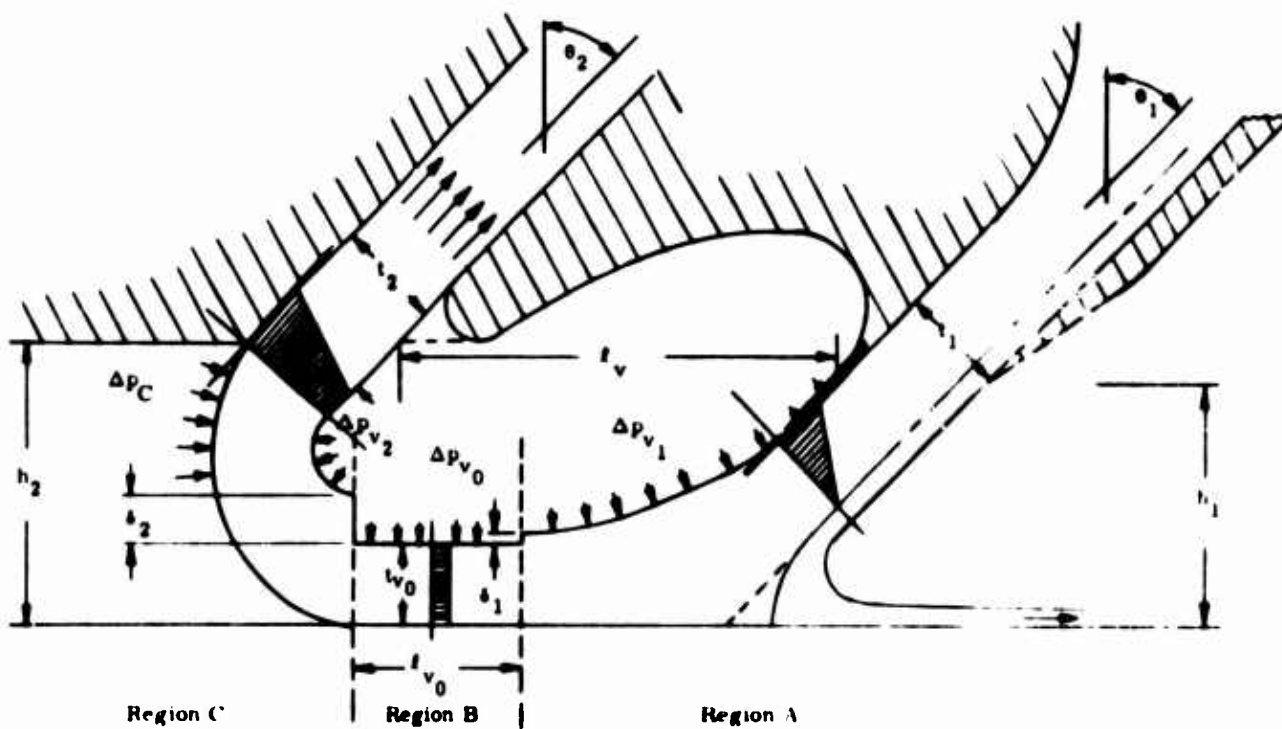


Figure 103. Assumed Static Pressure Distribution... for Thin Jet Analysis

and v_N is the mean effective peripheral velocity of the vortex, integrated throughout the region of interest.

7. Basic Momentum Equations

Region A: Equating horizontal momentum flux and pressure forces across the jet in region A of Figure 97, and utilizing Equation (84) to define p_{v_1} , one finds that

$$\begin{aligned} & (\Delta p_{v_0} + \frac{1}{2} \rho v_1^2) (h - t_{v_0} - \delta_1) + \Delta p_{v_0} (t_{v_0} + \delta_1) \\ & = J_{PO} + J_{PN} \sin \theta_1 - J_{SN} (1 - \sin \theta_1). \end{aligned}$$

Therefore,

$$\begin{aligned} \Delta p_{v_0} h_1 & = J_{PO} + J_{PN} \sin \theta_1 - J_{SN} (1 - \sin \theta_1) \\ & \quad - \frac{1}{2} \rho v_1^2 (h_1 - t_{v_0} - \delta_1). \end{aligned} \tag{85}$$

For the thin-jet theory,

$$t_{v_0} + \delta_1 = t_1$$

$$J_{PO} = J_{PN} = J_P.$$

Also,

$$J_P = \dot{m}_p v_p$$

$$J_{SN} = \dot{m}_s v_{SN}.$$

Therefore,

$$J_P = J_{SN} \left(\frac{\dot{m}_p}{\dot{m}_s} \right) \left(\frac{v_p}{v_{SN}} \right) = \phi J_{SN} \tag{86}$$

where

$$\phi = \left(\frac{\dot{m}_p}{\dot{m}_s} \right) \cdot \frac{v_p}{v_{SN}} \quad (87)$$

When these substitutions are made, Equation (85) becomes

$$\begin{aligned} \Delta p_{v_0} &= \frac{J_{SN}}{h_1} \left[\phi (1 + \sin \theta_1) - (1 - \sin \theta_1) \right] \\ &\quad - \frac{1}{2} \rho v_1^2 \left(1 - \frac{t_1}{h_1} \right). \end{aligned} \quad (88)$$

In evaluating ϕ , the mass ratio \dot{m}_p/\dot{m}_s is known, but not the velocity ratio v_p/v_{SN} unless we make a specific assumption with regard to the total head distribution across the jet nozzle. The total momentum flux at the exit is

$$J_N = J_{SN} + J_{PN} = J_{SN} (1 + \phi). \quad (89)$$

Region C: Equating momentum flux and pressure forces across the reentrant jet,

$$\begin{aligned} &\left(\Delta p_C - \Delta p_{v_0} - \frac{1}{2} \rho v_2^2 \right) (h_2 - t_{v_0} - \delta_2) \\ &+ (\Delta p_C - \Delta p_{v_0}) (t_{v_0} + \delta_2) = J_{SC} (1 + \sin \theta_2). \end{aligned}$$

Therefore,

$$\Delta p_C h_2 = J_{SC} (1 + \sin \theta_2) + \Delta p_{v_0} h_2 + \frac{1}{2} \rho v_2^2 (h_2 - t_{v_0} - \delta_2). \quad (90)$$

The re-entrant jet thickness is given by conservation of mass flow, that is,

$$v_{SC} (t_{v_0} + \delta_2) \rho = \dot{m}_s. \quad (91)$$

Therefore,

$$\Delta p_C = \frac{J_{SC}}{h_2} (1 + \sin \theta_2) + \Delta p_{v_0} + \frac{1}{2} \rho v_2^2 \left(1 - \frac{\dot{m}_s}{\rho v_{SC} h_2} \right). \quad (92)$$

The momentum flux J_{SC} can be related to the nozzle momentum flux by the local mean velocities, since

$$J_{SC} = \dot{m}_s v_{SC}, \text{ and, } J_{SH} = \dot{m}_s v_{SN}$$

$$\frac{J_{SC}}{J_{SN}} = \frac{v_{SC}}{v_{SN}}.$$

Therefore,

$$\begin{aligned} \Delta p_C &= \frac{J_{SN}}{h_2} \left(\frac{v_{SC}}{v_{SN}} \right) (1 + \sin \theta_2) + \Delta p_{v_0} \\ &+ \frac{1}{2} \rho v_2^2 \left[1 - \left(\frac{v_{SN}}{v_{SC}} \right) \frac{\dot{m}_s}{\rho v_{SN} h_2} \right]. \end{aligned} \quad (93)$$

8. Calculation of Mean Velocities for Uniform Total Head Distribution

In a practical system, the total head is by no means uniform across the jet, but this simplifying assumption is of value in yielding simple results from thin jet theory. Unless the more accurate layered-jet theory is used, there is little point in employing a more precise description of the total head variation.

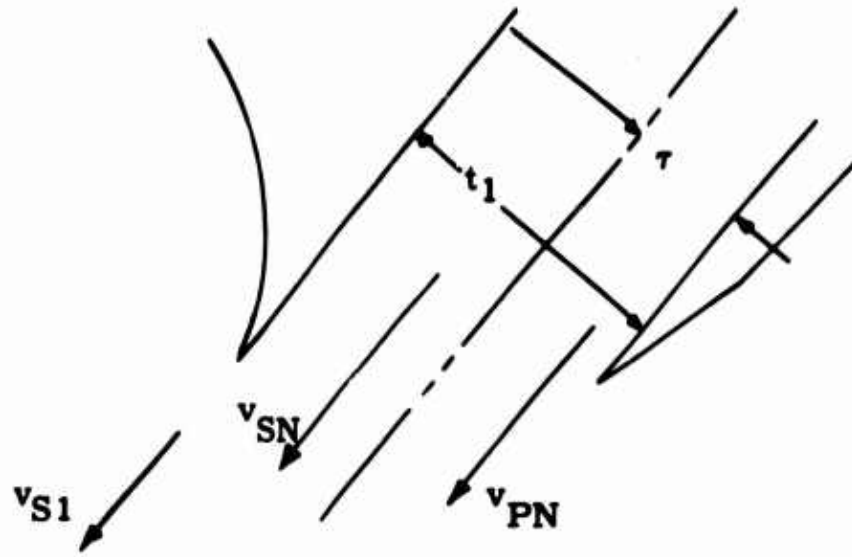


Figure 104. Nozzle Exit Velocities

By definition,

$$\left. \begin{aligned} \dot{m}_s &= \rho v_{SN} (t_1 - \tau) \\ \dot{m}_p &= \rho v_{PN} \tau \end{aligned} \right\} . \quad (94)$$

Now

$$\Delta P_N = \frac{1}{2} \rho v_{PN}^2 ,$$

so that

$$v_{PN} = \sqrt{\frac{2}{\rho} \Delta P_N} . \quad (95)$$

Also,

$$\Delta P_N = \frac{1}{2} (\Delta p_{v_0}) + \frac{1}{2} \rho v_1^2 + \frac{1}{2} \rho v_{SN}^2 .$$

Therefore,

$$v_{SN} = \sqrt{\frac{2}{\rho} \Delta P_N - \frac{\Delta p_{v_0}}{\rho} - \frac{1}{2} v_1^2}. \quad (96)$$

The velocity (v_{SI}) at the inner face of the jet is given by

$$\Delta P_N = \Delta p_{v_0} + \frac{1}{2} \rho v_1^2 + \frac{1}{2} \rho v_{SI}^2.$$

Hence,

$$v_{SI} = \sqrt{\frac{2}{\rho} (\Delta P_N - \Delta p_{v_0}) - v_1^2}. \quad (97)$$

By the time the jet has reached region B, it has suffered a total pressure loss which we define as

$$(1 - \eta_1) \frac{1}{2} \rho v_{SN}^2. \quad (98)$$

Thus from Bernoulli,

$$\frac{1}{2} (\Delta p_{v_0} + \frac{1}{2} \rho v_1^2) + \eta_1 \frac{1}{2} \rho v_{SN}^2 = \Delta p_{v_0} + \frac{1}{2} \rho v_{S_v}^2.$$

Therefore,

$$v_{S_v} = \sqrt{\eta_1 v_{SN}^2 + \frac{1}{2} v_1^2 - \frac{\Delta p_{v_0}}{\rho}}. \quad (99)$$

Reentrant Velocities:

By the time it has reached region C, the jet total pressure loss is

$$(1 - \eta_2) \frac{1}{2} \rho v_{SN}^2. \quad (100)$$

Thus

$$\frac{1}{2} \left(\Delta p_{v_0} + \frac{1}{2} \rho v_1^2 \right) + \eta_2 \frac{1}{2} \rho v_{SN}^2 = \frac{1}{2} \left(\Delta p_{v_0} + \Delta p_C + \frac{1}{2} \rho v_2^2 \right) + \frac{1}{2} \rho v_{SC}^2$$

and

$$v_{SC} = \sqrt{\eta_2 v_{SN}^2 - \frac{\Delta p_C}{\rho} + \frac{1}{2} (v_1^2 - v_2^2)}$$

or

$$\frac{v_{SC}}{v_{SN}} = \sqrt{\eta_2 - \frac{\Delta p_C}{\rho v_{SN}^2} + \frac{1}{2} \left[\left(\frac{v_1}{v_{SN}} \right)^2 - \left(\frac{v_2}{v_{SN}} \right)^2 \right]}$$

(101)

The velocity at the inner boundary of the jet is given by

$$\frac{1}{2} \left(\Delta p_{v_0} + \frac{1}{2} \rho v_1^2 \right) + \eta_2 \frac{1}{2} \rho v_{SN}^2 = \Delta p_{v_0} + \frac{1}{2} \rho v_2^2 + \frac{1}{2} \rho v_{S_2}^2$$

or

$$v_{S_2} = \sqrt{\eta_2 v_{SN}^2 - \frac{\Delta p_{v_0}}{\rho} + \left(\frac{1}{2} v_1^2 - v_2^2 \right)}$$

(102)

9. Relationship between Momentum Flux and Total Pressure

$$J_{SN} = \dot{m}_s v_{SN}$$

(103)

$$= \rho v_{SN}^2 (t_1 - \tau), \quad \text{from Equation (94)}$$

Also,

$$\frac{\dot{m}_s}{\dot{m}_p} = \frac{v_{SN}}{v_{PN}} \left(\frac{t_1}{\tau} - 1 \right).$$

Therefore,

$$\begin{aligned} \frac{t_1}{\tau} &= \left(\frac{\dot{m}_s}{\dot{m}_p} \right) \left(\frac{v_{PN}}{v_{SN}} \right) + 1 \\ J_{SN} &= \rho v_{SN}^2 t_1 \left[1 - \frac{1}{\left(\frac{\dot{m}_s}{\dot{m}_p} \right) \left(\frac{v_{PN}}{v_{SN}} \right) + 1} \right] \\ J_{SN} &= \rho v_{SN}^2 t_1 \left\{ \frac{\left(\frac{\dot{m}_s}{\dot{m}_p} \right) \left(\frac{v_{PN}}{v_{SN}} \right)}{\left[1 + \left(\frac{\dot{m}_s}{\dot{m}_p} \right) \left(\frac{v_{PN}}{v_{SN}} \right) \right]} \right\}. \end{aligned} \quad (104)$$

From Equation (94)

$$J_P = \left(\frac{\dot{m}_p}{\dot{m}_s} \right) \left(\frac{v_p}{v_s} \right) J_{SN} = \frac{\rho v_p^2 t_1}{\left[1 + \left(\frac{\dot{m}_s}{\dot{m}_p} \right) \left(\frac{v_p}{v_{SN}} \right) \right]} \quad (105)$$

Substituting Equation (95) for v_p ,

$$J_P = \frac{2 \Delta P_N t_1}{\left[1 + \left(\frac{\dot{m}_s}{\dot{m}_p} \right) \left(\frac{v_p}{v_{SN}} \right) \right]}. \quad (106)$$

10. Calculation of Cavity Pressure

From Equations (88) and (104),

$$\Delta p_{v_0} = \frac{\rho v_{SN}^2 \left(\frac{\dot{m}_s}{\dot{m}_p} \right) \left(\frac{v_p}{v_{SN}} \right) \left(\frac{t_1}{h_1} \right)}{\left[1 + \left(\frac{\dot{m}_s}{\dot{m}_p} \right) \left(\frac{v_p}{v_{SN}} \right) \right]} \left\{ \phi (1 + \sin \theta_1) - (1 - \sin \theta_1) \right. \\ \left. - \frac{1}{2} \rho v_1^2 \left[1 - \left(\frac{t_1}{h_1} \right) \right] \right\}.$$

Substituting Equation (96) for v_{SN} ,

$$\frac{\Delta p_{v_0}}{\Delta P_N} = \frac{\left(\frac{t_1}{h_1} \right) \left[2 - \frac{\Delta p_{v_0}}{\Delta P_N} - \frac{\frac{1}{2} \rho v_1^2}{\Delta P_N} \right] \left\{ \left[\left(\frac{\dot{m}_p}{\dot{m}_s} \right) \left(\frac{v_p}{v_{SN}} \right) (1 + \sin \theta_1) - (1 - \sin \theta_1) \right] \right.}{\left[1 + \frac{\dot{m}_p v_{SN}}{\dot{m}_s v_p} \right]} \\ \left. - \frac{\frac{1}{2} \rho v_1^2}{\Delta P_N} \left(1 - \frac{t_1}{h_1} \right) \right\}}. \quad (107)$$

Writing $\dot{m}_s = 0$, $v_p = v_{SN}$ and $v_1 = 0$, the above equation reduces to the familiar form,

$$\frac{\Delta p_{v_0}}{\Delta P_N} = \left[2 - \frac{\Delta p_{v_0}}{\Delta P_N} \right] \frac{t_1}{h_1} (1 + \sin \theta_1) \\ = 2 x_1 - x_1 \frac{\Delta p_{v_0}}{\Delta P_N}$$

or,

$$\frac{\Delta p_{v_0}}{\Delta P_N} = \frac{2 \chi_1}{1 + \chi_1} \quad (108)$$

which is the well-known thin jet solution for an annular jet.

Reverting to Equation (106),

$$\begin{aligned} \frac{\Delta p_{v_0}}{\Delta P_N} & \left\{ 1 + \frac{\left(\frac{t_1}{h_1} \right) \left[\left(\frac{\dot{m}_p}{\dot{m}_s} \right) \left(\frac{v_p}{v_{SN}} \right) (1 + \sin \theta_1) - (1 - \sin \theta_1) \right]}{\left[1 + \left(\frac{\dot{m}_p}{\dot{m}_s} \right) \left(\frac{v_{SN}}{v_p} \right) \right]} \right\} \\ & = \frac{\left(\frac{t_1}{h_1} \right) \left[\left(\frac{\dot{m}_p}{\dot{m}_s} \right) \left(\frac{v_p}{v_{SN}} \right) (1 + \sin \theta_1) - (1 - \sin \theta_1) \right]}{\left[1 + \left(\frac{\dot{m}_p}{\dot{m}_s} \right) \left(\frac{v_{SN}}{v_p} \right) \right]} \left\{ \left[2 - \frac{\frac{1}{2} \rho v_1^2}{\Delta P_N} \right] \right. \\ & \quad \left. - \frac{\frac{1}{2} \rho v_1^2}{\Delta P_N} \left(1 - \frac{t_1}{h_1} \right) \right\} . \end{aligned} \quad (109)$$

Solution for $v_p = v_{SN}$.

Since Δp_{v_0} is generally small, a logical simplification is to write

$$v_p / v_{SN} = 1.0.$$

Defining also

$$\chi_1 = \frac{\frac{1}{2} \rho v_1^2}{\Delta P_N}$$

$$C_m = 1 + \frac{\dot{m}_p}{\dot{m}_s} = \frac{\dot{m}_s + \dot{m}_p}{\dot{m}_s}$$

$$\begin{aligned} \frac{\Delta p_{v_0}}{\Delta P_N} &= \frac{\frac{1}{C_m} \left(\frac{t_1}{h_1} \right) \left[(C_m - 1) (1 + \sin \theta_1) - (1 - \sin \theta_1) \right] (2 - v_1^*) - v_1^* \left(1 - \frac{t_1}{h_1} \right)}{\frac{1}{C_m} \left\{ C_m + \left(\frac{t_1}{h_1} \right) \left[(C_m - 1) (1 + \sin \theta_1) - (1 - \sin \theta_1) \right] \right\}} \\ &= \frac{2 \left(\frac{t_1}{h_1} \right) \left[(C_m - 1) (1 + \sin \theta_1) - (1 - \sin \theta_1) \right]}{C_m + \left(\frac{t_1}{h_1} \right) \left[(C_m - 1) (1 + \sin \theta_1) - (1 - \sin \theta_1) \right]} \\ &\quad - \frac{v_1^* \left\{ \left(\frac{t_1}{h_1} \right) \left[(C_m - 1) (1 + \sin \theta_1) - (1 - \sin \theta_1) \right] + C_m \left(1 - \frac{t_1}{h_1} \right) \right\}}{C_m + \left(\frac{t_1}{h_1} \right) \left[(C_m - 1) (1 + \sin \theta_1) - (1 - \sin \theta_1) \right]} \quad (110) \end{aligned}$$

when $\dot{m}_s = 0$, $1/C_m = 0$, and this equation has the limit

$$\begin{aligned} \frac{\Delta p_{v_0}}{\Delta P_N} \bigg|_{\dot{m}_s \rightarrow 0} &\rightarrow \frac{2 \left(\frac{t_1}{h_1} \right) (1 + \sin \theta_1) - v_1^* \left[\left(\frac{t_1}{h_1} \right) (1 + \sin \theta_1) - (1 - \sin \theta_1) \right]}{1 - \left(\frac{t_1}{h_1} \right) (1 - \sin \theta_1)} \\ &\rightarrow \left(\frac{2\chi_1}{1 - \chi_1} \right) - \frac{v_1^* \left[\chi_1 + \left(1 - \frac{t_1}{h_1} \right) \right]}{(1 + \chi_1)} \quad (111) \end{aligned}$$

which of course reduces to Equation (108) when $\dot{v}_1^* = 0$. When $\dot{m}_p = 0$, $C_m = 1.0$, and Equation (110) has the limit,

$$\left. \frac{\Delta p_{v_0}}{\Delta P_N} \right|_{\dot{m}_p \rightarrow 0} \rightarrow \frac{-2 \left(\frac{t_1}{h_1} \right) (1 - \sin \theta) - \dot{v}_1^* \left[\left(1 - \frac{t_1}{h} \right) - \left(\frac{t_1}{h} \right) (1 - \sin \theta_1) \right]}{1 - \left(\frac{t_1}{h_1} \right) (1 - \sin \theta_1)} \quad (112)$$

Equation (112) is the same as Equation E. 11 of Reference 16 when $\dot{v}_1^* = 0$.

Equations (111)-(112) are plotted in Figure 101 for an example case, assuming no rotation in the cavity vortex in region A. The mass ratio coefficient C_m is plotted, as a function of mass ratio m/m' , in Figure 105, and a relatively large amount of primary air is seen to be required for $\Delta p_{v_0} > 0$.

Critical Mass Ratio for $\Delta p_{v_0} = 0$.

It is obvious from Equation (110) that $\Delta p_{v_0} = 0$, ($\dot{v}_1 = 0$)

when

$$(C_m - 1) (1 + \sin \theta_1) = (1 - \sin \theta_1)$$

or

$$\left[C_m \right]_0 = \frac{(1 - \sin \theta_1)}{(1 + \sin \theta_1)} + 1 = f(\theta_1). \quad (113)$$

In terms of the mass ratio,

$$\left[C_m \right]_0 = \frac{\left(\frac{m}{m'} \right)_0}{\left[\left(\frac{m}{m'} \right)_0 - 1 \right]} = f(\theta_1). \quad (114)$$

Therefore,

$$\left(\frac{m}{m'}\right)_0 = \frac{f(\theta_1)}{[f(\theta_1) - 1]} \quad (115)$$

This relationship is plotted in Figure 102. Obviously, if a positive cavity pressure is required, it will pay to make the jet angle θ_1 as large as possible.

11. Calculation of Cushion Pressure

From Equations (93) and (104),

$$\begin{aligned} \Delta p_C = \Delta p_{v_0} + 1/2 \rho v_2^2 & \left[1 - \left(\frac{v_{SN}}{v_{SC}} \right) \frac{\dot{m}_s}{\rho v_{SN} h_2} \right] \\ & + \rho v_{SN}^2 \left(\frac{\dot{m}_s}{\dot{m}_p} \right) \left(\frac{v_p}{v_{SN}} \right) \left(\frac{t_1}{h_2} \right) \left(\frac{v_{SC}}{v_{SN}} \right) (1 + \sin \theta_2) \\ & \left[1 + \left(\frac{\dot{m}_s}{\dot{m}_p} \right) \left(\frac{v_p}{v_{SN}} \right) \right] \end{aligned} \quad (116)$$

$$\text{Now, } \dot{m}_s = \rho v_{SN} t_1 \left(1 - \frac{\tau}{t_1} \right) \text{ and } \frac{\tau}{t_1} = \frac{1}{1 + \left(\frac{\dot{m}_s}{\dot{m}_p} \right) \left(\frac{v_p}{v_{SN}} \right)};$$

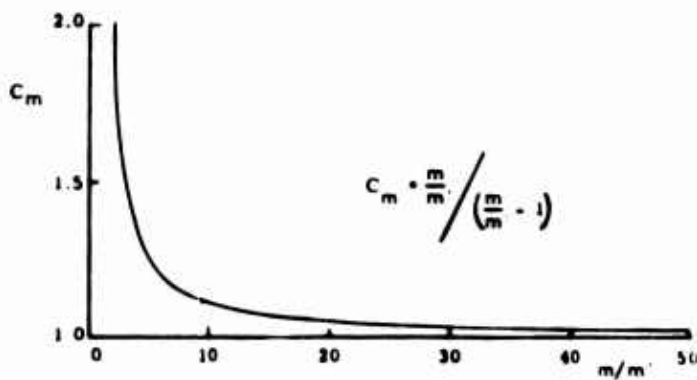


Figure 105. Variation of Mass Ratio Coefficient C_m with Mass Ratio m/m'

therefore,

$$\frac{\dot{m}_s}{\rho v_{SN} h_2} = \frac{\left(\frac{t_1}{h_2}\right) \left(\frac{\dot{m}_s}{\dot{m}_p}\right) \left(\frac{v_p}{v_{SN}}\right)}{\left[1 + \left(\frac{\dot{m}_s}{\dot{m}_p}\right) \left(\frac{v_p}{v_{SN}}\right)\right]}$$

and

$$\frac{1}{2} \rho v_2^2 \left[1 - \frac{v_{SN}}{v_{SC}} \frac{\dot{m}_s}{\rho v_{SN} h_2}\right] = \frac{1}{2} \rho v_2^2 \frac{\left[1 + \left(\frac{\dot{m}_s}{\dot{m}_p}\right) \left(\frac{v_p}{v_{SN}}\right) \left(1 - \frac{t_1}{h_2}\right)\right]}{\left[1 + \left(\frac{\dot{m}_s}{\dot{m}_p}\right) \left(\frac{v_p}{v_{SN}}\right)\right]}$$

Substituting the result of Equation (96) and Equation (116) for

$$\begin{aligned} \frac{\Delta p_C}{\Delta P_N} - \frac{\Delta p_{v_0}}{\Delta P_N} &= \frac{\left(\frac{t_1}{h}\right) \left(\frac{v_{SC}}{v_{SN}}\right) (1 + \sin \theta_2) \left[2 - \frac{\Delta p_{v_0}}{\Delta P_N} - \frac{\frac{1}{2} \rho v_1^2}{\Delta P_N}\right]}{\left[1 + \left(\frac{\dot{m}_p}{\dot{m}_s}\right) \left(\frac{v_{SN}}{v_p}\right)\right]} \\ &+ \frac{\frac{1}{2} \rho v_2^2 \left[1 + \left(\frac{\dot{m}_s}{\dot{m}_p}\right) \left(\frac{v_p}{v_{SN}}\right) \left(1 - \frac{t_1}{h}\right)\right]}{\left[1 + \left(\frac{\dot{m}_p}{\dot{m}_s}\right) \left(\frac{v_{SN}}{v_p}\right)\right]} \end{aligned} \quad (117)$$

where from Equation (101)

$$v_{SC} = \sqrt{\eta_2 \left[\frac{2}{\rho} \Delta P_N - \frac{\Delta p_{v0}}{\rho} - \frac{1}{2} v_1^2 \right] - \frac{\Delta p_C}{\rho} + \frac{1}{2} (v_1^2 - v_2^2)}$$

and

$$\frac{v_{SC}}{v_{SN}} = \sqrt{\frac{\eta_2 \left[2 - \frac{\Delta p_{v0}}{\Delta P_N} - \frac{\frac{1}{2} \rho v_1^2}{\Delta P_N} - \frac{\Delta p_C}{\Delta P_N} + \frac{\frac{1}{2} \rho v_1^2}{\Delta P_N} - \frac{\frac{1}{2} \rho v_2^2}{\Delta P_N} \right]}{\left[2 - \frac{\Delta p_{v0}}{\Delta P_N} - \frac{\frac{1}{2} \rho v_1^2}{\Delta P_N} \right]}} \quad (118)$$

Solution for $v_1 = v_2 = 0$, $v_p = v_{SN}$.

This simplification is obviously desirable, mathematically speaking, because of the complexity of Equation (117) when (118) is substituted.

It now becomes

$$\frac{\Delta p_C}{\Delta P_N} - \frac{\Delta p_{v0}}{\Delta P_N} = \frac{1}{C_m} \left(\frac{t_1}{h_1} \right) (1 + \sin \theta_2) \left[2 - \frac{\Delta p_{v0}}{\Delta P_N} \right] \sqrt{\frac{\eta_2 \left(\frac{\Delta p_{v0}}{\Delta P_N} \right) \cdot \eta_2 \left(\frac{\Delta p_C}{\Delta P_N} \right)}{\left(2 - \frac{\Delta p_{v0}}{\Delta P_N} \right)}}$$

If both sides are squared and if $x_2 = \frac{t_1}{h} (1 + \sin \theta_2)$,

$$\begin{aligned} & \left(\frac{\Delta p_C}{\Delta P_N} \right)^2 - 2 \left(\frac{\Delta p_C}{\Delta P_N} \right) \left(\frac{\Delta p_{v0}}{\Delta P_N} \right) + \left(\frac{\Delta p_{v0}}{\Delta P_N} \right)^2 \\ &= \left(\frac{x_2}{C_m} \right)^2 \left[2 - \frac{\Delta p_{v0}}{\Delta P_N} \right] \left[\eta_2 \left(2 - \frac{\Delta p_{v0}}{\Delta P_N} \right) - \eta \frac{\Delta p_C}{\Delta P_N} \right] \end{aligned}$$

Collecting terms,

$$\begin{aligned} & \left(\frac{\Delta p_C}{\Delta P_N} \right)^2 + \left\{ \left(\frac{\chi_2}{C_m} \right)^2 \left[2 - \frac{\Delta p_{v0}}{\Delta P_N} \right] - 2 \frac{\Delta p_{v0}}{\Delta P_N} \right\} \left(\frac{\Delta p_C}{\Delta P_N} \right) \\ & + \left\{ \left(\frac{\Delta p_{v0}}{\Delta P_N} \right)^2 - \left(\frac{\chi_2}{C_m} \right)^2 \eta_2 \left[2 - \frac{\Delta p_{v0}}{\Delta P_N} \right]^2 \right\} = 0 \end{aligned} \quad (119)$$

for the limit case $\dot{m}_p = 0$.

In the limit $C_m \rightarrow \infty$,

$$\left(\frac{\Delta p_C}{\Delta P_N} \right)^2 - 2 \left(\frac{\Delta p_{v0}}{\Delta P_N} \right) \left(\frac{\Delta p_C}{\Delta P_N} \right) + \left(\frac{\Delta p_{v0}}{\Delta P_N} \right)^2 = 0$$

so that $\Delta p_C = \Delta p_{v0}$, as we should expect.

Equation (119) is plotted in Figure 98 and compared with the theory of Reference 1, for the Reference 1 case of no cavity vortex rotation and no total pressure loss throughout the jet.

12. Effect of Cavity Vortex Rotation

Rather than attempt to solve Equations (117) and (118) explicitly for the case $v_2 \neq 0$, we calculate Δp_C by replacing $\Delta p_{v0}/\Delta P_N$ in Equation (119) by an equivalent value $\Delta p_{v0'}/\Delta P_N$.

From Equation (84) the pressure rise will be

$$\delta p_2 = \frac{1}{2} \rho v_2^2. \quad (120)$$

The maximum value for v_2 will be given by Equation (102). For $v_1 = 0$, which is the worst case,

$$v_{S_2} = \sqrt{\eta_2 v_{SN}^2 - \frac{\Delta p_{v_0}}{\rho} - v_2^2}$$

$$v_{S_2} = \sqrt{\eta_2 \frac{2}{\rho} \Delta P_N - \frac{\Delta p_{v_0}}{\rho} (1 + \eta_2) - v_2^2} .$$

Therefore,

$$\frac{\frac{1}{2} \rho v_{S_2}^2}{\Delta P_N} = \eta_2 - \left[\frac{\Delta p_{v_0}}{\Delta P_N} \right] \left[\frac{(1 + \eta_2)}{2} \right] - \frac{\frac{1}{2} \rho v_2^2}{\Delta P_N} . \quad (121)$$

Defining,

$$\frac{v_2}{v_{S_2}} = \psi$$

$$\frac{\frac{1}{2} \rho v_2^2}{\Delta P_N} \left[1 + \frac{1}{\psi} \right] = \eta_2 \left[\frac{\Delta p_{v_0}}{\Delta P_N} \right] \left[\frac{(1 + \eta_2)}{2} \right] \quad (122)$$

and

$$\frac{\delta p_2}{\Delta P_N} = \frac{\eta_2 \left[\frac{\Delta p_{v_0}}{\Delta P_N} \right] \left[\frac{(1 + \eta_2)}{2} \right]}{\left[1 + \frac{1}{\psi^2} \right]} . \quad (123)$$

The effective value of $\Delta p_{v_0} / \Delta P_N$, which replaces $\Delta p_{v_0} / \Delta P_N$ in Equation (119) is then

$$\begin{aligned}
\frac{\Delta p_{v'0}}{\Delta P_N} &= \frac{\Delta p_{v0}}{\Delta P_N} + \frac{\delta p_2}{\Delta P_N} \\
&= \frac{\psi^2 \eta_2}{[1 + \psi^2]} + \left(\frac{\Delta p_{v0}}{\Delta P_N} \right) \frac{\left[1 + \psi^2 - \frac{(1 + \eta_2)}{2} \psi^2 \right]}{[1 + \psi^2]}.
\end{aligned} \tag{124}$$

For the special case of $\eta_2 = 1.0$, $\psi = 1.0$, this becomes

$$\left[\frac{\Delta p_{v0}}{\Delta P_N} \right]_* = \frac{1}{2} \left(1 + \frac{\Delta p_{v0}}{\Delta P_N} \right). \tag{125}$$

This special case is plotted in Figure 100.

PRESSURE RECOVERY IN A RECIRCULATING JET

Experimental studies of recirculation systems have indicated substantial pressure drops in the jet, after the jet air has left the exit nozzle and before it has re-entered. The mechanism of the pressure loss is thus of vital importance to the future of the system, since only by understanding it clearly can we take steps to reduce the loss.

It is shown in this section that the jet pressure loss is almost wholly due to entrainment. For Martin Model No. 1 at a height of 15.2 inches, the component losses are as follows (from Reference 1):

	Percent
Entrainment of cushion air	2.5
Entrainment of cavity-zone air	40.0
Entrainment of outside air	14.0

The influence of the cavity zone is thus seen to be dominant. We can eliminate this loss almost entirely by so designing the cavity region that a stable low-loss vortex rotates within it. Then from Subsection 5 of this section, the loss will be of the order of 2 to 4 percent instead of 40 percent.

The 14 percent loss due to outside air entrainment can be reduced or even eliminated entirely by reducing the augmentation ratio m/m' , since the exhausted primary air acts as an "insulation sheath" against the deleterious effects of viscous mixing. The use of an external trunk will also benefit in this regard.

All mixing losses can be reduced by increasing the jet thickness, for a given hover height. It is suggested that the theory of this section and the previous section be used in order to determine numerically the optimum t/h ratio without (initially) reference to eductor* characteristics.

* Mr. Payne uses the term "eductor" instead of ejector, as this device is called elsewhere in the report.

The installation of a flexible diaphragm in the cavity-zone region, Figure 106 is also an interesting method of reducing losses and, specifically, of eliminating the cavity-zone-region mixing loss. The cavity zone could then be vented to the cushion region, giving an elegant and fairly "stiff" trunk assembly which profits from the unique characteristics of recirculation.

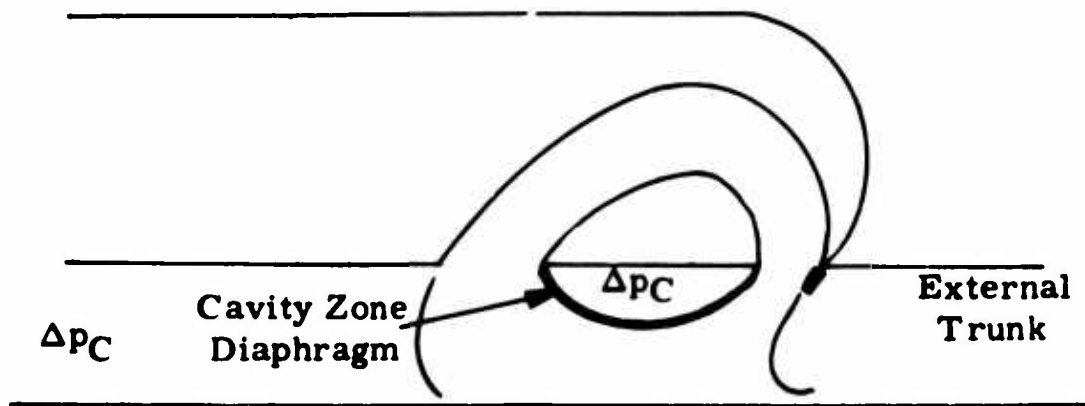


Figure 106. Cavity with Flexible Trunk

1. Entrainment in a Two-Dimensional Jet

From Reference 17 the mass flow at any position x from the jet nozzle is, in relation to the mass flow of the basic jet,

$$\frac{\dot{m}}{\dot{m}_j} = 1 + 0.08 \frac{x}{t} \quad (x < x_0) \quad (126)$$

$$= 0.62 \sqrt{\frac{x}{t}} \quad (x > x_0) \quad (127)$$

We define the mass of entrained air as m , nm_j , so that

$$\frac{\dot{m}}{\dot{m}_j} = n + 1 \quad \text{or} \quad n \left(\frac{\dot{m}}{\dot{m}_j} - 1 \right)$$

Thus

$$\left. \begin{aligned} n &= 0.08 \frac{x}{t} \quad (x < x_0) \\ &= 0.62 \sqrt{\frac{x}{t}} - 1 \quad (x > x_0) \end{aligned} \right\} \quad (128)$$

and the entrainment per unit (χ/t)

$$\left. \begin{aligned} \frac{d_n}{d} &= 0.8 & (\chi < \chi_0) \\ \frac{d_n}{d} &= \frac{0.31}{\sqrt{\frac{\chi}{t}}} & (\chi > \chi_0) \end{aligned} \right\} \quad (129)$$

These results are shown in Figure 107. It is interesting to note that the value of $d_n/d(\chi/t)$ is constant for $\chi < 5.2$, which is the region of greatest interest for most GEM applications.

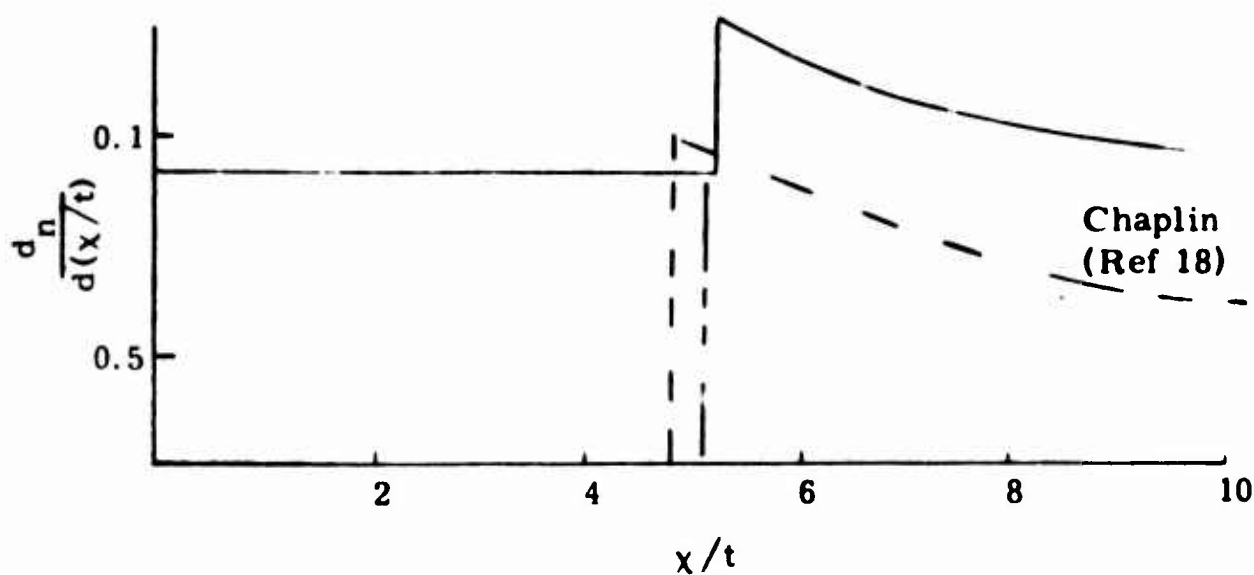
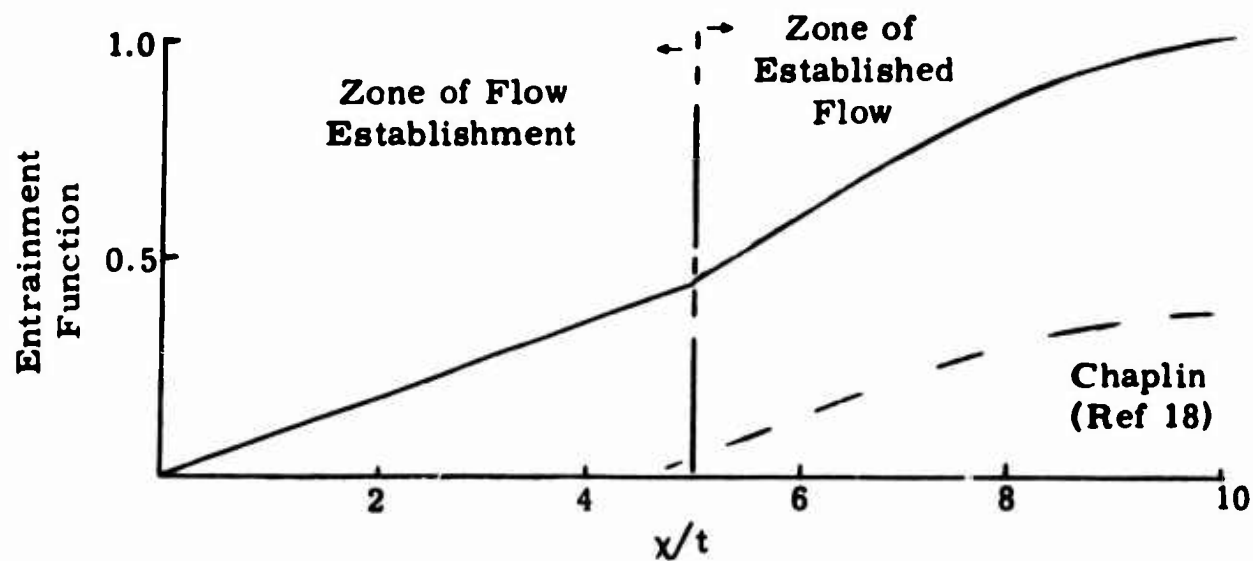


Figure 107. Entrainment in a Two-Dimensional Jet

In fact, for many applications, we can obviously take

$$\frac{dn}{d(\chi/t)} = 0.08 \quad (130)$$

as a universal constant.

These values are much larger than those assumed by Chaplin in Reference 18, which are

$$\eta = 0, \quad \frac{d\eta}{d(\chi/t)} = 0 \quad (\text{for } \frac{\chi}{t} < 5.0)$$

$$\eta = \sqrt{\frac{1\chi}{5t}} - 1, \quad \frac{d\eta}{d(\chi/t)} = \frac{0.1}{\sqrt{\chi/5t}} \quad (\text{for } \frac{\chi}{t} > 5.0).$$

2. Total Pressure Loss Due to Static Mixing

At constant static pressure, momentum remains constant along a jet, so that

$$\rho \int_0^\infty \mu^2 dA = \text{const.} \quad (131)$$

If we define \dot{m} as the mass flow of a jet, i.e.,

$$\rho \int_0^\infty \mu dA = f(\chi), \quad (132)$$

then the mean jet velocity v is defined by

$$\dot{m}v = \rho v \int_0^{\infty} \mu dA$$

or

$$\frac{\int_0^{\infty} \mu^2 dA}{\int_0^{\infty} \mu dA} = \frac{\dot{m}_o v_o}{\dot{m}} \quad (133)$$

The mean total head in the jet is therefore

$$\begin{aligned} P &= p + \frac{1}{2} \rho v^2 \\ &= p + \frac{1}{2} \rho v^2 \left(\frac{\dot{m}_o}{\dot{m}} \right)^2 \end{aligned} \quad (134)$$

Thus the dynamic head in the jet is a unique function of (χ/t) , i.e.,

$$\begin{aligned} \frac{q}{q_o} &= \left(\frac{\dot{m}_o}{\dot{m}} \right)^2 = f(\chi/t) \\ &= \frac{1}{[1 + 0.08 \chi/t]^2} \\ &= \frac{1}{0.3844 \chi/t} \end{aligned} \quad (135)$$

This equation is plotted in Figure 108.

3. Mixing Losses in a Recirculating Jet

The basic geometry of a recirculating jet is illustrated in Figure 109, where entrainment is seen to be possible in three areas. It is possible for entrainment of the outside air to influence only that part of the flow which is exhausted outwards, provided that this portion of the jet is thick enough. In this case, there is no total pressure loss in the recirculating jet, and the effect of entrainment on the outwardly exhausting air is similar to that for an annular jet.

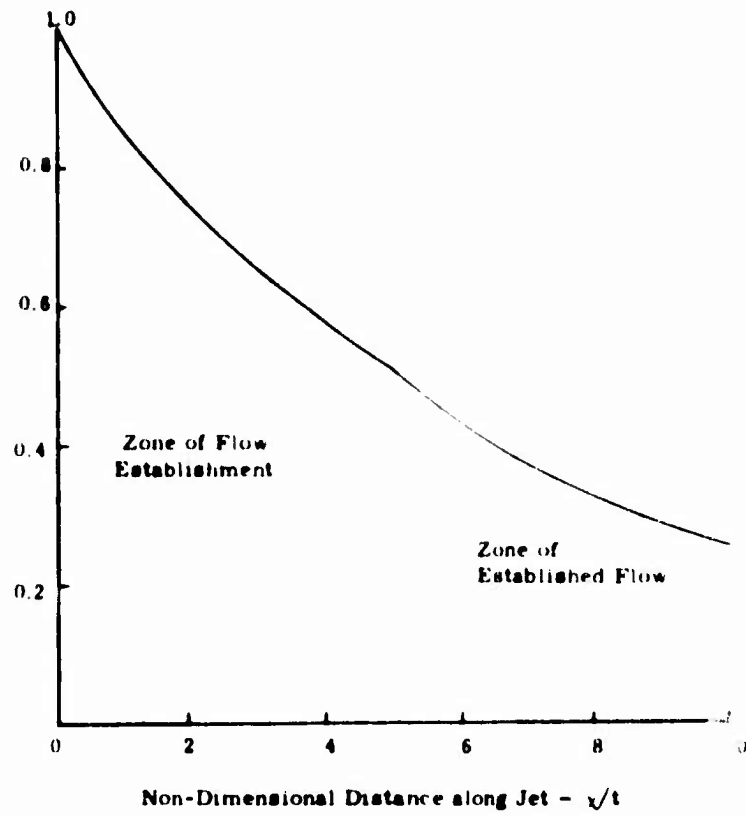


Figure 108. Ratio of Dynamic Pressure q Jet to Initial Value q_0 as a Function of Jet Length

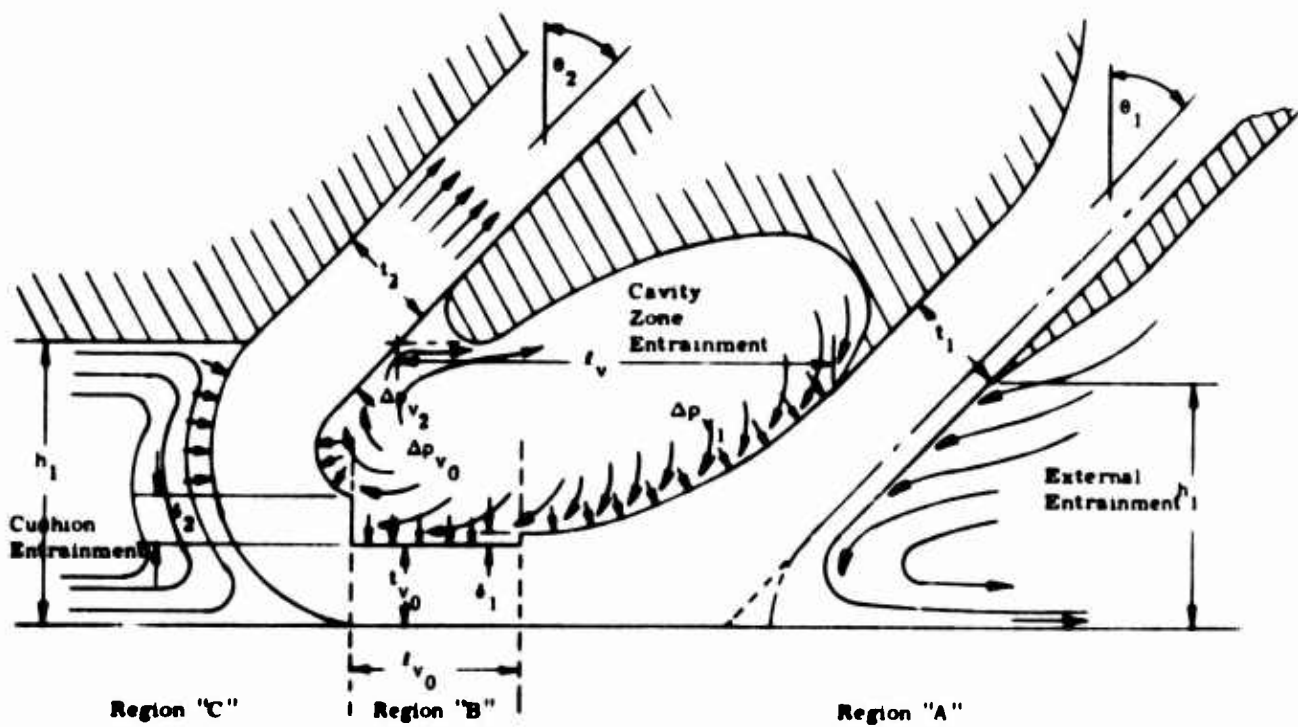


Figure 109. Entrainment in a Partially Recirculating Jet

The effective entrainment in the cavity zone can be zero if a stable, loss-free vortex is established. In the current configuration tried by Martin, however, there has been no possibility of such vortex flow, because of the large diffusion losses which would occur. Thus, present cavity zone geometries can be regarded as giving the "worst case" loss of free-air entrainment in the jet.

Finally, in the third mixing zone, the relatively slow-moving re-entrant jet can be assumed to experience free-air entrainment on its cushion side.

We shall now analyze each of these losses in detail, in order to determine the total pressure loss attributable to all three causes. The analysis will be restricted to constrained vortex flow.

a. Free-Air Entrainment Losses

This problem was examined in Reference 19 for the case of 100 percent recirculation flow, where it is shown that the length of jet affected is

$$\frac{S_F}{h} = \frac{\left(\frac{\Pi}{2} - \theta_1\right)}{(1 - \sin \theta_1)} \quad (136)$$

This equation is plotted in Figure 110. From Equation (136), the dynamic head reduction attributable to mixing over this length is

$$\frac{q}{q_{JN}} = \frac{1}{\left[1 + 0.04 \left(\frac{S_F}{h}\right) \left(\frac{h}{t}\right)\right]^2} \quad (137)$$

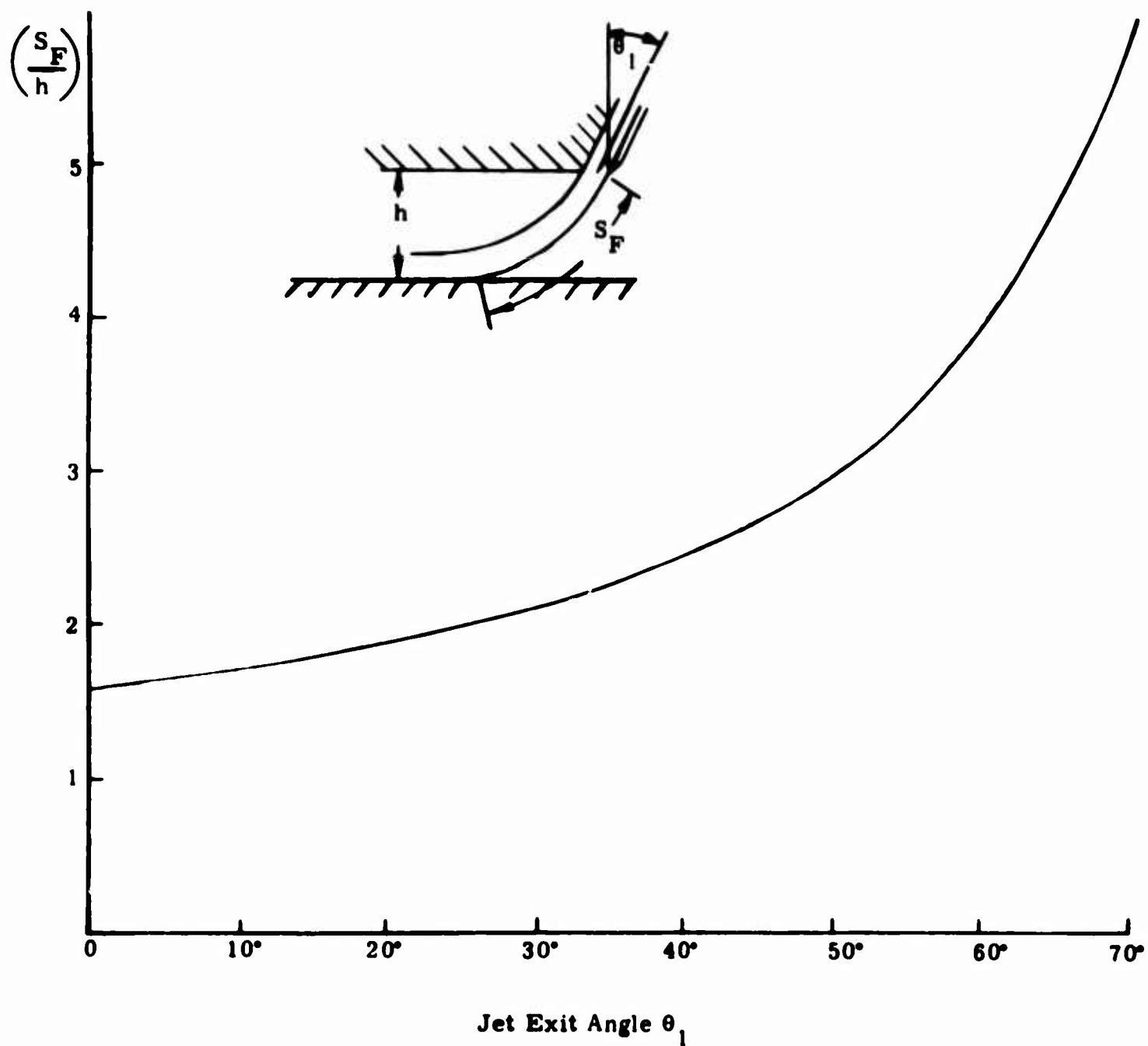


Figure 110. Free-Air Entrainment Periphery for Recirculating Jet

If we assume that the static pressure is essentially ambient in the outer portions of the jet,

$$\Delta P_{JN} = \frac{1}{2} \rho V_{JNF}^2 = q_{JN}.$$

Therefore,

$$q_F = \left(\frac{q}{q_{JN}} \right) q_{JN} = \frac{\Delta P_{JN}}{\left[1 + 0.08 \left(\frac{S_F}{h} \right) \left(\frac{h}{t} \right) \right]^2} \quad (138)$$

over the outer half of the jet.

b. Cavity-Zone Entrainment Loss

Assuming that no cavity vortex flow is generated, we can assume static entrainment (see Figure 111).

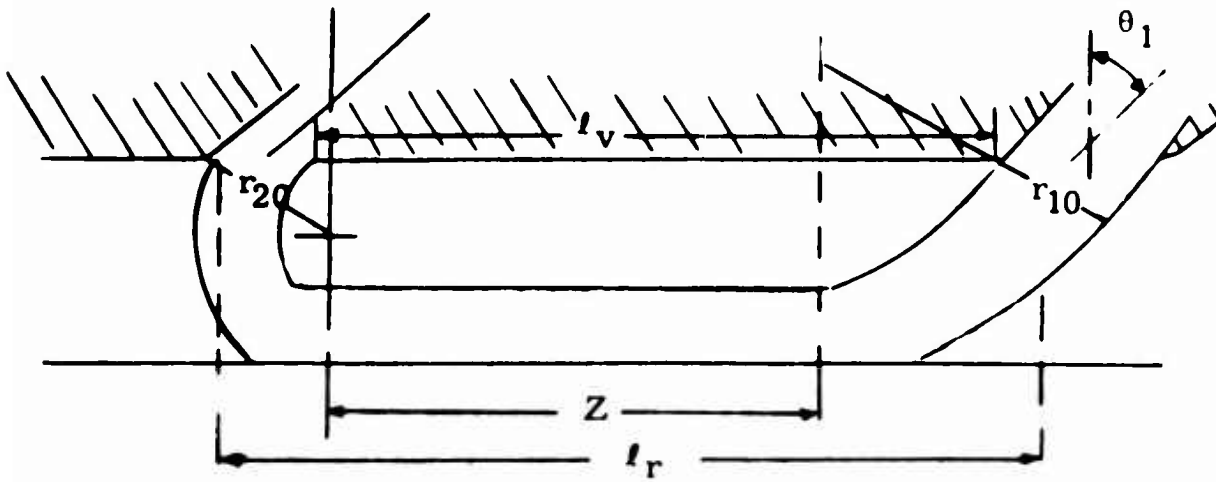


Figure 111. Cavity-Zone-Entrainment-Loss Sketch

From the Figure 109,

$$\left. \begin{aligned} \frac{r_{10}}{h} &= \frac{1}{1 - \sin \theta_1} \\ \frac{r_{20}}{h} &= \frac{1}{1 + \sin \theta_2} \end{aligned} \right\} \quad (139)$$

From the geometry,

$$r_{10} \cos \theta_1 + Z + r_{20} \cos \theta_2 = l_r ;$$

therefore,

$$\frac{Z}{h} = \frac{l_r}{h} - \frac{\cos \theta_1}{1 - \sin \theta_1} - \frac{\cos \theta_2}{1 + \sin \theta_2} \quad (140)$$

(Note that the critical height postulated in Reference 19 is reached when $Z = 0$ in this equation.)

The inner jet radii are, approximately,

$$\begin{aligned} \frac{n_1}{h} &= \frac{1 - \frac{t}{h}}{1 - \sin \theta_1} \\ &= \frac{1 - \frac{t}{h}}{1 + \sin \theta_2} \end{aligned} \quad (141)$$

assuming that the jet thickness is equal to the exit plane thickness, for simplicity. Thus the periphery in the entrainment zone is

$$\frac{S_F}{h} = \frac{Z}{h} + \frac{\left(\frac{\pi}{2} - \theta_1\right)\left(1 - \frac{t}{h}\right)}{(1 - \sin \theta_1)} + \frac{\left(\frac{\pi}{2} + \theta_2\right)\left(1 - \frac{t}{h}\right)}{(1 + \sin \theta_2)} \quad (142)$$

Substituting Equation (56) for Z/h ,

$$\frac{S_F}{h} = \frac{l_r}{h} - \frac{\cos \theta_1}{(1 - \sin \theta_1)} - \frac{\cos \theta_2}{(1 + \sin \theta_2)} + \left(1 - \frac{t}{h}\right) \left\{ \frac{\left(\frac{\pi}{2} - \theta_1\right)}{(1 - \sin \theta_1)} + \frac{\left(\frac{\pi}{2} + \theta_2\right)}{(1 + \sin \theta_2)} \right\}$$

If we assume that the pressure Δp_v acts over the inner half of the jet,

$$\Delta P_{JN} = \Delta p_v + \frac{1}{2} \rho v_{JNV}^2; \text{ therefore, } q_{JN} = \Delta P_{JN} - \Delta p_v.$$

Therefore,

$$q_v = \left(\frac{q}{q_{JN}} \right) q_{JN} = \frac{(\Delta P_{JN} - \Delta p_v)}{\left[1 + 0.08 \left(\frac{S_F}{h} \right) \left(\frac{h}{t} \right) \right]^2} \quad (143)$$

and

$$\frac{\Delta P_{v1}}{\Delta P_{JN}} = \frac{\Delta p_v}{\Delta P_{JN}} \left\{ 1 - \frac{1}{\left[1 + 0.08 \left(\frac{S_F}{h} \right) \left(\frac{h}{t} \right) \right]^2} \right\} + \frac{1}{\left[1 + 0.08 \left(\frac{S_F}{h} \right) \left(\frac{h}{t} \right) \right]^2}$$

measured at the intake nozzle, over the inner half of the jet.

c. Cushion-Zone Entrainment Loss

The jet periphery in the cushion is

$$\frac{S_c}{h} = \frac{\left(\frac{\pi}{2} + \theta_2 \right)}{(1 + \sin \theta_2)} \quad (144)$$

Assuming that the pressure Δp_c acts over the outer half of the jet,

$$\Delta P_{JN} - q_{JN} \left[1 - \frac{q_v}{q_{JN}} \right] = \Delta p_c + q_{co}$$

$$\begin{aligned}
q_{co} &= \Delta P_{JN} - q_{JN} \left[1 - \frac{q_F}{q_{JN}} \right] - \Delta p_c \\
&= \frac{\Delta P_{JN} - q_{JN} \left[1 - \frac{q_F}{q_{JN}} \right] - \Delta p_c}{\left[1 + 0.08 \left(\frac{S_c}{h} \right) \left(\frac{h}{t} \right) \right]^2}
\end{aligned} \tag{145}$$

Substituting Equation (138)

$$\frac{\Delta P_{c1}}{\Delta P_{JN}} = \frac{\Delta p_c}{\Delta P_{JN}} \left\{ 1 - \frac{1}{\left[1 + 0.08 \left(\frac{S_c}{h} \right) \left(\frac{h}{t} \right) \right]^2} \right\} + \frac{1}{\left[1 + 0.08 \left(\frac{S_c}{h} \right) \left(\frac{h}{t} \right) \right]^2} - \frac{\left\{ 1 - \frac{1}{\left[1 + 0.08 \left(\frac{S_c}{h} \right) \left(\frac{h}{t} \right) \right]^2} \right\}}{\left[1 + 0.08 \left(\frac{S_c}{h} \right) \left(\frac{h}{t} \right) \right]^2} \right\} \tag{146}$$

measured at the intake, over the outer half of the jet. The mean total pressure at the intake is obviously the mean of Equations (143) and (146).

If there is no cavity loss, the mean will be

$$\frac{\Delta P_1}{\Delta P_{JN}} = \frac{1 + \frac{\Delta P_{c1}}{\Delta P_{JN}}}{2} \tag{147}$$

If there is no free-air loss, due to insulation by the primary air, we can take $S_c = 0$.

4. Comparison with Experiment

Reference 1 contains some measurements of exit and reentry total head for a partial recirculation system, the exit total head varying linearly across the exit plane. For the test model (Martin Model No. 1) $\theta_1 = \theta_2 = 30$ degrees, $l_r = 41.86$ inches, and $t = 6.76$ inches. From Equation (140) the "critical height" would therefore be given by

$$\frac{l_r}{h_{crit}} = \cos \theta \left[\frac{1}{(1 - \sin \theta)} + \frac{1}{(1 + \sin \theta)} \right] = 2.31 \quad (148)$$

Therefore,

$$\frac{h_{crit}}{t} = \left(\frac{h_{crit}}{l_r} \right) \left(\frac{l_r}{t} \right) = 2.68.$$

The experimental data are for values of h/t at, or in excess of, this critical value.

If it is assumed that no loss in momentum flux is attributable to mixing, the theoretical values of cavity and cushion pressure can be plotted for this model (see Figure 112) by using the previous theory; some experimental values of Δp_c are plotted in Figure 97 for comparison.

Because both the nozzle pressure distribution and the mass augmentation ratio m/m' vary for the test data, the agreement is not good, in Figure 113, but the absolute order of the values is obviously reasonable.

These calculated values of Δp_c and Δp_v have been used to calculate the total pressure drop, which is the mean of Equations (143) and (146) the results being plotted in Figure 98. It is obvious that the agreement with experiment is reasonably good, having regard to the assumptions made, the accuracy of the tests, and the various imponderables introduced by the nonuniform velocity distribution in the jet.

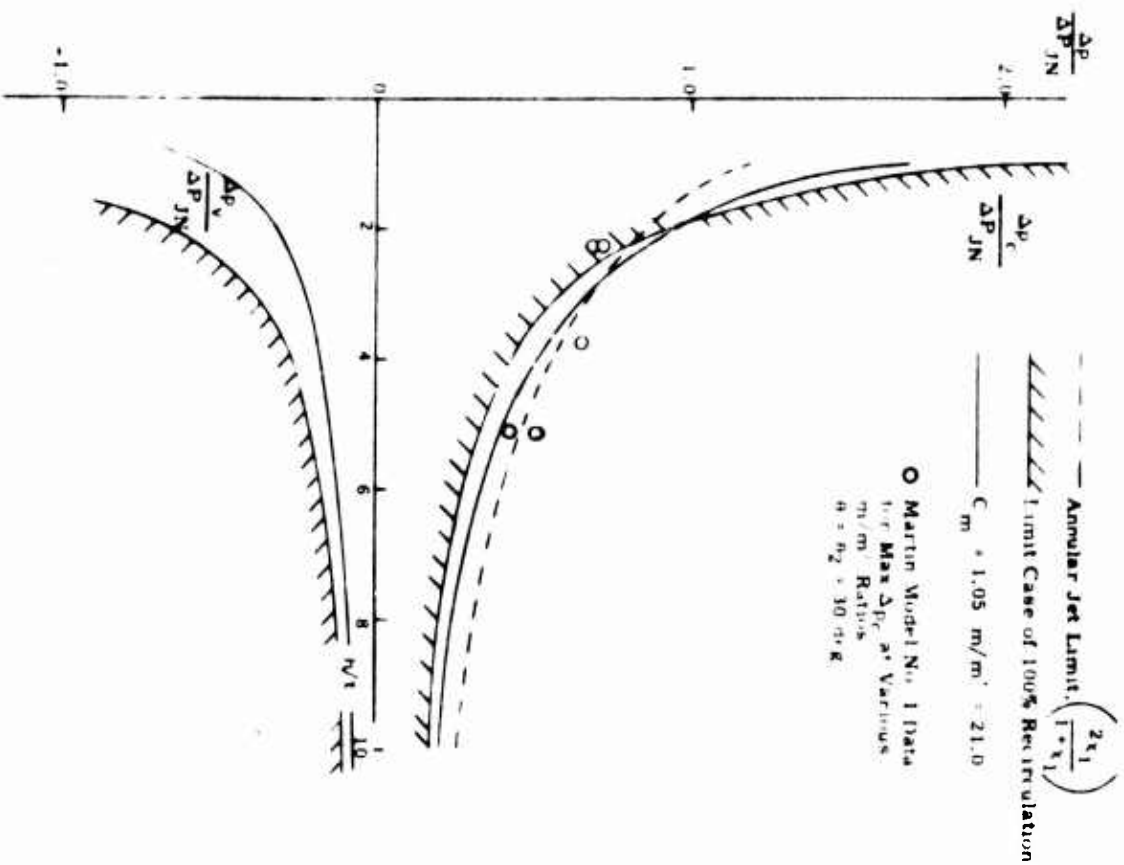


Figure 112. Theoretical Cushion and Cavity Pressure for a Recirculation Test Rig

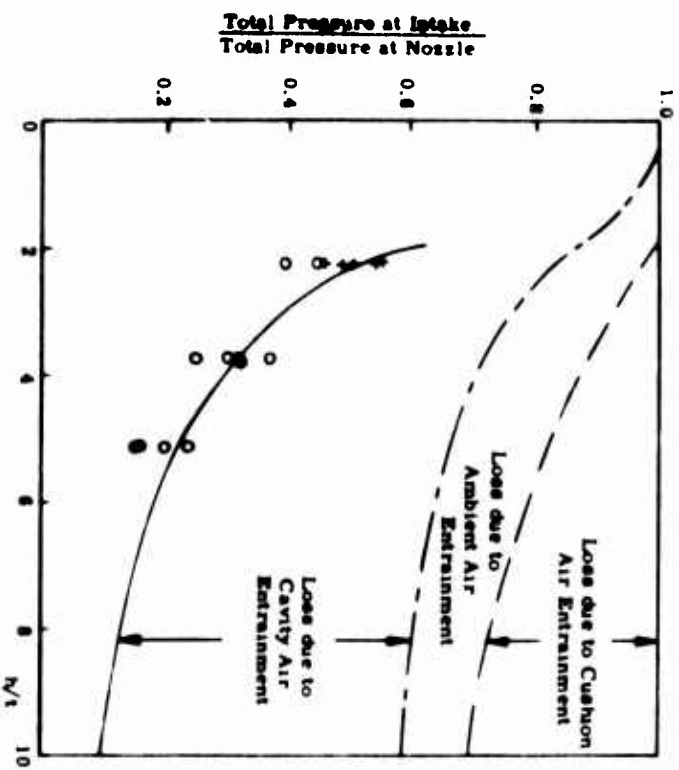


Figure 113. Predicted and Measured Total Head Loss for Martin Model No. 1

5. Losses Attributable to a Stable Vortex in the Cavity Zone (Figure 114)

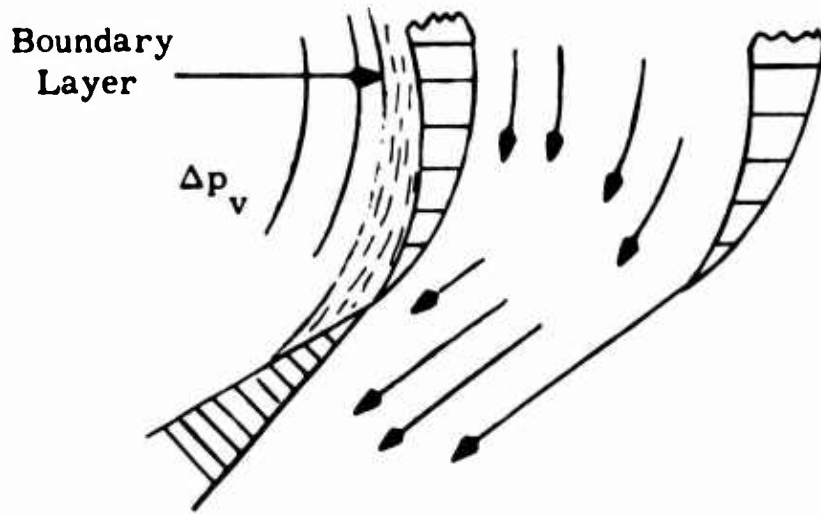


Figure 114. Losses due to Stable Vortex in Cavity Zone

When a stable low-loss vortex exists, we postulate that the boundary layer air in the cavity-zone region leaves the trailing edge of the cavity-zone structure with a mean velocity ω , the thickness of the layer being ζ . Thus the mass flow of this BL is $b\zeta\omega\rho$ and its momentum loss is $(U-\omega)b\zeta\omega\rho$. Equating this to the skin-friction force

$$\frac{1}{2}\rho U^2 C_{fc} = \omega U \zeta \rho - \omega^2 \zeta \rho \quad (149)$$

or

$$\zeta \left[\left(\frac{\omega}{U} \right) - \left(\frac{\omega}{U} \right)^2 \right] = \frac{1}{2} C_{fc}.$$

For mixing at constant pressure, the total pressure loss of air in the jet is a function only of the mass of air entrained, not the length over which entrainment occurs. Thus, if J_j is the momentum flux of the jet and ΔJ_{BL} is the momentum deficiency of the BL relative to J_j , then for mixing at constant pressure

$$\begin{aligned} J_{j+BL} &= J_j - \Delta J_{BL} \\ &= J_j - \frac{1}{2}\rho U^2 C_{fc} b. \end{aligned}$$

Assuming

$$J_j = tbv_j^2 \rho$$

and

$$U = v_j.$$

Then the down stream jet momentum flux is

$$J_{j+BL} = \frac{1}{2} \rho v_j^2 b \left[2t - cC_f \right]$$

of

$$\frac{J_{j+BL}}{J_j} = \left[1 - \frac{1}{2} \left(\frac{c}{t} \right) C_f \right]. \quad (150)$$

Obviously this source of loss is quite small if the skin friction coefficient is of the order of 0.004, as might be the case for a favorable pressure gradient. When an adverse pressure gradient causes rapid growth and separation of the BL, however, the loss can be very much greater.

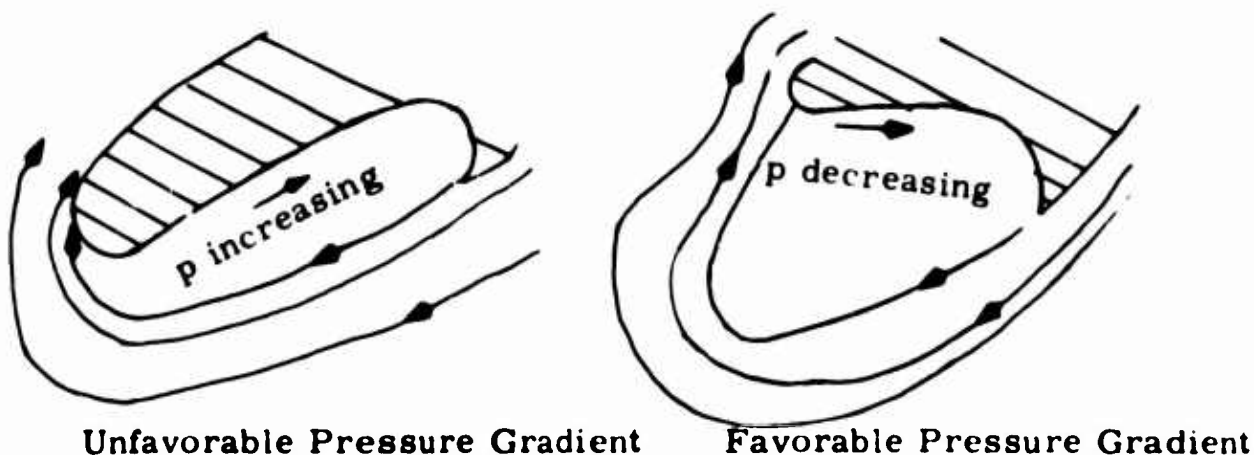


Figure 115. Losses Attributable to Adverse Pressure Gradient

Physical meaning to this is given in Figure 115. An obvious improvement in performance could also be obtained by the use of boundary layer suction.

SOME NOTES ON JET-PUMP AERODYNAMICS

The concept of an "optimum eductor" is introduced, and plots of optimum geometry and performance are given, for the static case of eduction from ambient and exhausting to ambient. Equations for optimum performance with greater than ambient inlet total head are also given.

By far the most important parameter is seen to be diffuser efficiency. It is apparent that the momentum flux of the Martin Recirculation system can be increased by a factor of as much as two or three by improving the ducting design to reduce turning and diffusion losses.

Best results will be obtained with boundary layer control by suction, which is easy to do, but significant improvements can be obtained without this. Minimum turning losses are expected to be obtained (without boundary layer control) from combining diffusion with turning, so that there is no pressure gradient on the inside wall. Minimum diffusion losses, without boundary layer suction, will probably be obtained with a centrifugal diffuser which has zero pressure rise along its walls.

It is shown that the optimum mixing pressure with total head recovery will be considerably greater than for the static case. Also, the required mixing length is greatly increased (for efficient diffusers), so that the primary nozzle size should be reduced and the number of nozzles increased. For optimum performance, the mixing pressure should remain constant. It is shown that this implies a progressive reduction of duct area during mixing.

1. Static Eductor

A jet pump or thrust augmentor is an energy exchange device of extreme conceptual simplicity and considerable aerodynamic complexity.

The fact that practical results are so often disappointing is generally attributable to the lack of an adequate theoretical description of jet-pump performance.



Figure 116. Simple Uniform Jet

Consider the simple (uniform) jet in the above sketch. Its thrust is given by Newton's law.

Thrust = rate of change of momentum; that is,

$$J = \frac{dm}{dt} . \quad (151)$$

The momentum of the air is $\rho A_j v_j^2$ (lb/sec), so that

$$J = \rho A_j v_j^2 = \dot{m}_j v_j \quad (152)$$

where, $\dot{m}_j = dm/dt$, the mass flow rate.

The power dissipated in the jet is

$$E_j = \frac{1}{2} \dot{m}_j v_j^2 . \quad (153)$$

Thus, the thrust per unit power is

$$\frac{T}{E_j} = \frac{\dot{m}_j v_j}{\frac{1}{2} \dot{m}_j v_j^2} = \frac{2}{v_j} . \quad (154)$$

In other words, for unit power, thrust varies inversely as the jet velocity, and since

$$v_j = \frac{T}{\dot{m}_j} , \quad (155)$$

$$\frac{J}{E_j} = 2 \frac{\dot{m}_j}{J} . \quad (156)$$

Thus, if we double the mass flow associated with the production of a given thrust we halve the power dissipated in the jet.

Confining ourselves now to power available in the form of a pressurized or moving gas, we see that the higher its total pressure, the lower will be its efficiency in terms of thrust per unit power. Given a supply of very high pressure compressed air with which we wish to generate a thrust force, we might logically design a system of the type shown in Figure 117, in order to lower the final jet velocity. Technically this "transformer" (to use an obvious electrical analogy) has two sources of inefficiency. In converting the compressed air energy to mechanical energy, we experience loss $(1 - \eta_T)$, and in reconvertitg it to flow energy, we encounter a fan loss $(1 - \eta_F)$. Thus, the air power required is given by,

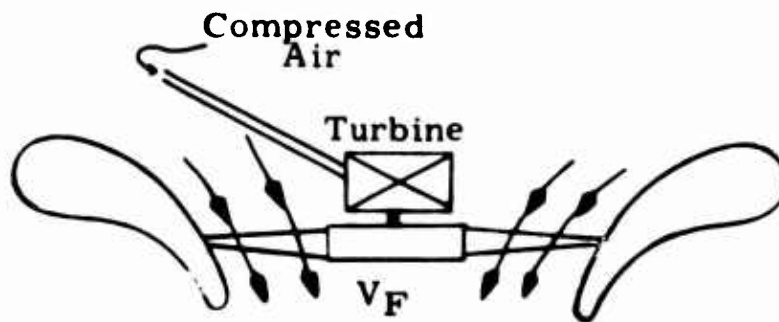


Figure 117. Sketch of System which Lowers Jet Velocity

$$\eta_T \eta_F \frac{1}{2} \dot{m}_j v_j^2 = \frac{1}{2} \dot{m}_F v_F^2 \quad (157)$$

Therefore

$$J_F = \dot{m}_F v_F = \eta_T \eta_F \frac{\dot{m}_j v_j^2}{v_F}$$

or

$$\frac{J_F}{J_j} = \eta_T \eta_F \frac{v_j}{v_F} \quad (158)$$

Since

$$J_F = \dot{m}_F v_F \text{ and } J_j = \dot{m}_j v_j$$

$$\frac{v_j}{v_F} = \left(\frac{J_j}{J_F} \right) \left(\frac{\dot{m}_F}{\dot{m}_j} \right) = \frac{J_j}{J_F} (\eta+1)$$

$(\eta+1)$ being the ratio of secondary to primary mass flow.

Therefore

$$\frac{J_F}{J_j} = \sqrt{\eta_T \eta_F (\eta+1)} \quad (159)$$

The ratio J_F/J_j is the "thrust augmentation" of the "transformer". If for $\eta_F \eta_T$ we write the energy exchange efficiency η_E of a jet pump, then Equation (75) also applies to a jet pump. We shall see later that the efficiency of a jet pump can be comparable with that of a more conventional energy transformer, provided that it has a fairly low mass flow ratio (η) and a very efficient diffuser.

If the secondary air in Figure 117 recirculates so that it does not have to be accelerated from ambient, the power required is

$$\eta_F E_F = \frac{1}{2} \dot{m}_F v_F^2 - \frac{1}{2} \dot{m}_F v_1^2. \quad (160)$$

We define an energy (or pressure) recovery factor,

$$\phi = \left(\frac{v_1}{v_F} \right)^2 \quad (\phi < 1.0).$$

Then

$$\eta_F \eta_T \frac{1}{2} \dot{m}_j v_j^2 = \frac{1}{2} \dot{m}_F v_F^2 (1 - \phi) \quad (161)$$

and Equation (75) becomes

$$\frac{J_F}{J_J} = \sqrt{\frac{\eta_T \eta_F (\eta + 1)}{(1 - \phi)}} \quad (162)$$

so that an intake pressure recovery of 50 percent could give 41 percent increase in augmentation, for example.

2. The Optimum Static Jet Pump

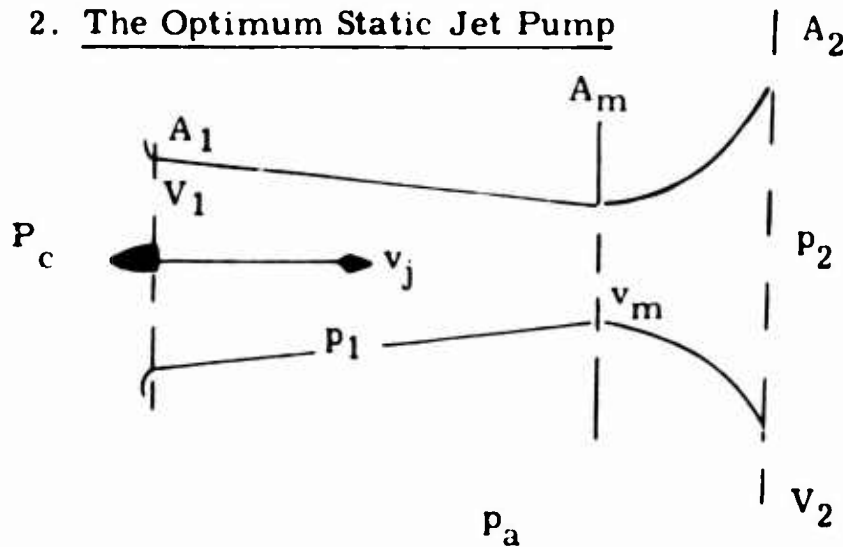


Figure 118. Basic Geometry of Jet Pump

Figure 118 shows the basic geometry of a jet pump. Its ability to generate additional thrust is predicated upon the fact that mixing

takes place at a static pressure p_1 which is less than the upstream total pressure P_c . Since $p_1 < P_c$ a secondary airflow into the augmentor takes place, giving the desired increase in mass flow.

In Reference 20 it is shown that there is an optimum mixing pressure (p_1). It is obvious that if p_1 is too great, the secondary flow will be too small to give the desired effect. If (p_1) is too small, on the other hand, the secondary flow velocity will be too large for efficient transference of energy to it from the primary jet.

We define the optimum value of p_1 as that value which gives the maximum possible thrust augmentation for a given ratio n of entrained to primary air. It is shown in Reference 17 that for $P_c = p_a$, static case,

$$-\Delta p_1 \bigg|_{\text{opt}} = \frac{n^2 \eta_D^2 [\Delta P_j - \Delta p_1]}{[(n+1)^2 - n^2 \eta_D]^2}$$

so that

$$\frac{-\Delta p_1}{\Delta P_j} \bigg|_{\text{opt}} = \frac{n - \eta_D^2}{[(n+1)^2 - n^2 \eta_D]^2 - n^2 \eta_D^2} \quad (163)$$

where

Δp_1 = mixing pressure (gauge)

ΔP_j = the primary jet total head (gauge)

n = the entrained air ratio

η_D = efficiency of the jet pump diffuser.

This optimum value ($-\Delta p_1$) is plotted in Figure 119 as a function of n and η_D . It is obvious that the 100 percent efficient diffuser solution is quite different to the others and that very rapid changes occur in the region ($0.9 < \eta_D < 1.0$).

The existence of an "optimum mixing pressure" enables us to discuss an "optimum jet pump", with a great consequent saving in calculations and complexity. We will now discuss some of its characteristics.

Optimum Geometry:

To preserve optimum performance, the mixing chamber requires a progressive reduction in area along its length, the final area after mixing being the value (A_m) shown in Figure 120.

It is interesting to note that

$$\frac{A_m}{A_1} \approx \eta_D.$$

The optimum inlet area ratio (A_1/A_J) is given in Figure 121, which also defines the ratio (v_1/v_J) of the entrained to jet velocity.

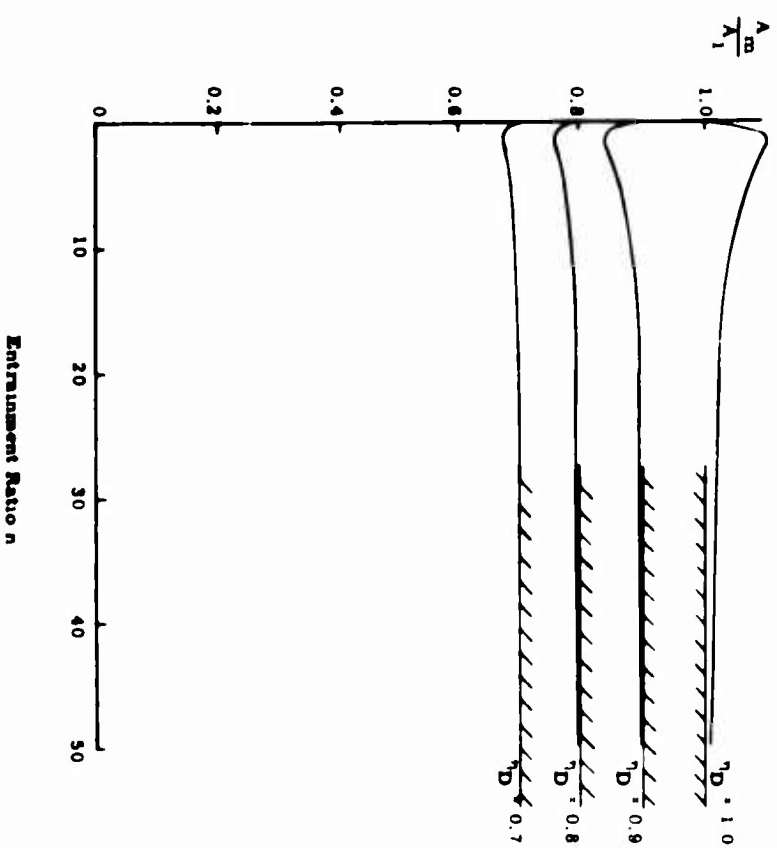
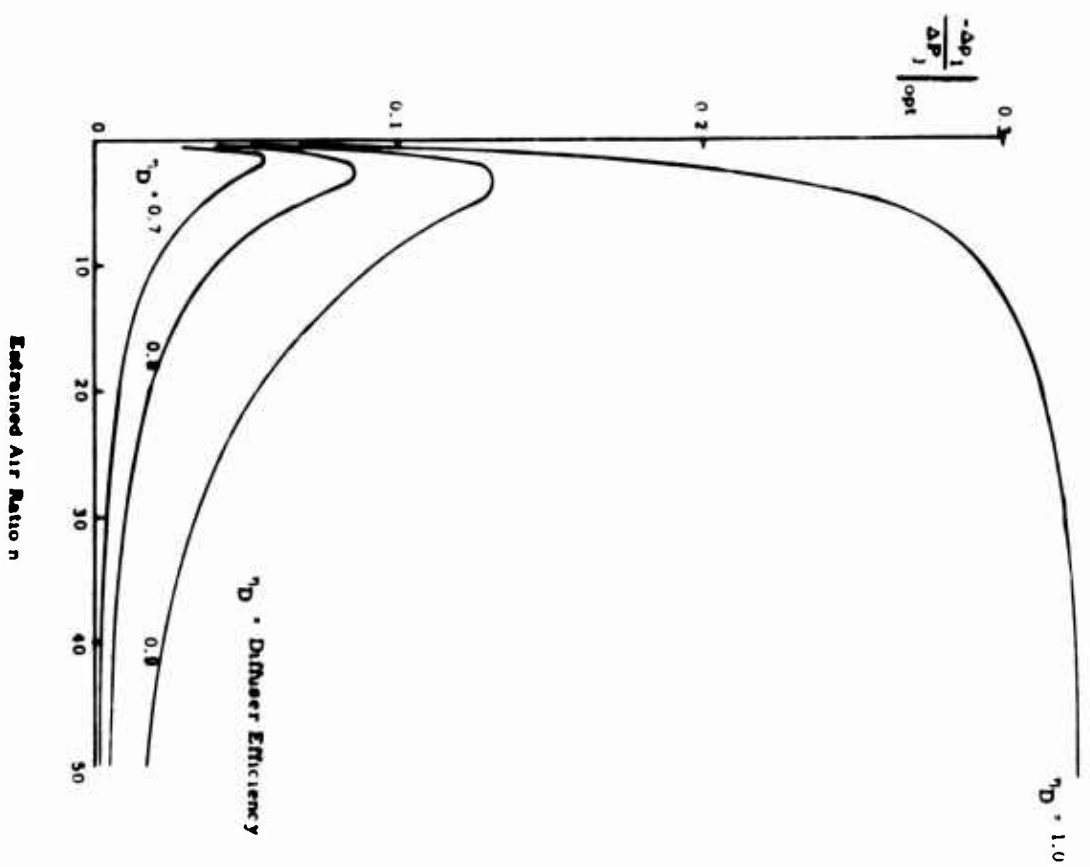
The diffuser ratio (A_2/A_m) associated with optimum performance is plotted in Figure 122, and it is interesting to note that these represent quite modest area ratios.

Optimum Thrust Augmentation:

Optimum thrust augmentation ratio is plotted in Figure 123 and the limit case as $n \rightarrow \infty$ in Figure 124. It is immediately obvious that diffuser efficiency (η_D) is the single most important parameter. For example a gain in (η_D) from 0.9 to 0.95 would give a 45-percent increase in augmentation,

Augmentor Efficiency:

Optimum augmentor efficiency is plotted in Figure 125. Again, as we should expect from the previous two figures, diffuser efficiency has an extremely powerful influence upon overall efficiency.



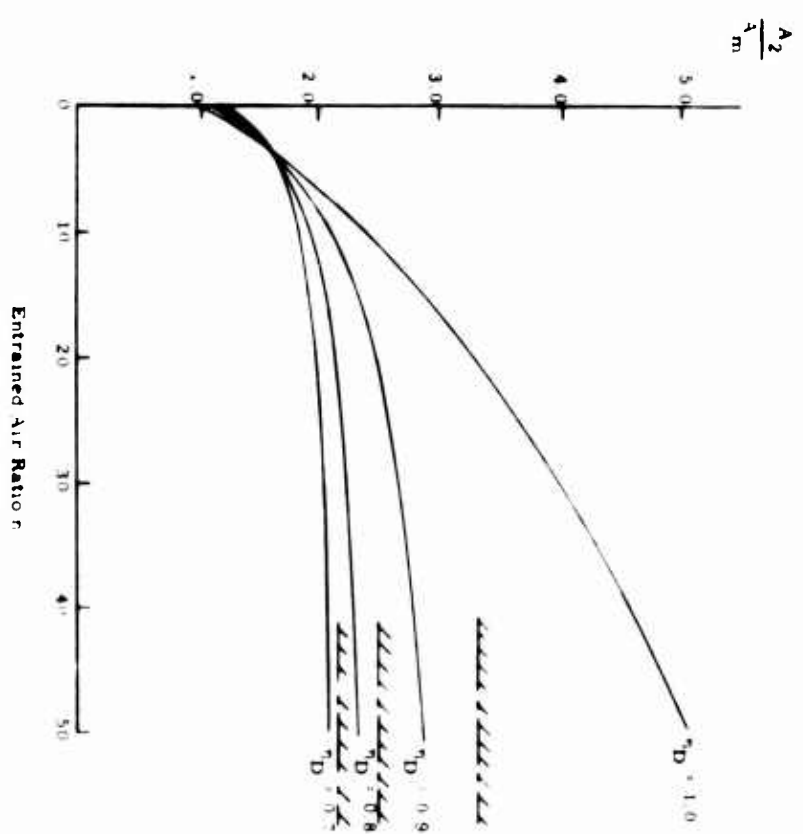
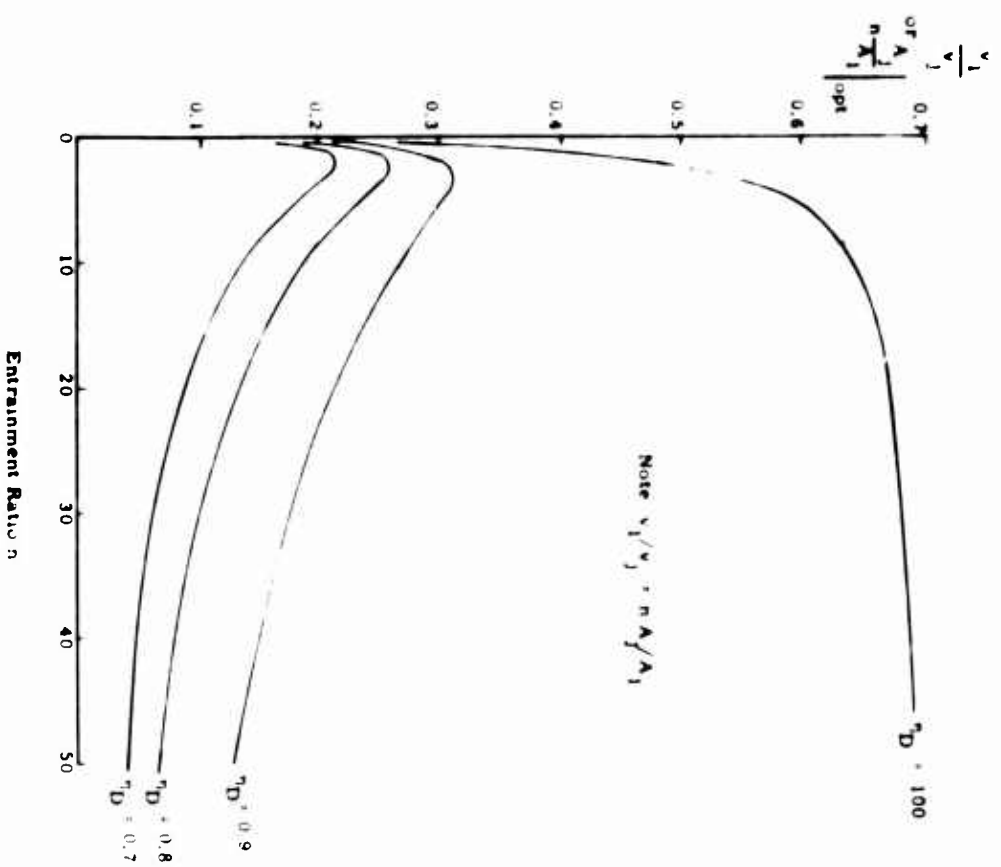


Figure 121. Variation of Optimum A_j/A_1 with n

Figure 122. Optimum Diffuser Ratios A_2/A_m with Static Educator

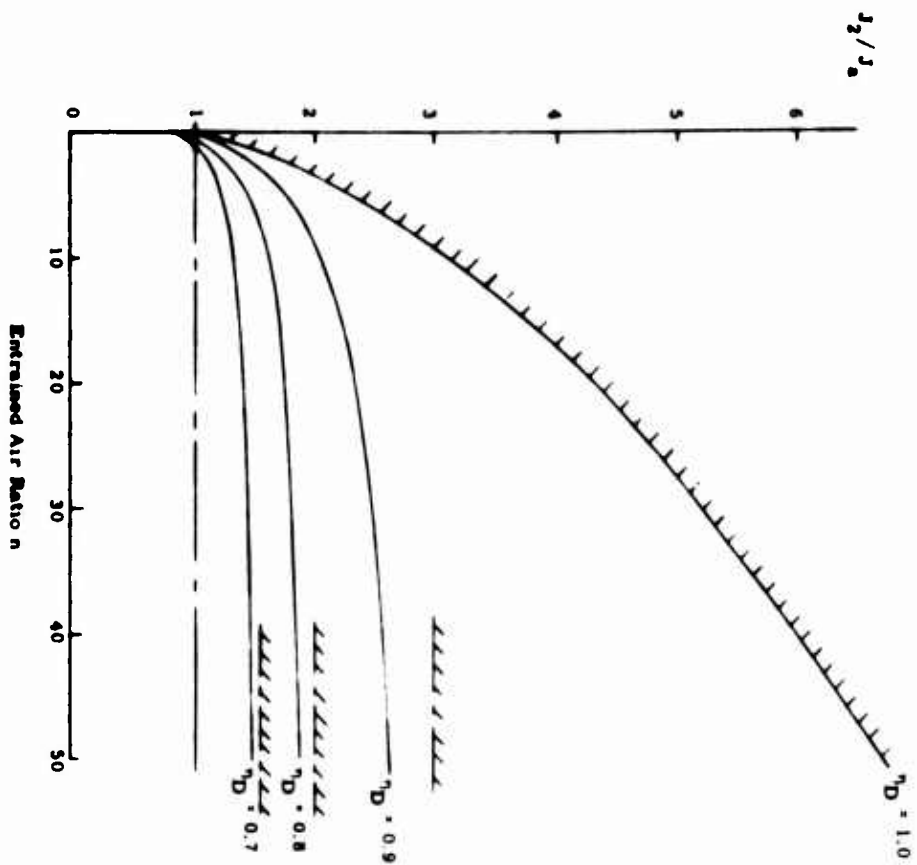


Figure 123. Variation of Optimum Thrust Augmentation with Diffuser Efficiency η_D

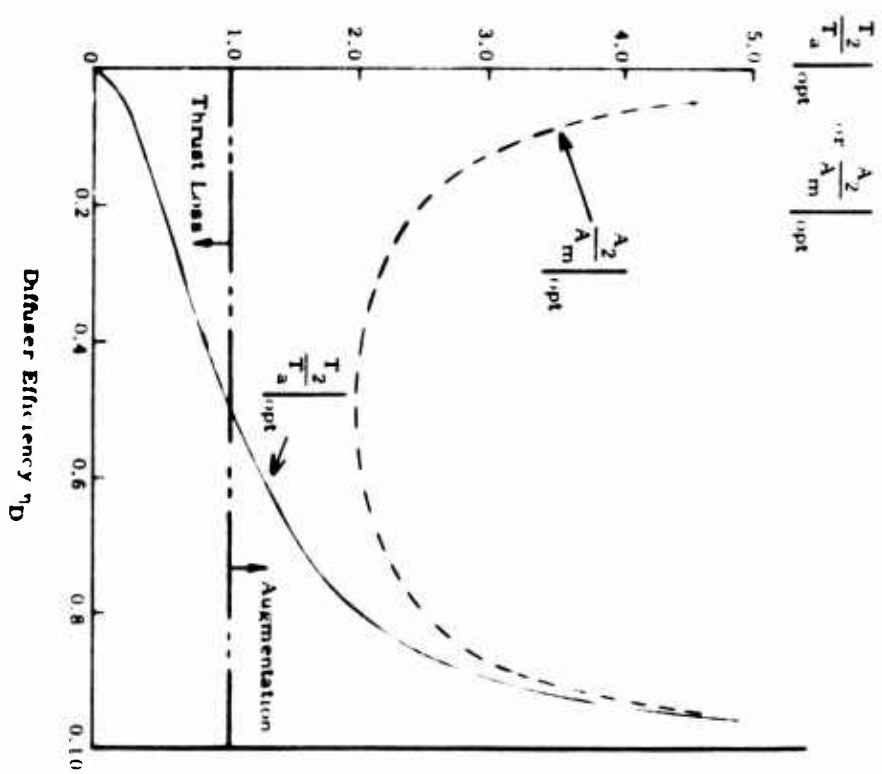


Figure 124. Limit Augmentation Available as $n \rightarrow \infty$

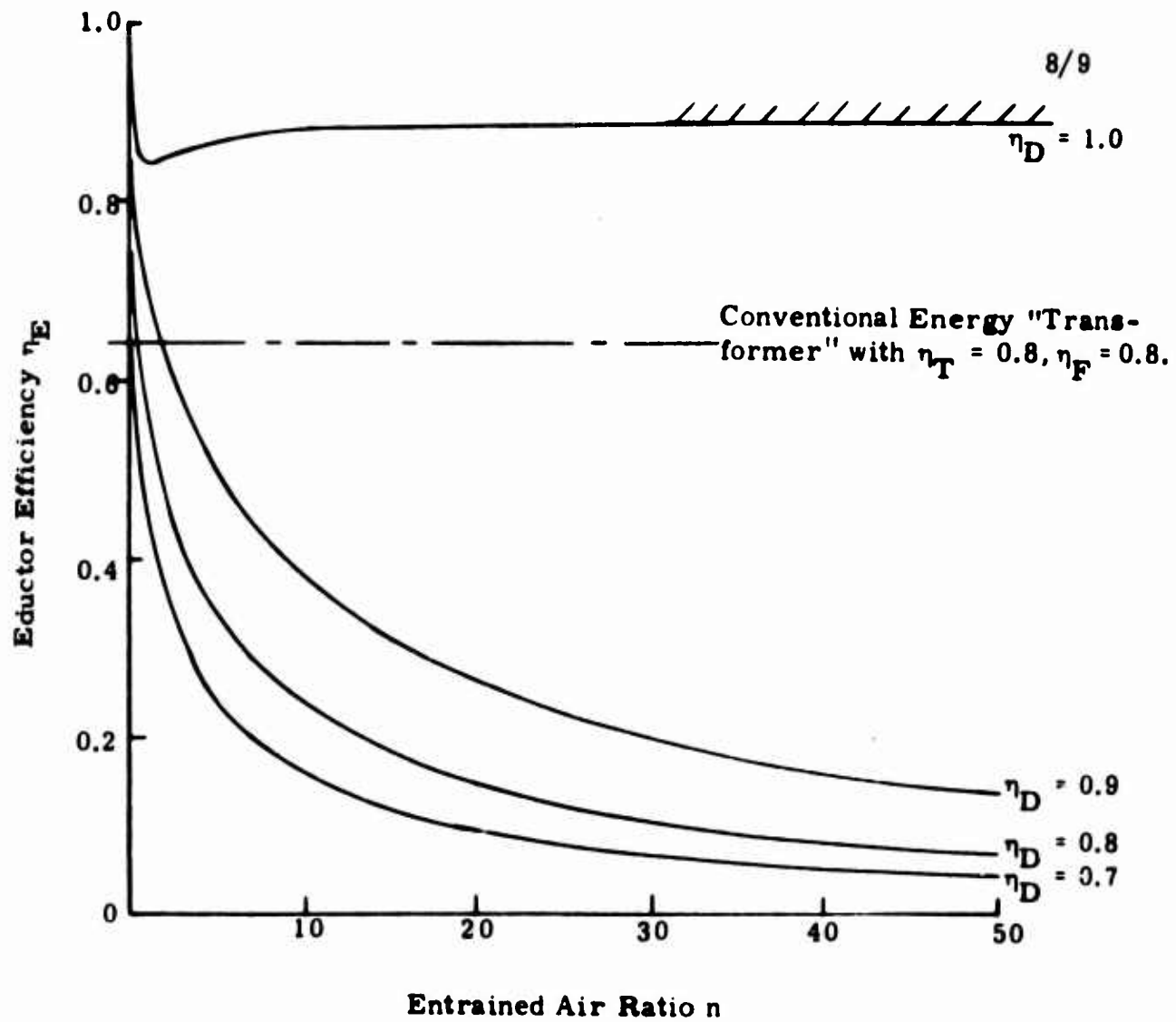


Figure 125. Efficiency of Optimum Jet Pump under Static Conditions

3. Jet Pump Mixing

The mixing between primary and secondary flows which occurs in an eductor depends upon the shear velocity between the secondary and primary flows. If the jet is exhausting into still air, the mass of air entrained (for a fully developed turbulent jet) is, from Reference 15,

$$n = \left(\frac{\dot{m}_{jx}}{\dot{m}_{jo}} - 1 \right) = 0.62 \sqrt{\frac{x}{t}} - 1. \quad (164)$$

Thus

$$\left(\frac{x}{t} \right)_{\max} = \frac{(n+1)^2}{0.3844}. \quad (165)$$

Equation (151) becomes, when the mixing occurs in a free-stream of velocity v_1 ,

$$n = 0.62 \sqrt{\frac{x}{t}} \left(1 - \frac{v_1}{v_{jo}} \right) - 1 \quad (166)$$

where v_1 is the entrained air velocity, as shown in Figure 126. Needless to say, if the mixing takes place at constant pressure, we can assume v_1 to be constant until mixing occurs.

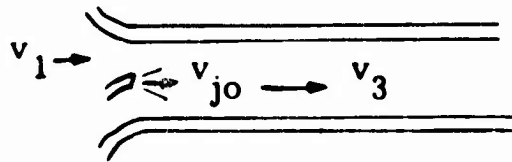


Figure 126. Velocities in an Eductor

For the optimum static eductor, Equation (166) has been used to plot the total mixing length required in Figure 127.

It will be noted that, except for very efficient diffusers, the required mixing length is roughly equal to the still air value given by Equation (166).

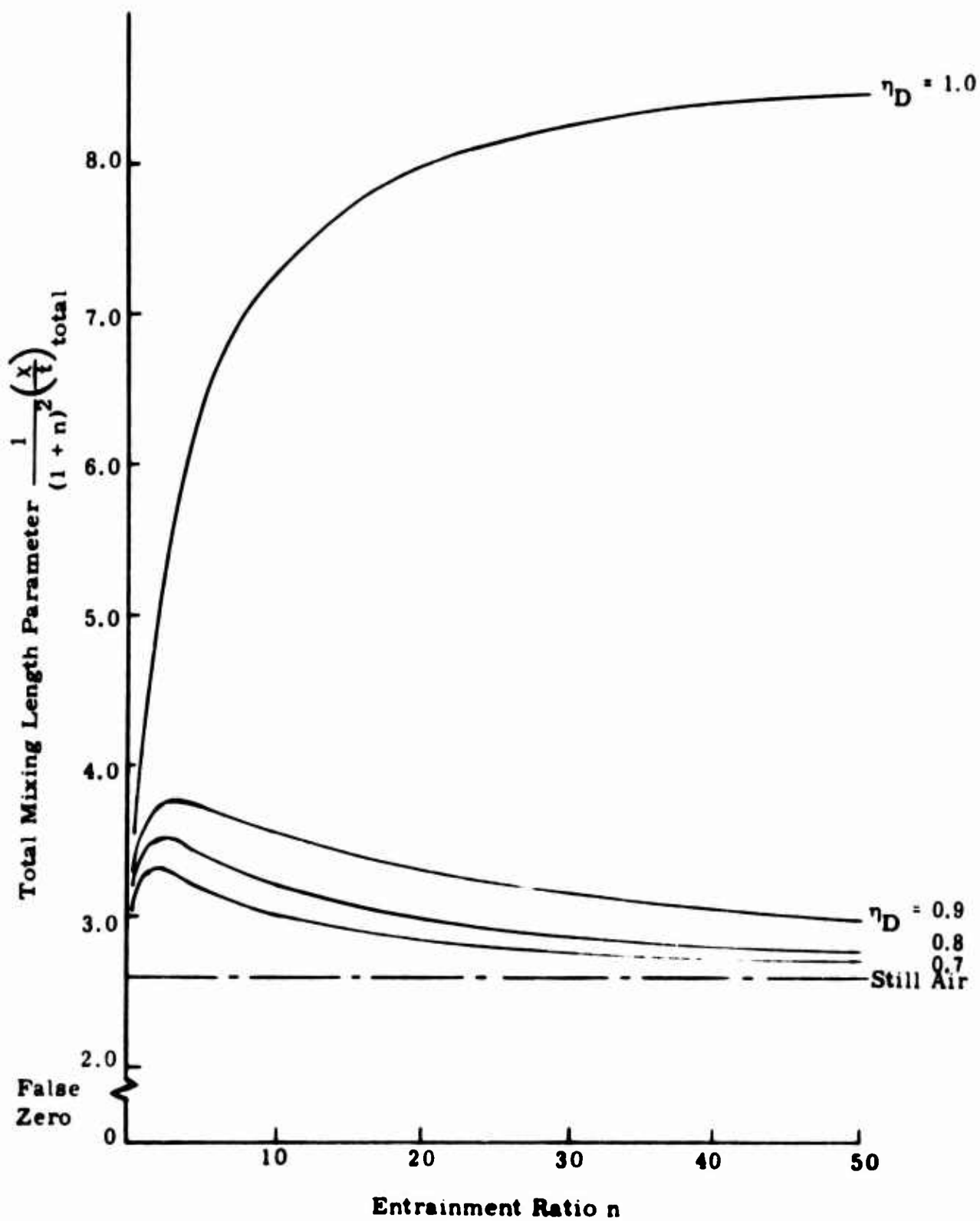


Figure 127. Total Mixing Length Parameter as a Function of Entrainment Ratio and Diffuser Efficiency

It is obvious that (from Figure 121) the very much larger mixing length requirement associated with efficient diffusion is due to the higher velocity (v_1) of the entrained air.

The implication of this result to a recirculation system is obvious, since total head recovery at the inlet implies a substantial increase in (v_1) and a substantial increase, therefore, in the mixing length required. The use of a mixing length based on static eductor tests could therefore result in a recirculation mixing length which is inadequate by a factor of four or five. Fortunately, this problem can be alleviated by reducing the size of the individual nozzles and by increasing their number, since the required mixing length is a linear function of nozzle size.

4. General Eductor Theory

Let

J_a = momentum flux of primary when exhausting to ambient.

J_o = momentum flux of primary exhausting to a pressure.

J_2 = total momentum flux at diffuser exit plane.

\dot{m}_j = primary mass flow.

$m_1 = n\dot{m}_j$, the mass of the entrained air.

$$\frac{J_2}{J_a} = \left(\frac{J_2}{J_o}\right)\left(\frac{J_o}{J_a}\right) \quad (167)$$

$$\frac{J_o}{J_a} = \frac{\rho A_j v_j^2}{\rho A_j v_{ja}^2} = \frac{P_J - p_1}{P_J - p_a} \quad (168)$$

Therefore,

$$\frac{J_2}{J_a} = \frac{(P_J - p_1)}{(P_J - p_a)} \left(\frac{v_2}{v_j}\right)^{(n+1)}. \quad (169)$$

Since

$$n = \frac{\rho v_1 A_1}{\rho v_j A_J},$$

$$n = \frac{A_1}{A_j} \sqrt{\frac{P_c - p_1}{P_J - p_a}}. \quad (170)$$

Now

$$\frac{1}{2} \rho v_2^2 = p_1 - p_2 + \eta_D \frac{1}{2} \rho v_m^2 \quad (171)$$

and

$$v_m = \frac{v_j + n v_1}{(n+1)}. \quad (172)$$

Therefore

$$v_2^2 = \frac{2}{\rho} (p_1 - p_2) + \frac{\eta_D [v_j + n v_1]^2}{(1+n)^2}.$$

Since

$$v_2^2 = \frac{2}{\rho} (p_1 - p_2) + \frac{\eta_D v_j^2 \left[1 + n \frac{v_1}{v_j} \right]^2}{(1+n)^2} \quad (173)$$

and

$$n = \frac{A_1}{A_j} \left(\frac{v_1}{v_j} \right)$$

$$v_2^2 = \frac{2}{\rho} (p_1 - p_2) + \frac{\eta_D \frac{2}{\rho} (P_J - p_1) \left[1 + n^2 \frac{A_J}{A_1} \right]^2}{(1+n)^2}$$

$$\frac{v_2}{v_j} = \sqrt{\left(\frac{p_1 - p_2}{P_J - p_1} \right) + \frac{\eta_D \left[1 + n^2 \frac{A_J}{A_1} \right]^2}{(1+n)^2}}. \quad (174)$$

Note that the upstream total pressure does not occur in this equation, except as it influences (n) from Equation (170).

From Equation (169)

$$\frac{J_2}{J_a} = \frac{(P_J - p_1)}{(P_J - p_a)} \sqrt{\frac{(p_1 - p_2)}{(P_J - p_1)} (n+1)^2 + \eta_D \left[1+n^2 \frac{A_j}{A_1} \right]^2} \quad (175)$$

For the augmentation factor J_2/J , the terms outside the square root are equal to unity, of course. For $p_2 = p_a$, Equation (175) reduces to

$$\frac{J_2}{J_a} = \sqrt{\frac{\Delta p_1}{\frac{1}{2}\rho v_j^2} (n+1)^2 + \eta_D \left[1+n^2 \frac{A_j}{A_1} \right]^2} \quad (176)$$

which agrees with Reference 20.

Writing $\bar{P}_n = \frac{P_n}{\frac{1}{2}\rho v_j^2} = \frac{P_n}{P_J - p_1}$ and $\Delta p = p - p_a$

$$\frac{J_2}{J_a} = \frac{1}{\Delta \bar{P}_J} \sqrt{(\bar{p}_1 - \bar{p}_2) (n+1)^2 + \eta_D \left[1+n\sqrt{\bar{P}_C - \bar{p}_1} \right]^2} \quad (177)$$

Differentiating with respect to p_1

$$\frac{d}{d\bar{p}_1} \left(\frac{J_2}{J_a} \right) = \frac{1}{2\Delta \bar{P}_J} \frac{\left[(n+1)^2 - \frac{\eta_D^n}{\sqrt{\Delta \bar{P}_C - \bar{p}_1}} - \eta_D n^2 \right]}{\sqrt{(\bar{p}_1 - \bar{p}_2) (n+1)^2 + \eta_D \left[1+n\sqrt{\bar{P}_C - \bar{p}_1} \right]^2}} \quad (178)$$

Equating to zero,

$$\frac{\eta_D^n}{\sqrt{\bar{P}_C - \bar{p}_1}} = (n+1)^2 - n^2 \eta_D$$

$$(\bar{P}_C - \bar{p}_1) \Big|_{\text{opt}} = \frac{\eta_D^{2n^2}}{[(n+1)^2 - n^2 \eta_D]^2}$$

or

$$\bar{p}_1 \Big|_{\text{opt}} = \bar{P}_C - \frac{\eta_D^{2n^2}}{[(n+1)^2 - n^2 \eta_D]^2} \quad (179)$$

Substituting in Equation (161),

$$\frac{J_2}{J_a} \Big|_{\text{opt}} = \frac{n+1 \sqrt{(\bar{P}_C - \bar{p}_2) [(n+1)^2 - n^2 \eta_D] + \eta_D}}{\Delta \bar{P}_J \sqrt{(n+1)^2 - n^2 \eta_D}} \quad (180)$$

which reduces to the Reference 15 equations for $\bar{P}_C = \bar{p}_2$ and $\Delta P_J = 1.0$.

Calculation of \bar{P}_n :

Equation (180) gives the optimum eductor performance in terms of the nondimensional pressure terms $\bar{p}_n = P_n / (P_J - p_1)$. By analogy with Equation (179),

$$p_1 \Big|_{\text{opt}} = \left\{ \bar{P}_C - \frac{n^2 \eta_D^2}{[(n+1)^2 - n^2 \eta_D]^2} \right\} (P_J - p_1)$$

$$\frac{p_1}{P_J} \Big|_{\text{opt}} = \frac{\{ \bar{P}_C [(n+1)^2 - n^2 \eta_D]^2 - n^2 \eta_D^2 \}}{\{ (1 + \bar{P}_C) [(n+1)^2 - n^2 \eta_D]^2 - n^2 \eta_D^2 \}} \quad (181)$$

Since

$$P_J - p_1 = P_j \left(1 - \frac{p_1}{P_J} \right) = P_j \left(1 - \frac{\left\{ \right\}}{\left\{ \right\}} \right)$$

$$\bar{P}_C = \frac{\frac{P_C}{P_J}}{1 - \frac{\left\{ \bar{P}_C \left[(n+1)^2 - n^2 \eta_D \right]^2 - n^2 \eta_D^2 \right\}}{\left\{ (1+\bar{P}_C) \left[(n+1)^2 - n^2 \eta_D \right]^2 - n^2 \eta_D^2 \right\}}} \quad (182)$$

In solving Equation (181) we therefore assume various values of P_C as an independent variable.

5. Optimization of a Static Eductor

From Reference 20:

$$\frac{J_2}{J_0} = \sqrt{(n+1)^2 \Delta \bar{p}_1 + \eta_D \left[1+n\sqrt{-\Delta \bar{p}_1} \right]^2} \quad (183)$$

But,

$$\frac{J_0}{J_a} = \frac{\Delta P_J - \Delta p_1}{\Delta P_J} = \frac{\frac{1}{2} \rho v_j^2}{\Delta P_j} = \frac{1}{\Delta P_j} \quad (184)$$

Therefore,

$$\frac{J_2}{J_a} = \left(\frac{J_2}{J_0} \right) \left(\frac{J_0}{J_a} \right) = \left(\frac{1}{\Delta P_j} \right) \sqrt{(n+1)^2 \Delta \bar{p}_1 + \eta_D \left[1+n\sqrt{-\Delta \bar{p}_1} \right]^2} \quad (185)$$

Differentiating with respect to $\Delta \bar{p}_1$, we find

$$-\Delta p_1 \Big|_{\text{opt}} = \frac{n^2 \eta_D^2}{\left[(n+1)^2 - n^2 \eta_D \right]^2} \quad (186)$$

$$\frac{J_2}{J_a} \Big|_{\text{opt}} = \frac{(n+1) \sqrt{\eta_D}}{\Delta \bar{P}_j \sqrt{(n+1)^2 - n^2 \eta_D}}. \quad (187)$$

Since

$$\begin{aligned} \frac{1}{2} \rho v_j^2 &= \Delta P_J - \Delta p_1 \\ &= \Delta P_J + \frac{n^2 \eta_D (\frac{1}{2} \rho v_j^2)}{\left[(n+1)^2 - n^2 \eta_D \right]^2} \end{aligned} \quad (188)$$

$$\left[1 - \frac{n^2 \eta_D^2}{\left[(n+1)^2 - n^2 \eta_D \right]^2} \right] = \frac{\Delta P_J}{\frac{1}{2} \rho v_j^2} = \Delta \bar{P}_J,$$

$$\frac{J_2}{J_a} \Big|_{\text{max}} = \frac{\left[(n+1)^2 - n^2 \eta_D \right]^2 (n+1) \sqrt{\eta_D}}{\left[(n+1)^2 - n^2 \eta_D \right]^2 - n^2 \eta_D^2 \sqrt{(n+1)^2 - n^2 \eta_D}}. \quad (189)$$

$$\text{As } n \rightarrow \infty, \frac{J_2}{J_a} \Big|_{\text{max}} \rightarrow \sqrt{\frac{\eta_D}{1-\eta_D}}, \quad (\eta_D \neq 1.0).$$

We can obtain the entrainment ratio n from the relationship

$$n = \left(\frac{A_1}{A_J} \right) \left(\frac{v_1}{v_j} \right) \quad (190)$$

since

$$\frac{1}{2} \rho v_1^2 = -\Delta p_1$$

$$v_1 = \sqrt{\frac{-2}{\rho} \Delta p_1} \quad (191)$$

and

$$n = \left(\frac{A_1}{A_J} \right) \left(\frac{\sqrt{-\Delta p_1}}{\sqrt{\Delta P_J - \Delta p_1}} \right).$$

In design, if we take the value of n to be the independent variable, then Equation (191) defines A_1/A_J ; that is,

$$\frac{A_J}{A_1} = \frac{1}{n} \sqrt{\frac{-\Delta p_1}{\Delta P_J - \Delta p_1}}. \quad (192)$$

Substituting Equation (102),

$$\left. \begin{aligned} \frac{A_J}{A_1} \Big|_{\text{opt}} &= \frac{\eta_D}{\sqrt{[(n+1)^2 - n^2 \eta_D]^2 + 2n^2 \eta_D^2}} \\ \text{or} \quad (n) \frac{A_J}{A_1} \Big|_{\text{opt}} &= \frac{\eta_D}{\sqrt{n^2 \left[\frac{(n+1)^2}{n^2} - \eta_D \right]^2 + 2\eta_D^2}} \end{aligned} \right\} \quad (193)$$

Note that the nozzle total pressure does not influence this optimum.

The exit area is obtained from the relationship

$$p_2 + \frac{1}{2}\rho v_2^2 = p_1 + \frac{1}{2}\rho v_m^2 \eta_D. \quad (194)$$

But,

$$A_2 v_2 = A_m v_m; \text{ therefore, } v_m = v_2 \frac{A_2}{A_m}.$$

Therefore,
$$\frac{1}{2}\rho v_2^2 \left[1 - \eta_D \left(\frac{A_2}{A_m} \right)^2 \right] = p_1 - p_2 = \Delta p_1$$

$$1 - \eta_D \left(\frac{A_2}{A_m} \right)^2 = \Delta \bar{p}_1 \left(\frac{v_j}{v_2} \right)^2. \quad (195)$$

Also, since $A_1 v_1 + A_J v_j = A_m v_m$

$$A_m = A_1 \frac{v_1}{v_m} + A_j \frac{v_j}{v_m}. \quad (196)$$

But

$$v_m = \frac{v_j + n v_1}{(n+1)};$$

therefore,

$$A_m = \frac{(A_1 v_1 + A_J v_j) (n+1)}{(n v_1 + v_j)} \quad (197)$$

$$\frac{A_m}{A_1} = \frac{\left(\frac{v_1}{v_j} + \frac{A_j}{A_1} \right) (n+1)}{\left(n \frac{v_1}{v_j} + 1 \right)} = \frac{\frac{A_J}{A_1} (n+1)^2}{\left[n^2 \frac{A_J}{A_1} + 1 \right]} \quad (198)$$

Note that as $n \rightarrow 0$,

$$\frac{A_J}{A_1} \rightarrow \eta_D, \frac{A_m}{A_1} \rightarrow \eta_D.$$

As, $n \rightarrow \infty$

$$n^2 \left(\frac{A_J}{A_1} \right) \rightarrow \frac{\eta_D}{1 - \eta_D} \left[= \left(\frac{J_2}{J_a} \right)^2 \right]$$

$$\frac{A_m}{A_1} \rightarrow \eta_D$$

since

$$\eta_D \left(\frac{A_2}{A_m} \right)^2 = 1 - \Delta p_1 \left(\frac{v_j}{v_1} \right)^2$$

$$\frac{A_2}{A_m} = \sqrt{\frac{1 - \Delta \bar{p}_1 \left(\frac{v_j}{v_2} \right)^2}{\eta_D}} \quad (199)$$

$$\frac{J_2}{J_o} = (n+1) \frac{v_2}{v_j}; \text{ therefore } \left(\frac{v_j}{v_2} \right)^2 = \frac{(n+1)^2}{\left(\frac{J_2}{J_a} \right)^2} \quad (200)$$

$$\left. \frac{J_2}{J_o} \right|_{\text{opt}} = \frac{(n+1) \sqrt{\eta_D}}{\sqrt{(n+1)^2 - n^2 \eta_D}}$$

$$\left. \Delta \bar{p}_1 \right|_{\text{opt}} = \frac{-n^2 \eta_D^2}{\left[(n+1)^2 - n^2 \eta_D \right]^2}.$$

Therefore,

$$\left.\frac{A_2}{A_m}\right|_{\text{opt}} = \frac{(n+1)}{\sqrt{\eta_D (n+1)^2 - n^2 \eta_D}} \tag{201}$$

Note that for the limit case, $\eta_D = 1.0$

$$\left.\frac{A_2}{A_m}\right|_{\eta_D=1} = \frac{(n+1)}{\sqrt{2n+1}}.$$

Also, as $n \rightarrow \infty$

$$\left.\frac{A_2}{A_m}\right|_{\text{opt}} \rightarrow \frac{1}{\sqrt{\eta_D(1-\eta_D)}}.$$

6. Optimization of a Recirculating Eductor

The "optimum eductor" concept is extended to include the effect of recirculation. Equation (211) of this section defines the maximum augmentation possible with recirculation, in compressible flow, and the results will of course be poorer for compressible flow.

It is shown that the performance of the optimum recirculating eductor is related directly to the optimum static eductor, by a factor $\left[1/\sqrt{1-\xi}\right]$, being the total head recovery in the jet. Thus a pressure recovery of 50 percent denotes a possible thrust increase of 41 percent, relative to the optimum static eductor with the same mass flow ratio. In development work we should aim at a pressure recovery of at least 80 percent therefore, which gives an increase of 124 percent.

Previously, it was shown that, if the diffuser exit static pressure p_2 is equal to ambient, then the augmentation factor is

$$\frac{J_2}{J_a} = \frac{1}{\Delta \bar{P}_J} \sqrt{\Delta \bar{P}_1 (n+1)^2 + \eta_D \left[1+n \sqrt{\Delta \bar{P}_C - \Delta \bar{P}_1} \right]^2} \quad (202)$$

where

Δ = denotes a gage pressure

P_C = the upstream total head

p_1 = the mixing pressure

n = the entrainment ratio

η_D = the diffuser efficiency

P_J = the total pressure of the primary nozzles

J_a = the primary nozzle thrust, when exhausting to ambient

J_2 = total eductor thrust.

The bar over a pressure (e.g., $\Delta \bar{p}_1$) denotes that the pressure is divided by $P_J - p_1 = \frac{1}{2} \rho v_J^2$.

By differentiating Equation (202) with respect to $\Delta \bar{p}_1$ and equating to zero we find the optimum value,

$$-\Delta \bar{p}_1 \Big|_{\text{opt}} = \Delta \bar{P}_C - \frac{n^2 \eta_D^2}{\left[(n+1)^2 - n^2 \eta_D \right]^2} \quad (203)$$

and hence,

$$\frac{J_2}{J_a} \Big|_{\text{opt}} = \frac{(n+1) \sqrt{\Delta \bar{P}_C \left[(n+1)^2 - n^2 \eta_D \right]} + \eta_D}{\Delta \bar{P}_J \sqrt{(n+1)^2 - n^2 \eta_D}} \quad (204)$$

In the static case, when $P_C = 0$,

$$\left(\frac{J_2}{J_a} \right)_{P_C=0} \Big|_{\text{opt}} = \frac{(n+1) \sqrt{\eta_D}}{\Delta \bar{P}_J \sqrt{(n+1)^2 - n^2 \eta_D}} \quad (205)$$

Therefore,

$$\left(\frac{J_2}{J_a}\right)_{\text{opt}}^2 = \left(\frac{J_2}{J_a}\right)_{P_C=0}^2 + (n+1)^2 \left(\frac{\Delta P_C}{\Delta P_J}\right) \frac{1}{\Delta \bar{P}_J}, \quad (206)$$

the second term being the effect of the increase above ambient of the inlet total head.

Now, since

$$\frac{J_2}{J_a} = \left(\frac{1}{\Delta \bar{P}_J}\right) \left(\frac{J_2}{J_o}\right) = \left(\frac{(n+1)}{\Delta \bar{P}_J}\right) \left(\frac{v_2}{v_j}\right) \quad (207)$$

$$v_2 = \Delta \bar{P}_J \left(\frac{J_2}{J_a}\right) \frac{v_o}{(n+1)} \quad (208)$$

$$\frac{\Delta P_2}{\Delta P_J} = \frac{\frac{1}{2} \rho v_2^2}{\Delta P_J} = \Delta \bar{P}_J \left(\frac{J_2}{J_a}\right)^2 \frac{1}{(n+1)^2}$$

$$\frac{\Delta P_C}{\Delta P_J} = \xi \frac{\Delta P_2}{\Delta P_J} = \frac{\xi \Delta \bar{P}_J}{(n+1)^2} \left(\frac{J_2}{J_a}\right)^2. \quad (209)$$

Substituting in Equation (206),

$$\left(\frac{J_2}{J_a}\right)^2 = \left(\frac{J_2}{J_a}\right)_{P_C=0}^2 + \xi \left(\frac{J_2}{J_a}\right)^2 \quad (210)$$

Therefore,

$$\frac{J_2}{J_a}_{\text{opt}} = \frac{1}{\sqrt{1-\xi}} \left(\frac{J_2}{J_a}\right)_{P_C=0}, \quad (211)$$

ξ being the total head recovery factor.

Thus optimum static eductor curves can be used directly to find the optimum augmentation possible with recirculation.

For,

$\xi =$	20%	40%	60%	80%	90%
$\frac{1}{1-\xi} =$	1.117	1.29	1.58	2.235	3.16

In other words, the thrust increase due to recirculation is not particularly large under optimum conditions, until the total head loss falls below 20 percent.

7. Detailed Recommendations on Present Eductor Design

- a. Determine and use the optimum mixing pressure, using the theory developed in this section.
- b. Reduce primary nozzle size and increase the number of nozzles in order to improve mixing, even to the point of using more rows of nozzles.
- c. Reduce the pressure losses due to the primary nozzle installations by fairing the air supply tubes inside the eductor.
- d. Redesign ducting to give zero pressure gradient on the inside wall and combine this with a centrifugal diffuser to minimize pressure gradient due to diffusion. Such a diffuser requires cascade turning vanes at its exit.
- e. Apply boundary layer suction to the inside of the duct corner, in order to reduce turning losses and improve the diffuser efficiency by use of a "streamline diffuser".

- f. Study the effect of nonuniform (exit) total head distribution on cushion pressure (in order to assess the losses, if any, associated with this) and the optimum distribution to be aimed at.
- g. Maintain the correct mean mixing pressure while the airflow is being turned.

PROPULSION INVESTIGATION

OFF-BOARD

From previous investigations (Reference 4) it was shown that larger quantities of primary air, delivered at a lower pressure than was originally used (Reference 1) would significantly improve the performance of the vehicle. Approximately 30 pounds of air per second at 5 to 10 pounds per square inch (gage) is required. It appears that this requirement is rather unusual, by conventional air compressor standards, and there are no airborne type engine-compressor units available. Therefore, as a part of this preliminary design effort, an investigation was conducted to determine the feasibility of providing an acceptable unit from standard production (GFE) components.

Numerous components had been considered and the final choice of the Continental Aviation Corporation J-69 first stage compressor and the General Electric Company T-58 engine was made for the following reasons:

1. Availability (as GFE);
2. Compatibility with air flow requirements;
3. Compatibility of engine and compressor (speed of rotation, ducting torque, etc.);
4. Extent of modification required;
5. Service and maintenance support.

The objective was to combine these two units (T-58 engine and J-69 compressor) in an off-board test setup and perform a functional test of this marriage. Figures 128 through 132 show the off-board test

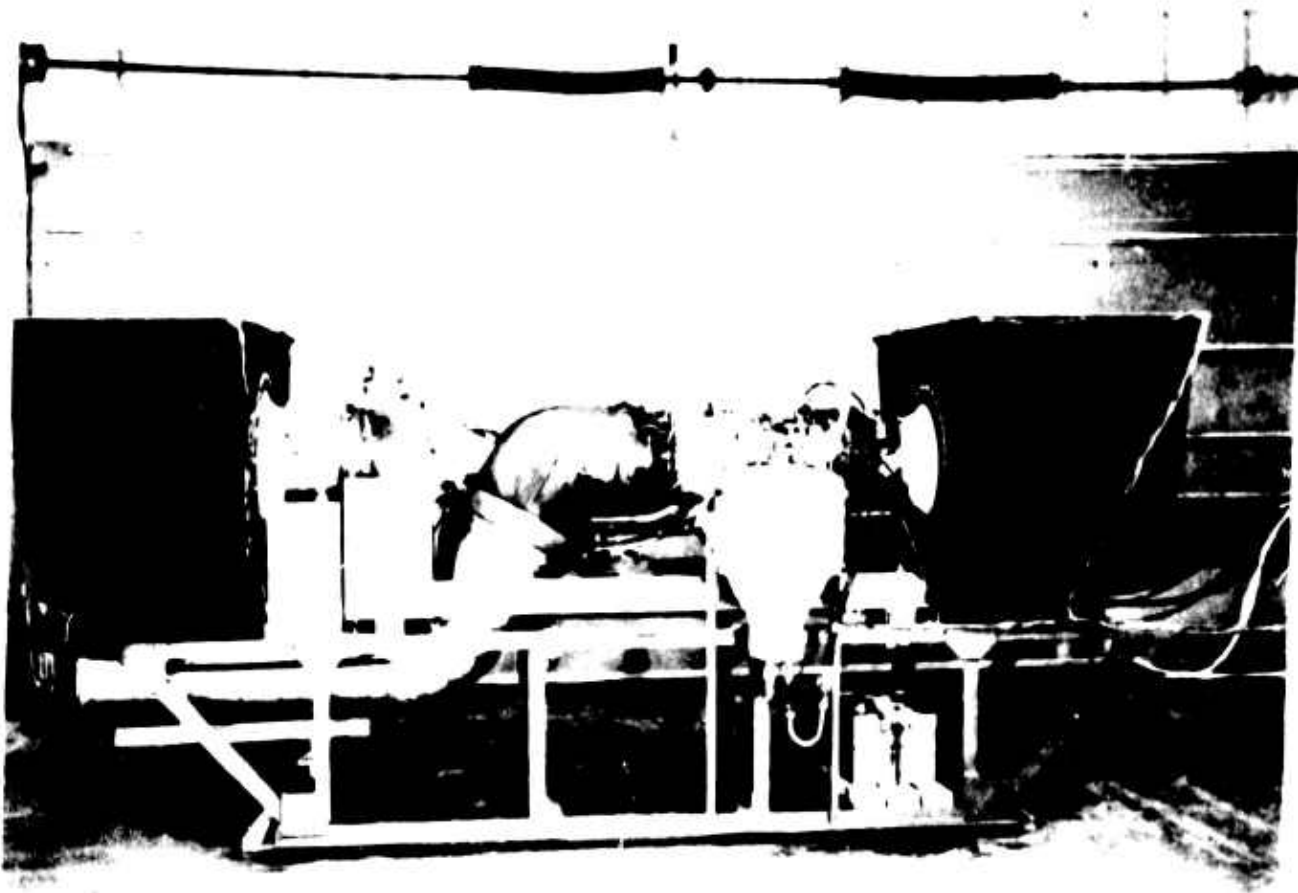


Figure 128. Propulsion Unit, Assembled, Side View

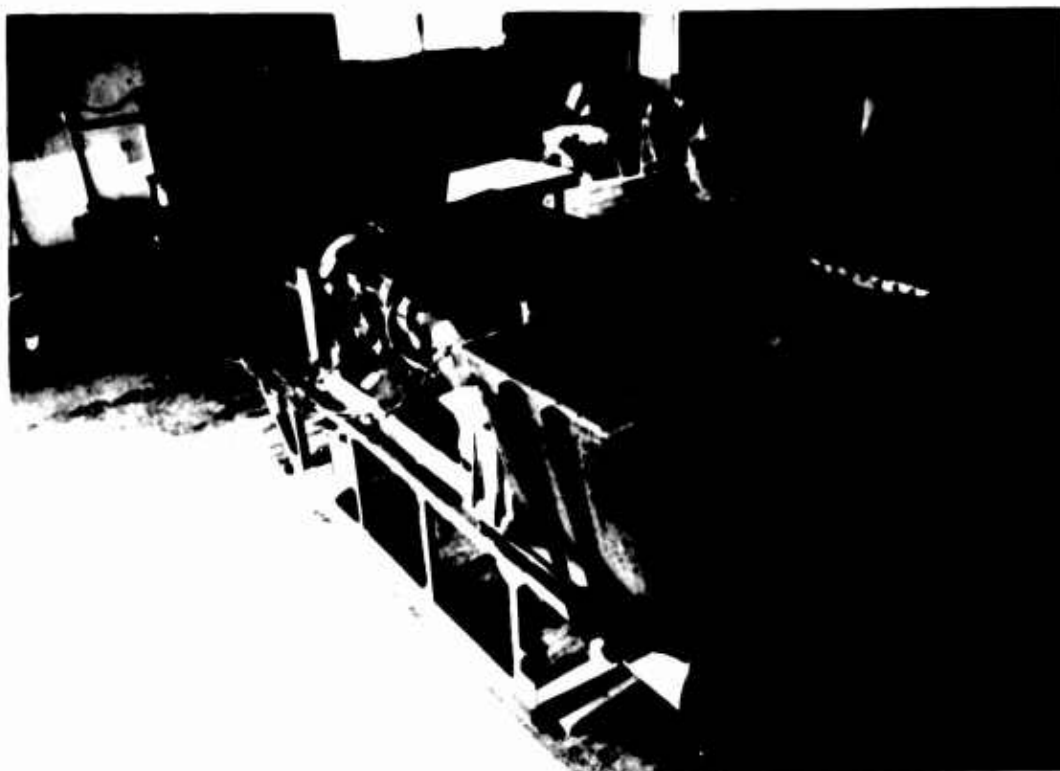


Figure 129. Propulsion Unit, Assembled, Rear View

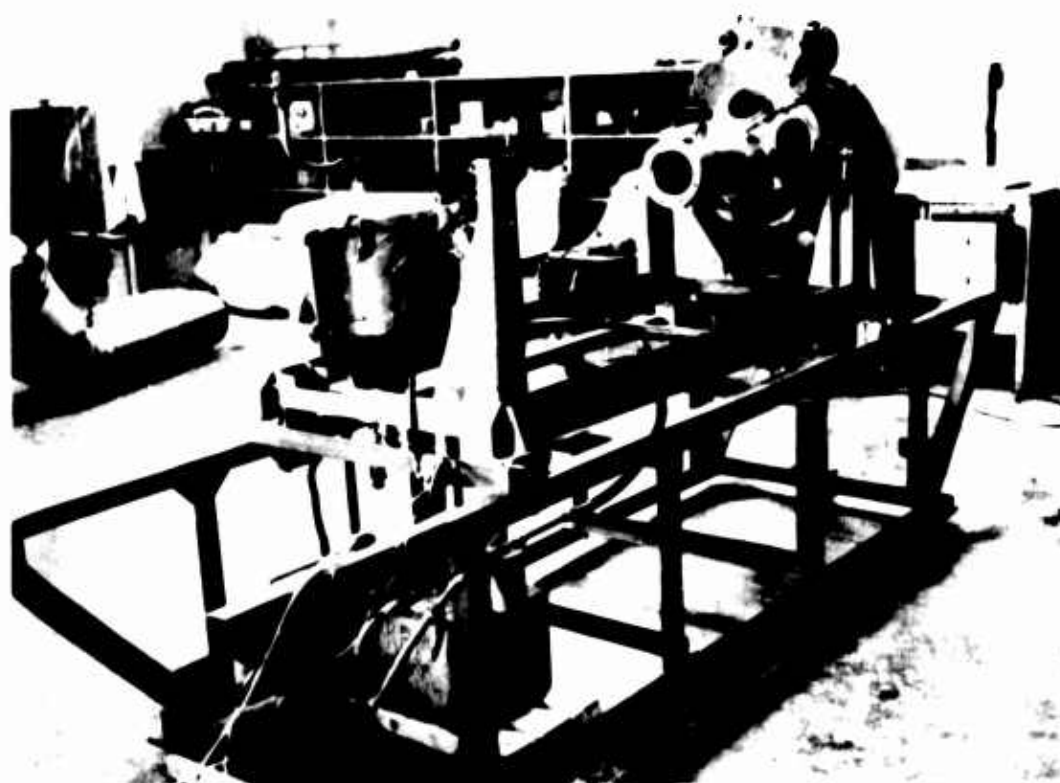


Figure 130. Propulsion Unit, Test Stand

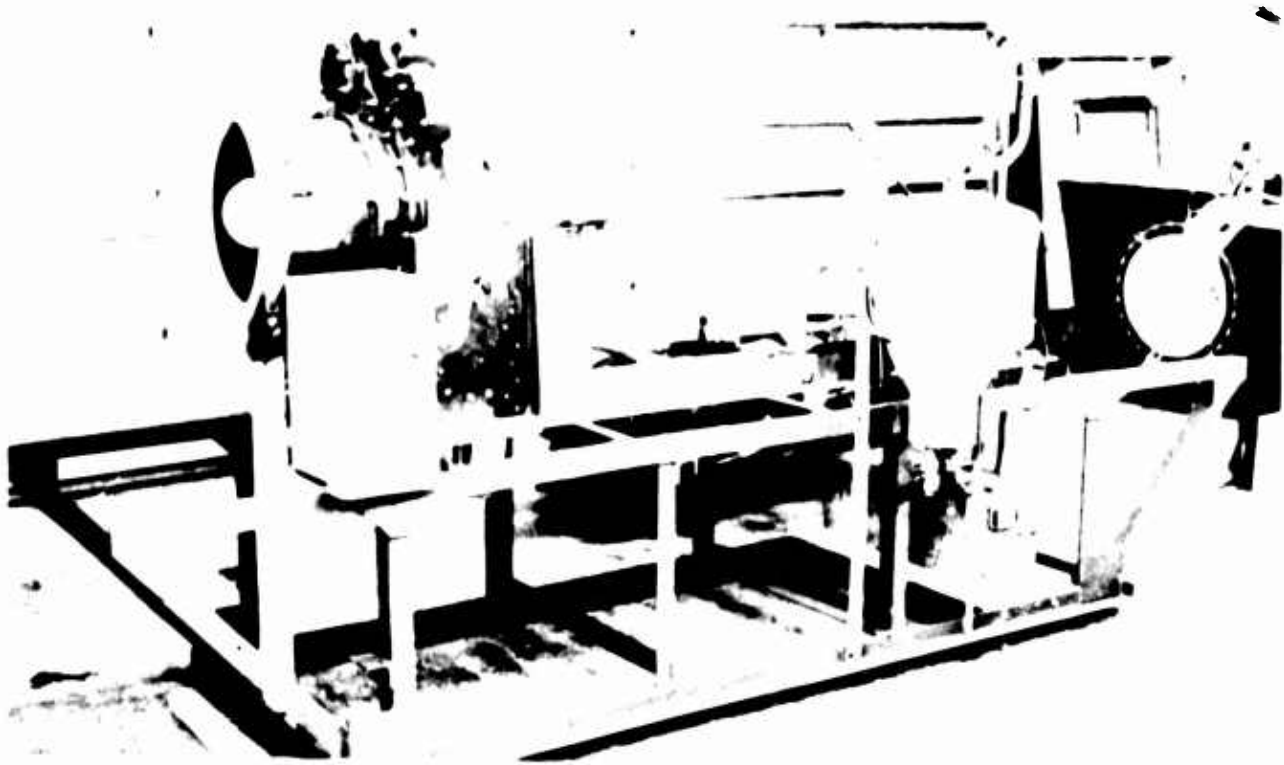


Figure 131. Propulsion Unit, Compressor, Front View

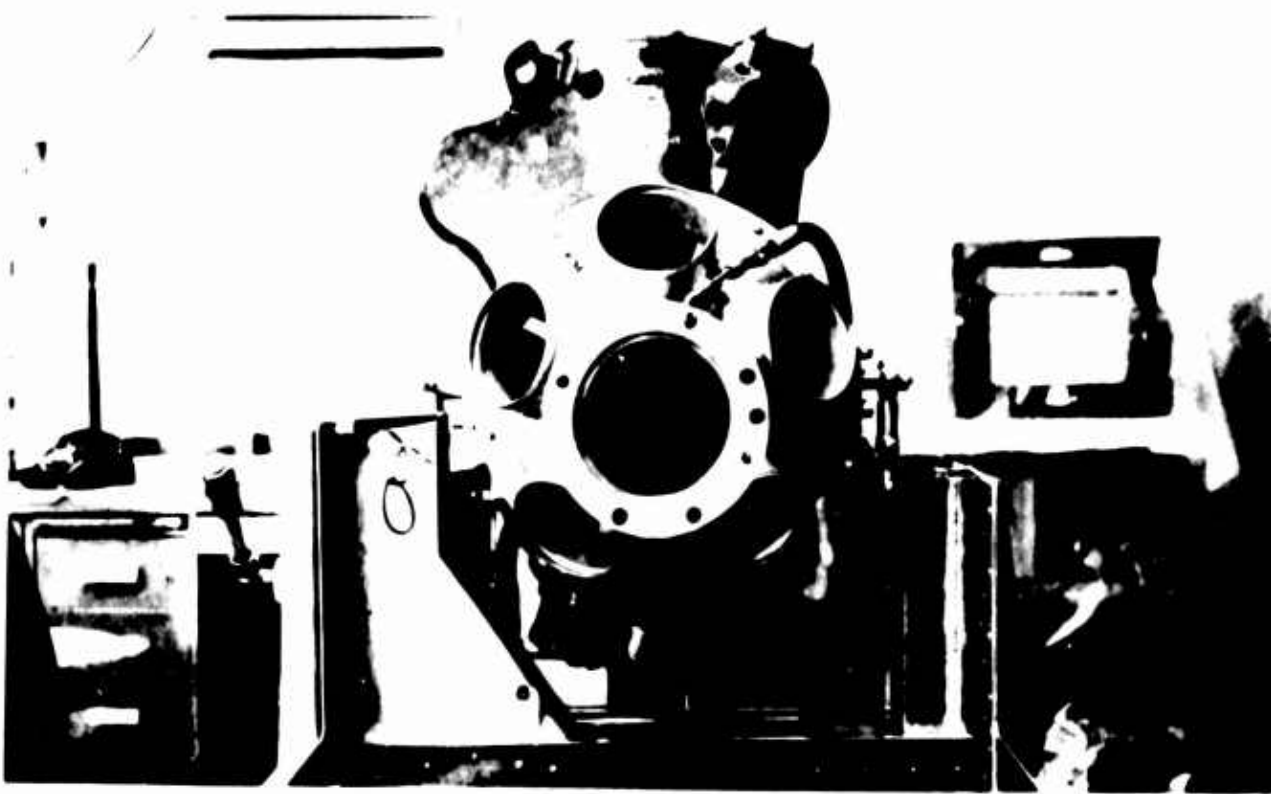


Figure 132. Propulsion Unit, Compressor, Rear View

setup in varying stages of completion. The following drawings show the details of the marriage as well as the installation, support structure, electrical and lubrication schematics, etc.

GB 2102 - Turbine and Compressor, Installation

GB 2103 - Turbine and Compressor Mount and Connection (2 sheets)

GB 2106 - Turbine and Compressor Instrumentation and Operation

GB 2107 - Turbine and Compressor Drive Shaft

Tests were performed on this unit as summarized below:

1. Over 60 starts were made with no problem;
2. Manual control of power (speed) is satisfactory;
3. Vibration pickups indicated an initial out of balance condition which was subsequently corrected;
4. Over 4 hours of intermittent operating time were accumulated on the unit; the last run was at 80 to 95 percent power for 1 hour;
5. The T-58 and J-69 appear to be matched reasonably well as there was no indication of a resonant or vibratory condition due to either mechanical or aerodynamic coupling;

6. The output of the compressor (manflow and total head) at maximum speed correlates well with the compressor map furnished by Continental. In addition, the distribution of the air in the five exhaust ports (shown in Figures 130 and 132) was uniform.

It is concluded that this union of the T-58 and J-69 is feasible and, in fact, would require only minor modifications for the on-board installation.

As was predicted by representatives from both the General Electric Company and Continental Aircraft Engineering Corporation, the most difficult part of accomplishing this marriage involved the alignment and precision dynamic balancing of the high speed rotating parts.

ON-BOARD

The majority of the details of the vehicle propulsion installation have been discussed elsewhere in this report, such as:

1. The engine installation drawings are tabulated under "Vehicle Characteristics" on page 20 with the complete set of vehicle drawings, and in the above "Off-Board" discussion.
2. The propulsion control is also discussed in "Vehicle Characteristics" as integrated with the vehicle controls.
3. A weight breakdown of the propulsion components was in Table I.
4. The output of the unit, mass flow and pressure was shown in Figures 69 and 70.
5. To provide forward propulsion, as described in a previous section, 100 to 150 pounds of residual thrust from the T-58 will be used.

One remaining factor to consider is the anticipated loss of total head between the exit of the J-60 compressor and primary nozzle header. A preliminary estimate of the worst condition is shown in Figure 133 and in Table IX. A maximum total loss of 0.84 psi is predicted for the assumed plumbing, of which 0.51 psi occurs between stations 1 and 3. This is considered to be greatly in excess of what can be obtained. A more realistic estimate of 0.50 psi maximum total head loss is estimated, primarily, by cleaning up the plumbing between stations 1 and 3 (Table X).

TABLE X

<u>P_o Loss</u>	
Station	P _r (psi)
1 - 2	0.350
2 - 3	0.161
3 - 4	0.032
4 - 5	0.031
5 - 6	0.027
6 - 7	0.027
7 - 8	0.078
8 - 9	0.019
9 - 10	0.011
10 - 11	0.033
11 - 12	0.015
12 - 13	0.059
	<u>0.838</u>

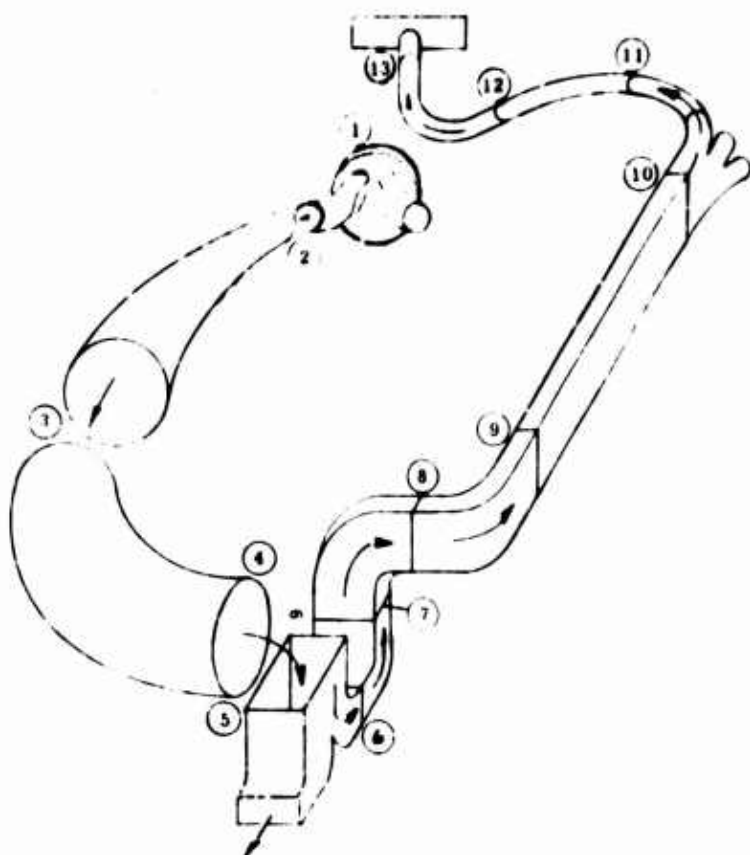


Figure 133. Primary Pressure Duct System
Critical Path Stations

Jet Thrust Factor versus Jet Pressure Ratio
for Full Isentropic Expansion
(Convergent-Divergent Nozzles)

$$F_j/W_g = \sqrt{\frac{2\gamma R}{\gamma(\gamma-1)}} \left[1 - \left(\frac{P_{tj}}{P_{sa}} \right)^{\frac{1}{0.2857}} \right] \sqrt{T_{tj}}$$

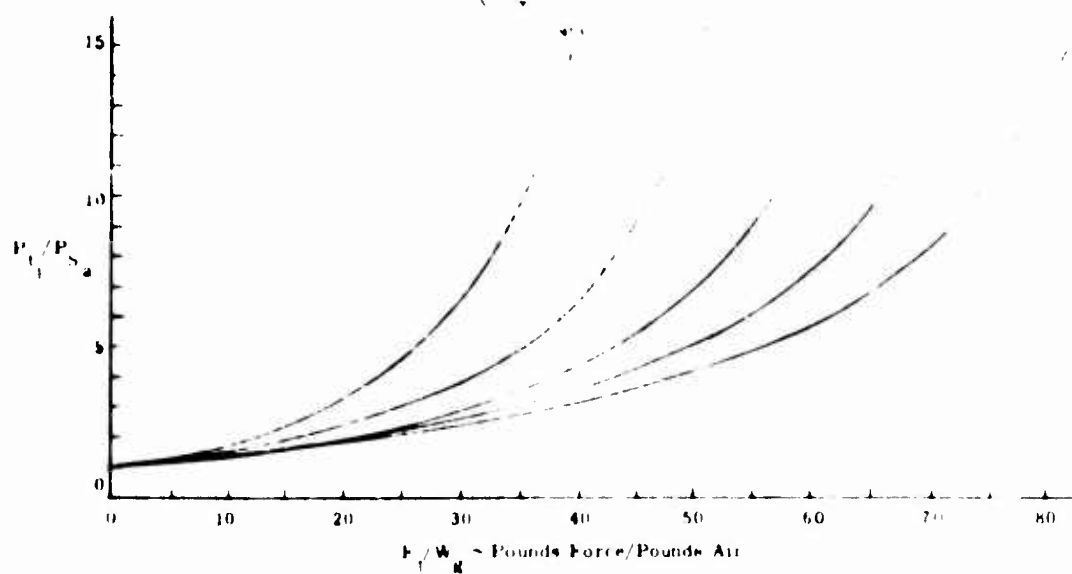


Figure 134. Jet Thrust Versus Jet Pressure
($P_{tj}/P_{sa} = 0$ to 15)

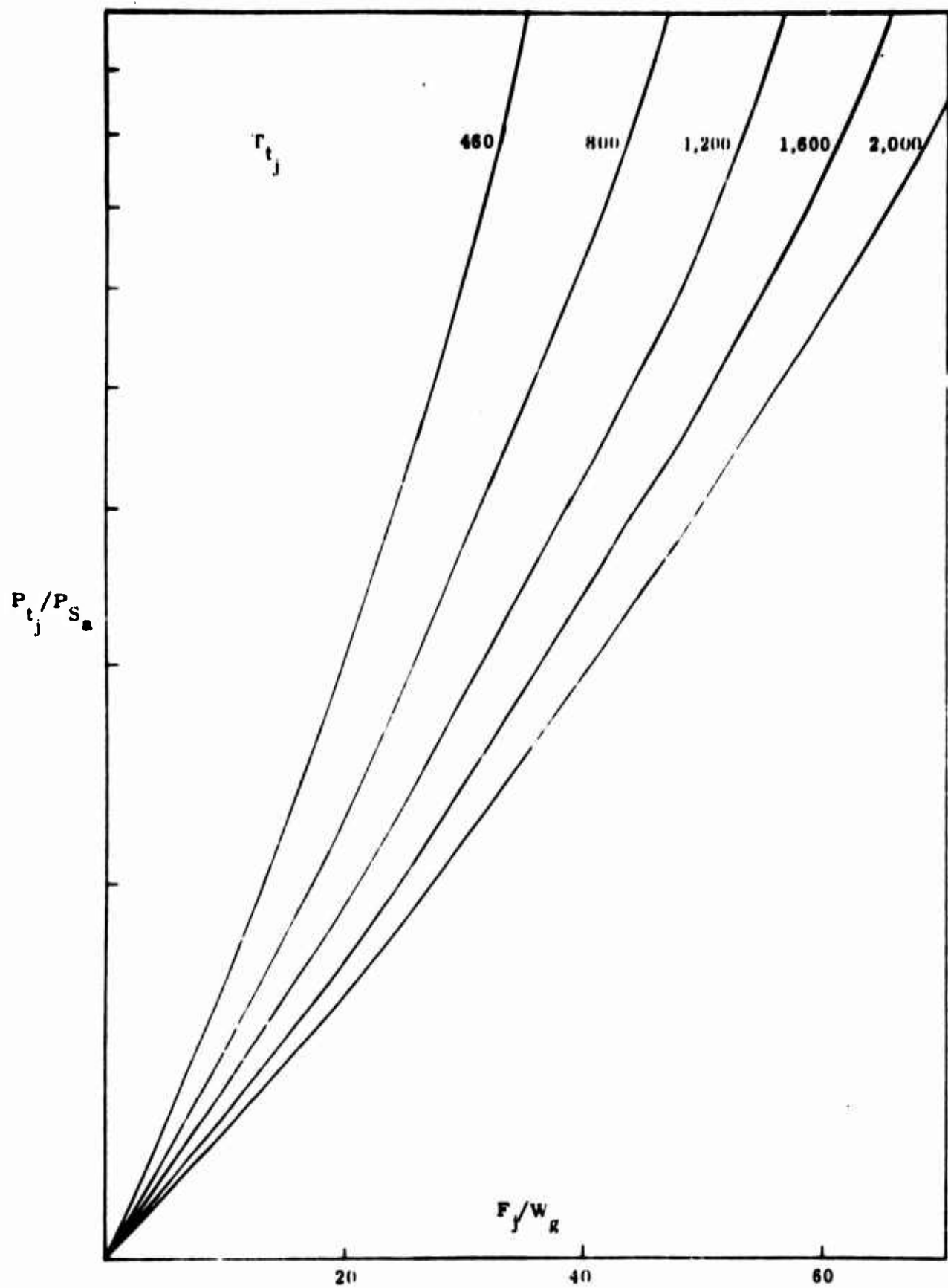


Figure 135. Jet Thrust Versus Jet Pressure Ratio ($P_{tj}/P_{s_a} = 0$ to 7)

BIBLIOGRAPHY

1. Ortell, A., et al., "Recirculation Principle for Ground Effect Machine: Two-Dimensional Tests", TCREC 62-66, U.S. Army Transportation Research Command, Fort Eustis, Virginia, January 1962
2. Vinson, P., et al., "Recirculation Principle for Ground Effect Machine: Three Dimensional Tests", TCREC 62-74, U.S. Army Transportation Research Command, Fort Eustis, Virginia, July 1962
3. Vinson, P., et al., "Recirculation Principle for Ground Effect Machine: MCTV Preliminary Flight Test Results", TCREC 62-100, U.S. Army Transportation Research Command, Fort Eustis, Virginia, December 1962
4. Cossairt, K., et al., "Recirculation Principle for Ground Effect Machines: Investigations of Improvements by Major Modifications to MCTV", TCREC 63-27, U.S. Army Transportation Research Command, Fort Eustis, Virginia
5. Report SR-13534-9, "A Generalized Approach to the Definition of Average Flow Quantities in Non-Uniform Streams", United Aircraft Corporation, dated December 1955
6. Walker, N. K., "Some Notes on the Lift and Drag of Ground Effect Machines", Proceedings of the National Meeting on Hydrofoils and Air Cushion Vehicles, Washington, D. C., I.A.S., September 1962
7. Chaplin, H. R., "Design Study of a 29Foot GEM", David Taylor Model Basin Report 1521 (Aero 949), April 1961
8. Walker, N. K., "Stability Control and Handling Criteria for Ground Effect Machines": I.A.S. Paper 61-49
9. Naval Analysis Report, "A Study of the Operational Feasibility of the Ground Effect Machine in the Amphibious Support Mission", ONR Report ACR/NAR-26, Washington, D. C., November 1962
10. Walker, N. K., "The Use of Tracking Tasks as Indicators of Stress", Norman K. Walker Associates, Inc. Report No. 4

11. **"Dragonfly Feasibility Study - Appendix No. 3" Control and Guidance Division, Johns Hopkins University Applied Physics Laboratory, 1960**
12. **Pegg, R. J. and Connor, A. B., "Effects of Control Response Characteristics on the Capability of a Helicopter as a Gun Platform", NASA Technical Note D-464, September 1960**
13. **Johnson, A. E., "Phase II Tethered and Low-Speed Free Flight Tests of GEM III". David Taylor Model Basin Report 1700 (Aero 1049), December 1962**
14. **Anderson, B. W., Boyle, R. V., Becker, O. A. "Progress Report of GEM Control Systems Study", Contract Nonr 3173 Report No. AP-5061-R AiResearch Manufacturing Company, December 1962**
15. **Payne, P. R., "An Introduction to Ground Effect Machine Recirculation Theory", Frost Engineering Report No. 142-6, February 1963**
16. **Payne, P. R., "An Introduction to Ground Effect Machine Recirculation Theory", Frost Engineering Report No. 142-2, January 1963**
17. **Payne, P. R., "Viscous Mixing of Two-Dimensional Jets with Particular Reference to Jets in Ground Proximity", Frost Engineering Report No. 197-4**
18. **Chaplin, H. R., "Effect of Jet Mixing on the Annular Jet", David Taylor Model Basin Report 1375, February 1959**
19. **Payne, P. R., "Preliminary Studies of the Application of Peripheral Fans in Ground Effect Machines", Frost Engineering Report 142-18, October 1963**
20. **Payne, P. R., "A Contribution to the Theory of Thrust Augmentors", Frost Engineering Report 197-2, August 1963**

APPENDIX I

THE CASE FOR THE SIMPLE AUTOPILOT*

INTRODUCTION

Often the magnitude of the penalty which must be paid for inherent stability in pitch and roll is not appreciated. The stabilizing airflow used in the compartmenting jets has been shown not only to produce no contribution to lift but also to distort severely the design of the main lift ducts and reduce their efficiency. Other performance penalties arise in structural weight and in momentum drag.

Since the expensive turbine engine is the major cost of a GEM, it is evident that considerable savings could result from exchanging stabilizing jet power for an autopilot.

The results are examined in this appendix.

GENERALIZED PERFORMANCE AND COST OF GEM

Insufficient information is available on the Martin recirculating GEM to assess the value of an autopilot. However, a recent ONR (ACR/NAR 26) study derived cost and performance data for a whole family of Ground Effect Machines, and as there has been no serious criticism of the overall result, this study forms a suitable basis for comparison.

PERFORMANCE AND COST ESTIMATES FOR THE INHERENTLY STABLE GEM

The ONR report showed that the ordinary annular jet GEM hovering at a 3-foot ground clearance was uneconomical as a transfer vehicle as compared to an improved machine fitted with 2-foot long flexible trunks with only one foot of air wall clearance.

*By N. K. Walker and R. J. Neal, Walker Associates, Bethesda, Md.

The latter has therefore been used as a basis for comparison and the detailed assumptions made below:

Performance

Range is 200 nautical miles at 60 knots with a 1-foot air wall clearance, and a 2-foot flexible skirt.

Lift Power

The appropriate Liberatore figure of merit is 5.0, giving lift power = $0.155 P_b \sqrt{W}$ where P_b = base loading (pounds/square foot) W = gross weight (pounds)

Drive Power

Momentum drag power is $0.182 \times$ lift power at the design speed of 60 knots.

Profile drag power (including cushion drag) is calculated on the assumption of a drag coefficient of 1.0 on the whole frontal area of the machine including the cushion.

In both cases a propulsive efficiency of 70 percent is assumed.

Weight

The structural weight is taken as $0.175 \times$ gross weight plus 5 pounds/square foot of base area. To this is added an allowance of 1.1 pounds per installed horsepower,

and the residue of the gross weight is assumed to be the payload.

Costs

The costs in production numbers of 200 are based on \$6 per pound of structure, plus \$70 per horsepower.

Tabulated results for three sizes of machines follow: Tables XI, XII, and XIII.

TABLE XI**"AMPHIBIAN" GEM****33.5 ft long x 13.5 ft wide; base area = 339 sq ft**

Base Loading (lb/sq ft)	50 psf	75 psf	100 psf
Gross Weight (lb)	16,950	25,450	33,900
Lift Power (hp)	1,010	1,850	2,850
Profile Drag Power (hp)	419	419	419
Momentum Drag Power (hp)	263	481	741
Total Installed Power (hp)	1,692	2,750	4,010
Fuel Weight (lb)	3,385	5,500	8,020
Structure Weight (lb)	4,670	6,150	7,630
Fixed Weight (lb)	650	650	650
Power Plant (lb)	1,860	3,030	4,410
Trunks (lb)	375	375	375
Payload	6,010	9,745	12,815

Costs

Power Plant	\$118,500	\$192,500	\$281,000
Structure	28,000	36,900	45,800
Total Cost	\$146,500	\$229,400	\$326,800

**Cost per Pound
of Payload**

\$24.3	\$23.6	\$25.5
---------------	---------------	---------------

TABLE XII**"SMALL" GEM****50 ft x 21 ft; base area = 740 sq ft**

Base Loading (lb/sq ft)	50 psf	75 psf	100 psf
Gross Weight (lb)	37,000	55,500	74,000
Lift Power (hp)	1,470	2,720	4,180
Profile Drag (hp)	1,000	1,000	1,000
Momentum Drag (hp)	400	720	1,100
Total Power	2,870	4,440	6,280
Fuel Weight (lb)	5,740	8,880	12,560
Structure Weight (lb)	10,150	13,400	16,600
Fixed Weight (lb)	650	650	650
Power Plant (lb)	3,150	4,890	6,910
Trunks (lb)	570	570	570
Payload	16,740	27,110	36,790

Costs

Power Plant	\$200,900	\$310,800	\$439,000
Structure	60,900	80,000	90,000
Total Cost	\$261,800	\$390,800	\$538,000
 Cost per Pound of Payload	 \$15.6	 \$14.4	 \$14.65

TABLE XIII

"LARGE" GEM

100 ft x 45 ft; base area = 3,540 sq ft

Base Loading(lb/sq ft)	50 psf	75 psf	100 psf
Gross Weight (lb)	177,000	266,000	354,000
Lift Power (hp)	3,770	5,970	9,170
Profile Drag (hp)	2,430	2,430	2,430
Momentum Drag (hp)	990	1,570	2,420
Total Power (hp)	7,190	9,970	14,020
Fuel Weight (lb)	14,380	19,940	28,040
Structure Weight (lb)	48,700	61,100	79,700
Fixed Weight (lb)	650	650	650
Power Plant (lb)	7,910	10,950	15,440
Trunks (lb)	1,160	1,160	1,160
Payload	104,190	172,190	229,010

Costs

Power Plant	\$503,000	\$697,000	\$982,000
Structure	292,000	367,000	478,000
Total Cost	\$795,000	\$1,064,000	\$1,460,000

Cost per Pound of Payload	\$7.6	\$6.2	\$6.35
------------------------------	-------	-------	--------

PERFORMANCE AND COST ESTIMATE FOR AUTO-STABILIZED GEMS

Performance and cost figures are generated in exactly the same way for the same three sizes of GEMs using an automatic pilot to stabilize the machine in pitch and roll.

The changes made to the critical assumptions are as follows:

Performance

Remains unchanged.

Lift Power

Assume that the appropriate Liberatore figure of merit is now 6.0, not 5.0, following the results presented in ONR Report ACR/NAR 26. This cuts the lift power by the factor 5/6.

Drive Power

Same method, but the reduction in lift power results in a reduction of momentum drag.

Weights

Same method as before, but the reduced total power will save power plant weight and fuel. No allowances made for the autopilot weight since it will be very small and will be offset by a saving in structural weight due to elimination of the stabilizing jets.

Costs

Estimated as before, and an allowance of \$3,000 plus \$1 per lift horsepower is made for the cost of the autopilot. (This may seem a low figure, but is supported by cost quotations for light aircraft autopilots.)

The results of the revised estimates are given in Tables XIV, XV, and XVI which follow.

A further series of cost and payload estimates has been made, based on the further assumption that the elimination of stabilizing jets will permit a reduction in structural weight of 10 percent. These are included in Tables XIV, XV, and XVI.

TABLE XIV

"AMPHIBIAN" GEM (WITH AUTOPILOT)

33.5 ft long x 13.5 ft wide; base area = 339 sq ft

Base Loading (lb/sq ft)	50 psf	75 psf	100 psf
Gross Weight (lb)	16,950	25,450	33,900
Lift Power (hp)	841	1,540	2,370
Profile Drag Power (hp)	419	419	419
Momentum Drag Power (hp)	219	401	618
Total Installed Power (hp)	1,479	2,360	3,407
Fuel Weight (lb)	2,960	4,720	6,810
Structure Weight (lb)	4,670	6,150	7,630
Fixed Weight (lb)	650	650	650
Power Plant Weight (lb)	1,630	2,600	3,740
Trunks Weight (lb)	375	375	375
Payload Weight (lb)	6,665	10,955	14,695
Costs			
Power Plant	\$103,600	\$165,200	\$238,500
Structure	28,000	36,900	45,800
Autopilot	3,840	4,540	5,370
Total Cost	\$135,440	\$206,640	\$289,670
Cost per Pound of Payload	\$20.4/lb	\$18.9/lb	\$19.7/lb
Results if structural weight reduced 10%			
Payload (lb)	7,132	11,570	15,460
Cost	\$132,640	\$204,720	\$285,140
Cost per Pound of Payload	\$18.6/lb	\$17.7/lb	\$18.45/lb

TABLE XV

"SMALL" GEM (WITH AUTOPILOT)

50 ft long x 21 ft wide; base area = 740 sq ft

Base Loading (lb/sq ft)	50 psf	75 psf	100 psf
Gross Weight (lb)	37,000	55,500	74,000
Lift Power (hp)	1,225	2,270	3,485
Profile Drag Power (hp)	1,000	1,000	1,000
Momentum Drag Power (hp)	335	600	915
Total Installed Power	2,560	3,870	5,400
Fuel Weight (lb)	5,120	7,760	10,800
Structure Weight (lb)	10,150	13,400	16,600
Fixed Weight (lb)	650	650	650
Power Plant Weight (lb)	3,810	4,260	5,940
Trunks Weight (lb)	570	570	570
Payload Weight (lb)	17,700	28,860	39,440
Costs			
Power Plant	\$179,200	\$270,400	\$378,000
Structure	60,900	80,400	99,600
Autopilot	4,220	5,270	6,490
Total Cost	<u>\$244,330</u>	<u>\$356,570</u>	<u>\$484,090</u>
Cost per Pound of Payload	\$13.8/lb	\$12.35/lb	\$12.3/lb
Results if structure weight reduced by 10%			
Payload (lb)	18,720	30,200	41,100
Cost	\$238,240	\$348,030	\$474,130
Cost per Pound of Payload	\$12.7/lb	\$11.5/lb	\$11.5/lb

TABLE XVI

"LARGE GEM (WITH AUTOPILOT)

100 ft long x 45 ft wide Base Area = 3,540 sq ft

Base Loading (lb/sq ft)	50 psf	75 psf	100 psf
Gross Weight (lb)	177,000	266,000	354,000
Lift Power (hp)	3,140	4,980	7,640
Profile Drag Power (hp)	2,430	2,430	2,430
Momentum Drag Power (hp)	819	1,290	1,980
Total Installed Power	6,389	8,700	12,050
Fuel Weight (lb)	12,750	17,400	24,100
Structure Weight (lb)	48,700	61,100	79,700
Fixed Weight (lb)	650	650	650
Power Plant Weight (lb)	7,020	9,550	13,250
Trunks Weight	1,160	1,160	1,160
Payload	106,720	176,140	235,140
Costs			
Power Plant	447,000	609,000	843,000
Structure	292,000	367,000	478,000
Autopilot	6,140	7,980	10,640
Total Cost	\$745,140	\$983,980	\$1,331,640
Cost per Pound of Payload	\$7.0/lb	\$5.6/lb	\$5.65/lb
Results if structural weight reduced 10%			
Payload (lb)	111,590	182,250	243,110
Cost	\$715,940	\$947,280	\$1,283,840
Cost per Pound of Payload	\$6.4/lb	\$5.2/lb	\$5.3/lb

RESULTS

The results are shown in Figures 136 and 137 and are also given in Table XVII for the typical bore loading of 75 pounds per square foot.

TABLE XVII
COST AND PAYLOAD ESTIMATES FOR
INHERENTLY STABLE GEMS

	Amphibian	Small	Large
Base Estimates for Inherently Stable Gems			
Payload	9,745 lb	27,120 lb	172,190 lb
Installed Power	2,750 hp	4,440 hp	9,970 hp
Cost	\$229,400	\$391,000	\$1,064,000
Cost per Pound Payload	\$23.6/lb	\$14.4	\$6.2
Results for Autopilot GEM - No Structural Weight Savings			
Payload	10,955 lb	28,860 lb	176,140
Installed Power	2,360 hp	3,870 hp	8,700
Cost	\$206,640	\$356,070	\$973,980
Cost per Pound Payload	\$18.9/lb	\$12.4/lb	\$5.6/lb
Results for Autopilot GEM with 10% Saving of Structure Weight			
Payload	11,570 lb	30,200 lb	182,250 lb
Installed Power	2,360 hp	3,870 hp	8,700 hp
Cost	\$204,720	\$348,030	\$947,280
Cost per Pound Payload	\$17.7/lb	\$11.5/lb	\$5.2/lb

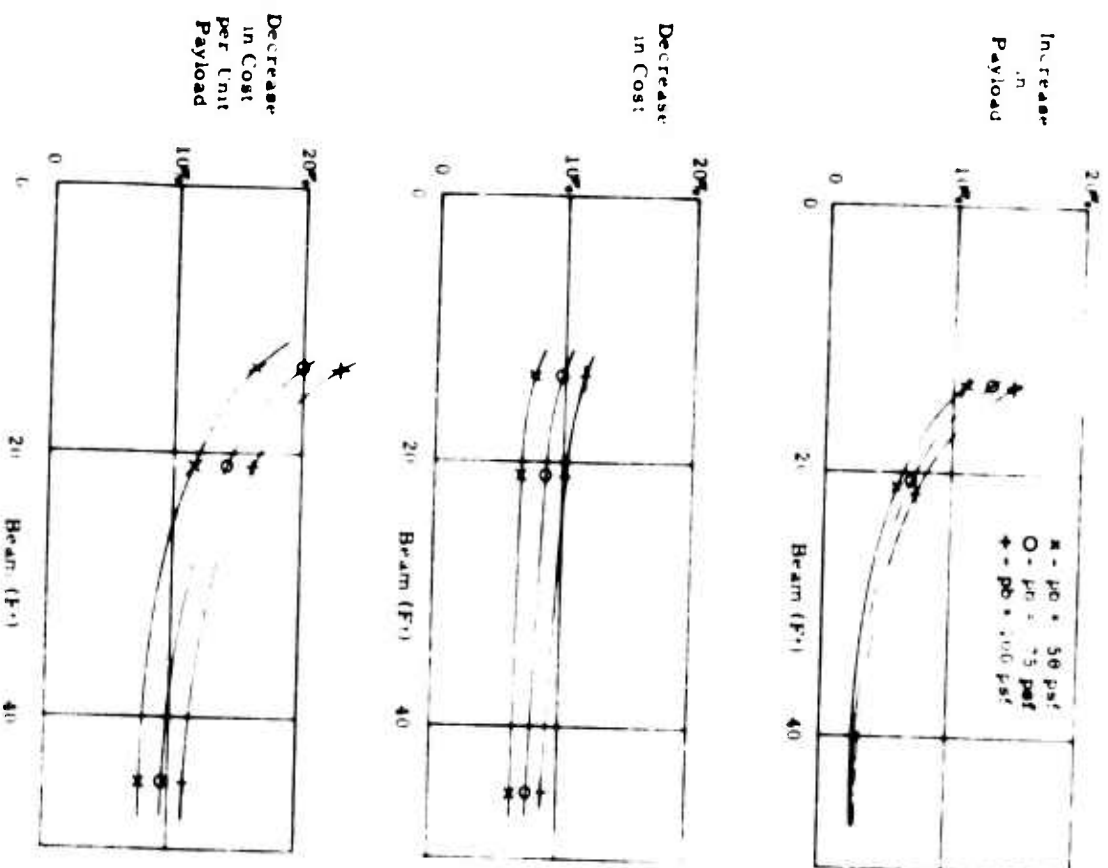


Figure 136. Improvement in GEM Performance and Cost Due to the Use of an Autopilot - No Allowance for Structural Weight Savings

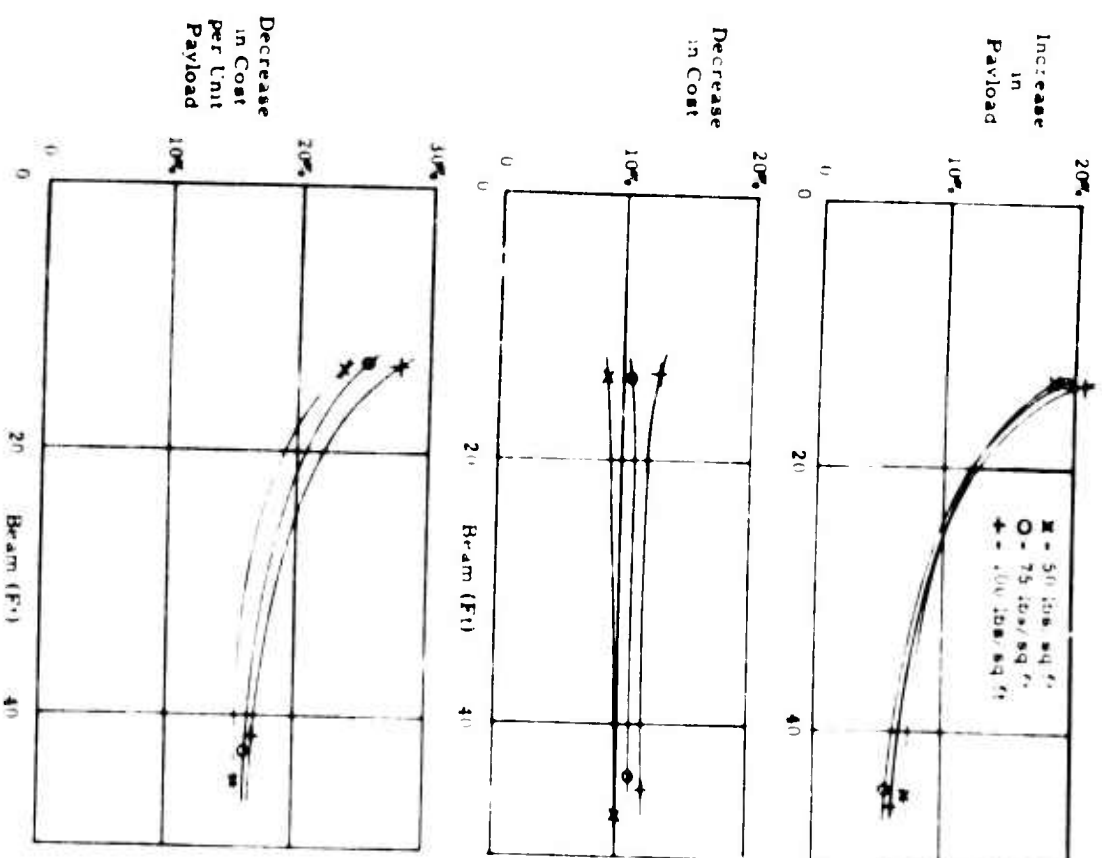


Figure 137. Improvement in GEM Performance and Cost Due to the Use of an Autopilot - Allowing 10 Percent Reduction in Structural Weight

The results show that for all sizes of machine there is a significant decrease in cost per pound of payload of from 10 percent to 20 percent, even if no allowance is made for the simplification of the structure that is made possible by omitting the compartmenting jets.

The cost of these jets is quite high in terms of weight, and Appendix II shows that wave impacts are less likely and less severe for a GEM with an autopilot, so an appreciable reduction in structural weight should be possible.

The second set of figures shows that the effect of a 10-percent saving in structural weight is also appreciable. In particular, it should certainly be possible to build an amphibian GEM to carry 5 tons of payload with an overall length of less than 12 feet, a result of immediate interest to the U. S. Army and the U. S. Marine Corps.

CONCLUSIONS

The savings in cost and size to be expected from the use of an autopilot are so large that they will not be greatly affected by changes to the assumptions.

Moreover, most GEMs are difficult to fit with an autopilot owing to the large size and sluggish nature of the controls.

It would seem desirable to make practical tests on various forms of autopilots on a suitable machine before committing a future design to the principle.

APPENDIX II

WATER ANALOGY OF THE RECIRCULATION GEM*

The laws for the similarity of different flows about geometrically similar bodies have been known and used since the turn of the century. This includes gas-gas and gas-liquid similarities. The beauty of the water analogy used by the early investigators was the ease of obtaining flow visualization. This is, of course, useful today. However, there are serious limitations placed on the utilization of the water analogy in modern flow problems because many of the applications require account be taken of compressibility. This cannot be done using water unless one forms his analogy on a free surface.

The laws of similitude are based upon the idea that all the terms of an equation describing a physical situation must be dimensionally homogeneous. The Buckingham Pi theorem then states that the equation of interest may be reduced to a relation between a complete set of dimensionless products. Similarity simply requires the parameters for the model to be equal to those for the full-scale body.

One of the major problems in applying the similarity laws is the selection of the variables pertaining to the problem. The obvious ones for the flow in the GEM of interest are: density of fluid (ρ), velocity (v), size (l), viscosity (μ), and pressure (p). These are the usual variables in flow processes where heat transfer is not involved. However, in the present case, it is desirable to characterize the turbulent mixing by some pertinent variable. The "friction velocity" was selected for this purpose since it is supposed

*By Dr. K. Millsaps, University of Florida, Gainesville

to represent the degree of turbulence in the flow. The friction velocity is defined as:

$$v_* = \left(\frac{\tau}{\rho} \right)^{\frac{1}{2}}$$

where: τ = shear stress in the fluid. Since the density (ρ) is already contained in the list of variables, only the shear stress will be used to represent the mixing process.

The problem may now be written in functional form as:

$$f(\rho, v, l, \mu, p, \tau) = 0. \quad (212)$$

All of the variables above may be represented in a system of three fundamental dimensions, namely, mass (M), length (L), and time (T). This means three variables may be selected arbitrarily from the list as fundamental variables of the problem. Let the three be ρ , v , and μ . Now, according to Buckingham there will result three dimensionless products, which will be indicated by π_1 , π_2 , and π_3 , in which the problem may be formulated. Equation (212) is now written as:

$$\psi = (\pi_1, \pi_2, \pi_3) = 0 \quad (213)$$

where

$$\pi_1 = \pi_1(l, \rho, v, \mu)$$

$$\pi_2 = \pi_2(p, \rho, v, \mu)$$

$$\pi_3 = \pi_3(\tau, \rho, v, \mu)$$

also

$$\pi_1 = l \rho^a v^b \mu^c = (L) \left(M^a L^{-3a} \right) \left(L^b T^{-b} \right) \left(M^c L^{-c} T^{-c} \right).$$

This results in the set of equations for

$$M: \quad a + c = 0$$

$$L: \quad 1 - 3a + b - c = 0$$

$$T: \quad -b - c = 0$$

$$a = -c = b = 1 \quad \text{and}$$

$$\pi_1 = \frac{\rho v l}{\mu} \quad \text{the Reynold's number.}$$

Using the same method:

$$\pi_2 = \frac{p}{\rho v^2} \quad \text{the pressure coefficient}$$

$$\pi_3 = \frac{\tau}{\rho v^2}.$$

In the last product, τ may be written in terms of the friction factor (f), where

$$f = g(R_e) = g(\pi_1)$$

that is,

$$\tau = \text{const } f \rho v^2,$$

Therefore

$$\pi_3 = \text{const.}$$

Equation (213) now becomes:

$$\psi(R_e, C_p) = 0$$

where

R_e = Reynold's number

C_p = pressure coefficient.

Therefore, if a model test is conducted at some Reynold's number R_{e_m} and a C_{p_m} then a geometrically similar full-scale vehicle operated at the same Reynold's number will have the same pressure coefficient.

The application of this theory to the recirculating GEM flow of present interest raises the question of selecting a station in the flow at which to calculate the characteristic Reynold's number. The answer to this question lies in the fact that the entire flow field will be similar. Therefore, any convenient station will be suitable. The Reynold's number of the primary nozzle exit was selected in this report.

Experimental Program

A working two-dimensional model of a recirculating GEM was constructed to demonstrate the applicability of the water analogy to such a problem and to develop laboratory techniques. A schematic drawing is shown in Figure 138.

The pressure was measured at the indicated positions.

The model was designed so that both water and air could be used as a working fluid. The instrumentation was set up for only a so-called "quick and dirty" evaluation since the method of the water analogy was not in question. The main purpose was a feel for the operating parameters (e.g., temperature) and their effects upon results.

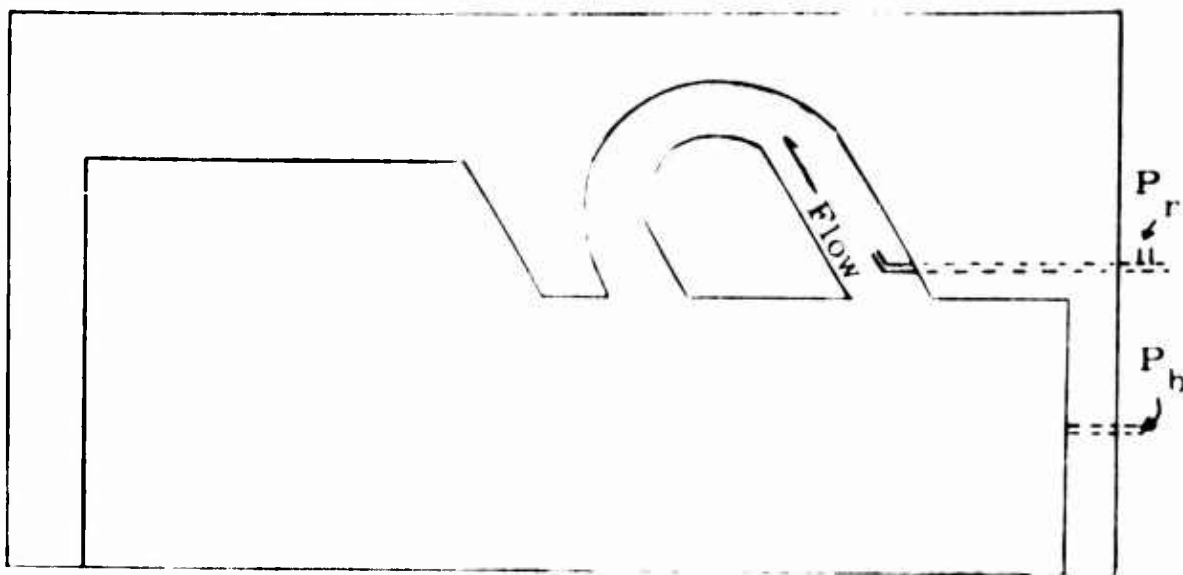


Figure 138. Sketch of Two-Dimensional Working Model

Procedure

The model was constructed in the horizontal position to avoid the effect of gravity upon the flow, as indicated by Froude's number. The tank could be held completely full of water in this position by use of a long shallow spillway (1/8" x 4"). Even with no flow, the surface tension of the water would keep the tank full, up to within 1 or 2 inches from the spillway. The surface tension did cause difficulties in the pressure readings. This will be discussed later in the report. The water flow rate was measured by using a stop watch and a graduated cylinder at the exit of the tank. The measurements were calibrated against a pressure gage on the supply pipe (indicated as p_r in Figure 138). The temperature of the water was measured by use of mercury in a glass thermometer at the exit.

The calibration of the primary nozzle used a velocity survey taken 1/16" down stream of its exit. The average of this survey is used

as the velocity of the jet. It is realized that this method is not at all accurate particularly since only a single diameter was surveyed. However, the necessary equipment was not readily available so that the averaged value was used. With this velocity, the temperature of the primary flow was calculated by use of the energy equation. The total temperature was taken as the temperature of the room in which the storage tank was located.

Pressure taps were located for P_a and P_b as indicated in Figure 138. These pressures were measured with a Meriam Micromanometer when air was used as a working fluid. When water was used, a stand-pipe was connected to a height gage by means of a flexible tube. The values for the change in pressure were obtained from the change in height required to keep the meniscus at a reference line. When this method is used, the change in height could be measured to 0.001 inch. This is not to imply that the measured pressures were this accurate. Two sources of error dropped the accuracy to something like 0.01 inch. The first source is the surface tension at the spillway under no-flow conditions. It was found that the no-flow reading would shift as much as 0.075 inch and that the zero would change with a change in the bubble at the spillway. The value of the shift given above is an extreme case. The more usual value was about 0.01 inch. The second difficulty was fluctuations in the pressure during the run caused by unsteadiness in the water supply (tap water). In addition, there seemed to be an unsteadiness in the pressure due to the flow, as is the case in most experimental work of this type. A useful technique for the latter fluctuation is to use a length of small-diameter tubing to cut down the response time of the manometer and thus to obtain an average pressure.

An Example Test Run

Water was forced through the primary jet at 15.2 fps and a temperature of 25°C. The temperature of the air was estimated to be 24°C. The simulated air velocity is calculated by using the similarity condition that the Reynold's numbers in air and water are the same.

$$v_a = \frac{v_a}{v_w} v_w \quad (214)$$

where

v = kinematic viscosity.

The kinematic viscosities were found to be:

v_a at 24°C is $0.165 \times 10^{-3} \text{ ft}^2/\text{sec}$

v_w at 25°C is $0.965 \times 10^{-5} \text{ ft}^2/\text{sec}$.

From Equation (214)

$$v_a = 260 \text{ fps.}$$

Suppose an error of 1°C is made in the temperature of the air. Then with

$$v_a \text{ at } 25^\circ\text{C} = 0.166 \times 10^{-3} \text{ ft}^2/\text{sec}$$

the velocity being simulated is, from Equation (214),

$$v_a \text{ at } 25^\circ\text{C} = 261.5 \text{ fps.}$$

So that in this range, the error in velocity due to a change in temperature is equal to 1.5 fps/°C. If the error is in the temperature of the water,

$$v_a = 265.7 \text{ fps}$$

or error = 5.7 fps/°C.

Let us see what happens in the case of the pressure coefficient (C_p).

From similarity

$$C_{p_a} = C_{p_w}$$

Therefore,

$$\frac{\Delta P_a}{\Delta P_w} = \frac{\rho_a}{\rho_w} \left(\frac{v_a^2}{v_w^2} \right) = \frac{\rho_a}{\rho_w} \left(\frac{v_a}{v_w} \right)^2$$

where

ρ = density of the fluid.

At 25°C $\rho_w = 0.997 \text{ gr/cc}$

At 24°C $\rho_a = 0.001189 \text{ gr/cc}$

all at 1 atm.

Therefore,

$$\frac{\Delta P_a}{\Delta P_{w_{25}}} = 0.3486 \quad (215)$$

Again let the air temperature vary 1°C. Then

$$\frac{\Delta P_a}{\Delta P_{w_{25}}} = 0.3517$$

or an error of 0.889%/°C.

In an actual case, the ratio of pressures was found to be:

$$\frac{\Delta P_a}{\Delta P_w} = 0.197. \quad (216)$$

The analogy was set up for air and water both being at 23°C when actually the air was at approximately 24°C while the water was at 25°C. Ten per cent of the error in Equation (216) can be accounted for by the 1°C air temperature and 2°C water temperature error.

Photography

In addition to pressure measurements, the water channel was used for a motion picture study of the flow in a recirculation GEM. The flow was made visible by introducing red food dye into the primary nozzle. The pictures were made with a Bolex motion picture camera with Kodachrome II type A film. The most successful runs were made at 64 frames/second giving a shutter speed of 1/120 second. The ASA rating of the film is 40, which worked very well with a lense opening f/5.6 using three small tungsten floods.

Conclusion

Three conclusions can be drawn from this work:

1. The method may certainly be used for qualitative work such as optimization of the geometry. If the model is operating in the same Reynold's number range as the full-scale vehicle, the trends will surely be the same in both cases. For example, the geometry yielding the maximum base pressure will be the same in water and air.

2. Quantitative results may also be obtained from the water analogy. This would be accomplished by operating the water model over a range of Reynold's numbers and recording the pressures at the desired locations on the model. Plots of pressure coefficient versus Reynold's number for various positions from the water test would result in a curve that would give the pressure at corresponding points on the full-scale vehicle once the Reynold's number of the primary jet is known.

Too much emphasis cannot be placed on the care with which the experimental setup is made. Previous calculations show that for quantitative results the temperature of the water must be maintained within at least 1°C during each test run. The velocity, and hence the pressure of the primary jet, must be held constant. These requirements seem to indicate an indoor tank that is allowed to come to thermal equilibrium before each run.

It should be pointed out that although all the work in this report was performed in two dimensions, there are no restrictions. A three-dimensional model should work equally well.

3. The water analogy should prove very useful in that the flow visualization may be easily accomplished and photographed. This should prove useful in studying jet mixing as well as the general flow. For example, it seems that flow visualization would be appropriate in studying the sensitivity of the position of the primary jet in the channel and in three dimensions, the corner flow problem.

In summing up, it is felt that the water analogy will prove to be a very valuable tool in the design and understanding of the flow in a recirculating GEM.

•

APPENDIX III

VEHICLE PERFORMANCE ESTIMATE (IBM MACHINE PROGRAMMED)

Lift and propulsion power requirements are computed for the ejector recirculation ground effect machines in hovering and forward flight. Efficiencies, drag coefficients, augmentation ratio and planform geometry (Elliptical or Rectangular) are among the input items. Four calculation options are available:

- Option 1 Generalized nondimensional performance computed over a range of lift coefficients.
- Option 2 Vehicle lift and base pressure specified. Computes GEM size and power required at a specified flight velocity.
- Option 3 Vehicle size and base pressure specified. Computes total lift and power required at a specified flight velocity.
- Option 4 Vehicle size and lift specified. Computes base pressure and power required over a range of flight velocities.

Assume:

- 1 Compressor Inlet Pressure = $\eta_r q_\infty$
- 2 Cushion Back Pressure = $P_B/2$
- 3 $P_o' = f(q_j, m/m, \text{ejector design})$
- 4 $P_B = q_j \left(1 - e^{-2(t/h)(1 + \cos \theta)}\right)$

$$P_j = \left(\frac{1}{\epsilon_c \cdot \epsilon_l \cdot \epsilon_R} \right) \times \frac{m V_j^2}{2} - \frac{m' V_\infty^2}{2}$$

ϵ_c = compressor efficiency
 ϵ_l = line efficiency
 ϵ_R = ejector efficiency
 $\epsilon_o = \epsilon_c \cdot \epsilon_l \cdot \epsilon_R$

$$P_j = \frac{m}{2\epsilon_o} \left(V_j^2 \right) - \frac{m V_\infty^2}{2} = \frac{m}{2} \left[\frac{2}{\rho \epsilon_o} \left(\frac{\rho V_j^2}{2} \right) - \frac{2}{\rho(ma)} \left(\frac{\rho V_\infty^2}{2} \right) \right]$$

$$P_j = \frac{m}{\rho} \left[\frac{q_j}{\epsilon_o} - \frac{q_\infty}{ma} \right]$$

$$m = \rho V_j t C$$

$$P_j = V_j t C \left[\frac{q_j}{\epsilon_o} - \frac{q_\infty}{ma} \right]$$

$$V_j = \sqrt{\frac{2}{\rho} q_j}$$

$$P_j = \sqrt{\frac{2}{\rho} q_j} \left[\frac{q_j}{\epsilon_o} - \frac{q_\infty}{ma} \right] t C$$

$$L = P_B S_B + 0.4 q_\infty S + J(\sin \theta_1 + \sin \theta_2) - (\text{primary momentum and cavity lift})$$

$$J = 2 q_j t C$$

$$L = P_B S_B + 0.4 q_\infty S + 2 q_j t C (\sin \theta_1 + \sin \theta_2)$$

$$L = q_j \left(1 - e^{-2x} \right) S_B + 0.4 q_\infty S + 2 q_j t C (\sin \theta_1 + \sin \theta_2)$$

$$L - 0.4 q_\infty S = \left[1 - e^{-2x} + \frac{2 t C (\sin \theta_1 + \sin \theta_2)}{S_B} \right] q_j S_B$$

$$q_j = \frac{L}{S_B} \frac{\left(1 - 0.2 \frac{2}{C_L}\right)}{\left[\left(1 - e^{-2x}\right) + \frac{2 t C (\sin \theta_1 + \sin \theta_2)}{S_B}\right]}$$

$$P_j = \sqrt{\frac{2}{\rho}} (q_j)^{3/2} \left[\frac{1}{\epsilon_0} - \frac{1}{ma} \frac{q_\infty}{q_j} \right] t C$$

$$\left(\frac{L}{q_\infty S} - 0.4 \right) = \frac{q_j}{q_\infty} \left(1 - e^{-2x} \right) \left(\frac{S_B}{S} \right) + \left(\frac{q_j}{q_\infty} \right)^2 \frac{\left(\frac{t}{h} \right) (\sin \theta_1 + \sin \theta_2)}{\left(\frac{S}{hC} \right)}$$

$$\frac{q_\infty}{q_j} = \frac{1}{(C_L - 0.4)} \left[\left(1 - e^{-2x} \right) \frac{S_B}{S} + \frac{2 \left(\frac{t}{h} \right) (\sin \theta_1 + \sin \theta_2)}{\frac{S}{hC}} \right]$$

$$P_j = \sqrt{\frac{2}{\rho}} \left(\frac{L}{S} \right)^{3/2} \left[\frac{\left(1 - 0.2 \frac{2}{C_L} \right)}{\left(1 - e^{-2x} \right) \frac{S_B}{S} + \frac{2 \frac{t}{h} (\sin \theta_1 + \sin \theta_2)}{\left(\frac{S}{hC} \right)}} \right]^{3/2} \frac{1}{\epsilon_0} -$$

$$\frac{1}{ma} \left\{ \left(\frac{2}{C_L} \right) \left(\frac{0.5}{1 - 0.2 \frac{2}{C_L}} \right) \left[\left(1 - e^{-2x} \right) \frac{S_B}{S} + \frac{2 \left(\frac{t}{h} \right) (\sin \theta_1 + \sin \theta_2)}{\left(\frac{S}{hC} \right)} \right] \right\} t C$$

$$\rho_j = \frac{P_j}{\frac{L^{3/2}}{\sqrt{\rho S}}}$$

$$\rho_j = \frac{\sqrt{2} \left(1 - 0.2 \frac{2}{C_L}\right)^{\frac{1}{2}} \left(\frac{t}{h}\right)}{\left(\frac{S}{hC}\right) \left[\left(1 - e^{-2x}\right) \frac{S_B}{S} + \frac{2 \left(\frac{t}{h}\right) (\sin \theta_1 + \sin \theta_2)}{\left(\frac{S}{hC}\right)} \right]^{3/2}} \left[\frac{1}{c_o} \left(1 - 0.2 \frac{2}{C_L}\right) - \right. \\ \left. \left(\frac{2}{C_L}\right) \left(\frac{0.5}{ma}\right) \left\{ \left(1 - e^{-2x}\right) \frac{S_B}{S} + \frac{2 \left(\frac{t}{h}\right) (\sin \theta_1 + \sin \theta_2)}{\left(\frac{S}{hC}\right)} \right\} \right]$$

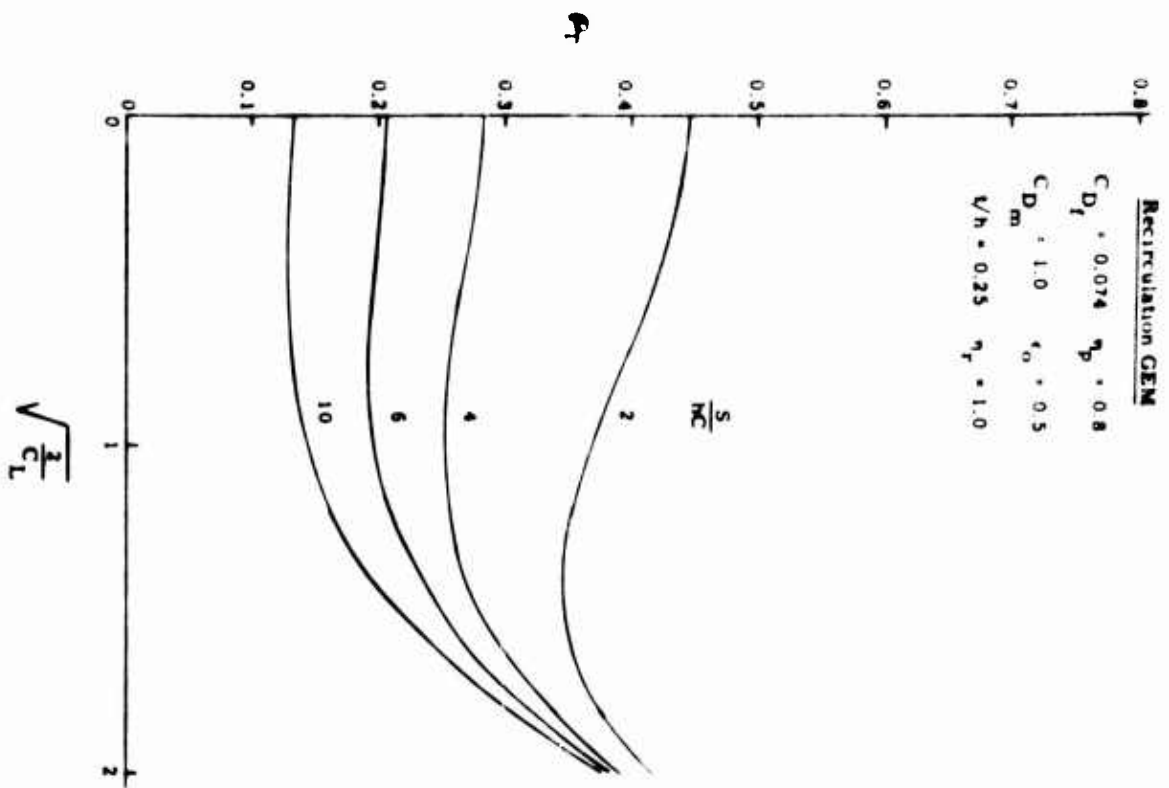


Figure 139. Total Power Parameter

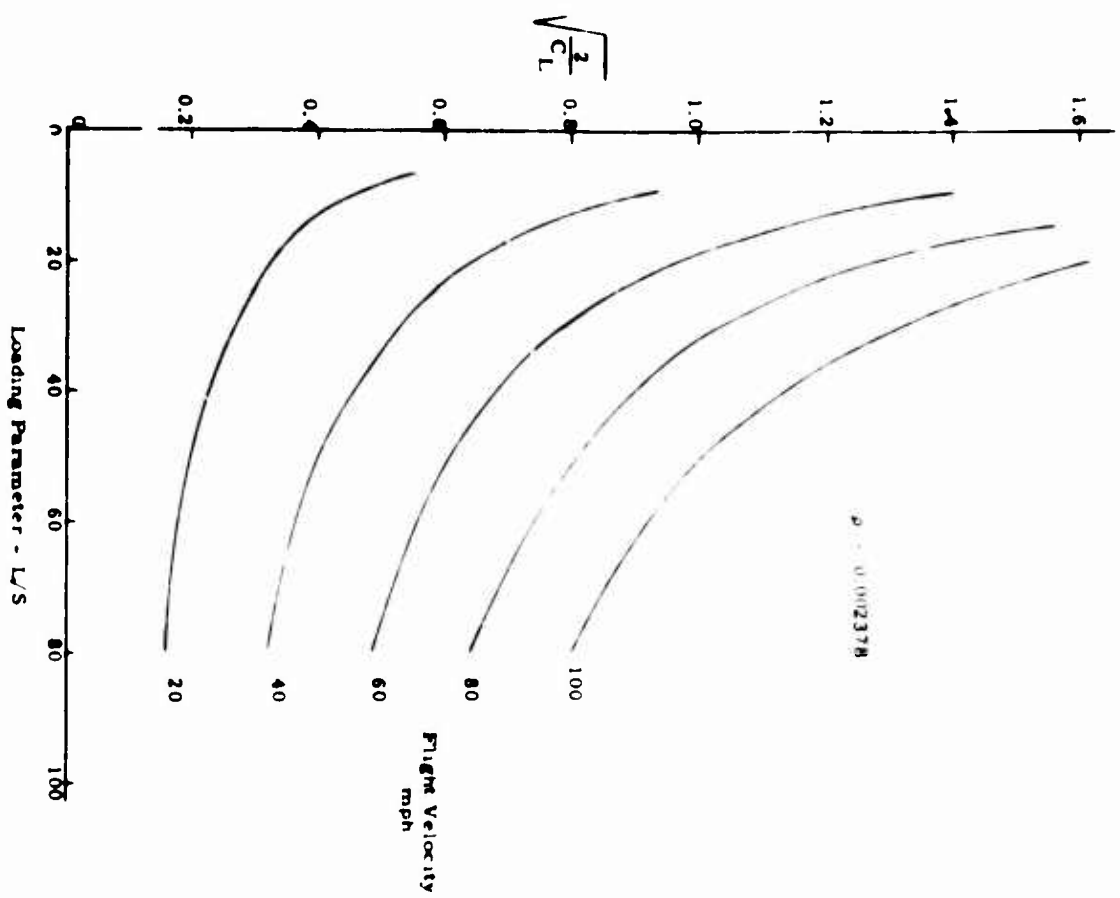


Figure 140. Lift Coefficient Versus Loading Parameter

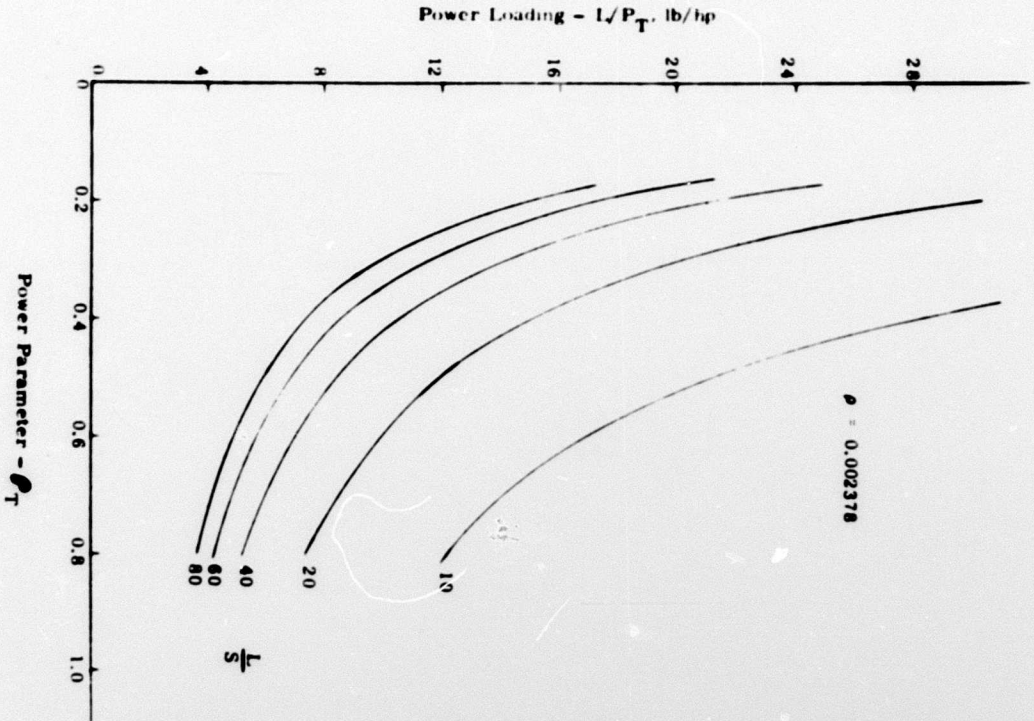


Figure 141. Power Loading Versus Power Parameter

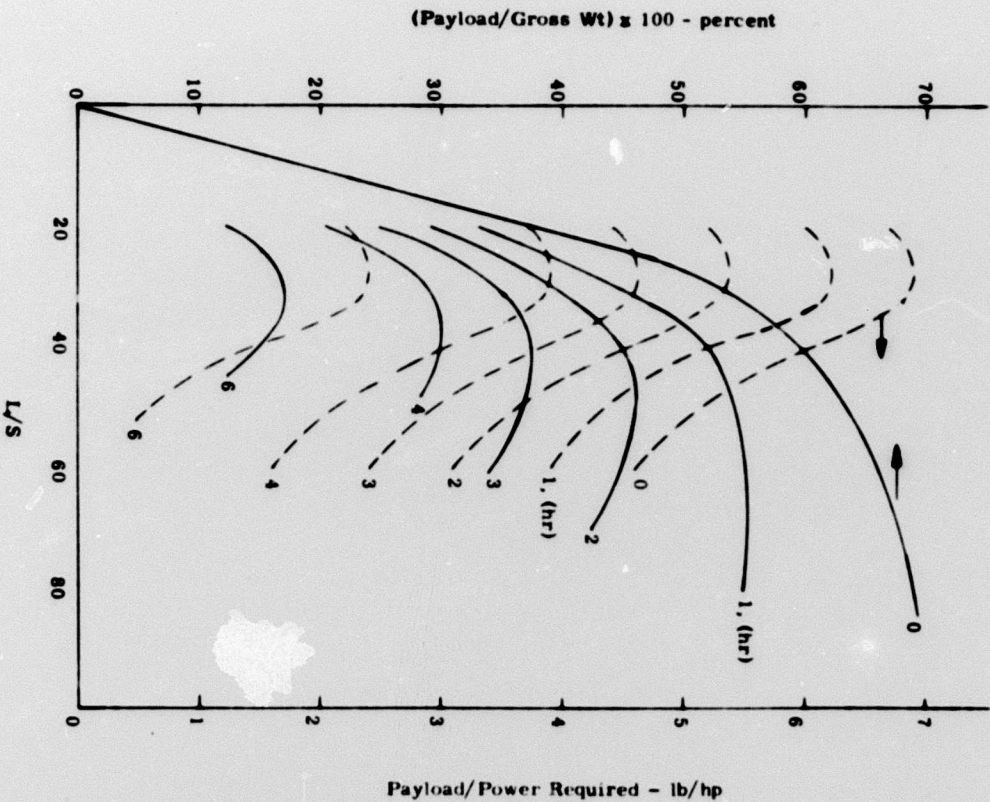


Figure 142. Ejectijet GEM Performance, $60,000 < W_g < 100,000$

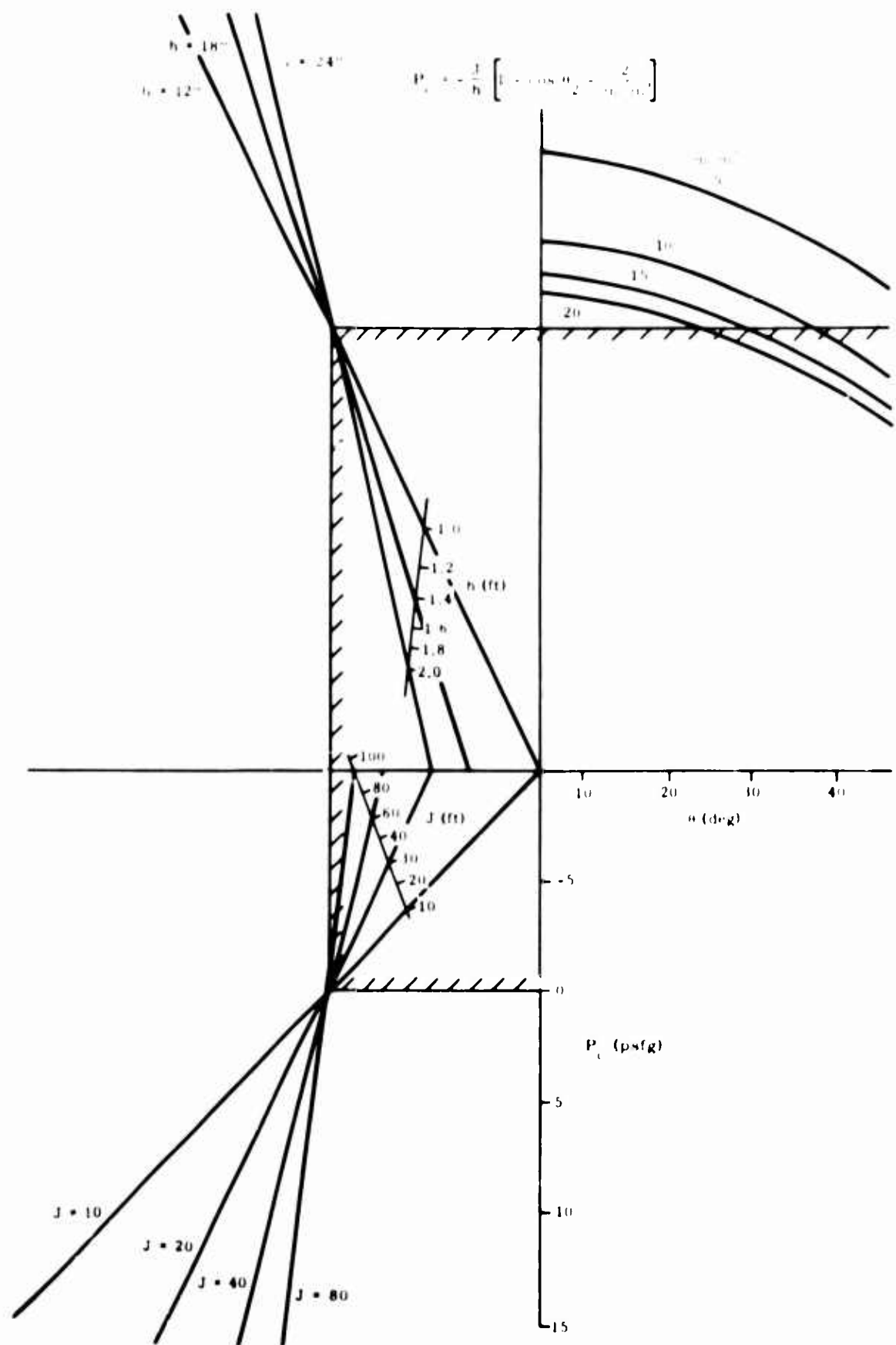


Figure 143. Theoretical Cavity Pressure

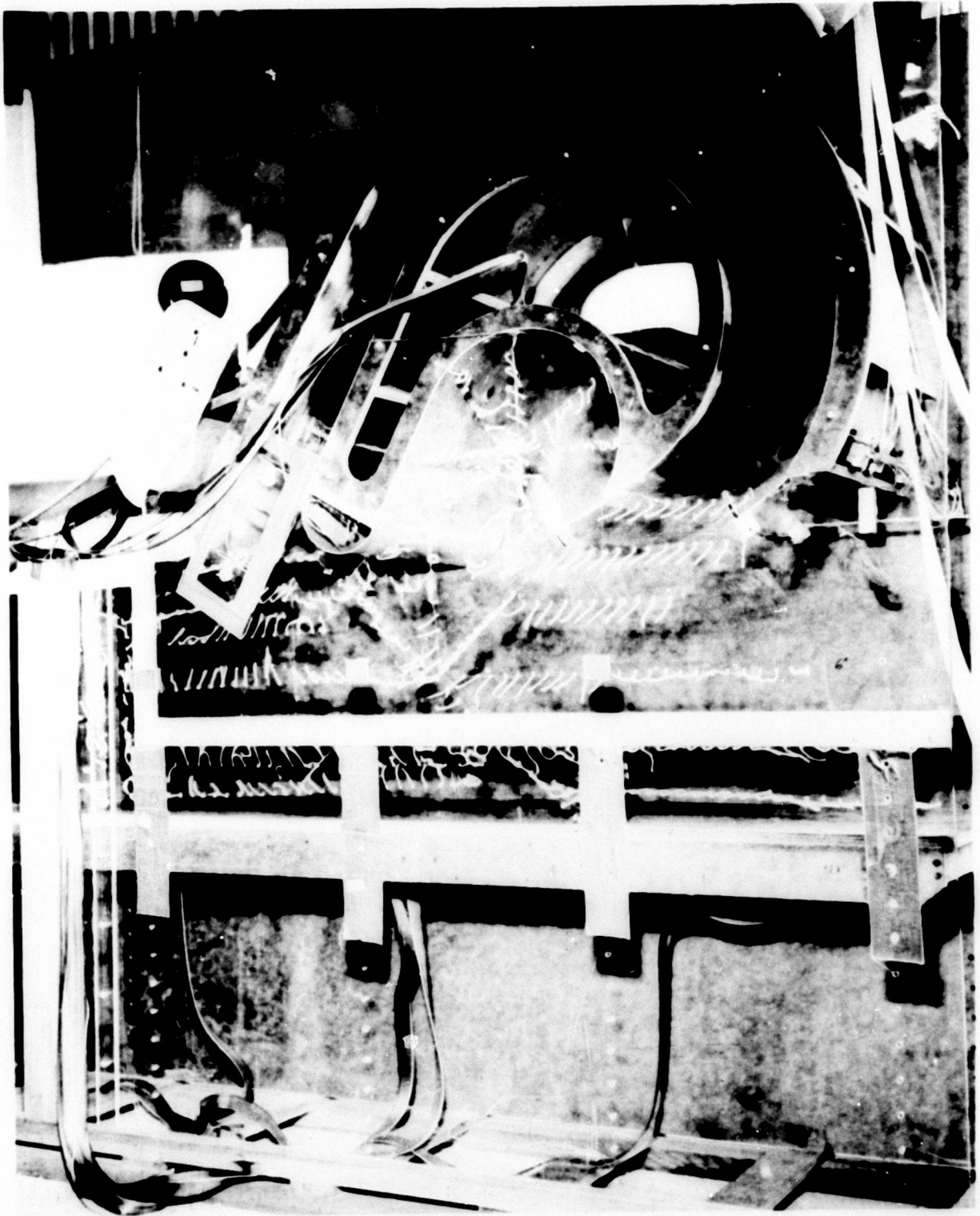


Figure 144. Visualization of Flow

DISTRIBUTION

U. S. Army Materiel Command	7
U. S. Army Mobility Command	4
U. S. Army Aviation Materiel Command	4
U. S. Strike Command	1
Chief of R&D, D/A	2
U. S. Army Transportation Research Command	68
U. S. Army Research and Development Group (Europe)	2
U. S. Army Engineer Research and Development Laboratories	4
U. S. Army Limited War Laboratory	1
U. S. Army Human Engineering Laboratories	1
Army Research Office-Durham	2
U. S. Army Polar Research and Development Center	1
U. S. Army Medical Research and Development Command	1
U. S. Army Engineer Waterways Experiment Station	1
U. S. Army Combat Developments Command	
Transportation Agency	1
U. S. Army War College	1
U. S. Army Command and General Staff College	1
U. S. Army Transportation School	1
U. S. Army Tank-Automotive Center	2
U. S. Army Arctic Test Board	1
U. S. Army Transportation Board	1
U. S. Army Airborne, Electronics and Special Warfare Board	1
Chief of Naval Operations	1
Bureau of Ships	1
Bureau of Naval Weapons	2
Bureau of Supplies and Accounts, N/D	1
U. S. Naval Supply Research and Development Facility	1
U. S. Naval Postgraduate School	1
David Taylor Model Basin	1
Marine Corps Landing Force Development Center	1
Marine Corps Educational Center	1
Ames Research Center, NASA	2
NASA-LRC, Langley Station	2
Lewis Research Center, NASA	2
NASA Representative, Scientific and Technical Information Facility	2
Human Resources Research Office	2
U. S. Army Standardization Group, Canada	2
Canadian Liaison Officer, U. S. Army Transportation School	3
British Army Staff, British Embassy	4
U. S. Army Standardization Group, U. K.	1
Defense Documentation Center	10
U. S. Government Printing Office	1

BLANK PAGE

<p>Martin Company (Orlando Division, Orlando, Fla) RECIRCULATION PRINCIPLE FOR GROUND EFFECT MACHINE PRELIMINARY DESIGN OF A RESEARCH VEHICLE K R Coesair Report No. OR 3725-1, TRCUM Technical Rept 66-27, August 1966, 295 pp (Contract DA 44-177- AMC 96(T) Task ID021701A04804 (Unclassified Report</p> <p>An analytical and experimental investigation was conducted in conjunction with the preliminary de- sign of an ejector powered recirculation ground effect machine. The adequacy of the primary air supply system coupled with reliable performance data, assures the feasibility of constructing a full scale operating vehicle adequate for the environ- mental research and performance evaluation of the recirculation GEM</p>	<ol style="list-style-type: none"> 1 Fluid Dynamics 2 Aerodynamics 3 GEM Machines 4 Contract DA44-177-AMC 96(T) 	<p>Martin Company (Orlando Division, Orlando, Fla) RECIRCULATION PRINCIPLE FOR GROUND EFFECT MACHINE PRELIMINARY DESIGN OF A RESEARCH VEHICLE K R Coesair Report No. OR 3725-1, TRCUM Technical Rept 66-27, August 1966, 295 pp (Contract DA 44-177- AMC 96(T) Task ID021701A04804 (Unclassified Report</p> <p>An analytical and experimental investigation was conducted in conjunction with the preliminary de- sign of an ejector powered recirculation ground effect machine. The adequacy of the primary air supply system coupled with reliable performance data, assures the feasibility of constructing a full scale operating vehicle adequate for the environ- mental research and performance evaluation of the recirculation GEM</p>	<ol style="list-style-type: none"> 1 Fluid Dynamics 2 Aerodynamics 3 GEM Machines 4 Contract DA44-177-AMC 96(T)
<p>Martin Company (Orlando Division, Orlando, Fla) RECIRCULATION PRINCIPLE FOR GROUND EFFECT MACHINE PRELIMINARY DESIGN OF A RESEARCH VEHICLE K R Coesair Report No. OR 3725-1, TRCUM Technical Rept 66-27, August 1966, 295 pp (Contract DA 44-177- AMC 96(T) Task ID021701A04804 (Unclassified Report</p> <p>An analytical and experimental investigation was conducted in conjunction with the preliminary de- sign of an ejector powered recirculation ground effect machine. The adequacy of the primary air supply system coupled with reliable performance data, assures the feasibility of constructing a full scale operating vehicle adequate for the environ- mental research and performance evaluation of the recirculation GEM</p>	<ol style="list-style-type: none"> 1 Fluid Dynamics 2 Aerodynamics 3 GEM Machines 4 Contract DA44-177-AMC 96(T) 	<p>Martin Company (Orlando Division, Orlando, Fla) RECIRCULATION PRINCIPLE FOR GROUND EFFECT MACHINE PRELIMINARY DESIGN OF A RESEARCH VEHICLE K R Coesair Report No. OR 3725-1, TRCUM Technical Rept 66-27, August 1966, 295 pp (Contract DA 44-177- AMC 96(T) Task ID021701A04804 (Unclassified Report</p> <p>An analytical and experimental investigation was conducted in conjunction with the preliminary de- sign of an ejector powered recirculation ground effect machine. The adequacy of the primary air supply system coupled with reliable performance data, assures the feasibility of constructing a full scale operating vehicle adequate for the environ- mental research and performance evaluation of the recirculation GEM</p>	<ol style="list-style-type: none"> 1 Fluid Dynamics 2 Aerodynamics 3 GEM Machines 4 Contract DA44-177-AMC 96(T)

<p>Martin Company, Orlando Division, Orlando, Fla RECIRCULATION PRINCIPLE FOR GROUND EFFECT MACHINE PRELIMINARY DESIGN OF A RESEARCH VEHICLE K R Coasair Report No. OR 3725-1, TRFCON Technical Rept 64 27 August 1964, 295 pp (Contract DA 44-177- AMC 96(T) Task 1D021701A04804 Unclassified Report</p> <p>An analytical and experimental investigation was conducted in conjunction with the preliminary de- sign of an ejector powered recirculation ground effect machine. The adequacy of the primary air supply system, coupled with reliable performance data, assures the feasibility of constructing a full scale operating vehicle adequate for the environ- mental research and performance evaluation of the recirculation GEM</p>	<ol style="list-style-type: none"> 1 Fluid Dynamics 2 Aerodynamics 3 GEM Machines 4 Contract DA44-177-AMC 96(T)
<p>Martin Company, Orlando Division, Orlando, Fla RECIRCULATION PRINCIPLE FOR GROUND EFFECT MACHINE PRELIMINARY DESIGN OF A RESEARCH VEHICLE K R Coasair Report No. OR 3725-1, TRFCON Technical Rept 64 27 August 1964, 295 pp (Contract DA 44-177- AMC 96(T) Task 1D021701A04804 Unclassified Report</p> <p>An analytical and experimental investigation was conducted in conjunction with the preliminary de- sign of an ejector powered recirculation ground effect machine. The adequacy of the primary air supply system, coupled with reliable performance data, assures the feasibility of constructing a full scale operating vehicle adequate for the environ- mental research and performance evaluation of the recirculation GEM</p>	<ol style="list-style-type: none"> 1 Fluid Dynamics 2 Aerodynamics 3 GEM Machines 4 Contract DA44-177-AMC 96(T)
<p>Martin Company, Orlando Division, Orlando, Fla RECIRCULATION PRINCIPLE FOR GROUND EFFECT MACHINE PRELIMINARY DESIGN OF A RESEARCH VEHICLE K R Coasair Report No. OR 3725-1, TRFCON Technical Rept 64 27 August 1964, 295 pp (Contract DA 44-177- AMC 96(T) Task 1D021701A04804 Unclassified Report</p> <p>An analytical and experimental investigation was conducted in conjunction with the preliminary de- sign of an ejector powered recirculation ground effect machine. The adequacy of the primary air supply system, coupled with reliable performance data, assures the feasibility of constructing a full scale operating vehicle adequate for the environ- mental research and performance evaluation of the recirculation GEM</p>	<ol style="list-style-type: none"> 1 Fluid Dynamics 2 Aerodynamics 3 GEM Machines 4 Contract DA44-177-AMC 96(T)
<p>Martin Company, Orlando Division, Orlando, Fla RECIRCULATION PRINCIPLE FOR GROUND EFFECT MACHINE PRELIMINARY DESIGN OF A RESEARCH VEHICLE K R Coasair Report No. OR 3725-1, TRFCON Technical Rept 64 27 August 1964, 295 pp (Contract DA 44-177- AMC 96(T) Task 1D021701A04804 Unclassified Report</p> <p>An analytical and experimental investigation was conducted in conjunction with the preliminary de- sign of an ejector powered recirculation ground effect machine. The adequacy of the primary air supply system, coupled with reliable performance data, assures the feasibility of constructing a full scale operating vehicle adequate for the environ- mental research and performance evaluation of the recirculation GEM</p>	<ol style="list-style-type: none"> 1 Fluid Dynamics 2 Aerodynamics 3 GEM Machines 4 Contract DA44-177-AMC 96(T)